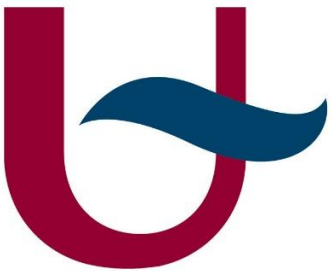

Faculteit Wetenschappen

Departement Fysica

Study of the effect of cation substitution on the local structure and the properties of perovskites and Li-ion battery cathode materials

---

Studie van het effect van kation substitutie op de lokale structuur en de eigenschappen van perovskieten en Li-ion batterij kathodematerialen

Proefschrift voorgelegd tot het behalen van de graad van
Doctor in de Wetenschappen: Fysica
aan de Universiteit Antwerpen, te verdedigen door:

Mylène Hendrickx

Promotor
Prof. Dr. Joke Hadermann

Antwerpen, 2020

Doctoral Committee

Chairman

Prof. Dr. Jan Sijbers, University of Antwerp – Belgium

Promotor

Prof. Dr. Joke Hadermann, University of Antwerp – Belgium

Members

Prof. Dr. Sofie Cambré, University of Antwerp – Belgium

Prof. Dr. Dirk Lamoen, University of Antwerp – Belgium

Prof. Dr. An Hardy, University of Hasselt – Belgium

Prof. Dr. Peter Battle, University of Oxford – England

Contact Information

Mylène Hendrickx
University of Antwerp – Department of Physics
EMAT – Electron Microscopy for Materials Science
Groenenborgerlaan 171, B-2020 Antwerp
Belgium
Mylene.Hendrickx@uantwerpen.be

Table of contents

Preface

The physical properties of materials are determined by the type and arrangement of the atoms present in the material. Therefore, the characterization of the crystal structure is necessary to investigate the physical properties. Understanding the relationship between the crystal structure and the physical properties allows us to adjust the properties by changing the composition and symmetry using cation substitution.

In this thesis, I investigated the effect of cation substitution on the crystal structure of two main groups of materials: perovskites and Li-ion battery cathode materials using transmission electron microscopy. In the first chapter, **Chapter 1**, I explain in more detail the aim of this study, followed by an introduction to the used experimental techniques to determine the crystal structure of the different materials. The following chapters can be divided into three parts.

In **Part I**, I studied how the crystal structure of perovskites changes when different cations are substituted, and how it affects the physical properties.
Chapter 2 provides an introduction about the different types of distortion that can occur in perovskites along with the physical properties that are related to the studied materials. In **Chapter 3,** I report on the structural investigation of two series ALa$_2$FeBSbO$_9$ and A_2LaFe$_2$SbO$_9$ with cation substitution A = Ca, Sr, Ba, and B = Ni, Co. The studies revealed that the substitution of the A and B cation changes the symmetry of the crystal structure and the degree of B cation ordering, which results in different magnetic properties. The crystal structure of the perovskite Zn$_2$FeBO$_6$ with cation substitution B = Nb and Ta is solved in **Chapter 4**, where the local structural variations discovered by TEM explain the measured physical properties. This part ends with a **conclusion** about the complexity of cation substitution in perovskites.

In **Part II**, I studied the structure evolution of layered Li-ion battery cathode materials during electrochemical cycling and how the cation substitution and the synthesis affects the crystal structure and electrochemical properties.
Chapter 5 provides a brief overview of Li-ion batteries and the relationship between the crystal structure and their performance. In **Chapter 6**, I examine the influence of the synthesis on the crystal structure, performance and structure evolution upon charging and discharging of a well-known cathode material: Li-rich Mn-rich $Li_{1.2}Ni_{0.13}Mn_{0.54}Co_{0.13}O_2$ (LMR-NMC). In **Chapter 7** and **Chapter 8**, I investigate two types of cation substitution to improve the electrochemical performance: Sn substitution in LMR-NMC and Ti substitution in Li_2MnO_3. At the end of this part, a **conclusion** is drawn about the influence of the synthesis and the cation substitution on the crystal structure and electrochemical performance of LMR-NMC and Li_2MnO_3. Further, I also demonstrate the need for *in-situ* experiments to study the structural changes caused by electrochemical cycling directly.

Part III is dedicated to my first attempts to work with an electrochemical liquid cell inside the TEM, where I investigated the abilities to follow the structure evolution of layered Li-ion battery cathode materials *in-situ* in the TEM during electrochemical cycling.
In **Chapter 9**, I first explain the importance of these *in-situ* experiments. Then the challenges and problems that I have encountered during the experiments are pointed out, along with the possible solutions to tackle these problems. In the conclusion of this part, the following steps needed to succeed in the *in-situ* experiment are summarized.

Finally, the thesis ends with a **general conclusion** about the work discussed in the thesis and an **outlook** about the future developments that can be done on the different studies.

List of abbreviations

1D	One dimensional
2D	Two dimensional
3D	Three dimensional
ABF	Annular bright-field
AFM	Antiferromagnetic
CW	Curie-Weiss law
DMC	Dimethyl carbonate
EC	Ethylene carbonate
ED	Electron diffraction
EDT	Electron diffraction tomography
EDX	Energy-dispersive X-ray spectroscopy
FM	Ferromagnetic
(FP)DFT	(First-principle) density functional theory
FFT	Fast Fourier transform
FOJT	First-order Jahn-Teller
HAADF	High-angle annular dark-field
HPT	High-pressure and temperature
HT	High-temperature
LCN	Local charge neutrality
NPD	Neutron powder diffraction
SAED	Selected area electron diffraction
SEM	Scanning electron microscopy
SOJT	Second-order Jahn-Teller
STEM	Scanning transmission electron microscopy
SPXD	Synchrotron powder X-ray diffraction
TEM	Transmission electron microscopy
T_B	Burns temperature
T_C	Curie temperature
T_N	Néel temperature
XRPD	X-ray powder diffraction

Chapter 1. Introduction

A crystalline material consists of an arrangement of atoms that are periodically ordered in the three dimensional (3D) crystal lattice, which is called the crystal structure. The type and the arrangement of the atoms determine the physical properties of the material. Therefore, to investigate the physical properties, the crystal structure has to be determined, and more importantly, the correlation between the crystal structure and the physical properties. Understanding the relationship between the structure and the properties allows adjusting the properties by changing the composition and symmetry of the material using cation substitution. For example, $SrSnO_3$ is a diamagnetic semiconductor [1], but when Co or Mn is substituted, the material becomes, in the case of Sr_2SnCoO_6, a ferromagnetic metal and for Sr_2SnMnO_6 a ferromagnetic semiconductor [2]. By investigating how the crystal structure and the corresponding properties change for specific cation substitutions, a guideline can be designed to help researchers to choose the best cation substitution in order to produce their desired physical properties.

The family of perovskite materials is well-known for its compositional flexibility that results in a wide variety of physical properties. Therefore, cation substitution in perovskites is widely studied to find new materials with properties, such as magnetoelectricity, which is of great importance in micro- and nano-electronics. During my PhD, I investigated a number of series of cation substitution in perovskites, of which I describe three different series in the first part of my thesis.

Furthermore, cation substitution is also used to find new materials that exhibit similar properties, but that can replace the expensive or toxic materials that are currently used in applications. For example, for lithium batteries, $LiCoO_2$ is a widely used cathode material, but cobalt is very rare and toxic. Therefore, cation substitution is used to find new cathode materials that are safer and less expensive, but also exhibit better electrochemical performance. In the second part of my thesis, I focus on cation substitution in layered Li-ion battery cathode materials.

In order to investigate the crystal structure, waves should be used that can interact with the crystal lattice, which means that the incident wavelength must be of the order of magnitude of the distance between the atoms. Electrons, neutrons and X-rays are all suitable for structure characterization. Electrons interact very strongly with matter and can only reach a few hundred angstroms (Å) in the crystal before they start to lose energy due to the multiple scattering and inelastic interactions with atoms. The major advantage of electrons (for both imaging and diffraction techniques) is that areas of just a few hundred Å of a crystal can be studied, in contrast to X-rays and neutrons. The latter two require a large volume of the specimen due to the low incident beam intensity (neutrons) or low interaction (X-rays) compared to electrons. Due to the relatively large volume needed for neutrons and X-rays, powder diffraction is often used. In that case, the diffraction pattern consists of a line profile, showing intensity versus collection angle, that only provides information about the average structure. Moreover, the line profile suffers from peak broadening and peak overlap, and structures determined from powder diffraction patterns are therefore often ambiguous. Furthermore, the scattering function of electrons is proportional to the atomic number Z by a factor 1/3 ($\sim Z^{1/3}$), while the factor for X-rays is 1 ($\sim Z$). This means that heavy atoms scatter X-rays much stronger than light elements such as oxygen, which makes it more difficult to obtain information of light elements nearby heavy elements in the case of X-ray diffraction than for electrons.

As the physical properties of the material strongly depend on the crystal structure, local variations in the structure can affect the properties. Therefore, we investigate the crystal structure at local scale with electrons in order to determine both the local and average structure. In some cases, we will combine electron microscopy with X-ray powder diffraction (XRPD) and/or neutron powder diffraction (NPD). XRPD and NPD provide information about the average structure, while electron microscopy can determine the local structure. Furthermore, neutrons are scattered by the nuclei and the magnetic spin of electrons, while electrons are scattered by the electrostatic potential. Consequently, neutron diffraction provides information about the magnetic nature of the material, which will be used to investigate the physical properties.

1.1. Goal of the thesis

The goal of this study is to characterize the crystal structure of new materials and to relate it to their physical properties in order to investigate the role of the cation substitution. More specific objectives can be summarized for the perovskites and the Li-ion battery cathode materials separately:

Objectives for the study of the perovskite materials:

- What are the average and local crystal structure of the new perovskites?
- If local variations are present in the structure, how are they related to the cation substitution?
- How does the cation substitution change the physical properties?
- Can we predict how the structure and physical properties will change according to the choice of cation substitution?

Objectives for the study of the Li-ion battery cathode materials:

- What is the crystal structure of the layered cathode materials, and how does the structure change upon electrochemical cycling?
- What is the effect of the synthesis on the crystal structure and the electrochemical properties?
- Which cation substitutions should we use to mitigate the voltage fade of the battery?
- Is it possible to investigate the crystal structure during cycling in an electrochemical liquid cell inside the TEM?

1.2. Strategy of the analysis

To characterize the crystal structure of the materials, we have to determine the unit cell parameters, the symmetry and the composition of these materials. For the determination of the unit cell parameters and symmetry, we used the diffraction technique of selected area electron diffraction (SAED), and the imaging techniques of high-angle annular dark-field scanning transmission electron microscopy (HAADF-STEM) and annular bright-field scanning transmission electron microscopy (ABF-STEM). We investigated the composition of the studied materials using energy-dispersive X-ray spectroscopy (STEM-EDX).

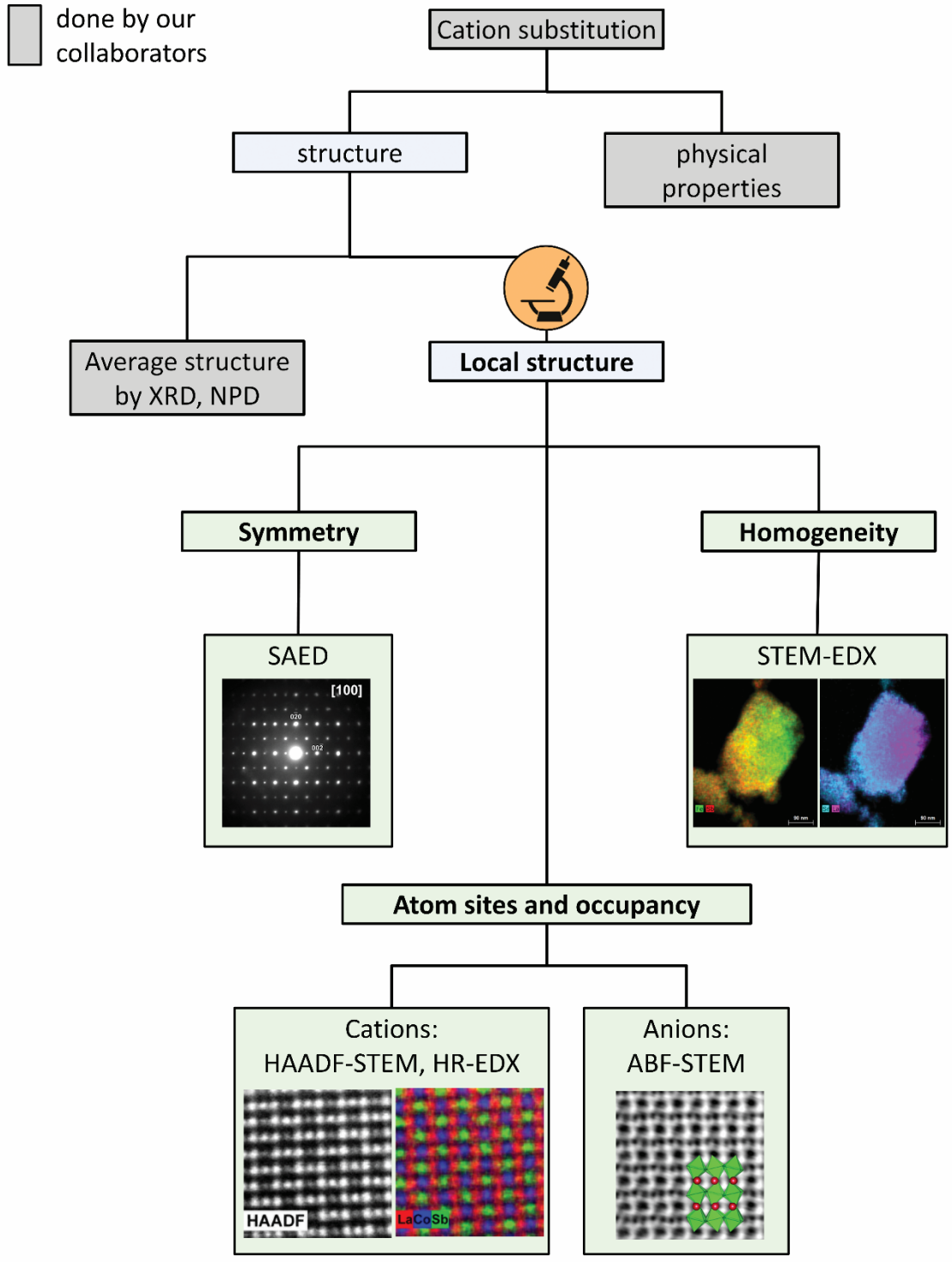

Figure 1. *Work scheme illustrating the research of this thesis. When cation substitution is applied, the crystal structure and the corresponding physical properties of the new material are investigated. The average crystal structure is investigated by powder diffraction using X-rays and/or neutrons. The local structure is investigated by transmission electron microscopy, where different techniques are performed to extract different types of information.*

1.3. Basics of the applied techniques

As all the techniques that I have used to investigate the crystal structure are based on transmission electron microscopy (TEM), I will first explain the transmission electron microscope and the interactions that occur between the electron beam and the sample in order to explain how we extract the information about the crystal structure using these techniques. Readers familiar with these techniques can skip this part as it holds no research results specific to this thesis.

1.3.1. Transmission electron microscopy

A transmission electron microscope is composed of an electron gun, a column containing a series of electromagnetic lenses with apertures, and different types of electron detectors located at the end of the column. The microscope is connected to a vacuum system to achieve a pressure lower than 10^{-5} Pa within the column to reduce possible side interactions of the electron beam with particles in the column, as electrons are strong scatters [3].

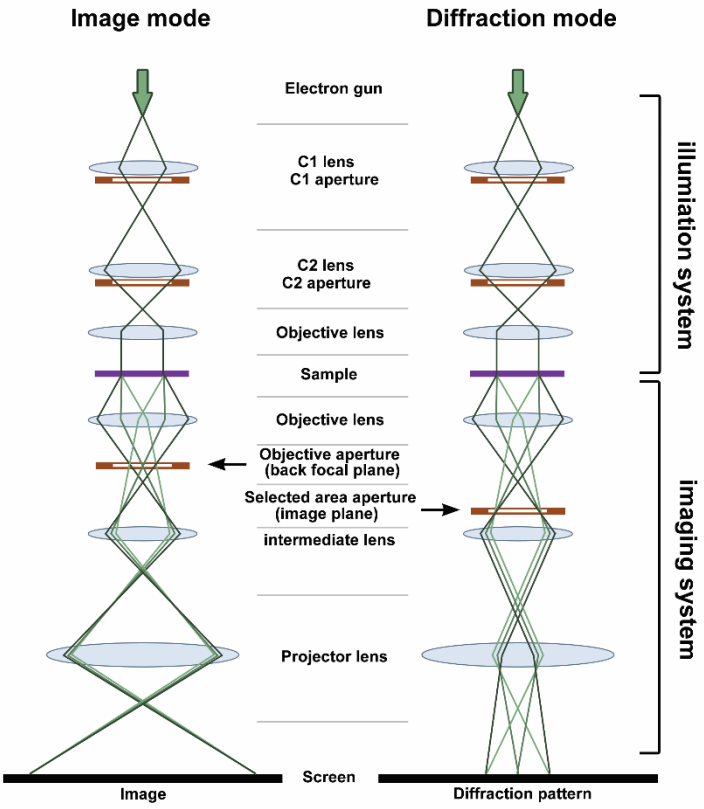

Figure 2. *Simplified illustration of the electron beam path through the column of the TEM, based on [3].*

The electron gun generates electrons with a given kinetic energy controlled by the accelerator, which is placed directly under the electron gun. The accelerated electrons then enter the column, where the sample stage is located in the middle. The lenses above the sample correspond to the illumination system and are responsible for the formation of the electron beam onto the sample. The electrons interact with the sample, and the scattered electron rays interfere with each other and generate a diffraction pattern in the back focal plane of the objective lens and form the image in the image plane of the objective lens (see **Figure 2**). The last part of the column is the imaging system that determines how the image or diffraction pattern is formed and allows to switch between the visualization of the image and the diffraction pattern.

Figure 2 illustrates a simplified version of the electron rays that travel through the column of the TEM. Note that the electron paths shown in **Figure 2** correspond to the formation of an image (i.e. image mode) or diffraction pattern (i.e. diffraction mode) in TEM mode, where the incident beam is parallel. In scanning-TEM (STEM), the beam is focused to a nanoprobe that scans parallel to the optic axis across the sample (**Figure 3**). The image is built up by plotting the signal generated by the detected scattered electrons as a function of the probe position. The lenses in the illumination system allow us to switch between TEM and STEM mode.

The images taken on an electron microscope can suffer from many aberrations caused by the electromagnetic lenses, which results in a smeared image and reduces the resolution. For an aberration-corrected TEM, a probe-corrector and/or image corrector is mounted in the column to eliminate these aberrations. Such a microscope can obtain a resolution of 0.8 Å.

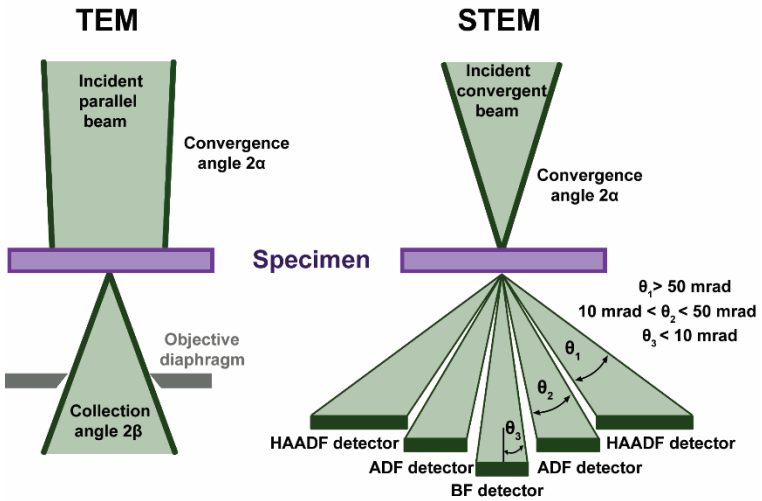

Figure 3. *Schematic illustration of the electron beam in TEM and STEM mode with the different electron detectors. Figure based on [3].*

When the incident electron beam travels through the sample, the electrons can either remain unaffected or interact with the sample. The techniques used in the thesis are based on the detection of different electrons or radiation, as shown in **Figure 4**.

The electrons that go through the sample unaffected are referred to as the direct electrons, which form the direct beam. A part of this direct beam is used for ABF-STEM imaging, which is explained further in this chapter. The electrons that interact can be scattered in two ways: elastic or inelastic, each of which can also be coherent or incoherent

1.3.2. EDX

In the case that the electrons are scattered inelastically, a reduction of impulse and energy takes place along with the generation of other interactions. When high-energy electrons bombard the atoms in the sample, the collision can eject an inner-shell electron from an atom (i.e., secondary electron). Then, an electron from an outer, higher energy shell jumps to the lower energy shell to fill the vacancy and emit the energy difference in the form of an X-ray. As these energy differences between the different electron shells are characteristic for the element, these characteristic X-rays can be used for chemical analysis. This technique is called energy-dispersive X-ray spectroscopy (EDX) and is used in the thesis to analyse the composition of the studied materials.

Furthermore, an electron can also be decelerated due to the nucleus of an atom by giving up some of its energy. This energy is emitted in the form of X-ray radiation called Bremsstrahlung. The electrons can give any amount of their energy, but it is more likely that the electrons emit a low amount of their energy.

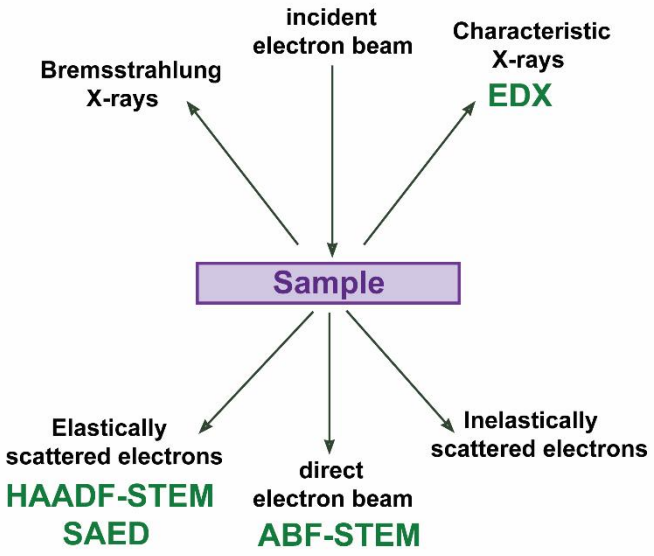

Figure 4. *Interaction between the electron beam and the examined sample.*

An energy-dispersive spectrometer measures the number and energy of the emitted X-rays and generates an EDX spectrum. Besides the characteristic X-rays, the detector will also collect the X-ray Bremsstrahlung, which results in a continuous background in the spectrum with discrete peaks corresponding to the characteristic X-rays. In the TEM instruments used in this thesis, a Super-X EDX detector was present, which consists of four silicon drift detectors in a windowless design. They are symmetrically placed around the sample stage resulting in a substantially bigger collection angle and higher detection efficiency.

1.3.3. Electron diffraction

When the electrons are scattered elastically, the energy is conserved. The electrons interact with either the negatively charged electron cloud around the nuclei of an atom or the nuclei itself, resulting in an angular deviation due to the Coulomb force, which is called Rutherford scattering. Electrons can also be treated as waves, where the scattered electrons are either coherent (i.e. the frequency of the scattered electrons remains constant) or incoherent (i.e. the frequency of the scattered electrons differs). Both selected area electron diffraction (SAED) and high-angle annular dark-field scanning transmission electron microscopy (HAADF-STEM) are based on the detection of elastically scattered electrons (**Figure 4**). The main difference between both techniques is the degree of coherence. SAED is based on coherent elastically scattered electrons, whereas the detected electrons in HAADF-STEM imaging are rather incoherent.

When the elastic scattering is coherent, only a shift of the phase occurs. The interference of these waves generates a diffraction pattern, where the lattice symmetry and cell parameters of the crystal define the position of the maxima. The intensity of the diffraction peaks is related to the chemical nature and position of the atoms.

A crystalline structure can be described by a three-dimensional (3D) lattice, defined by its unit cell with cell parameters *a*, *b*, and *c* and the angles α ($\widehat{bc}$), β ($\widehat{ac}$), and γ ($\widehat{ab}$). The origin of the lattice corresponds to the origin of the unit cell, where any lattice point can be described by the vector:

$$\vec{q} = u\vec{a} + v\vec{b} + w\vec{c},$$

with u, v and w integer numbers.

A lattice plane within the unit cell that intersects the $\vec{a}$-axis in 1/h, the $\vec{b}$-axis in 1/k en the $\vec{c}$-axis in 1/l is described by the miller indices *hkl*. A family of crystallographic planes is defined as a set of lattice planes that are parallel to each other and equally spaced [4].

The reciprocal lattice is the Fourier transform of the crystal lattice in real space, which is constructed by the vectors $\vec{a}$*, $\vec{b}$* and $\vec{c}$*:

$$\vec{a}^* = \frac{\vec{b} \times \vec{c}}{V}, \vec{b}^* = \frac{\vec{a} \times \vec{c}}{V}, \text{ and } \vec{c}^* = \frac{\vec{a} \times \vec{b}}{V},$$

where $\vec{a}$, $\vec{b}$ and $\vec{c}$ are the cell parameters and V the volume in real space.

Each point represents a set of (*hkl*) lattice planes and can be described by the vector

$$\vec{H} = h\vec{a}^* + k\vec{b}^* + l\vec{c}^*,$$

where *h*, *k*, and *l* are integers. The direction of the vector $\vec{H}$ is perpendicular to the corresponding crystallographic planes, and its length is inversely proportional to the interplanar distance d_{hkl} with C the scale factor from the projected diffraction pattern:

$$\left|\vec{H}\right| = \frac{C}{|d_{hkl}|}.$$

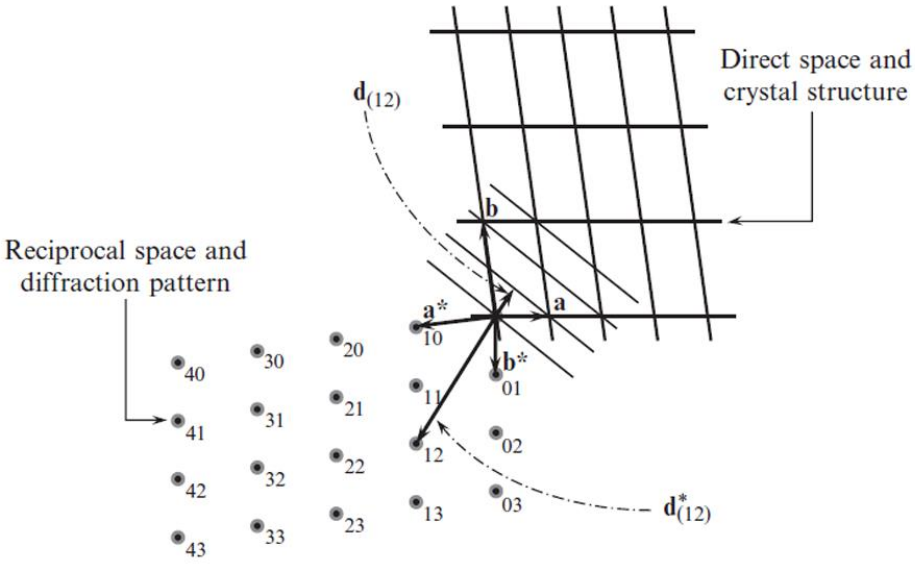

***Figure 5**. Scheme of the relationship between the crystal lattice in real space and the reciprocal lattice in reciprocal space [5]. d* corresponds to the 2D $\vec{H}$ vector.*

When the incident beam is diffracted at a set of (*hkl*) planes, the diffracted electrons will interfere. Constructive interference arises when the phase difference is an integer of the wavelength, which is related to the diffraction angle. Thus the diffraction peaks occur at a set of (*hkl*) lattice planes of the crystal with interplanar distance d_{hkl} when the Bragg condition is satisfied [5]:

$$\lambda = 2\, d_{hkl} \sin(\theta_{hkl}),$$

with λ the wavelength of the incident beam and θ_{hkl} is the scattering angle.

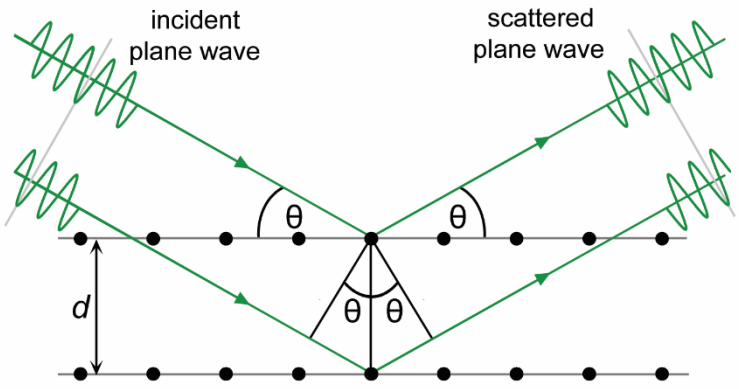

Figure 6. *Geometric construction of the Bragg's law.*

An incident electron can be described by the wave vector $\overrightarrow{k_0}$ with a length defined by the wavelength: $|\overrightarrow{k_0}| = 1/\lambda$. When that electron is scattered elastically at a set of (*hkl*) planes, the length of the wave vector remains constant, but the direction changes. The scattered wave vector is referred to as $\overrightarrow{k_1}$, where the diffraction angle (2θ) defines the change in direction. In the reciprocal lattice, the end of $\overrightarrow{k_0}$ can be drawn as the origin of the reciprocal lattice, whereas the end of $\overrightarrow{k_1}$ corresponds to the corresponding *hkl* lattice point. The *hkl* point is described by the $\vec{H}$ vector in the reciprocal lattice, as shown in **Figure 7**. If all the possible elastically scattered electrons are included, the corresponding wave vectors $\overrightarrow{k_i}$ delineate a sphere, which is called the Ewald sphere. The Ewald sphere has a radius of $1/\lambda$ and passes through the origin of the reciprocal lattice. If a point in the reciprocal lattice intersects with the surface of the Ewald sphere, the set of planes corresponding to that point must satisfy the Bragg equation, and hence the planes will diffract strongly. Thus, a diffraction pattern is the intersection of the Ewald sphere with the reciprocal lattice of the examined material.

Since the wavelength of high-energy incident electrons is very small (λ = 0.025Å at 200kV), the radius of the Ewald sphere (~ 40 $Å^{-1}$) is large compared to the distance between the reciprocal lattice points (order of $Å^{-1}$). Therefore, the Ewald sphere can be approximated as a flat plane perpendicular to the incident beam, and the diffraction pattern can be considered as a two dimensional (2D) intersection of the reciprocal lattice. The sample examined in a TEM is very thin, resulting in that the reciprocal lattice points are elongated in the direction parallel to the incident beam. Therefore, also diffraction peaks (referred to as reflections in the diffraction pattern) that do not satisfy the Bragg condition can still be visible in the formed diffraction pattern.

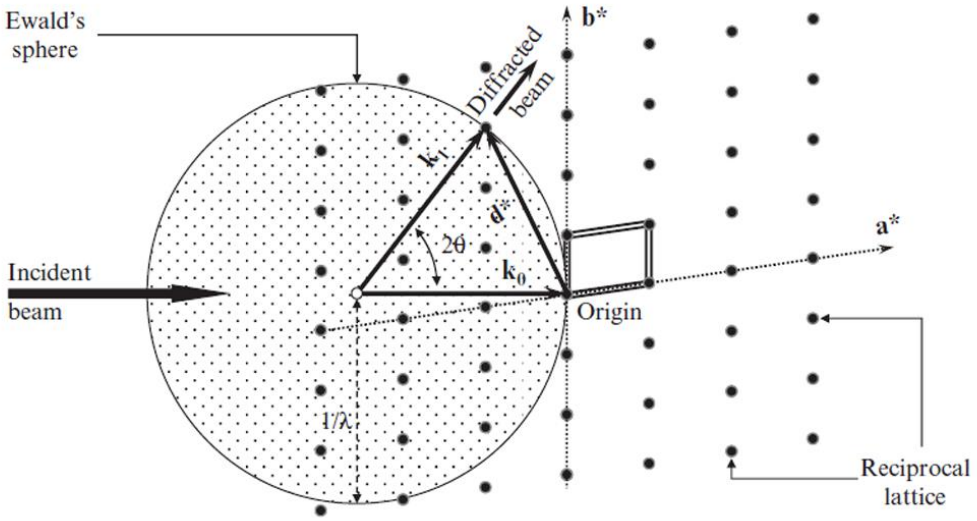

Figure 7. *Visualization of diffraction using the Ewald sphere with radius 1/λ and the 2D reciprocal lattice with unit vectors $\vec{a}$* and $\vec{b}$*. Diffraction can only be observed when a reciprocal lattice point, other than the origin, intersects with the surface of the Ewald's sphere. The unit cell of the reciprocal lattice is shown using double lines. d* represents the 2D $\vec{H}$ vector [5].*

The structure factor F_{hkl} is a mathematical description of how a material scatters the incident electron beam and expresses both the amplitude and the phase of the diffracted beam.

$$F_{hkl} = \sum_i f_i \left(\sum_j e^{2\pi i (hx_j + ky_j + lz_j)} \right),$$

with f_i the scattering factor of element i and (x_j,y_j,z_j) the coordinates of atom j. The intensity of a diffracted beam is approximately equal to the square of the structure amplitude $|F_{hkl}|^2$. Each point in the reciprocal space is represented by its coordinates h, k, l and the corresponding structural factor F_{hkl}. Since the intensity of the structure factor varies according to the hkl planes, information about the arrangement of the atoms can be obtained from this. Extinguished reflections (i.e. extinctions) can be mathematically represented in the form of reflection conditions. Because certain symmetry elements cause specific reflection conditions, the space group can thus be determined from the diffraction patterns.

The kinematic approach is used when it is assumed that the electrons scatter only once, but when electrons are scattered multiple times, it becomes dynamical diffraction. The contribution of dynamical scattering increases with heavier elements and increasing thickness of the sample. When dynamical scattering occurs, the intensities are no longer directly related to the structure factor described above. Also, intensities can appear at reciprocal lattice points that should be extinct due to the symmetry, which is called double diffraction.

For SAED (selected area electron diffraction), a parallel beam interacts with the sample and generates a diffraction pattern that is projected onto a CCD camera. The SA (selected area) aperture (see **Figure 2**) selects the region of which the diffraction pattern is projected. From the acquired diffraction patterns, the symmetry and unit cell parameters of the studied material can be deduced. In combination with the imaging techniques, which will be discussed in the next section, SAED allows to derive the crystal structure.

1.3.4. HAADF-STEM

When the electron penetrates through the electron cloud and approaches the nucleus, the electron will be strongly attracted and scattered through a larger angle, which is called high-angle Rutherford scattering. The angle of the scattered electron depends on the atomic number (Z) of the atom. When the scattering angle becomes larger, the degree of coherency becomes less, and the electrons that are Rutherford-scattered through high angles become incoherent.
In the case of HAADF (high-angle annular dark-field) STEM, high-angle Rutherford scattered electrons are detected, which are incoherent. This means that the electrons do not have a phase relationship. Therefore, they are not subject to the orientation of the sample and thus involve no diffraction contrast. The image contrast is related to the Z value ($I \sim Z^2$), as electrons interacting with heavier elements are more likely to be scattered over large angles. This means that the atom columns appear as bright dots on a dark background where the intensity is related to the Z value, which makes that the intensity in the image is directly interpretable. In order to only detect these high-angle scattered electrons, a disk-shaped detector with a hole (so-called annular detector) is used. Typically the detector angles range from 50 mrad (~3°) to 200 mrad (~11.5°). When detectors with lower angle are used in the dark-field mode (i.e. the diffracted electrons are selected to form the image), the coherent Rutherford scattered electrons will contribute more to the image. The intensity of the image is then related to both diffraction contrast and Z contrast, which makes the image not directly interpretable.

1.3.5. ABF-STEM

The electrons detected in ABF (annular bright-field) STEM are collected with an annular detector that typically ranges from 11 mrad to 23 mrad, which is the outer area of the so-called bright-field region. In bright-field imaging, the direct beam electrons are selected to form the image. When the electron beam is placed on an atomic column, the electrons will scatter, and fewer electrons are detected in the bright-field region. Therefore, the atom columns appear as dark dots on a bright background. In the range for annular bright-field, the electron intensity is less sensitive to the atomic number ($I \sim Z^{1/3}$), which makes it possible to visualize light elements nearby heavy elements.

Part I: Perovskites

In the first part of my thesis, I study the effects of cation substitution on the crystal structure of perovskites, and in collaboration with groups from the University of Oxford and Rutgers, we investigated what these changes in structure mean for the physical properties of these perovskites.

The structural changes are related to distortions in the structure that are typical for perovskites, therefore, in **Chapter 2** I will first explain the different types of distortions along with the physical properties that are related to the studied materials. Then in **Chapter 3 and 4,** the structural investigation of three different perovskite series with cation substitution is discussed. Also the relationship to the measured properties will be discussed in order to explain why certain substitutions have or have not produced the desired physical properties. Finally, Part I ends with a **conclusion** about the effect of cation substitution on the crystal structure of perovskites.

Chapter 2. Introduction to Perovskites

During this research, perovskites with many different types of distortions, such as octahedral tilt and Jahn-Teller effect were observed. Hence I will give an introduction so that the reader is aware of both the ideal perovskite structure and the distortions that can occur in perovskites and how they are conventionally described.

2.1. Ideal and distorted perovskites

Perovskites are widely investigated due to their wide variety of physical properties, which is a result of their enormous compositional and structural flexibility.

The perovskite structural family is based on the mineral $CaTiO_3$, named after the Russian mineralogist, Count Lev Aleksevich von Perovski [6]. The perovskite structure has a general stoichiometry ABX_3, where A and B are cations, and X is an anion. The structure consists of a framework of BX_6 octahedra with the A cations occupying the cuboctahedral places. As the perovskites investigated in this thesis are oxide perovskites, I will continue with the notation of O instead of X.

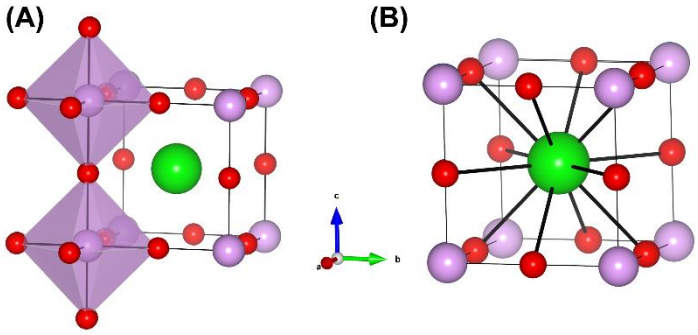

Figure 8. *The crystal structure of the ideal cubic perovskite with $Pm\bar{3}m$ symmetry, where the green, purple and red atoms represent the A cation, B cations and oxygen, respectively.* ***(A)*** *Emphasizes the BO_6 octahedra, whereas* ***(B)*** *shows the 12-coordinated cuboctahedral position of the A cation.*

The ideal perovskite ABO_3 is cubic, described by the $Pm\bar{3}m$ symmetry, as shown in **Figure 8**. The cubic lattice parameter a_p varies between 3.8 Å − 4.2 Å, and is related to the bonding distances *A*-O and *B*-O. The radius of the different ions determines the lattice parameter:

$$a_p = \sqrt{2}(r_A + r_O) = 2(r_B + r_O)$$

The ratio between the two expressions for the lattice parameter is called the Goldschmidt tolerance factor t and allows to measure the degree of distortion in case of a non-ideal perovskite [7,8]:

$$t = \frac{r_A + r_O}{\sqrt{2}(r_B + r_O)}$$

For an ideal cubic perovskite structure t = 1, but when the tolerance factor deviates from 1, i.e. when the ionic radii of the A and B cations do not satisfy the equality, distortions will occur. In the case that $t < 1$, the relative size of the A cation is too small to occupy the cuboctahedral place, and consequently octahedral tilts will occur to fill the space between the octahedra in order to stabilize the structure. Along the tilt axis, the octahedra can rotate either in the same direction, which is referred as an in-phase tilt (**Figure 9A**) or in the opposite direction, which is referred as an anti-phase tilt (**Figure 9B**) [9]. All possible tilt systems were derived theoretically using group theory analysis and are commonly designated using the Glazer notation [10]. These notations use the symbol a*b*c*, where a, b and c represent the relative magnitude of the tilting along the [100], [010] and [001] pseudo-cubic directions. The subscript '*' denotes the phase of the tilt: "0" indicates no tilts, "-" means the tilt is anti-phase, and "+" stands for an in-phase tilt. Any possible tilt system can be expressed by a linear combination of the six basic tilts [9]:

$a^+b^0b^0$	$b^0a^+b^0$	$b^0b^0a^+$
$a^-b^0b^0$	$b^0a^-b^0$	$b^0b^0a^-$

These can be combined into more complex tilts, in which the same letters indicate the same magnitude of the tilt, and different letters indicate different magnitudes of the tilt.

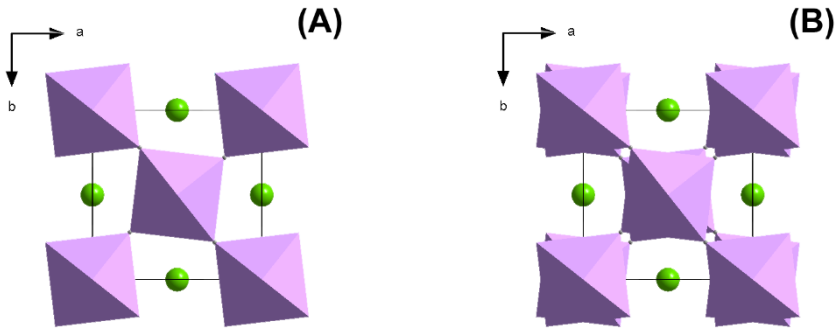

Figure 9. *Illustration of the* ***(A)*** *in-phase and* ***(B)*** *anti-phase octahedral tilt along the c-direction. The four adjacent octahedra in the plane perpendicular to the tilt axis rotate in the opposite direction.*

By collecting extensive structural data and calculations of tolerance factors, Reaney *et al.* [11] demonstrated that at room temperature, the structure of perovskites with $0.985 < t < 1.06$ often adopt untilted structures. Perovskites with $0.964 < t < 0.985$ are usually tilted in anti-phase and perovskites with $t < 0.964$ are prone to show in-phase and anti-phase tilting. In this study, only the octahedral tilts have been taken into account; however, it is not the only cause of structural changes.

Besides octahedral tilts, the Jahn-Teller (JT) distortion can occur, which describes the geometrical distortion that is associated with the electron configuration of the B cations. The Jahn-Teller effect can be grouped into two categories. The first arises from incomplete d^n shells of degenerate orbitals and is referred to as the first-order Jahn-Teller (FOJT) deformation. A nonlinear molecular system that is in a degenerate state will undergo a deformation that lifts up the degeneracy in order to lower the energy whereby *B-O* bond lengths will either elongate or compress (**Figure 10A**). FOJT is typical for the transition metal cations with an odd number of *d*-electrons in the e_g orbitals. The FOJT distortion is accompanied by a change in the electronic configuration and orbital ordering, and therefore, is closely linked to the magnetic behaviour of the perovskite [12,13].

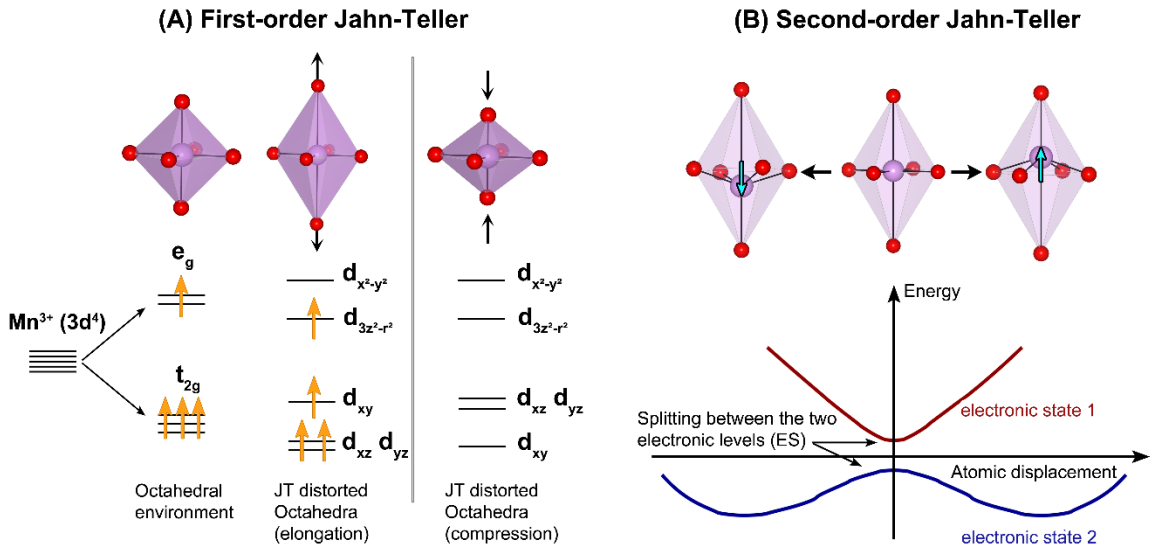

Figure 10. (A) *The first-order Jahn-Teller distortion destroys the degeneracy and split the e_g and t_{2g} orbitals of Mn^{3+} into the $d_{x^2-y^2}$, $d_{3z^2-r^2}$, d_{xy}, d_{xz} and d_{yz} orbitals, causes an elongation. In other cases, it is energetically more favourable to compress the two B-O bond lengths perpendicular to the four in-place B-O bond lengths.* ***(B)*** *To lower the energy of the structure, a displacement of the cation relative to the anions occurs, which is called the second-order Jahn-Teller distortion. Based on [14].*

The second group, the so-called second-order Jahn-Teller (SOJT) deformation, arises from empty and filled molecular orbitals that are close in energy [15]. The energy of the structure will decrease when a small energy gap is created between the empty d^0 orbitals of the B cation and the filled O $2p^6$ orbitals, which leads to the off-centre displacement of the B cation inside the BO_6 octahedra (**Figure 10B**) [16].

2.1.1. A- and B-site ordering

Substitution of the A and/or B cations can induce order. Ordering of the cations is more likely to occur when there is a significant difference in size and/or charge of the cations. These differences serve as a driving force for the cations to occupy crystallographically different positions within the structure. In the absence of a significant difference in charge and/or size, a disordered distribution of the cations is more likely.

There are three simple patterns of ordering for the A and B cations (**Figure 11**) [17]. The most symmetrical ordering is the so-called rock-salt arrangement. For the B cations, this means that the octahedron BO_6 alternates along the three pseudo-cubic directions with the octahedron $B'O_6$, which can be represented as (111) because the BO_6 and $B'O_6$ octahedra form alternating layers parallel with the (111) planes. Rock-salt ordering can be compared to a 0D situation because every BO_6 octahedron is isolated from all other BO_6 octahedra.

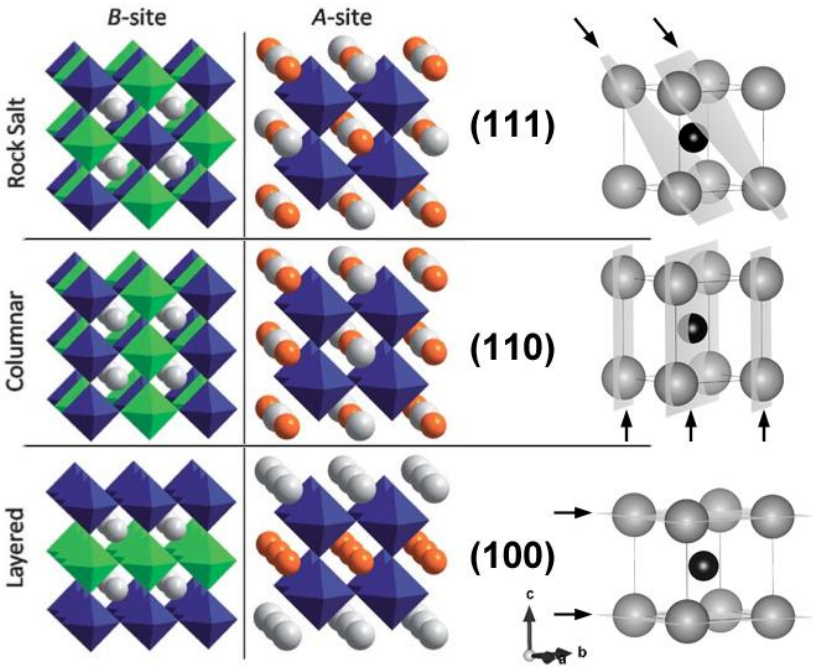

Figure 11. *Schematic illustration of the three types of A/B cation ordering that can be present in the structure [16]. The rock-salt, column and layered ordering arise from ordering on respectively the (111), (110) and (100) planes, which are marked by arrows.*

Another type of order is the column order, in which the octahedra are alternated along only two pseudo-cubic directions. This ordering is called (110) because the BO_6 and $B'O_6$ octahedra alternate in layers parallel with the (110) planes. It can also be described as a 1D arrangement because the BO_6 octahedron only has the same neighbours in one dimension. Finally, the last type is layered ordering (100). This can also be described as a 2D situation, in which the BO_6 octahedra have the same neighbours in 2 dimensions. The BO_6 octahedra alternate with the $B'O_6$ octahedra in layers parallel to the (100) planes. This (100) order has the lowest symmetry. For B cations, the rock-salt ordering is the most common because in this arrangement the oxygen atoms that lie between the different B cations are able to shift towards the smallest B cation in order to reduce the lattice stress that is induced by the difference in the size of the B cations. The almost complete absence of rock-salt arrangement in the A cations in perovskite has to do with the environment of the oxygen atom. In the rock-salt arrangement for A cations, the oxygen atoms cannot shift to the smallest A cation, which leads to permanent lattice stress in the structure. When the A cations are ordered in accordance with the layered arrangement, the oxygen atoms can shift to the layer with the smallest A cations, which reduces the lattice stress. Therefore, in perovskites of the form $AA'BB'O_6$, we often see a layered arrangement of the A/A' cations and a rock-salt ordering for the B/B' cations [16].

By the substitution of A and B cations, more complex perovskites can be synthesized. Depending on the number of different elements and their ratio, they can form double perovskites such as $AA'BB'O_6$, or triple perovskites like $AA'_2BB'_2O_9$ or $A_3BB'B''O_9$, or other combinations.

2.2. Physical properties

Perovskite materials display numerous interesting and useful physical properties. The perovskites investigated in this thesis are synthesized with the focus on magnetic properties or multiferroic behaviour.

2.2.1. Magnetism

Magnetic order in a material occurs due to the magnetic interaction between the magnetic moments, which can be calculated by the Ising model, where the interactions between neighbouring spins are described by the Hamiltonian [18,19]:

$$\boldsymbol{H} = -\sum_{<i,j>} J_{ij} \boldsymbol{s}_i \boldsymbol{s}_j,$$

where J_{ij} is the spin-spin coupling constant where i and j refer to neighbouring sites on the lattice and $\boldsymbol{s}_i$ is the spin corresponding to the lattice site i. The spin-spin coupling constant describes the exchange interaction between the nearest neighbouring spins. When $J_{ij} > 0$, the spins prefer to align parallel to each other (**Figure 12b**), and the structure becomes ferromagnetic (FM). When $J_{ij} < 0$, the neighbouring spins prefer to align antiparallel (**Figure 12c**), and then the structure becomes antiferromagnetic (AFM). In the FM case, the structure possesses a net magnetization even in the absence of an external magnetic field, whereas, in the AFM case, the ordered magnetic moments cancel each other completely out, which leads to a zero net magnetization. When the magnitude of the magnetic moment at positions i and j differs, the magnetic moment cancellation is incomplete, resulting in a small net magnetization. In that case, the structure is ferrimagnetic (**Figure 12d**).

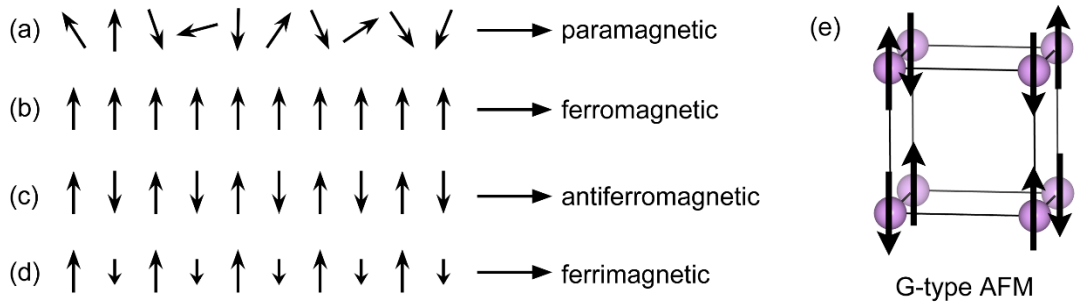

Figure 12. *A scheme of the* ***(a)*** *paramagnetic,* ***(b)*** *ferromagnetic,* ***(c)*** *antiferromagnetic, and* ***(d)*** *ferrimagnetic order arrangement of the magnetic moments. The perovskite in* ***(e)*** *demonstrates the G-type ordering of the B cations that leads to antiferromagnetism.*

In a magnetic material, the spontaneous magnetization disappears above a specific temperature. This temperature is referred to as the Curie temperature T_C for ferromagnetic and ferrimagnetic materials, and the Néel temperature T_N for antiferromagnetic materials.

2.2.2. Spin glass

Besides the typical magnetic systems, the structure can become a spin glass at low temperature. A spin glass is a disordered magnetic system where competition between exchange interactions prevents long-range magnetic ordering and leads to magnetic frustration. The term 'glass' refers to the magnetic disorder, which can be associated to the positional disorder in conventional glass, which has a highly irregular bond structure in contrast to a crystal with a uniform pattern of atomic bonds, which can be seen as a ferromagnet. The magnetic frustration arises from a roughly equal amount of positive and negative interactions J_{ij} in the system leading to a mean value of the interactions close to zero. Note that in FM or AFM the spin-spin coupling J_{ij} is respectively positive or negative, whereas in a spin glass, J_{ij} can be both positive and negative, which, in turn, leads to disordered-induced frustration. At low temperatures, the spins freeze in place without strong thermal fluctuations. The randomly oriented spins result in an overall magnetization:

$$m = \frac{1}{N}\sum_{i=1}^{N}\langle \boldsymbol{s_i}\rangle = 0,$$

while the spin-glass order parameter is non-zero:

$$q = \frac{1}{N}\sum_{i=1}^{N}\langle \boldsymbol{s_i}\rangle^2 \neq 0.$$

The non-zero order parameter indicates the freezing of spins into the disordered ground state. The main difference that distinguishes spin glasses from other magnetic systems is the time dependence. A spin glass exhibits spin glass behaviour when an external magnetic field is applied below the transition temperature T_C. When then the external magnetic field is removed, the magnetization rapidly lowers to the remanent magnetization and then slowly decays to zero. Spin glasses differ from ferromagnets because for ferromagnets the remanent magnetization remains constant after removing the external magnetic field. In the case of a paramagnet, the magnetization immediately drops to zero when the external magnetic field is removed [20–22].

2.2.3. Relaxor ferromagnetic

The term relaxor ferromagnets is based on the behaviour of relaxor ferroelectric materials. At high temperature, a relaxor ferroelectric behaves similar to a normal ferroelectric, but upon cooling the material transforms to a relaxor state in which nanoscale polar domains are formed with randomly distributed directions of dipole moments. The transformation occurs at the so-called Burns temperature (T_B). The polar nanoregions are dynamical at a temperature close to T_B, but freeze at lower temperatures [23].

Similarly, for relaxor ferromagnetic materials, ferromagnetic nanodomains appear below a specific temperature that arises from compositional disorder, i.e. the disorder in the arrangement of different ions on the crystallographically equivalent sites. The term 'relaxor ferromagnet' has been used for the first time by Kimura *et al.* [24] to describe the behaviour of Cr^{3+} doped $Nd_{0.5}Ca_{0.5}MnO_3$ (~2% Cr^{3+}), in which ferromagnetic domains were formed within the antiferromagnetic ordered structure of the undoped material. Later, relaxor behaviour was found in the perovskite $La_3Ni_2SbO_6$, in which the B cation disorder of the two crystallographically different B-sites Ni and (Ni, Sb) leads to the formation of small ferromagnetic domains [25,26].

In contrast to a spin glass, where spins can be aligned on atomic scale, the relaxor state is characterized by the presence of nanoscale ferromagnetic clusters of variable sizes.

2.2.4. Multiferroic

Multiferroic materials display two or all three of the 'ferroic' properties: ferroelectricity, ferromagnetism and ferroelasticity. However, nowadays, this definition is extended to materials with antiferromagnetic ordering.

The possibility for a material to exhibit ferroelectricity and ferromagnetism depends on the structure. A material cannot be ferroelectric if there is spatial inversion, because then the inversed dipole will cancel out the initial dipole and destroy the polarity (**Figure 13A**). In the case for ferromagnetism, magnetism will be destroyed when time inversion symmetry is included in the material, as the spins and their reversed spins will cancel each other out (**Figure 13B**). This means that both the spatial inversion symmetry and time inversion symmetry should be eliminated from the structure.

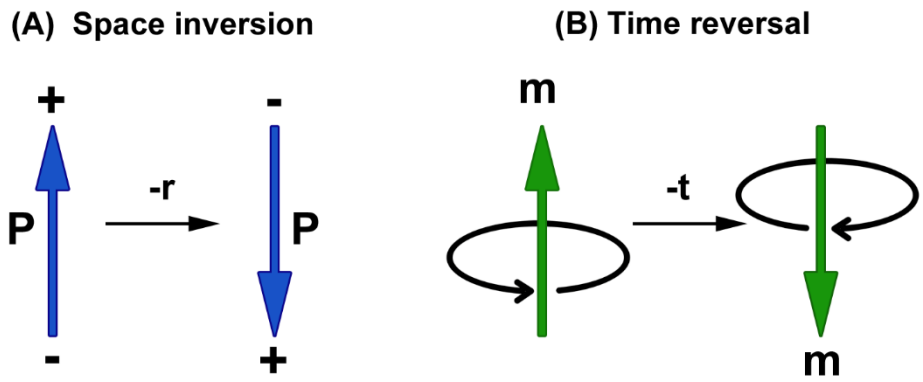

Figure 13. *A simplified illustration of (**A**) space inversion and (**B**) time reversal. For ferroelectric materials, no space inversion symmetry is present, while in ferromagnetic materials the time inversion symmetry should be eliminated. As a consequence, for multiferroics, both the space inversion and time inversion symmetry is broken.*

Moreover, ferromagnetism is induced by the presence of B cations with unpaired electrons in the d^n shell to carry the magnetic moment, while in all conventional ferroelectric perovskites, ferroelectricity is induced by the off-centre displacement of the B cations with empty d^0 shells caused by the SOJT effect. Such compounds are non-magnetic, and thus the electronic requirements for the B cations are in conflict with those for magnetic compounds. However, ferroelectricity can also originate from non-conventional patterns, such as from octahedral tilting (i.e. rotation of the octahedral, which is accompanied by A cation displacement inducing ferroelectric distortion, e.g. $LaMnO_3$ [27]), charge order (i.e. noncentrosymmetric ion arrangement that can induce ferroelectricity, e.g. $Pr_{1-x}CaMnO_3$ [28]), lone pair effects (i.e. lone pairs of electrons on the A-site distort the geometry of the BO_6 leading to ferroelectricity, e.g. $BiFeO_3$ [29]) or induced by the magnetic order present in the structure (i.e. long-range magnetic order in which the magnetic dipole arrangement breaks the space inversion symmetry, e.g. $TbMnO_3$ [30]).

Magnetoelectric materials show a strong electromagnetic coupling that allows inducing polarization by a magnetic field and vice versa. The effect can be described by the free energy F of the system in terms of the applied magnetic field **H** whose *i*th component is denoted H_i, and an applied electric field **E** whose *i*th component is denoted E_i [31]:

$$-F(E,H) = \frac{1}{2}\varepsilon_0\varepsilon_{ij}E_iE_j + \frac{1}{2}\mu_0\mu_{ij}H_iH_j + \alpha_{ij}E_iH_j + \frac{\beta_{ijk}}{2}E_iH_jH_k + \frac{\gamma_{ijk}}{2}H_iE_jE_k + \cdots$$

The first term $\frac{1}{2}\varepsilon_0\varepsilon_{ij}E_iE_j$ describes the electrical response to an electric field where ε_0 is the permittivity of free space and ε_{ij} the relative permittivity. The second term $\frac{1}{2}\mu_0\mu_{ij}H_iH_j$ is the magnetic response to a magnetic field, where μ_0 and μ_{ij} denote the permeability of free space and the relative permeability, respectively. The third term $\alpha_{ij}E_iH_j$ represents the linear magnetoelectric coupling, whereas the other terms represent higher-order magnetoelectric coefficients. The magnetoelectric effect can be established by the polarisation $P_i(H_j)$ and magnetization $M_i(E_j)$:

$$P_i = \left(\frac{-\partial F}{\partial E_i}\right)_{E_i=0} = \alpha_{ij}H_j + \frac{\beta_{ijk}}{2}H_jH_k + \cdots$$

$$M_i = \left(\frac{-\partial F}{\partial H_i}\right)_{H_i=0} = \alpha_{ij}E_j + \frac{\gamma_{ijk}}{2}E_jE_k + \cdots$$

As the magnetoelectric coupling describes the influence of the magnetic field (electric field) on the polarization (magnetization), in practice, the linear magnetoelectric coefficient can be determined by measuring the polarization (magnetization) when applying a magnetic field (electric field):

$$\alpha = \frac{\partial P}{\partial H} = \frac{\partial M}{\partial E}$$

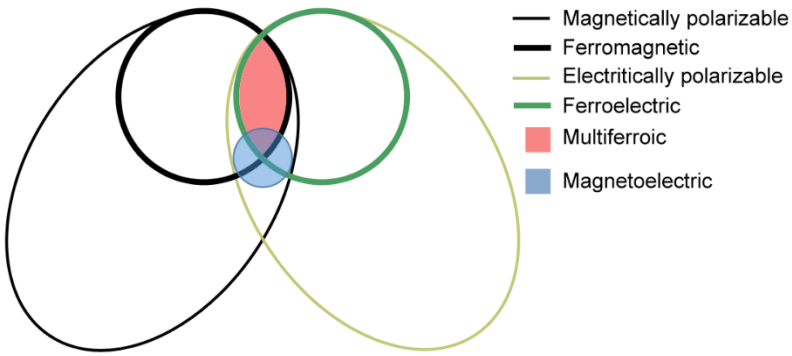

Figure 14. *The relationship between multiferroic and magnetoelectric materials. Ferromagnetics (ferroelectrics) form a subset of magnetically (electrically) polarizable materials such as paramagnets and antiferromagnets (paraelectrics and antiferroelectrics). The intersection (red) represents materials that are multiferroic. Magnetoelectric coupling (blue region) is an independent phenomenon that can but need not, arise in any of the materials that are both magnetically and electrically polarizable. In practice, it is likely to arise in all such materials, either directly or via strain [31].*

2.2.5. Applications

Perovskites and derivative structures have a wide variety of useful physical properties such as magnetoresistance, superconductivity, photovoltaic properties, etc. The flexibility of cation substitution in perovskites results in the possibility of tuning the electric and magnetic properties in a desired manner.

The field of magnetic perovskites finds potential applications in storage and sensing/actuating devices. Some examples are listed in **Table 1**.

As interest in micro and nanoscale devices and high-density data storage grows, an integration of multi-functions into one material has become highly desirable. The coexistence of several properties will possibly reveal novel physical phenomena and offers possibilities for the development of new devices. The new prototype devices based on multiferroic functions may offer particularly good performance for spintronics, e.g., reading the spin states, and writing the polarization states to reverse the spin states by an electric field, to overcome the high-writing energy in magnetic random-access memories [32].

Table 1. *Some perovskites with their properties and existing or potential applications.*

Compound	Properties	Existing and potential applications	Ref
$NdCoO_3$, $Nd_{0.8}Sr_{0.2}CoO_3$, $Nc_{0.9}Ca_{0.1}CoO_3$	Soft ferromagnets	Recording heads, magnetic cores and transformers	[33]
$SrRuO_3$	Ferromagnetism	Electrode material for epitaxial ferroelectric thin films	[34]
(La, A)MnO_3 A = Ca, Sr, Ba	Ferromagnetism, spin-polarized electrons, giant magnetoresistance	Magnetic field sensors, spin-electronic devices	[34]
$BiFeO_3$	Multiferroic, magnetoelectric coupling	Magnetic field detectors, memories	[32]
$YFeO_3$	Multiferroic	Magnetic field sensors and magneto-optical data storage devices	[35]
$Lu_{1-x}In_xFeO_3$	Multiferroic thin film	Memory devices and spintronic applications	[36]

Chapter 3. *A*La$_2$Fe*B*SbO$_9$ & *A*$_2$LaFe$_2$SbO$_9$ (*A* = Ca, Sr, Ba; *B* = Ni, Co) series

This section is based on the papers:

1) **M. Hendrickx**, Y. Tang, E.C. Hunter, P.D. Battle, J.M. Cadogan and J. Hadermann, *CaLa$_2$FeCoSbO$_9$ and ALa$_2$FeNiSbO$_9$ (A=Ca, Sr, Ba): cation-ordered, inhomogeneous, ferrimagnetic perovskites*, Journal of Solid State Chemistry, 2020, 285, 121226 [37]
2) Y. Tang, E.C. Hunter, P.D. Battle, **M. Hendrickx**, J. Hadermann and J.M. Cadogan. *Ferrimagnetism as a consequence of unusual cation ordering in the perovskite SrLa$_2$FeCoSbO$_9$.* Inorganic Chemistry, 2018, 57, 12, 7438-7445 [38]
3) *(in preparation)* **M. Hendrickx**, Y. Tang, E.C. Hunter, P.D. Battle and J. Hadermann, *Structural and magnetic properties of the perovskites: A$_2$LaFe$_2$SbO$_9$ (A=Ba, Sr, Ca)*

Due to the many samples discussed in this section, not all the TEM data shown in the corresponding papers are also shown in this thesis, rather the results are clustered, using, when possible, images that are representative for several samples at the same time.

3.1. Introduction

One of the strategies that have been used to control the physical properties of perovskites is partial cation substitution. The substitution can take place at the A-site, the B-site or both, resulting in more complex formulae, for example, AA'BB'O$_6$ and A$_2$A'B$_2$B'O$_9$. It is possible for the different cation species on the A-and B-sites to occupy their respective sites in either an ordered or disordered manner [39,40]. This ordering is highly significant because it can control the distortion away from the cubic symmetry and consequently, the magnetic and electric properties of the compound.

An unequal occupation of magnetic cations at two crystallographically distinct B-sites in the structure of a double or triple perovskite can generate interesting magnetic behaviour. For example, relaxor ferromagnetic behaviour was found in the triple perovskite, La$_3$Ni$_2$SbO$_9$, below the transition temperature of 105 K. B cation ordering was observed, where one of the two B-sites is occupied only by Ni^{2+}, while the other site is occupied by 2/3 Sb^{5+} and 1/3 Ni^{2+}. The presence of the diamagnetic ion Sb^{5+} at only one B-site causes that the perovskite behaves as a ferrimagnet below the transition temperature, but the local irregularities in the cation

distribution cause the formation of magnetic microdomains that are too small to be detected by neutron diffraction but were observed using TEM [25,26]. Hence the compound can be classified as a relaxor ferromagnet. $La_3Co_2SbO_9$ shows the same cation ordering pattern as $La_3Ni_2SbO_9$, but the sharp increase in magnetization observed in the latter at the transition temperature is not observed in the former [41].

In general, magnetic transition temperatures are expected to be highest in the members of an isostructural series that contain the most strongly magnetic cations. In an attempt to prepare a relaxor ferromagnet with an enhanced transition temperature, Fe^{2+}-containing analogues of $La_3Ni_2SbO_9$ were synthesized, such as $Sr_3Fe_2TeO_9$. However, the majority of the Fe^{3+} and Te^{6+} cations in this compound adopt a 2:1 ordering pattern over the B-sites that, in turn, leads to the adoption of an antiferromagnetic structure; neither ferrimagnetism nor relaxor behaviour was observed [42]. Therefore, in the first study, compositions were prepared in which only 1/3 of the B-sites is occupied with Fe^{3+}, accompanied by partial A cation substitution to balance the charge, in the form of $ALa_2FeBSbO_9$ (A = Ca, Sr; B = Ni, Co) and $BaLa_2FeNiSbO_9$. The crystal structure of the series is studied and then compared to the observed magnetic properties. Then, the study was extended to the investigation of the Fe-rich $A_2LaFe_2SbO_9$ (A = Ca, Sr, Ba) perovskites.

The samples have been prepared in solid-state reactions by the group of Prof. Dr. Peter Battle at Oxford University. More details about the synthesis can be found in the appendix at the end of Part I. The experimental details of the used TEM techniques are also listed in the same appendix. The experimental details of the other experiments can be found in the corresponding papers [37,38].

3.2. *A*La$_2$Fe*B*SbO$_9$ (*A*=Ca,Sr; *B*=Ni,Co) & BaLa$_2$FeNiSbO$_9$

3.2.1. Experimental results and discussion

X-ray powder diffraction (XRPD) and neutron powder diffraction (NPD) were performed by the group of Prof. Dr. Peter Battle at Oxford University on the five compounds at 300K and 5K to derive the crystal structure. Both the XRPD and NPD patterns of each compound were indexed and analysed in the primitive monoclinic space group *P2$_1$/n* with a ~$\sqrt{2a_p}$, b ~$\sqrt{2a_p}$ and c ~$2a_p$, where a_p is the unit cell parameter of the primitive pseudo-cubic perovksite. CaLa$_2$FeCoSbO$_9$ shows the largest monoclinic distortion. In the *P2$_1$/n* space group, the structural model, see **Figure 15a**, involves a 4*e* site that accommodates a disordered distribution of *A* and La, three further 4*e* sites occupied by oxide anions and two independent B-sites corresponding to 2*d* and 2*c* which accommodate the three cation species Fe^{3+}, Co^{2+}/Ni^{2+} and Sb^{5+}. For all the compounds except for CaLa$_2$FeCoSbO$_9$, the B cation distribution over the two crystallographically distinct sites derived from the NPD data can be represented by *A*La$_2$(Fe$_{0.5}$*B*)$_{2d}$(Fe$_{0.5}$Sb)$_{2c}$O$_9$. In the case of CaLa$_2$FeCoSbO$_9$, a slightly different distribution was found that is equal to CaLa$_2$(Fe$_{0.32}$CoSb$_{0.18}$)$_{2d}$(Fe$_{0.68}$Sb$_{0.82}$)$_{2c}$O$_9$.

Magnetometry and NPD performed by the group of Prof. Dr. Peter Battle show that these perovskites are ferrimagnets with a G-type magnetic structure (**Figure 15b**). The magnetic moments of the nearest-neighbour B cation positions are aligned in an antiparallel manner, and the presence of the diamagnetic Sb^{5+} on the 2*c* site results in a non-zero remanent magnetization. The remanent magnetization and the coercive field of each component at 5K are presented in **Table 2**, together with their Curie temperatures.

Table 2.*Coercive fields and remanent magnetization per formula unit, H_c (kOe) and M_r (μ_B) at 5 K and the corresponding Curie temperature T_c (K) of ALa$_2$FeBSbO$_9$ (A=Ca, Sr, Ba; B = Ni, Co). The compounds are ordered from high to low Hc and M_r.*

Compound	H_c (kOe)	M_r (μ_B)	T_C *(K)*
SrLa$_2$FeCoSbO$_9$	6.1	~1.0	~ 215 K
CaLa$_2$FeCoSbO$_9$	5.0	1.0	~ 250 K
SrLa$_2$FeNiSbO$_9$	0.7	0.35	~ 350K
CaLa$_2$FeNiSbO$_9$	0.3	0.24	~ 350K
BaLa$_2$FeNiSbO$_9$	0.5	0.21	~ 350K

Despite the cobalt-containing compounds exhibiting magnetic behaviour different to that shown by the nickel-containing compounds, the only structural difference detected by XRPD and NPD was the presence of antimony on both six-coordinate sites in the $CaLa_2FeCoSbO_9$ component. In order to investigate the origin of the differences in magnetic properties and whether the difference in B cation distribution is related to the magnetic properties, I studied the local structure using transmission electron microscopy.

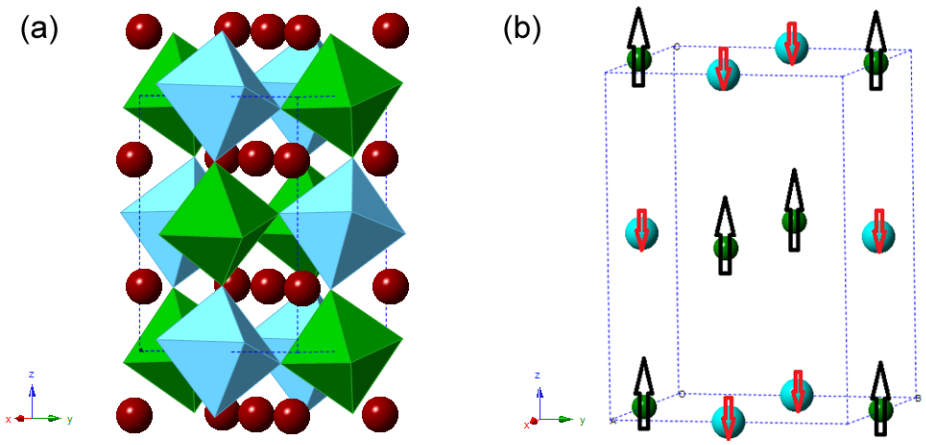

Figure 15. *(**a**) Crystal structure, derived from XRPD and NPD, adopted by $ALa_2FeBSbO_9$ (A=Ca, Sr, Ba; B=Ni, Co). Green octahedra and blue octahedra are occupied by different B cations. The corners of the octahedra represent the oxygen atoms. The red atoms represent the alkaline earth and La atoms at the A-site. (**b**) The G-type magnetic structure adopted by $ALa_2FeBSbO_9$ (A=Ca, Sr, Ba; B=Co, Ni). Arrows indicate the direction of ordered spins at the B-sites. Green spheres represent the 2d sites, and blue spheres represent the 2c sites.*

All SAED patterns obtained from $CaLa_2FeCoSbO_9$, $CaLa_2FeNiSbO_9$, $SrLa_2FeCoSbO_9$, and $SrLa_2FeNiSbO_9$ could be indexed with the $P2_1/n$ model. Representative patterns of the main zones are shown in **Figure 16**. Also, the high-resolution HAADF-STEM images of the four compounds are very similar, and therefore only the image from $CaLa_2FeCoSbO_9$ taken along the [010] zone is displayed in **Figure 17**. As the crystal structures of the four compounds are very similar, only the TEM data of $CaLa_2FeCoSbO_9$ will be displayed in this thesis, as representative for all four compounds. The TEM data of the other three compounds can be found in the corresponding papers [37,38]. The barium-containing compound showed a different main phase and will be discussed separately below.

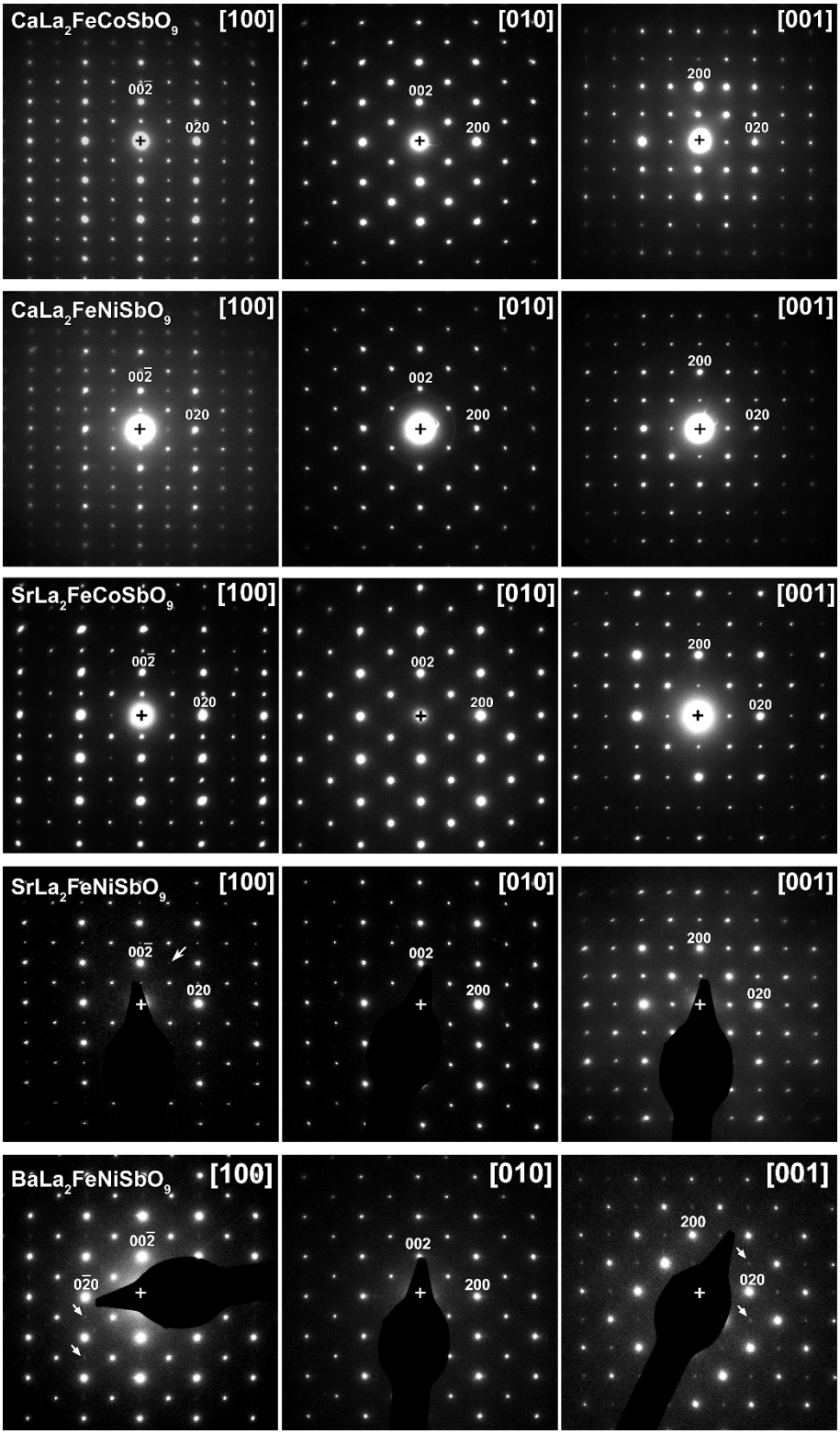

Figure 16. *SAED patterns along the zone axes [100], [010] and [001] of the $P2_1/n$ symmetry obtained from the five $ALa_2FeBSbO_9$ samples. The SAED patterns corresponding to the calcium and strontium compounds represent the main phase, while the SAED patterns obtained from the barium compound represent the additional phase present in the $BaLa_2FeNiSbO_9$ sample.*

In HAADF-STEM images, the intensity of the atom columns is proportional to the atomic number of the elements: $I \sim Z^2$. Therefore, in **Figure 17** the rows with alternation of darker and brighter dots along the *a*-axis correspond to, respectively, the alternating (Co,Fe) ((Ni,Fe) in the nickel-containing compounds) and (Sb,Fe) atom columns, and show clear ordering of the B cations. This is supported by the accompanying EDX maps, shown in **Figure 18**. The continuous rows of bright dots along the *a*-axis correspond to the A-sites occupied statistically by La and Ca (Sr in the other compounds). The EDX maps also show that Co (Ni) and Sb occupy separate B-sites, while Fe is present on both B-sites. The maps of Ca and Sb show artefacts due to the overlap of the K-line of Ca (3.692 keV) and the L-line of Sb (3.604 keV). The intensity at B positions in the Ca maps is due to the overlapping Sb peak, oppositely, the intensities observed at A positions in the Sb maps are due to the overlapping Ca peak. The true signal on the Ca maps is only the homogeneous, much weaker signal overlapping with the La positions.

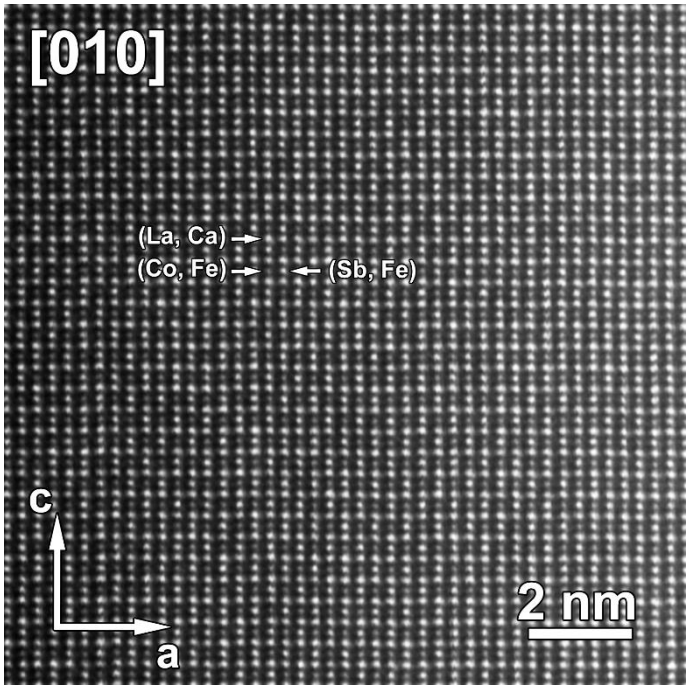

Figure 17. *High-resolution HAADF-STEM image of $CaLa_2FeCoSbO_9$ along the [010] zone axis, where the continuous rows of bright dots along the a-axis are occupied by both La and Ca. The rows with alternation of darker and brighter dots along the a-axis correspond to (Co, Fe) and (Sb, Fe) atom columns, respectively.*

Whereas the NPD refinement for $CaLa_2FeCoSbO_9$ resulted in a distribution $CaLa_2(Fe_{0.32}CoSb_{0.18})_{2d}(Fe_{0.68}Sb_{0.82})_{2c}O_9$, a line profile (**Figure 19**) taken along the alternating B-site positions in the high-resolution EDX (HR-EDX) map revealed a slight preference of Fe for the Co positions instead.

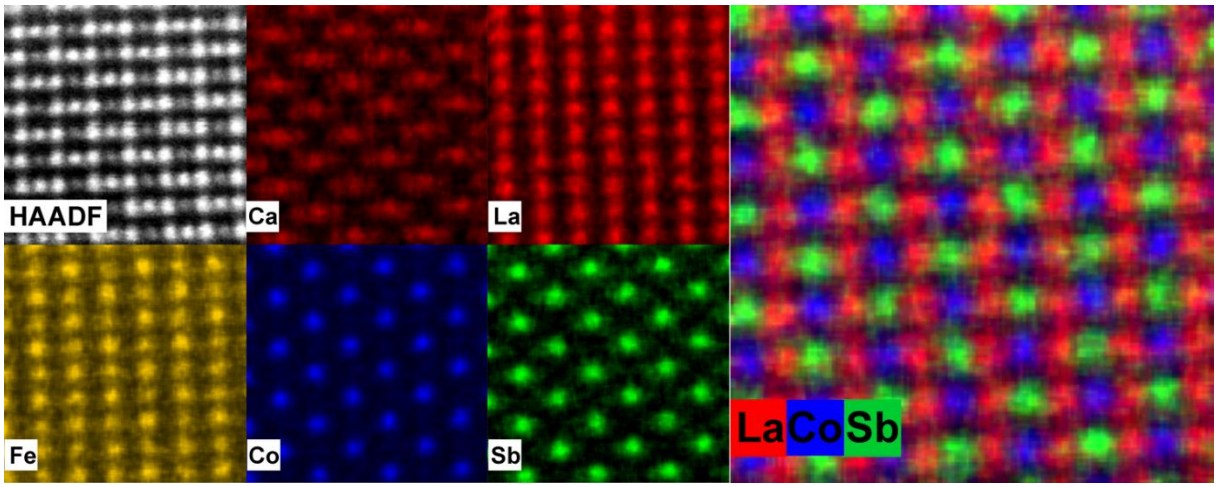

***Figure 18. Left**: The high-resolution HAADF-STEM image of the $CaLa_2FeBSbO_9$ sample along [010] together with the individual Ca/La/Fe/Co/Sb elemental maps. **Right**: the mixed {La,Co,Sb} element map.*

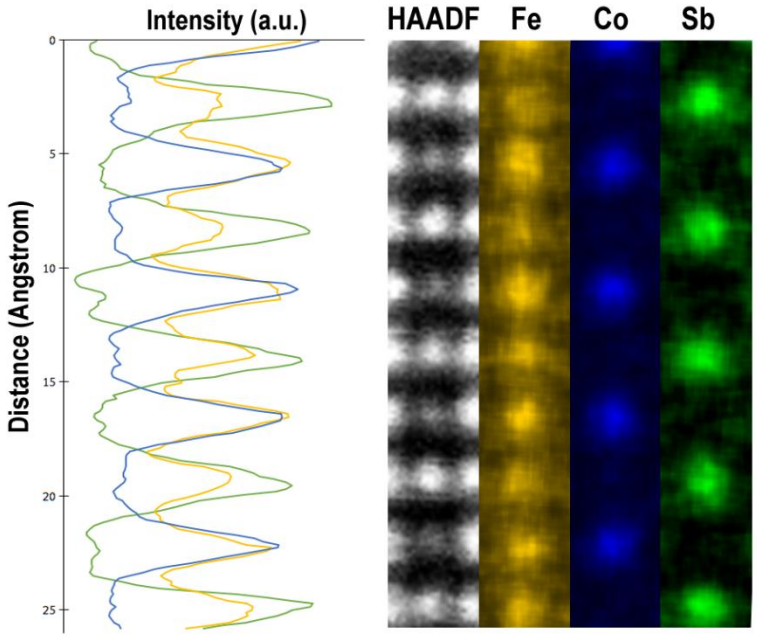

***Figure 19. Left:** Line profile of the elements Fe, Co and Sb in counts. **Right:** the HAADF-STEM image, with the individual EDX maps of Fe, Co and Sb, of which the line profile has been taken.*

Since converting the HR-EDX maps to atomic percentage introduces broadening of the peaks, we have quantified the occupancies at the two different B-site positions by applying the Cliff-Lorimer method manually after averaging the HR-EDX maps in counts. **Figure 20** shows the averaged individual element maps of the three B cations. The line profile of every element map is fitted by a combination of Gaussian functions using the program Fityk [43]. Note that the line profiles were taken from element maps in the same colours, as the display colours affect the intensity line profiles. The FWHM of the different Gaussian peaks were fixed per element. The FWHM of Co-K is 1.94 Å, Sb-L is 1.98 Å, and Fe-K is 2.15 Å.

The Cliff-Lorimer method, assuming the thin specimen conditions [3,44], is based on the following formula:

$$\frac{C_{Sb}}{C_{Co(Fe)}} = k_{Sb,Co(Fe)} \frac{I_{Sb}}{I_{Co(Fe)}},$$

where c_B stands for the concentration of element B in atomic percentage, I_B indicates the measured X-ray counts corresponding to element B, and $k_{B,B'}$ is the proportionality factor between element B and B'. By using $C_{Sb} + C_{Co} + C_{Fe} = 1$ together with the Cliff-Lorimer formula, where $\frac{I_{Sb}}{I_{Co(Fe)}}$ is determined by taking the ratio of the area under the Gaussian peaks of Sb and Co (Fe) at one of the B-site positions, we were able to quantify the occupancies of Sb, Co and Fe at that position. In order to apply this method, we first have to determine the $k_{Sb,Co}$ en $k_{Sb,Fe}$ factors by linking the ratio of the sum of the Gaussian peaks of both B-site positions to the ratio of the concentration derived from the entire HR-EDX map itself: 32.4 at% Sb, 33.6 at% Co and 34.0 at% Fe.

The quantification of the occupancies of both B-site positions is shown in **Table 3.** The error on the occupancies is calculated by propagation with the k factor variation $\Delta k_{B,B'}/k_{B,B'} \sim 0.1$ and assuming the error on the counts I_B is $\sqrt{I_B}$ [3]. Note that the values derived from HR-EDX maps are always only an estimate due to electron beam channelling and broadening [45]. All three B cations are present at both sites but in different ratios. A higher Fe concentration is present at the 2*d* site position, which is mainly occupied by Co, than at the 2*c* site, which is mainly occupied by Sb.

Table 3. *The occupancies calculated by the Cliff-Lorimer method for both B-site positions of the $CaLa_2FeCoSbO_9$ sample. The average composition over both positions is in agreement with the overall measured composition shown in Table 5.*

	Sb [at%]	Co [at%]	Fe [at%]
2*c* site	56(2)	15(1)	29(2)
2*d* site	9(1)	52(3)	39(3)
Average	33(2)	34(3)	34(4)

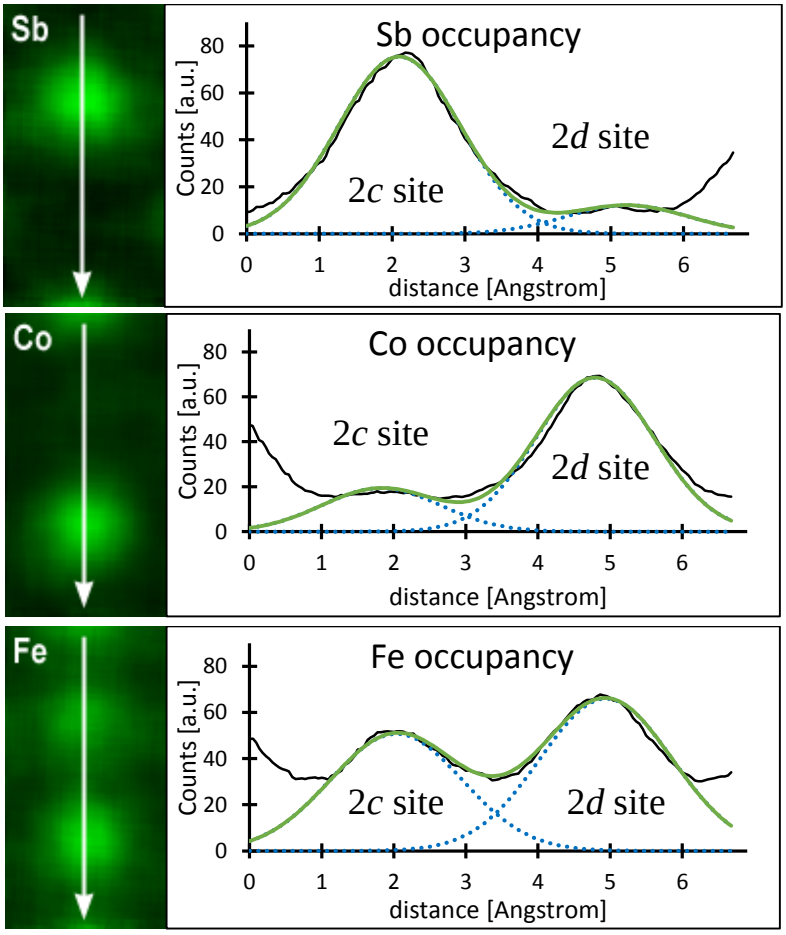

Figure 20. *The individual element maps are shown for Sb, Co and Fe with on the right the corresponding line profiles (black) given in counts. Each peak is fitted by a Gaussian peak displayed in a blue dashed line, where the FWHM is fixed for each element. The green line shows the sum of the Gaussian peaks.*

However, an attempt to use this cation distribution in the analysis of the neutron diffraction data, which were collected from the bulk sample rather than from local regions, resulted in a significantly worse fit. In the cases of $CaLa_2FeNiSbO_9$ and $SrLa_2FeNiSbO_9$, the line profiles taken over the HR-EDX maps show a preference of Fe for the Ni-dominated positions, while NPD and XRD showed an equal distribution of Fe between the 2*d* and 2*c* positions. The discrepancy between the derived B cation distributions will be further discussed after the structure characterization of $BaLa_2FeNiSbO_9$.

$BaLa_2FeNiSbO_9$ stands out from the other compounds as the sample shows two phases with different symmetries, whereas for the other compounds, all SAED patterns could be indexed using $P2_1/n$. In HAADF-STEM (see **Figure 25**), all regions, and thus both phases, were ordered. Taking the B cation ordering into account, the SAED patterns of the main phase, shown in **Figure 21**, allow several possible space groups: cubic $Fm\bar{3}m$ ($a^0a^0a^0$), rhombohedral $R\bar{3}$ ($a^-a^-a^-$), tetragonal $I4/m$ ($a^0a^0c^-$) or monoclinic $I2/m$ ($a^-a^-c^0$). The corresponding tilts of the octahedra around the three basis vectors $<100>_p$ of the pseudo-cubic perovskite are indicated following the space groups using the Glazer notation [46]. The difference between the space groups is related to the presence of either an anti-phase tilt (denoted with '-') or the absence of a tilt (denoted with '0'). The characteristics of the different space groups are presented in **Table 4**. The cubic space group $Fm\bar{3}m$ describes a structure without any octahedral tilt, while the rhombohedral $R\bar{3}$, monoclinic $I2/m$ and tetragonal $I4/m$ describe a structure with respectively three, two or one anti-phase octahedral tilt along the different $[100]_p$, $[010]_p$ and $[001]_p$ directions. Therefore, ABF-STEM images were taken along the pseudo-cubic zone axes to investigate whether octahedral tilts are present or not. The contrast of ABF-STEM images is proportional to $Z^{1/3}$ so that atomic columns appear as dark spots on a white background, and allows visualizing the light oxygen atomic columns (Z_O=8) in the presence of heavy elements.

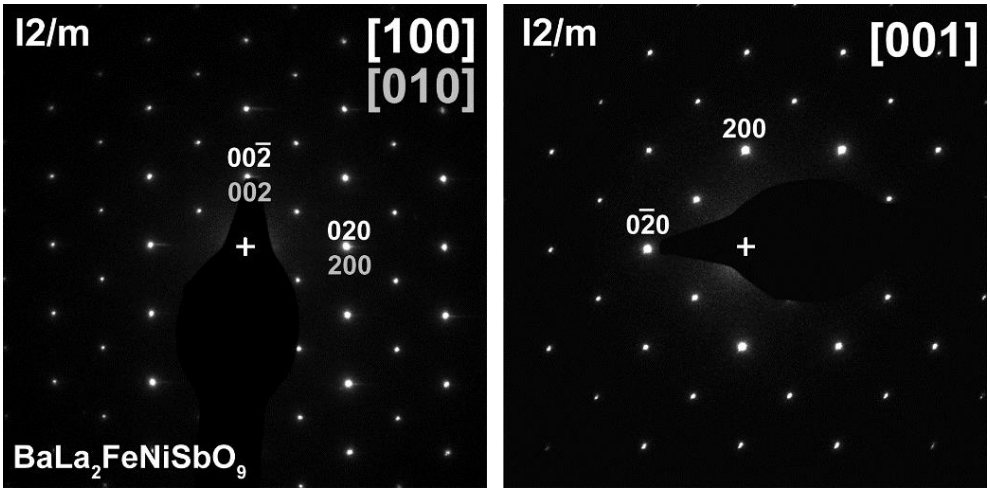

Figure 21. *SAED patterns of the $BaLa_2FeNiSbO_9$ sample along the zone axes [100]/[010] and [001], indexed using space group I2/m.*

Table 4. *The four considered possible space groups for the main phase of $BaLa_2FeNiSbO_9$, with the corresponding transformation matrices and octahedral tilts, as well as the space group corresponding to the second additional phase of $BaLa_2FeNiSbO_9$.*

Crystal class	**Space group**	**Lattice vectors w.r.t. the parent perovskite axes $[100]_p[010]_p[001]_p$**	**Glazer notation***
Cubic	$Fm\bar{3}m$	[200] [020] [002]	$a^0a^0a^0$
Rhombohedral	$R\bar{3}$	[$\bar{1}$10] [0$\bar{1}$1] [222]	$a^-a^-a^-$
Tetragonal	*I4/m*	[1$\bar{1}$0] [110] [002]	$a^0a^0c^-$
Monoclinic	*I2/m*	[1$\bar{1}$0] [110] [002]	$a^-a^-c^0$
Monoclinic	$P2_1/n$	[1$\bar{1}$0] [110] [002]	$a^-a^-c^+$

* An anti-phase tilt is denoted with '-', in-phase with '+' and absence of a tilt with '0' and an equal letter denotes an equal size of the tilt angle [46].

Figure 22A shows elongation, up to splitting in the best parts of the image, of the oxygen columns, indicating the presence of an anti-phase octahedral tilt, which means that the main phase has at least one pseudo-cubic axis containing an anti-phase octahedral tilt, and thus allows to eliminate the cubic space group $Fm\bar{3}m$ ($a^0a^0a^0$). Likewise, the rhombohedral space group $R\bar{3}$ ($a^-a^-a^-$) can also be discarded, since the ABF-STEM image in **Figure 22B** shows no tilt, indicating that there is at least one a^0. Including the ABF-STEM images in our TEM study limits the possible space groups to only two, namely the tetragonal *I4/m* and monoclinic *I2/m*. The transition from the pseudo-cubic structure to the tetragonal or monoclinic unit cell is the same as for the space group of the additional phase $P2_1/n$ ($a^-a^-c^+$). The difference lies in the direction in which the anti-phase octahedral tilt is present; for *I4/m* ($a^0a^0c^-$) an anti-phase tilt is only present along the c-axis (=c_p), while for *I2/m* ($a^-a^-c^0$) anti-phase tilts are present along the [$1\bar{1}0$] (=a_p) and [110] (=b_p) orientations.

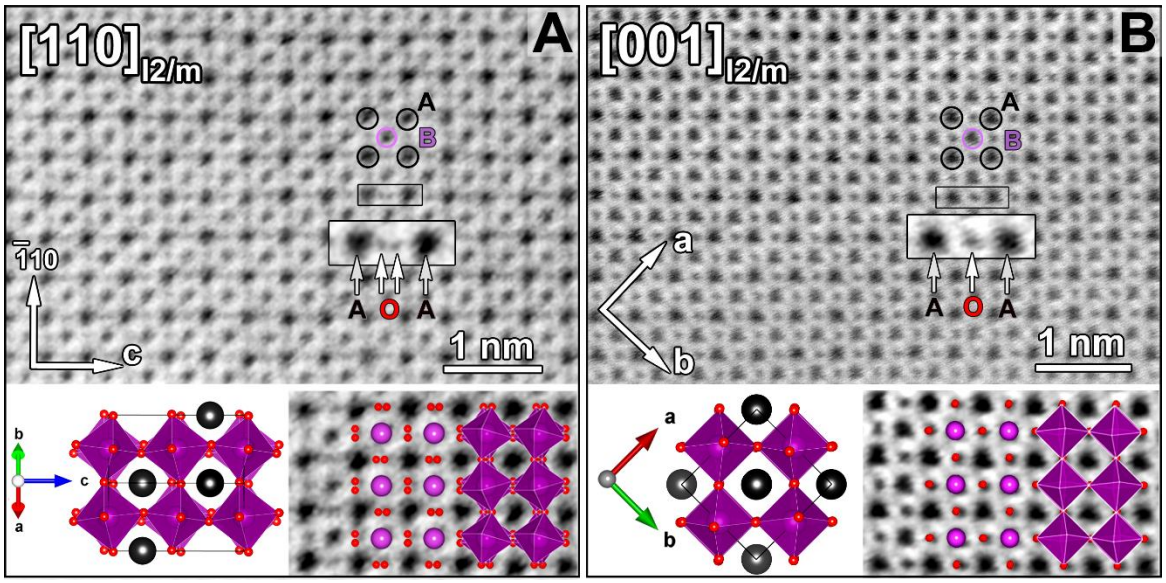

Figure 22. *ABF-STEM images taken from the main phase I2/m of $BaLa_2FeNiSbO_9$.* ***(A)*** *ABF-STEM image taken along the [110] orientation ($[010]_p$), where the arrows show splitting of the oxygen column confirming the presence of anti-phase octahedral tilts.* ***(B)*** *ABF-STEM image taken along the [001] orientation (i.e. $[001]_p$), where the arrow shows the absence of a tilt. The different tilts are also illustrated in the close-up at the bottom together with the corresponding view of the model, where the black atoms represent the A cations, the red atoms represent oxygen, and the purple octahedra represent the B cations with oxygen at the corners.*

Due to twinning and high similarity between many zones, we cannot distinguish between *I2/m* ($a^-a^-c^0$) and *I4/m* ($a^0a^0c^-$) using convergent beam electron diffraction. However, the FFT (**Figure 23**), taken from the same area as **Figure 22A**, shows diffuse intensities at positions corresponding to the extra reflections $\bar{h}hl$: *l=2n+1* in the [110] orientation of the secondary phase $P2_1/n$ ($a^-a^-c^+$). Diffuse intensities indicate short-range order between the two phases. The diffuse intensities allow us to locate the c_p axis on the image, and index it as [110] of $P2_1/n$, and consequently also as [110] of *I2/m* or *I4/m*. As we see splitting of the oxygen columns in two 90° directions, there is a tilt around an axis perpendicular to c_p. This agrees with *I2/m* but not with *I4/m*. The deduction of *I2/m* is also supported by the diagram in **Figure 24** that shows the group-subgroup relationship between the possible space groups for perovskites with rock-salt B cation ordering and octahedral tilts (using different settings, *I2/m* corresponds to *C2/m*, and $P2_1/n$ corresponds to $P2_1/c$). This shows that $P2_1/n$ is a subgroup of *I2/m*, while there is no group-subgroup relation between $P2_1/n$ and *I4/m*. The group-subgroup relation between the two phases $P2_1/n$ and *I2/m* makes them more likely to coexist within a single crystal.

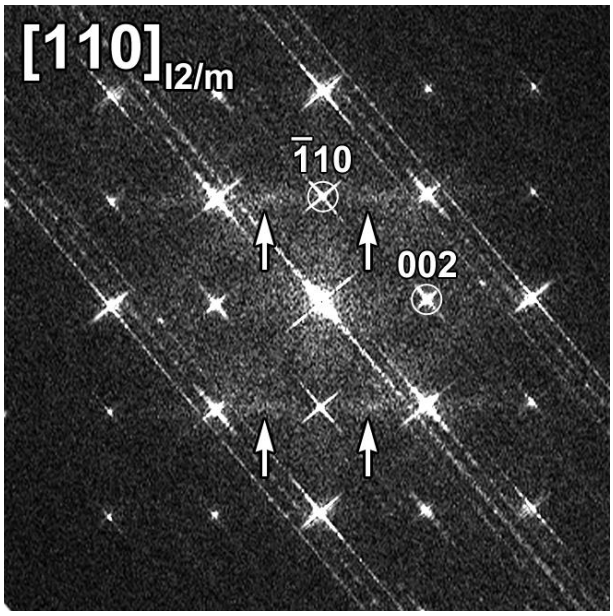

Figure 23. *The FFT was taken from the same area as Figure 22A, but with lower magnification to visualize the diffuse intensities better, which are marked by the arrows. The bright reflections can be indexed by the I2/m symmetry, while the diffuse intensities correspond to the extra reflections* $\bar{h}hl$*: l=2n+1 seen in the [110] orientation of the* $P2_1/n$ *symmetry*

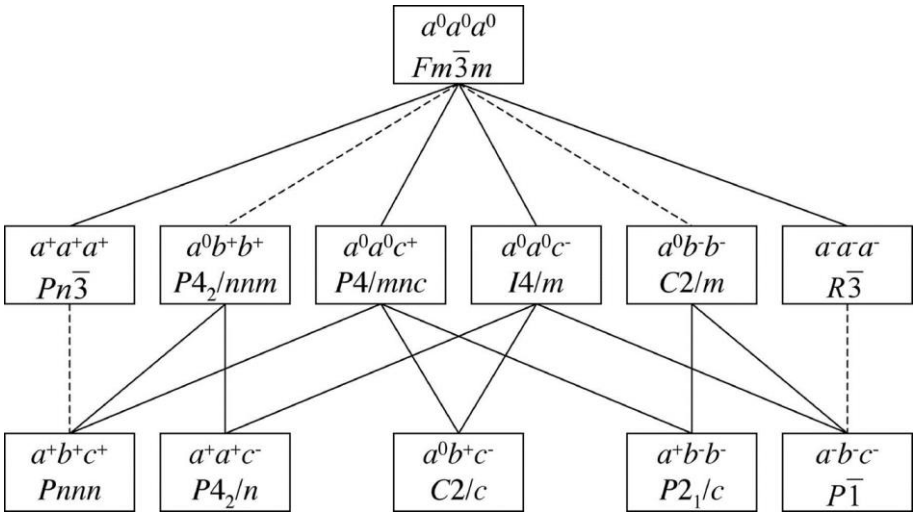

***Figure 24**. A schematic diagram indicating the group-subgroup relations among the 12 space groups, derived as the isotropy subgroups of $Pm\bar{3}m$, including cation ordering and octahedral tilts. A dashed line joining a group to its subgroup indicates that the corresponding phase transition is required by Landau theory to be first-order [46].*

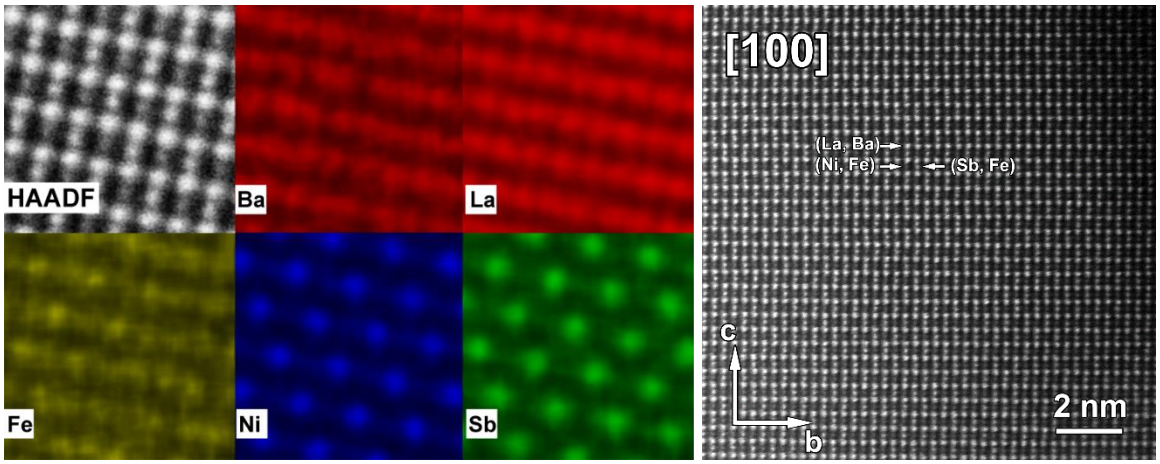

***Figure 25. Left:** High-resolution HAADF-STEM image of the $BaLa_2FeNiSbO_9$ sample along [010]. Ordering is present between Ni and Sb over B-sites (Ni:Sb = 1:1), while Fe is present at both B-sites with a preference for the Sb position. **Right:** High-resolution HAADF-STEM image of $BaLa_2FeNiSbO_9$ in $P2_1/n$ symmetry along the [100] zones axis, where the continuous rows of bright dots along the b-axis are occupied by both La and Ba. The rows with alternation of darker and brighter dots along the b-axis correspond to (Ni, Fe) and (Sb, Fe) atom columns, respectively.*

The SAED patterns of the second phase are shown in **Figure 16** and are consistent with the $P2_1/n$ ($a^-a^-c^+$) model found for the calcium and strontium analogues. Similar to the calcium and strontium analogues, the atomic-resolution HAADF-STEM image and EDX maps (**Figure 25**) clearly show ordering between Ni and Sb, with Fe present on both sites. However, unlike the other compounds, the atomic-resolution EDX map implies a preference of Fe for the Sb-dominated positions, whereas, for the other compounds, it showed a preference for the Ni/Co shared positions. Note that NPD and XRPD showed an equal distribution of Fe between the 2*d* and 2*c* positions.

The discrepancy between the refined occupancies from NPD and XRPD and the preferences derived from the EDX maps are explained by our overview EDX results, which show that all samples have a certain degree of inhomogeneity, except for $SrLa_2FeCoSbO_9$. The overview EDX maps are shown in **Figure 26**, where only $SrLa_2FeCoSbO_9$ shows a homogeneous distribution for both the A and B cations. The maps from the other compounds show an inhomogeneous distribution for both the A cations (La, *A*) and the B cations (Fe, *B*, Sb), which is also clarified using scatter plots shown in **Figure 27**. Regions and entire crystallites with deviating compositions are present, although the A to B ratio is always approximately 1. In addition to the expected composition, various measurements correspond to either a phase deficient in both Fe and La, with increased concentrations of *A* (Ba/Ca/Sr), *B* (Ni/Co) and Sb, or a phase rich in Fe and La, with lower concentrations of *A* (Ba/Ca/Sr), *B (*Ni/Co) and Sb. The variations in both the A cations and B cations are much more significant in the nickel-containing compounds than in the cobalt-containing compound. The average element contents for the five compounds, each calculated from approximately 50 crystallites, are shown in **Table 5**. The homogeneity increases in the sequence $BaLa_2FeNiSbO_9$ < $SrLa_2FeNiSbO_9$ < $CaLa_2FeNiSbO_9$ < $CaLa_2FeCoSbO_9$ < $SrLa_2FeCoSbO_9$.

Table 5. *The average cation contents in atomic percentage of $ALa_2FeBSbO_9$ (A=Ca, Sr, Ba; B = Ni, Co).*

	A	La	Fe	B	Sb
$SrLa_2FeCoSbO_9$	19(2)	33(1)	15(1)	16(1)	16(1)
$CaLa_2FeCoSbO_9$	18(3)	35(3)	15(4)	15(2)	17(2)
$CaLa_2FeNiSbO_9$	18(3)	35(3)	15(5)	15(3)	17(3)
$SrLa_2FeNiSbO_9$	15(3)	36(4)	17(8)	15(4)	17(4)
$BaLa_2FeNiSbO_9$	15(4)	37(5)	18(7)	15(4)	15(4)

The targeted values, corresponding to $ALa_2FeBSbO_9$ would be 16.7, 33.3, 16.7, 16.7 and 16.7.

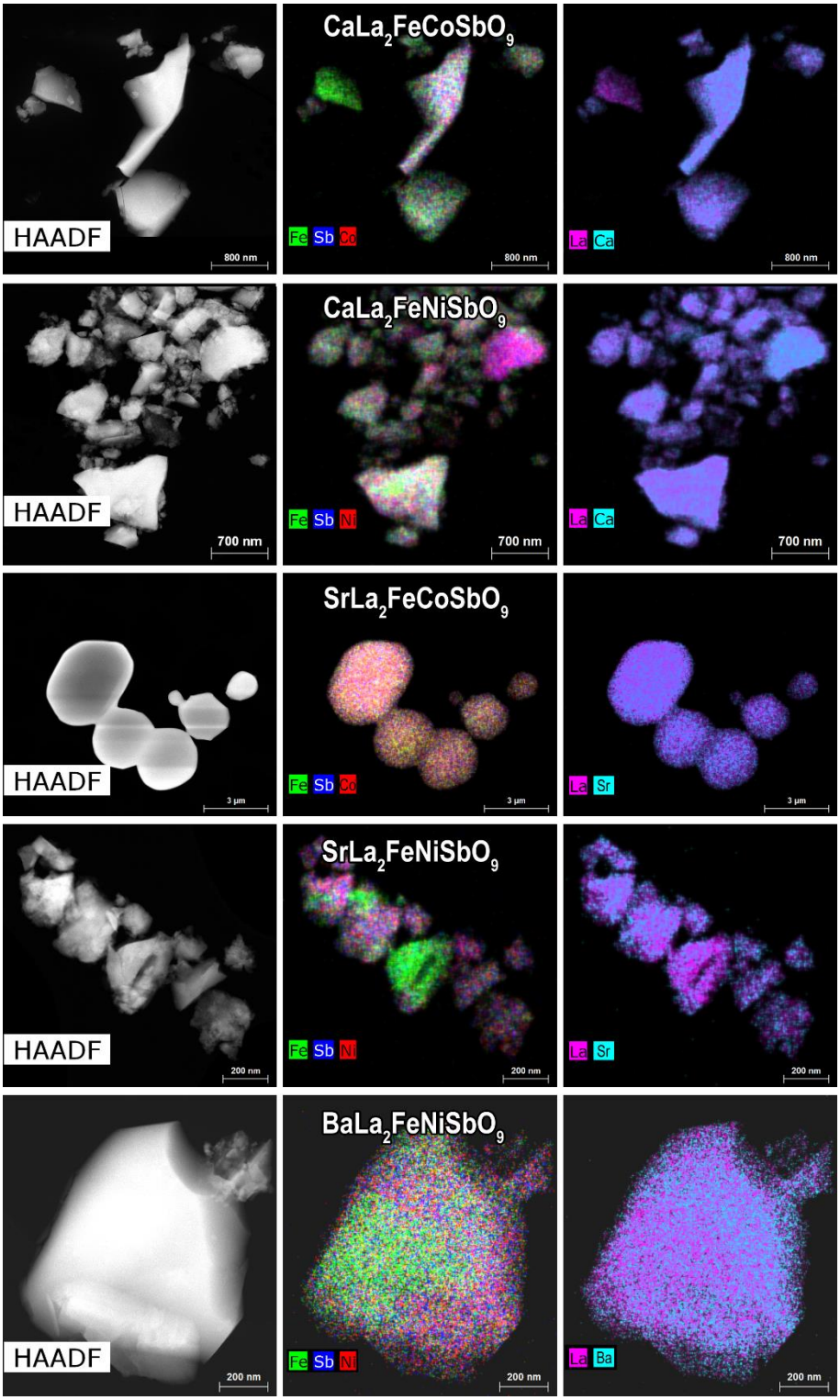

Figure 26. *HAADF-STEM image of particles in the $ALa_2FeBSbO_9$ samples with mixed (A/Ca, Fe/B/Sb) element maps in counts. The A and B cations in $SrLa_2FeCoSbO_6$ are homogeneously distributed, compared to the other compounds.*

The correlation between the A cations and B cations can be explained by local charge neutrality (LCN). For all four compounds, the formula can be written as $La_{2-x}A_{1+x}Fe_{1-y}B_{1+y/2}Sb_{1+y/2}O_9$ (A=Ca^{2+}, Sr^{2+}, Ba^{2+}; B=Co^{2+}, Ni^{2+}), where the (La, *A)* to (Fe, Sb, *B)* ratio is always approximately 1 (i.e. both the perovskite A and B cation positions are fully occupied) and where it is assumed that an increased La content implies an increase in Fe content and that the content of B and Sb changes equally. The latter is an approximation necessary to reduce the number of variables to allow a quantitative analysis of the general tendencies and is supported by the scatter plots in **Figure 28**, but not always perfectly valid. If there is local charge neutrality, this complex formula can be rewritten using a single variable, x, by taking into account the oxidation states of La^{3+}, Fe^{3+} and Sb^{5+}; i.e. $La_{2-x}A_{1+x}Fe_{1-2x}B_{1+x}Sb_{1+x}O_9$. Using this formula, a theoretical relationship that preserves the charge balance between the La:*A* and (*B*+Sb):Fe ratios can be drawn, shown as the grey line in the scatter plots of **Figure 27**. The measured compositions of the calcium-containing compounds agree well with the calculated relationship, showing that despite the variations in the composition throughout the crystals, the local charge neutrality is well maintained. Note that some of the error bars in **Figure 27** are very large because the error bars are determined by propagation and taking the ratio of the measured contents can lead to large error bars.

The strontium and barium analogues show a worse fit. The regions that do not fit the curves within the error margins, marked in the scatterplots of $ALa_2FeNiSbO_9$ (A=Sr, Ba), actually do not agree with the assumption that an increased Fe concentration implies an increase in the La concentration nor with the assumption that the *B* cations Ni/Co and Sb increase concomitantly (see **Figure 28**). Unfortunately, the inclusion of an extra variable allowing for this variation makes it impossible to produce an interpretable visualization.

Only in the case of the strontium-containing compound is the Gaussian curve of the charge per region, assuming a perovskite structure with full oxygen occupancy, not centred at 0 (neutral charge), but at +0.2(2). We cannot currently explain this slight deviation from charge neutrality. We propose that it might be due to the presence of a non-perovskite phase. The deviations are then artefacts caused by the assumption of the perovskite structure for all crystallites. However, no conclusive evidence was seen for such phase among the SAED patterns or HAADF-STEM images.

In general, the cobalt-containing compounds are more homogeneous than the nickel-containing compounds, which could be related to the different reaction rates of Co^{2+} and Ni^{2+} during the synthesis of the samples; a d^8 cation possesses greater crystal field stabilization energy than a d^7 cation, and thus tends to react and diffuse more slowly during the synthesis of the sample. Besides the B cations, also the A cation substitution has an effect on the homogeneity. Since the A cations are disordered, the size difference between La and *A* will induce lattice stress, which will increase as the mismatch between La and *A* increases. Most probably, this lattice stress will force the A and B cations to distribute into domains with different compositions in order to lower the lattice stress. As the size difference between *A* and La increases with the atomic number of the *A* cations: Ca (Δ=0.02 Å), Sr (Δ=0.08 Å) and Ba (Δ=0.25 Å), it is expected that the degree of inhomogeneity also increases with the following sequence: Ca-compounds < Sr-compounds < Ba-compound, which is in agreement with the observed TEM results.

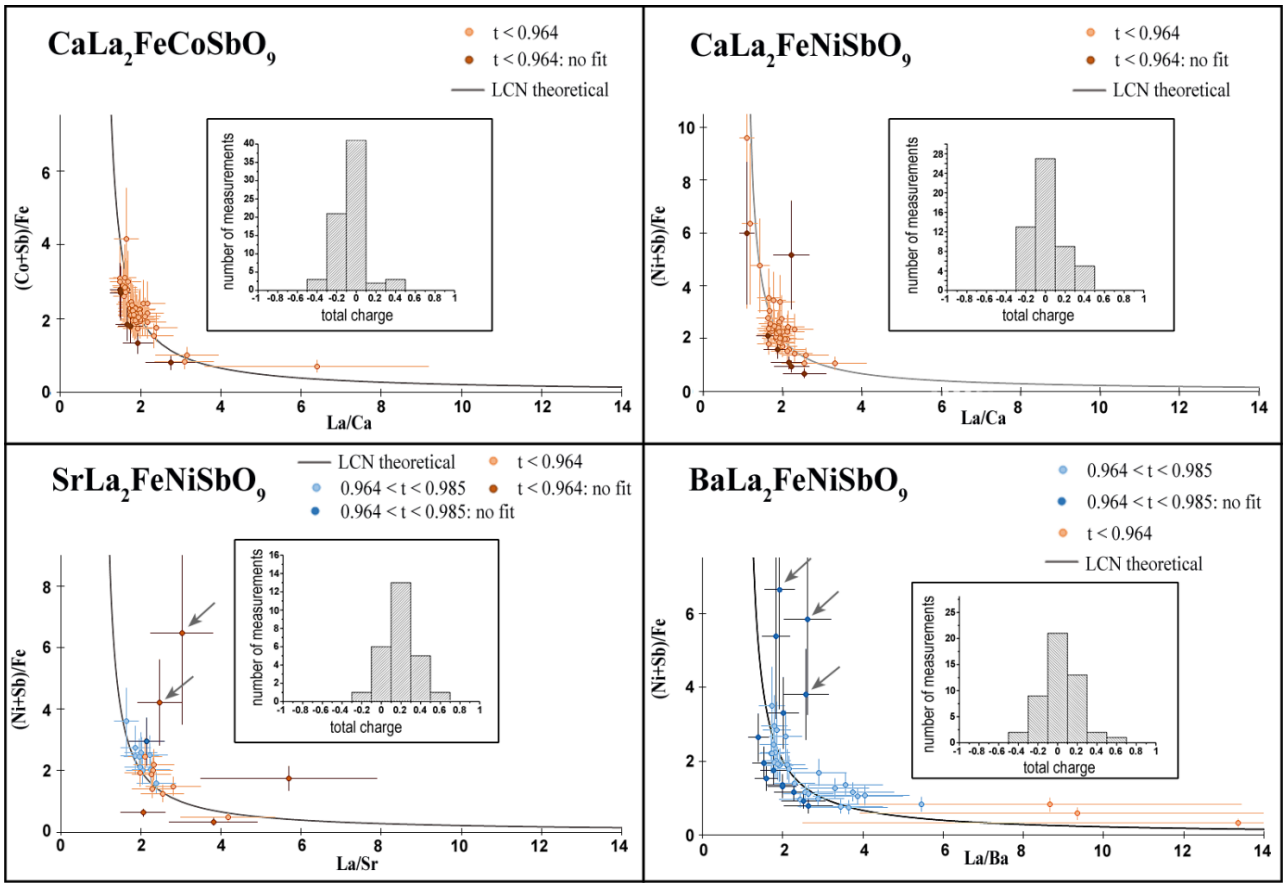

Figure 27. *Scatterplot taken from the experimental compositions obtained from the inhomogeneous $ALa_2FeBSbO_9$. The x-axis shows the ratio between the A cations, La/A, and the y-axis shows the ratio between the B cations (B+Sb)/Fe. The 't' in the legend stands for the calculated tolerance factors. The experimental compositions that do not fit the theoretical relationship between the A and B cations based on the local charge neutrality, taking into account the error bars, are shown in dark orange/blue. The arrows mark experimental compositions that do not satisfy the assumption that an increase in La implies an increase in Fe. The inset show the total charge of all the experimental compositions.*

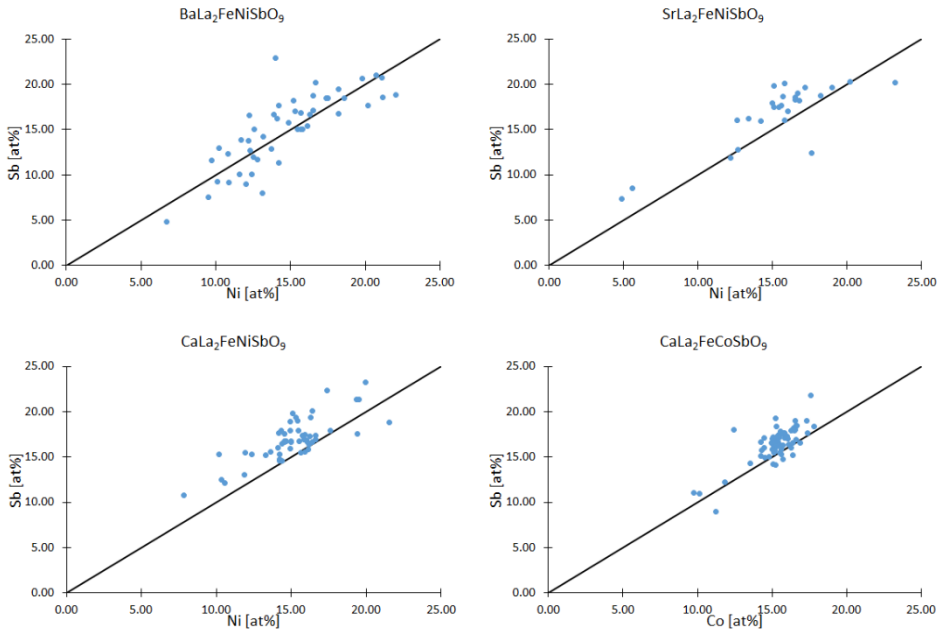

***Figure 28**. Scatterplots were taken from the four inhomogeneous compounds. The x-axis and the y-axis show respectively the Ni/Co and Sb concentrations for each measured composition, given in atomic percentage. The black line corresponds to a 1:1 ratio, corresponding to both B cations always varying in the same way, as taken as an assumption in the quantitative treatment described in the main text. These scatterplots show the assumption is not valid for all crystals but can be taken as a general tendency.*

Since the ionic radius of Ba^{2+} (1.61 Å) is significantly larger than the ionic radii of Ca^{2+}, Sr^{2+} and La^{3+}, which are equal to respectively 1.34 Å, 1.44 Å and 1.36 Å [47], the average ionic radius of the A cations, Ba and La, will vary much more than for the strontium and calcium analogues, causing clear structural variations with different symmetries. In general, when a significantly smaller A cation or larger B cation are introduced into the structure, octahedral tilts can appear to fill the space between the octahedra in order to stabilize the structure. The presence of such octahedral tilts can be predicted by the Goldschmidt tolerance factor, which is described in the introduction. Using this as a rough guideline, we found that the measured compositions for $BaLa_2FeNiSbO_9$ mainly lie in the range where only anti-phase tilts are expected, which are shown as blue dots in the scatterplot in **Figure 27**, while a few variations belong to the range where both in-phase and anti-phase tilts are expected, which are shown as orange dots and can be ascribed to the $P2_1/n$ ($a^-a^-c^+$) phase. The measured tolerance factors agree with our conclusion from TEM that the main phase is *I2/m*, as the most plausible transition is from an in-phase tilt around the *c*-axis (i.e. $P2_1/n$ ($a^-a^-c^+$)) to no tilt around the c-axis (i.e. *I2/m* ($a^-a^-c^0$)) with increasing A cation size. A similar phase transition has also been reported for $Ba_{2-x}Sr_xInTaO_6$ [48].

In the case of the calcium-containing compounds, the difference in ionic radii is negligible, and all the calculated tolerance factors (**Figure 27**) correspond to the *P2₁/n* symmetry, as expected. XRPD analysis also suggested a larger monoclinic distortion, which can be explained by the smaller average ionic radius of the A cations, La and Ca, causing higher octahedral tilts. For $Sr_2LaFeNiSbO_9$ (**Figure 27**), some of the measured compositions would point towards a structure with only anti-phase octahedral tilts, similar to $BaLa_2FeNiSbO_9$, although all SAED patterns could also be adequately indexed using *P2₁/n*. However, the calculated tolerance factors vary between $0.956 < t < 0.965$, and the tolerance factor is only a rough guideline. In the case of the homogeneous $Sr_2LaFeCoSbO_9$, the calculated tolerance factor derived from the average composition corresponds to 0.956(1), which agrees with the *P2₁/n* symmetry.

The magnetic model used by our collaborators to account for the magnetic scattering observed in the NPD patterns is essentially an antiferromagnetic G-type magnetic structure, albeit with different ordered moments on the 2*c* and 2*d* sites. A G-type structure occurs when antiferromagnetic superexchange between nearest-neighbour (NN) cations is the dominant magnetic interaction. If we assume that the samples are homogeneous with B cation ordering (i.e. 2*c* site: 2/3 Sb^{5+} and 1/3 Fe^{3+}; 2*d* site: 2/3 Ni/Co^{2+} and 1/3 Fe^{3+}) and that the NN coupling is the only significant interaction operating, then we expect to see a mean ordered moment of $M_{Fe}/3$ on the 2*c* site and $(M_{Fe}+2M_{Co/Ni})/3$ on the 2*d* site, where the M_{Fe} and $M_{Co/Ni}$ represent the magnetic moments of respectively Fe^{3+} and Co^{2+}/Ni^{2+}, which are equal to ~5μ_B and ~3μ_B/~2μ_B, respectively. In the total G-type structure, the magnetic moments of Fe^{3+} will cancel each other out, resulting in a net magnetic moment of $M_{Co/Ni}$ per formula unit. However, the observed net magnetization is lower than the one calculated from this simplistic model. This might be explained due to the presence of the diamagnetic Sb^{5+} that might reduce the effectiveness and dominance of the NN coupling. Although the antiferromagnetic Fe–O–Fe and Ni/Co–O–Fe interactions between NN sites seem to dominate, it is likely that significant next-nearest-neighbour (NNN) 90° interactions along Fe–O–O–Fe or Fe–O–O–Ni/Co pathways will compete with them. The frustration thus introduced might be responsible for the low magnetic moments. Similar behaviour has been reported in other magnetically dilute, cation-disordered perovskites [49].

However, the discussion of the magnetic properties presented above is largely based on the assumption that our samples are homogeneous while in reality, only $SrLa_2FeCoSbO_9$ satisfies this assumption. All the different particles have the perovskite structure, and this allows us to model the neutron diffraction data to get an average structure, even when the cation distribution is inhomogeneous. However, the magnetic properties of each particle will be governed by different local interactions. For example, a crystallite rich in lanthanum and iron might be expected to have magnetic properties similar to those of $LaFeO_3$ [50–52]. The nickel-containing compounds have a lower saturated moment per formula unit than the cobalt-containing compounds, which is to be expected given the lower moment of Ni^{2+}. However, the decrease might be partly attributable to the higher level of inhomogeneity present in these compositions. This is consistent with the fact that $BaLa_2FeNiSbO_9$, which shows the greatest level of inhomogeneity, has the lowest susceptibility and saturated moment, while $CaLa_2FeNiSbO_9$ and $SrLa_2FeNiSbO_9$ are rather similar to each other.

The magnetic transition temperature of these $ALa_2FeBSbO_9$ (*A*=Ca, Sr, Ba; *B*=Ni, Co) perovskites is higher than those of $La_3Ni_2SbO_9$, which might in part be attributed to the large magnetic moment associated with Fe^{3+}.

3.2.2. Conclusion

The diffraction and microscopy data show that the trio of cations are distributed in a way which, to the best of our knowledge, has not been seen in any other perovskite-related compound; one is occupied by B^{2+} and Fe^{3+} in a 2:1 ratio and the other by Sb^{5+} and Fe^{3+} in the same ratio. While X-ray and neutron powder diffraction data agreed for all four compounds with a single-phase, monoclinic crystal structure in space group $P2_1/n$, TEM images revealed different levels of compositional inhomogeneity at the subcrystal scale. The deviations in the composition appear to adhere to charge neutrality; this was seen most clearly for the calcium-containing compounds. In $BaLa_2FeNiSbO_9$, the most inhomogeneous compound, the compositional inhomogeneity leads to the occurrence of both a primitive $P2_1/n$ phase and a body centred $I2/m$ phase. Magnetometry data, together with neutron diffraction data, have shown that these perovskites are ferrimagnets with relatively high Curie temperatures, and their ferrimagnetism can be explained by a G-type magnetic structure model by assuming single-phase compositions. The decreased average magnetization compared to the predicted one is ascribed to the inhomogeneity of the compounds. A key conclusion from this work is that structural models which account well for X-ray and neutron diffraction data and which contain entirely plausible bond lengths may be flawed because they do not include features in the microstructure that play an important role in determining the physical properties of the compound; these features only become apparent when the microstructure is studied by electron microscopy.

3.3. $A_2LaFe_2SbO_9$ (A = Ca, Sr, Ba)

3.3.1. Experimental results and discussion

In a continuation of this work, we have investigated the iron-rich $A_2LaFe_2SbO_6$ (A=Ca, Sr, Ba) perovskite series. As we have seen in the previous $A La_2Fe B SbO_9$ (A=Ca, Sr, Ba; B=Ni, Co) series that partial substitution of an A cation with a significantly different size affects the crystal structure, we expect to also observe different symmetries for the $A_2LaFe_2SbO_6$ compounds.

The XRPD and NPD analyses indeed show different phases for the different A-compounds; however, the symmetries derived from XRPD and NPD do not always agree with each other. For $Ca_2LaFe_2SbO_9$, both analyses describe the structure by the monoclinic $P2_1/n$ symmetry with two crystallographically distinct B-sites with a cation distribution of $Ca_2La(Fe_{1.25}Sb_{0.25})_{2d}(Fe_{0.75}Sb_{0.75})_{2c}O_9$. In the case of $Sr_2LaFe_2SbO_9$, the XRPD pattern could be accounted for in terms of a single perovskite phase having a triclinic unit cell with $a \sim\sqrt{2}a_p$, $b \sim\sim\sqrt{2}a_p$ and $c \sim 2a_p$, where the absence of many reflections indicated that this cell was I-centred. However, the reflections observed in the NPD pattern did not satisfy the reflection condition for an I-centred unit cell; hkl: $h+k+l = 2n$. Although these reflections are very weak, the presence of these reflections reduces the space group to triclinic $P\bar{1}$. Finally, for $Ba_2LaFe_2SbO_9$, the XRPD pattern could be indexed by the disordered cubic $Pm\bar{3}m$ symmetry; however, the NPD analysis demonstrated broad peaks with tails suggesting some deviations in the cubic structure.

Therefore, it was necessary to investigate the samples with electron microscopy. Since in the previous study the discrepancies arise from the inhomogeneity of the A and B cations, we have first performed an EDX study to examine the homogeneity of the compounds. The EDX maps, shown in **Figure 29**, reveal a high degree of inhomogeneity for all three samples with the experimentally derived average compositions presented in **Table 6**. The calculated compositions reveal a B cation ratio Fe:Sb of 3:2 instead of the targeted ratio 2:1. The ratio of the A cations A:La is approximately 2:1 for the calcium and barium compounds, while for the strontium compound, the ratio corresponds to 3:2. Nevertheless, the relationship between the A and B cations is similar as seen in the previous $A La_2Fe B SbO_9$ series: an increase of the lanthanum content implies an increase of the iron content.

Table 6. *The average cation contents per element, in percentage of the total cation content.*

	A	La	Fe	Sb
$Ca_2LaFe_2SbO_9$	34(6)	17(6)	30(3)	19(3)
$Ba_2LaFe_2SbO_9$	34(5)	18(6)	30(3)	18(3)
$Sr_2LaFe_2SbO_9$	30(7)	20(8)	32(5)	18(5)

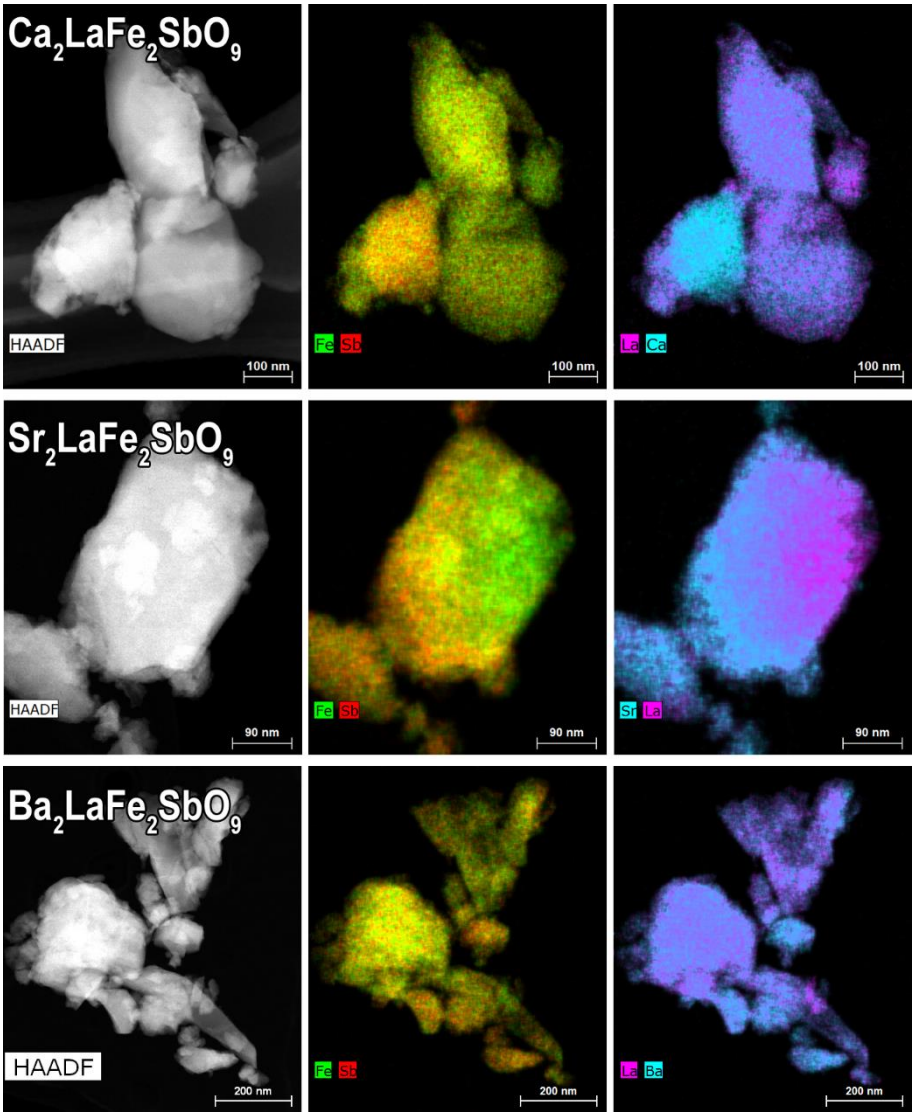

Figure 29. *HAADF-STEM image of particles in the $A_2LaFe_2SbO_9$ (A=Ca, Sr, Ba) perovskites with mixed (Fe, Sb) and (La, A) element maps, given in counts.*

Scatterplots of the experimental compositions of the three samples are depicted in **Figure 30**, where the black dot represents the experimentally derived average composition, showing a deviation from the targeted one, which is marked by a red dot. Therefore, we will describe the compositional variation of the A and B cations with respect to the experimentally derived average composition, in which the total charge is held constant, leading to the formula

$$A^{2+}_{<A>-x}La^{3+}_{<La>+x}Fe^{3+}_{<Fe>+x/2}Sb^{5+}_{<Sb>-x/2}O_9^{2-},$$

where <element> stands for the average content of the element. In this simplified model, the ratio of the (La, *A*) and (Fe, Sb) cations is approximately 1, and it is assumed that no oxygen vacancies are present. The relation between the variation of the (*A*, La) and (Fe, Sb) concentrations is shown in **Figure 30** as a grey line and results in a good fit with the experimental compositions. This means that for all three samples, the variation in composition satisfies the derived relationship that preserves the charge balance.

In the case of $Sr_2LaFe_2SbO_9$, the total charge is shifted to a positive net charge with an average of ~ 0.3(3)e. Moreover, the average composition of only the strontium compound does not agree with the targeted *A*/La ratio, which might be the cause of the shift in total charge. Assume that the experimentally derived Sr/La ratio is wrong and is equal to 2:1 as observed in the other two compounds instead of 3:2. The local charge would then become lower, and thus, closer to zero, as the oxidation of Sr^{2+} is lower than the oxidation of La^{3+}. Comparing the element lines of the A cations used for the EDX quantification: the energy of the X-rays corresponding to the L-line of strontium (1.806 keV) is much lower than the energy of the X-rays corresponding to the lines of La (L-line 4.647 keV), Ca (K-line 3.692 keV), and Ba (L-line 4.466 keV). As low energy X-rays are more likely to be absorbed by the sample [3], the detected X-rays of strontium will suffer more from absorption than the X-rays from the other elements. As a consequence, it might be that the measured strontium content is lower than in reality present in the sample, causing a positive shift of the net charge. This might also explain the slight shift of the net charge that is only observed in the strontium sample in the previous study.

The total charge for $Ba_2LaFe_2SbO_9$ lies around zero, while for $Ca_2LaFe_2SbO_9$ a shift to +0.2(1)e is observed, which can be attributed to the overlap of the K-line of Ca (3.692 keV) and the L-line of Sb (3.604 keV). It is possible that during the quantification a very small amount of calcium was considered as Sb, which leads to a higher positive net charge for the cations due to the higher oxidation of Sb^{5+} compared to Ca^{2+}. In the $CaLa_2Fe*B*SbO_9$ samples from the previous study, the concentration of calcium is much lower compared to lanthanum, which reduces the possible EDX error found in $Ca_2LaFe_2SbO_9$.

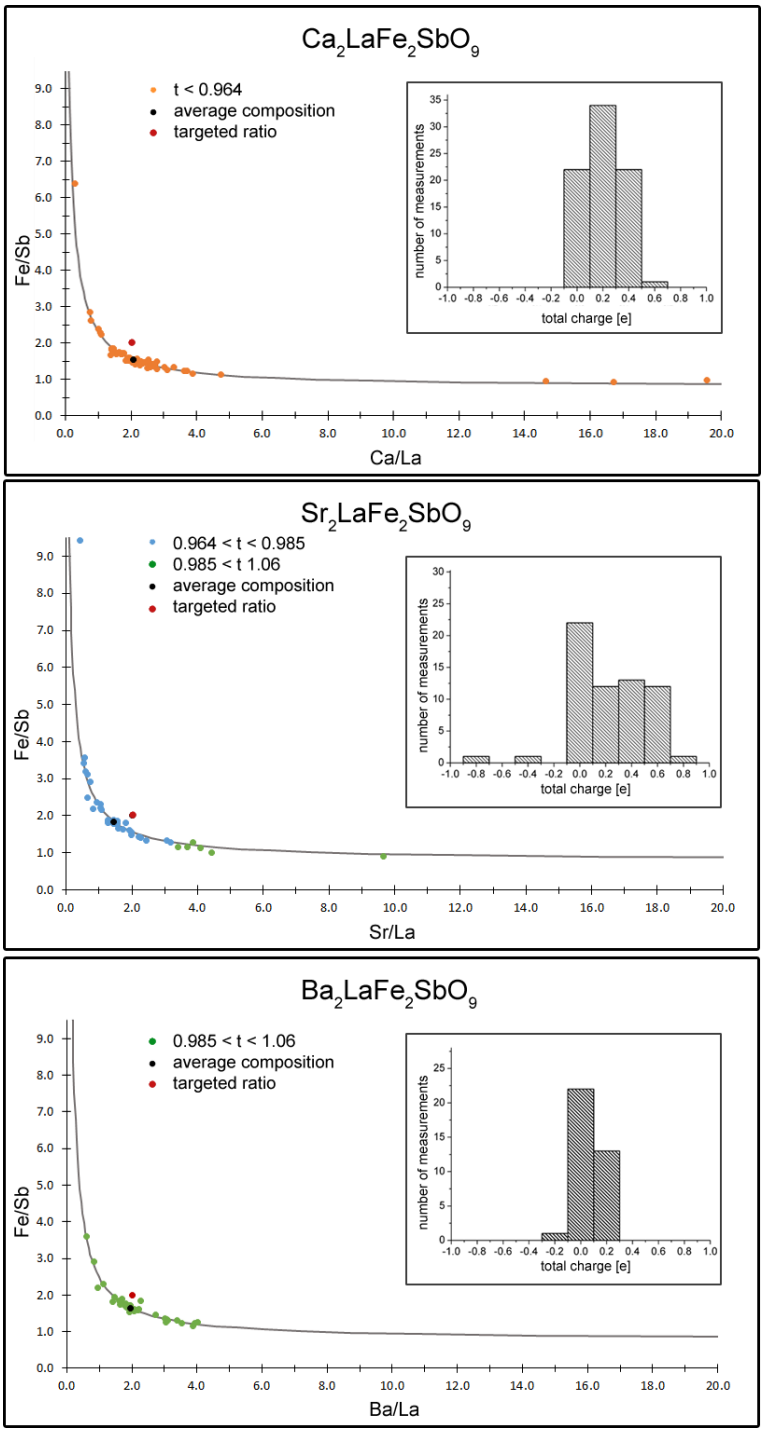

Figure 30. *Scatterplots, taken from the experimental compositions obtained from the $A_2LaFe_2SbO_9$ perovskites. The x-axis shows the ratio between the A cations, A/La, and the y-axis shows the ratio between the B cations Fe/Sb. The 't' in the legend stands for the calculated tolerance factors. Inset shows the total charge of all the experimental compositions. The grey line represents the relation between the variations of the (A, La) and (Fe, Sb) concentrations while preserving the total net charge.*

In contrast to the *A*La_2Fe*B*SbO_9 series, the sequence of the degree of homogeneity is $Ba_2LaFe_2SbO_9 \geq Ca_2LaFe_2SbO_9 > Sr_2LaFe_2SbO_9$; although in both series the greatest level of inhomogeneity is accounted to a sample with multiple phases. The TEM study, discussed below, shows that $Sr_2LaFe_2SbO_9$ consists of two phases, which is supported by the tolerance factor. The calculated tolerance factors of the different compositions found for $(Ca,La)_3(Fe,Sb)_3O_9$ are all lower than 0.964 (see **Figure 30**) and indicate that the structure contains both anti-phase and in-phase octahedral tilts, which is in agreement with the $P2_1/n$ symmetry derived from XRPD and NPD analysis. According to the tolerance factors calculated from the experimental compositions of $(Ba,La)_3(Fe,Sb)_3O_9$ (all *t*-values > 0.985), the crystal structure is untilted, which supports the cubic $Pm\bar{3}m$ symmetry derived from XRPD. In the case of $(Sr,La)_3(Fe,Sb)_3O_9$, the majority of the tolerance factors calculated from the different experimental compositions correspond to the range with only anti-phase tilts (i.e. the compositions shown as blue dots in the scatterplot in **Figure 30**), which can be seen as the main phase. The remaining tolerance factors (i.e. the compositions shown as green dots) lie in the range where the structure is described without tilts, similar to $Ba_2LaFe_2SbO_9$, and would come from particles of a second phase.

The symmetries of the three samples were determined by a combination of SAED patterns, HAADF-STEM images and in the case of $Sr_2LaFe_2SbO_9$ also ABF-STEM images. The SAED patterns (**Figure 31**) and HAADF-STEM image (**Figure 32**) obtained from $Ca_2LaFe_2SbO_9$ confirm the $P2_1/n$ symmetry and cation ordering proposed for $Ca_2LaFe_2SbO_9$ based on the XRPD and NPD data.

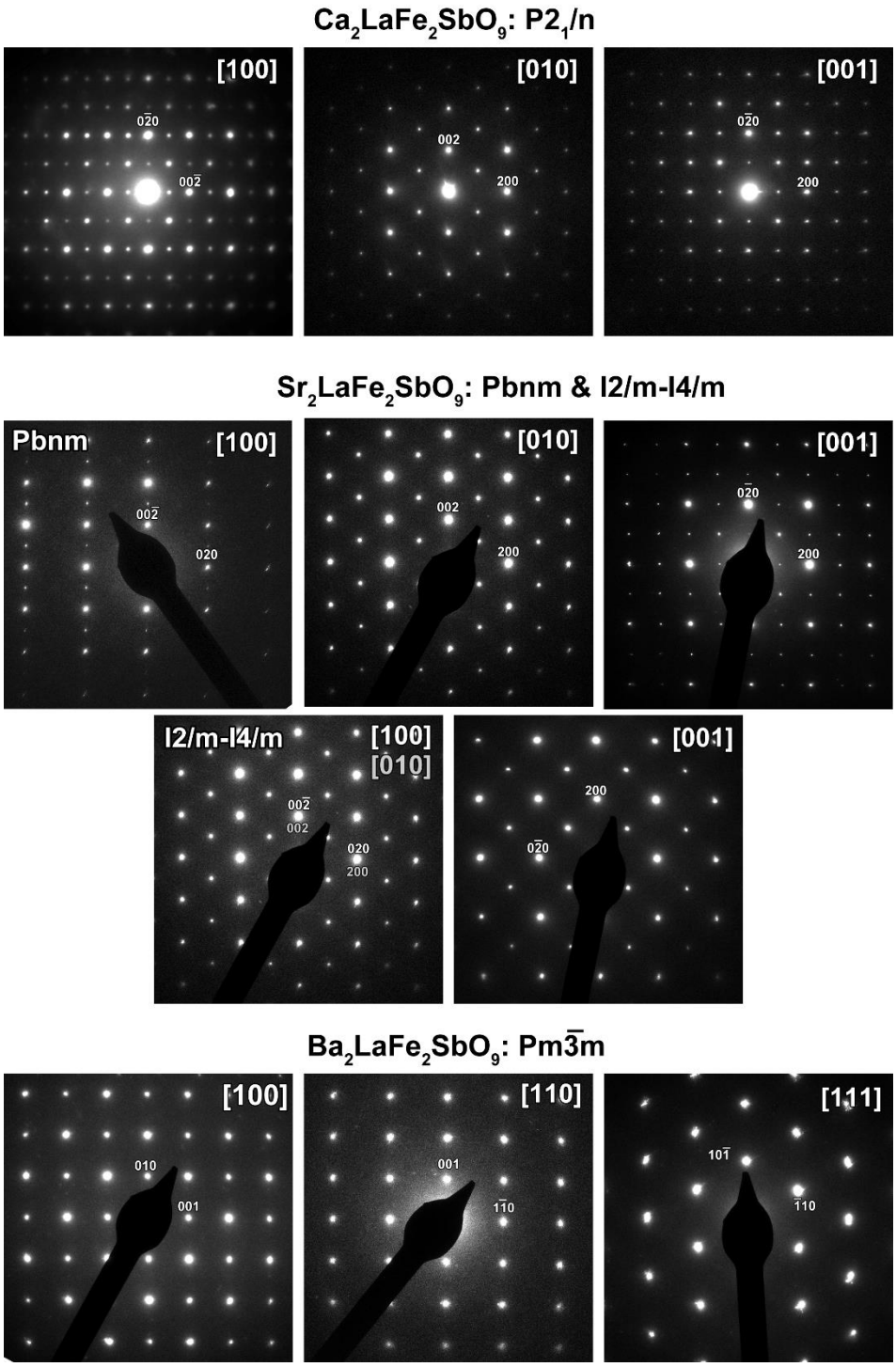

Figure 31. *SAED patterns of $A_2LaFe_2SbO_9$ (A=Ca, Sr, Ba). The SAED patterns obtained from $Ca_2LaFe_2SbO_9$ could be indexed by the monoclinic $P2_1/n$ symmetry. The SAED patterns of $Sr_2LaFe_2SbO_9$ show the presence of two phases; the main phase corresponds to an ordered I2/m or I4/m phase, whereas the additional phase is a disordered phase with the orthorhombic Pbnm symmetry. All SAED patterns of $Ba_2LaFe_2SbO_9$ could be indexed using the disordered cubic $Pm\bar{3}m$ symmetry.*

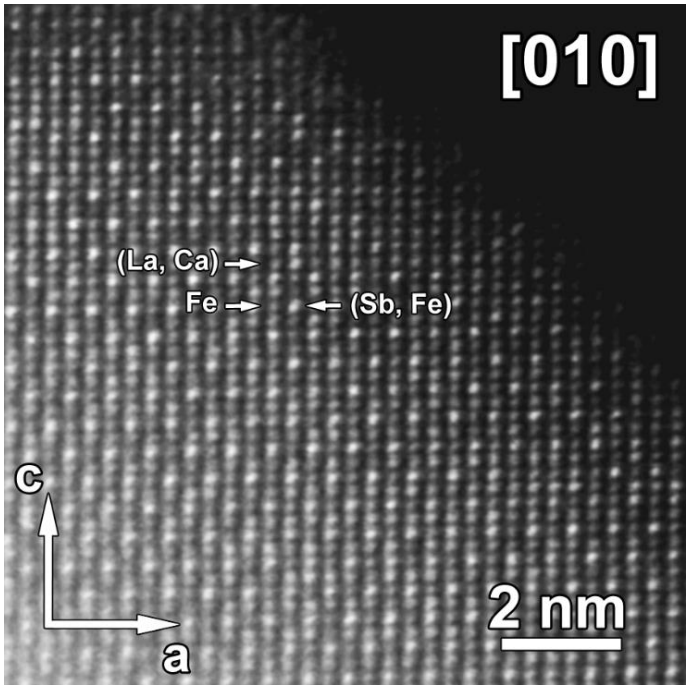

Figure 32. *High resolution HAADF-STEM image of $Ca_2LaFe_2SbO_9$ along the [010] zone axis.*

From electron diffraction, it was found that $Sr_2LaFe_2SbO_9$ consists of two phases with different symmetry (**Figure 31**). The HAADF-STEM image, shown in **Figure 33**, reveals that the structure has both ordered as well as disordered regions. **Figure 33A and C** illustrate the original HAADF-STEM image and the corresponding FFT, respectively. **Figure 33B** represents the inverse FFT when only the diffuse intensities marked by the red arrows in **Figure 33C** are taken into account, which reveals the presence of areas that contain B cation ordering, represented by the black and white dots. The combination of the inverse FFT and the original HAADF-STEM image results in the image shown in **Figure 33D**, in which the B cation ordering is represented by the yellow and red dots, corresponding to atom columns that contain more Sb and Fe, respectively. Comparing the FFTs taken from these regions with the SAED patterns, the disordered phase could be described by the *Pbnm* ($a^-a^-c^+$) symmetry where the Fe^{3+} and Sb^{5+} cations are distributed in a disordered manner. The SAED patterns corresponding to the ordered phase can be indexed using the following space groups, which all allow an ordered cation distribution: *I*2/*m* ($a^-a^-c^0$), *I*4/*m* ($a^0a^0c^-$), $R\bar{3}$ ($a^-a^-a^-$) and $Fm\bar{3}m$ ($a^0a^0a^0$). These are the same space groups as discussed for the $BaLa_2FeNiSbO_9$ sample, and the characteristics of these space groups were summed in **Table 4**.

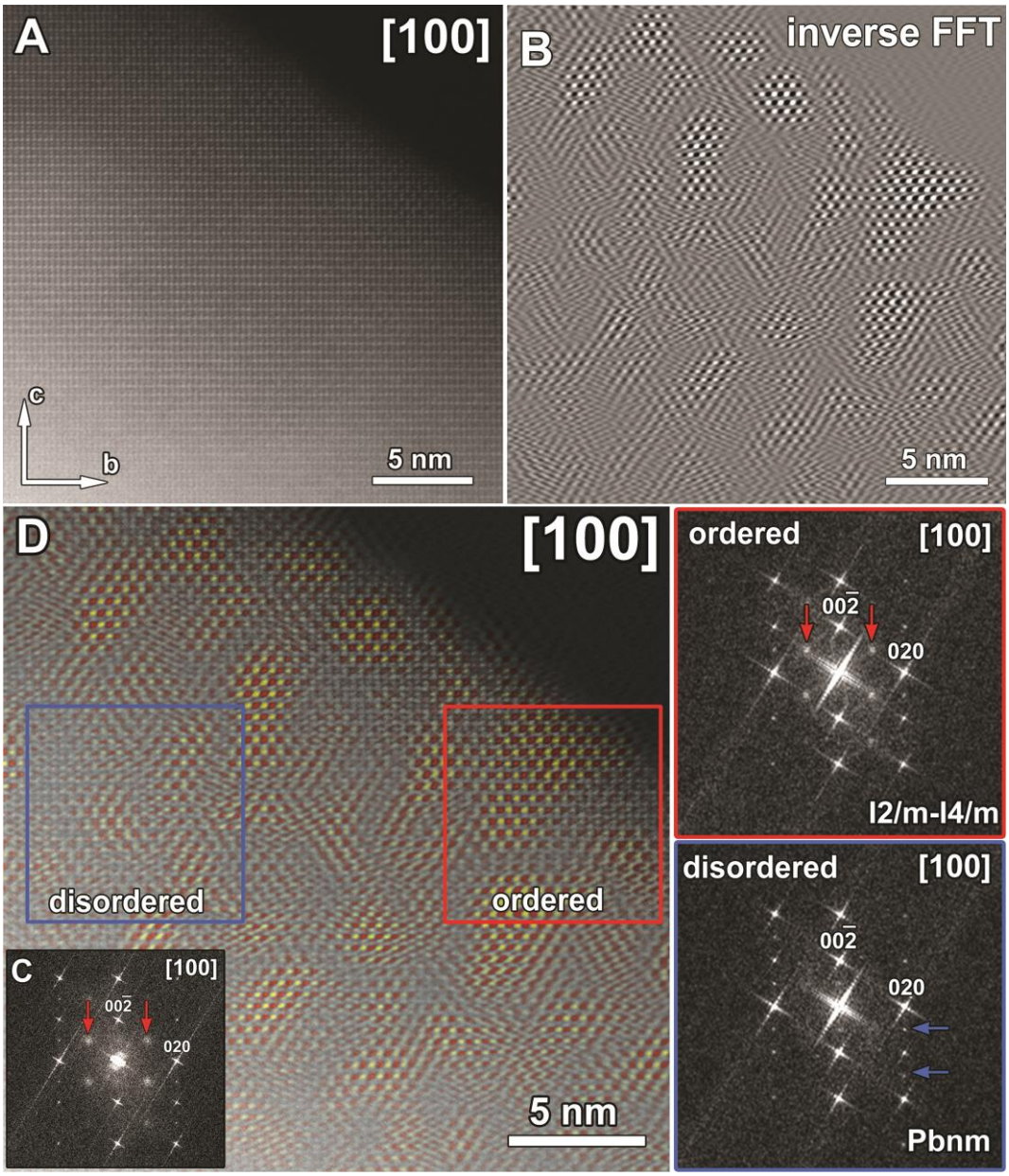

Figure 33. ***A)*** *High resolution HAADF-STEM image of $Sr_2LaFe_2SbO_9$ along the [100] zone axis.* ***B)*** *The inverse FFT obtained from the reflections marked by the red arrows in (C). The black and white dots show areas with B cation ordering.* ***C)*** *The FFT corresponding to the HAADF-STEM image in (A).* ***D)*** *The original HAADF-STEM image (A) combined with the inverse FFT (C). The yellow and red dots represent atom columns that contain more Sb and Fe, respectively. The FFT corresponding to the red region can be indexed by the ordered space group I2/m or I4/m. The FFT corresponding to the blue region confirms the disordered Pbnm symmetry*.

In order to determine the correct space group of the ordered phase, ABF-STEM images were taken, which are shown in **Figure 34** and **Figure 35**. In the case of the ABF-STEM image in **Figure 34**, the corresponding HAADF-STEM image shows ordering between the Fe and Sb cations, indicating that the ABF-STEM image represents the ordered phase. The oxygen atom columns in the ABF-STEM image are shifted upwards and downwards by an octahedral tilt. Consequently, we can exclude the tilt-free ($a^0a^0a^0$) space group $Fm\bar{3}m$. **Figure 35** shows the ABF-STEM image along one of the <100> directions of the cubic parent, of which the FFT corresponds to the ordered phase. The HAADF-STEM image shows no tilt, which means that $R\bar{3}c$ ($a^-a^-a^-$) can also be excluded, leaving $I2/m$ ($a^-a^-c^0$) and $I4/m$ ($a^0a^0c^-$) as possible space groups, which would look identical in ABF-STEM images. As a consequence of the domain structure, twinning and the high degree of similarity between many zones, we were unable to distinguish between these two space groups using CBED. Further, no diffuse intensities were observed that could be used to exclude one of the two space groups, as was possible in the case of $BaLa_2FeNiSbO_9$.

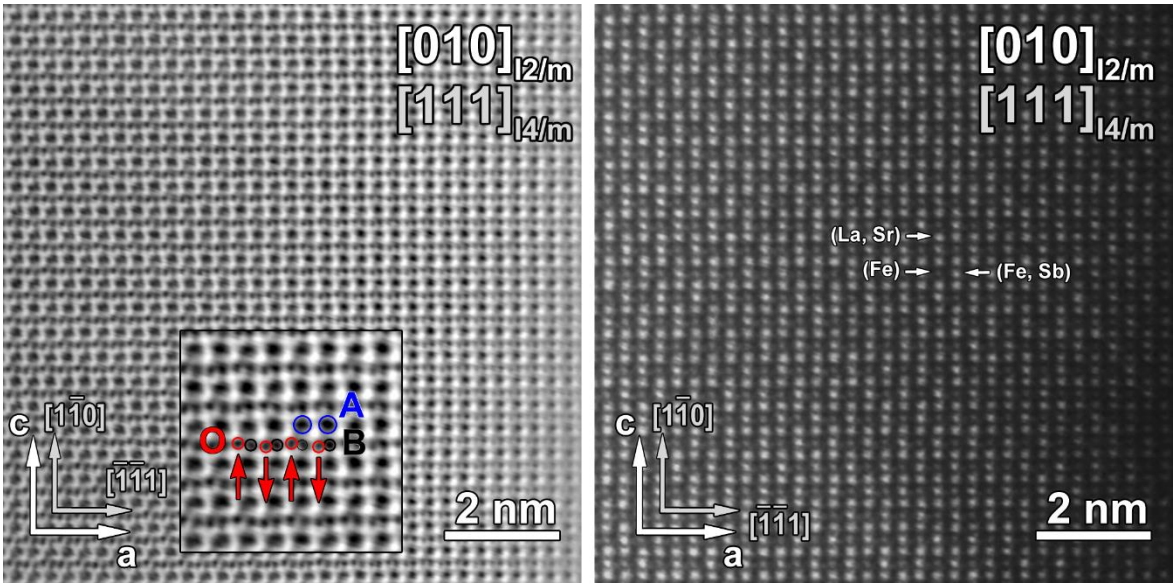

Figure 34. *High resolution ABF-STEM (left) and HAADF-STEM (right) image of the ordered phase in $Sr_2LaFe_2SbO_9$ along the [010] or [111] zone axis in respectively I2/m or I4/m. The red arrows in the ABF-STEM image show the up and downwards shift of the oxygen atom columns along the c direction caused by the presence of an octahedral tilt. The HAADF-STEM image is taken simultaneously with the ABF-STEM image and shows the ordering between the B cations.*

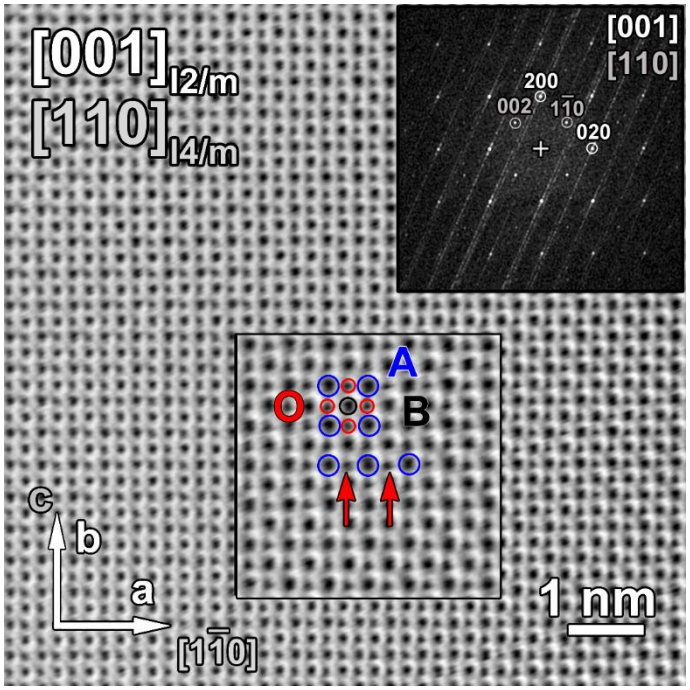

Figure 35. *High resolution ABF-STEM image of the ordered phase in $Sr_2LaFe_2SbO_9$ along the [001] zone axis in the I2/m symmetry or [110] in the I4/m symmetry.*

The element maps in **Figure 36** demonstrate that the two phases, defined by the corresponding FFTs, arise due to the inhomogeneity of the A and B cations. Region 2 shows extra reflections corresponding to symmetry *Pbnm*, while region 1 does not show these extra reflections and corresponds to the *I2/m* or *I4/m* symmetry.

The region corresponding to the disordered *Pbnm* phase contains more iron and lanthanum than the ordered phase. The compositions calculated from these two regions are:

→ Region 1 (ordered *I2/m – I4/m*): $Sr_{38.5}La_{9.5}Fe_{27.7}Sb_{24.3}O_x$ t = 0.987 (= no tilts)

→ Region 2 (disordered *Pbnm*): $Sr_{29.3}La_{20.3}Fe_{32.4}Sb_{18.0}O_x$ t = 0.978 (= anti-phase tilts)

The comparison between the calculated tolerance factors and observed symmetries show that the predicted two phases do not correspond to the observed phases. For the ordered phase, both *I2/m* ($a^-a^-c^0$) and *I4/m* ($a^0a^0c^-$) describe a structure with only anti-phase tilts, while the calculated tolerance factor predicts an untilted phase (which belongs to the range of green dots in **Figure 30**). The disordered *Pbnm* ($a^-a^-c^+$) phase contains both in-phase and anti-phase tilts, whereas the predicted phase only contains anti-phase tilts (which belongs to the range of blue dots in **Figure 30**). The expected tolerance factors t should be lower in order to be consistent with the

observed two phases. This means that for the disordered *Pbnm* phase (i.e. in-phase and anti-phase tilts) *t* should be smaller than 0.964, and for the ordered *I2/m* or *I4/m* phase (i.e. only anti-phase tilts) *t* should vary between 0.964 – 0.985. From the EDX study, we suggested that the EDX quantification might introduce an error and might detect a lower strontium content than present in the structure. When the strontium concentration (Sr^{2+} 1.44 Å) is higher, and thus the lanthanum concentration (La^{3+} 1.36 Å) lower, the net charge decreases and become closer to zero, which supports our hypothesis. However, the ionic radius of strontium is larger than the ionic radius of lanthanum, which means that the tolerance factor would become higher, which is in contradiction with what we would expect. On the other hand, the ordered phase is similar to the ordered perovskite Sr_2FeSbO_6 that is known in literature to adopt an *I2/m* structure at room temperature [53], with a reported tolerance factor of 0.993. This again shows that the tolerance factor can only be used as a rough guideline, but not as a method to determine the crystal structure.

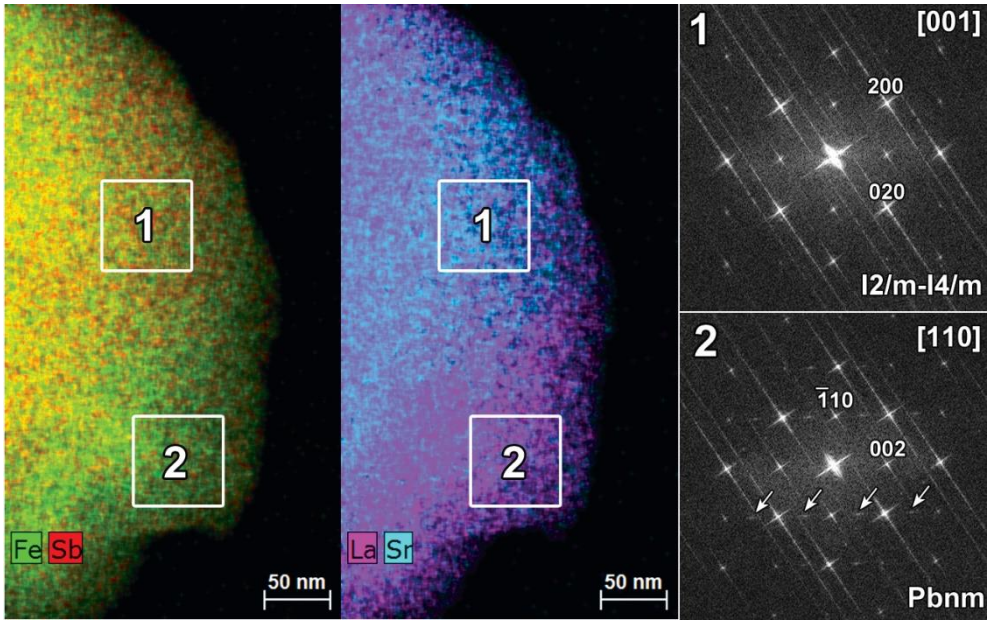

Figure 36. *At the left and in the middle the mixed elemental maps of respectively (Fe, Sb) and (La, Sr) are shown, with on the right the FFTs corresponding to region 1 and 2, marked in the elemental maps.*

Finally, the TEM study of $Ba_2LaFe_2SbO_9$ confirmed that the structure is cubic. The SAED patterns shown in **Figure 31** are consistent with the cubic model $Pm\bar{3}m$; however, we cannot rule out lower-symmetry space groups with the same reflection conditions: $R\bar{3}c$, $I4/mcm$ and $Imma$. Moreover, the HAADF-STEM image shown in **Figure 37** together with the FFTs of the two regions marked on the HAADF-STEM image and the line profiles obtained from these two regions (**Figure 38**), show that region 1 has ordered B cations, while region 2 does not. Thus cation-ordered nanodomains are present in the main $Pm\bar{3}m$ phase. These are probably a consequence of the compositional variations. Similarly to the disordered phase, the ordered nanodomains can be equally well described by several space groups, in this case by $Fm\bar{3}m$, $R\bar{3}$, $I4/m$ or $I2/m$. Comparing the possible space groups to the average tolerance factor calculated for $Ba_2LaFe_2SbO_6$: t = 1.02(1), and taking into account the large average A cation size, it is unlikely that the structure adopts a tetragonal $I4/mcm$ ($I4/m$) or orthorhombic $Imma$ ($I2/m$) structure. Since no improvement in fit quality of the NPD analysis was achieved when the symmetry was lowered to rhombohedral space group $R\bar{3}c$, we therefore concluded that the data did not justify the use of a symmetry lower than cubic, which means that the structure can be described by the disordered $Pm\bar{3}m$ phase with ordered nanodomains that adopt the cubic $Fm\bar{3}m$ symmetry.

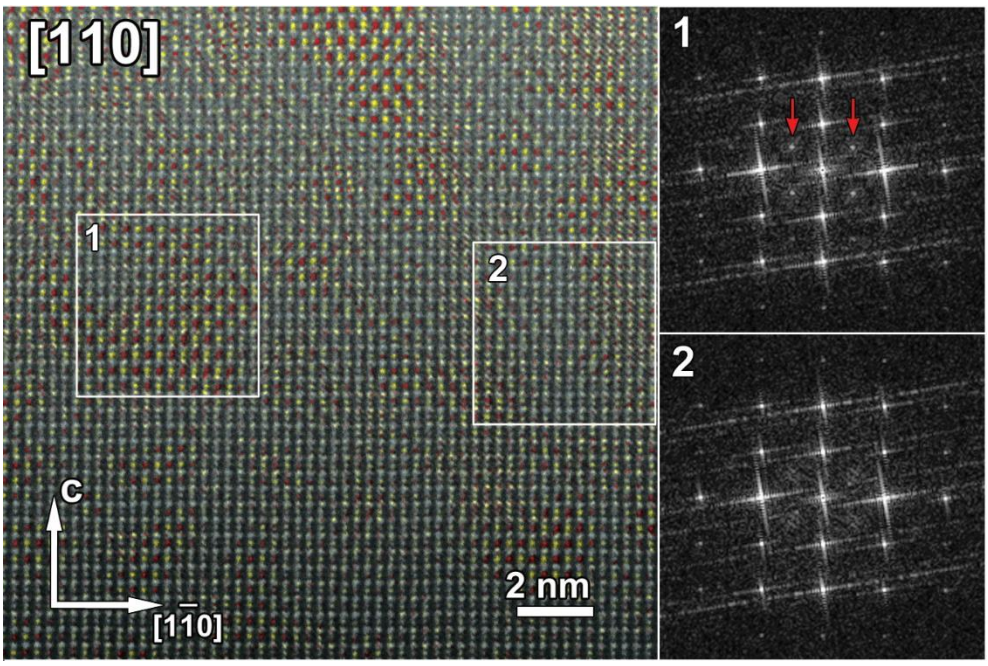

Figure 37. *High resolution HAADF-STEM image of $Ba_2LaFe_2SbO_9$ along the [110] zone axis combined with an inverse FFT calculated from the extra reflections marked by the red arrows in the FFT of region 1. The extra reflection in the FFT of region 1 are related to the presence of B cation ordering. The B cation in region 2 are not ordered, and thus no extra reflections appear in the corresponding FFT.*

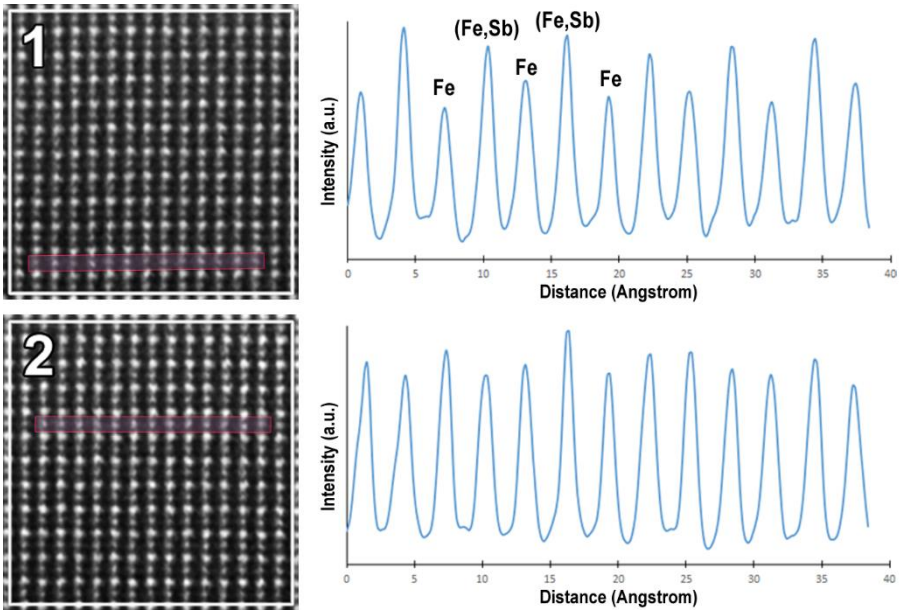

Figure 38. *High resolution HAADF-STEM images of $Ba_2LaFe_2SbO_9$ of regions 1 and 2 of Figure 37, and the corresponding line profiles along the indicated rows of B cations.*

Magnetometry demonstrated that all three compounds show a small remanent magnetization at 300 K suggesting that none of the three compounds is a simple paramagnet at 300 K. At 5 K, the remanent magnetization M_r decreases and the coercive field H_c increases as the radius of the alkaline-earth cation increases, which are listed in **Table 7**. Magnetic scattering was also observed in neutron diffraction for the $Ca_2LaFe_2SbO_9$ and $Ba_2LaFe_2SbO_9$ samples at both 300 K and 5 K. Both samples can be described by a G-type magnetic structure, where the Fe^{3+} cations on the 2*c* and 2*d* sites couples antiferromagnetically with their six nearest-neighbours (NN) on respectively the 2*d* and 2*c* sites. In the case of $Ca_2LaFe_2SbO_9$, the presence of different concentrations of Fe^{3+} cations on the two crystallographic sites results in ferrimagnetism whereas the cation disorder in $Ba_2LaFe_2SbO_9$ results in equal populations of Fe^{3+} on the two sites and, consequently, antiferromagnetism. However, in both cases, the ordered magnetic moment per cation is lower than would be expected for a simple Fe^{3+} system. This might be explained by the formation of a spin glass under the transition temperature of ~40 K for $Ca_2LaFe_2SbO_9$ and ~50 K for $Ba_2LaFe_2SbO_9$, where some spins freeze instead of order and form a glassy phase.

Table 7. *Coercive fields and remanent magnetization per formula unit, H_c (kOe) and M_r (μ_B) at 5 K and the transition temperature (K) of $A_2LaFe_2SbO_9$ (A=Ca, Sr, Ba).*

	H_c (kOe)	M_r (μ_B)	T *(K)*
$Ca_2LaFe_2SbO_9$	0.60	0.18	~ 215 K
$Sr_2LaFe_2SbO_9$	2.0	0.074	~ 250 K
$Ba_2LaFe_2SbO_9$	3.0	0.058	~ 350K

In the case of $Ca_2LaFe_2SbO_9$, also no long-range ferrimagnetic ordering is observed at 5 K. By analogy with $Sr_2LaCr_2SbO_9$ [54], we suggest that some of the decoupled spins might lie in the domain walls that separate different ferrimagnetic regions. TEM has shown that the local cation composition varies throughout the $Ca_2LaFe_2SbO_9$ sample and, by analogy with Sr_2FeSbO_6 where the NNN interactions dominate [55], in antimony-rich regions, there will be competition between the NN and NNN interactions which will lead to frustration and hence the absence of long-range magnetic order. We suggest that it is the spins in these regions that do not belong to the G-type structure favoured by NN interactions and instead undergo a transition to a glassy state at ~40 K. This explanation can also be extended to $Sr_2LaFe_2SbO_9$ where the composition variation is large enough to cause phase separation, giving that the magnetic behaviour is the sum of contributions from iron-rich and antimony-rich regions. Unfortunately, the coexistence of the ordered and disordered phase makes it impossible to refine the NPD pattern and analyse the magnetic ordering in detail.

Different from $Ca_2LaFe_2SbO_9$, the random distribution of the B cations in $Ba_2LaFe_2SbO_9$ results in an antiferromagnet instead of a ferrimagnet, leading to the coexistence of an antiferromagnetic phase with a spin glass at low temperatures. As the level of variations in the composition is similar to $Ca_2LaFe_2SbO_9$, we propose that the observed behaviour is again attributable to frustration caused by competition between NN and NNN neighbours in antimony-rich regions.

From a structural point of view, $Ca_2LaFe_2SbO_9$ is the simplest of the three compositions described above. The X-ray, neutron and TEM data are all consistent with a monoclinic structure in which the B-sites are occupied by a partially-ordered arrangement of Fe^{3+} and Sb^{5+} cations. The two sites are also of a similar size in Ca_2FeSbO_6, where the Fe:Sb cation occupancy ratio at the larger B-site has been reported to be 94:6 [53], although, a more marked difference was apparent in Sr_2FeSbO_6 for which less-well-ordered cation occupancy ratios of 79.5:20.5 and 89:11 have been reported in independent studies [53,55]. From TEM it was found that $Sr_2LaFe_2SbO_9$ contains two phases: an ordered I-centred phase *I2/m* or *I4/m* with a cation ratio Fe:Sb ~ 1:1, and orthorhombic phase *Pbnm* showing a disordered cation ratio Fe:Sb ~ 3:2. The ordered phase is consistent with the structure of Sr_2FeSbO_6 reported by Faik *et al.* [53]. The different cation ratio Fe:Sb in the disordered phase compared to the ordered phase (i.e. 3:2 instead of 1:1) might be the driving force for the high degree of disorder. The discrepancy between the phases derived from XRPD (i.e., $I\bar{1}$) and NPD (i.e., $P\bar{1}$) is attributed to the coexistence of both an I-centred and primitive phase. Since the extra reflections present in the primitive phase are very weak, these reflections were missed in the XRPD analysis. The combination of both symmetries prevented the refinement from achieving a good fit with high symmetry and reduced the space group to triclinic that allows getting a better fit by giving more freedom to the structural parameters.

Cation ordering is also essentially absent from $Ba_2LaFe_2SbO_9$. The TEM study confirmed the disordered cubic $Pm\bar{3}m$ structure, but also revealed a low concentration of ordered nanodomains with $Fm\bar{3}m$ symmetry. The broad peaks and tails observed in the NPD pattern can be explained by the occurrence of these ordered nanodomains.

It appears that the larger the radius ratio r_A/r_B, the more likely the cations are to be disordered [56], with calcium-based compositions tending to order, their strontium analogues adopting both ordered and disordered forms and the barium analogues being disordered. Vasala *et al.* [40] have commented on this trend in the past and ascribed it to the greater need to maximise the separation between highly-charged cations when the unit cell volume is reduced.

3.3.2. Conclusion

The complexities in the $A_2LaFe_2SbO_9$ compounds stem from the presence of two cations, Fe^{3+} and Sb^{5+}, with differences in size and charge that place them on the borderline between cation order and disorder. Only $Ca_2LaFe_2SbO_9$ can be considered to be a true, single-phase compound, albeit with some degree of compositional inhomogeneity. The barium analogue can be treated as such, although the level of inhomogeneity is sufficient to support the formation of a few ordered nanodomains within a matrix of disordered cations. In the case of $Sr_2LaFe_2SbO_9$, the inhomogeneity causes a significant degree of phase separation within the sample.

We can conclude that when the *A* cation size increases, the disorder of the B cations increases and the symmetry of these triple perovskites $A_2LaFe_2SbO_9$ becomes higher. The variation in the degree of cation ordering leads to a change from ferrimagnetism in $Ca_2LaFe_2SbO_9$ to antiferromagnetism in $Ba_2LaFe_2SbO_9$. In both cases, the inhomogeneity results also in the presence of a spin glass phase.

3.4. Conclusion of $ALa_2FeBSbO_9$ and $A_2LaFe_2SbO_9$

These studies were originally motivated in an attempt to observe relaxor ferromagnetism, as in $La_3Ni_2SbO_9$ [22]. We have synthesized a number of triple perovskites containing Fe^{3+} in an attempt to find more examples of relaxor behaviour but without success. We have invoked competition between NN and NNN interactions to explain the observed behaviour of our samples. This leads us to suggest that the relaxor phenomenon is most likely to be observed in compounds containing Ni^{2+} because the d^8:t_{2g}^6 e_g^2 electron configuration leads to a NNN interaction that is weaker than those involving d^5:t_{2g}^3 e_g^2 configurations as Fe^{3+}.

The compounds described in the two studies exemplify the structural complexities that can exist within the perovskite family. It is possible to synthesize samples whose chemical formulae suggest that multiple elements are present on the six-coordinate site within the structure and it is possible that the XRPD and NPD patterns of the sample will be consistent with the formation of a monophasic product and that still TEM reveals variations in composition, cation ordering and symmetry that are not seen by XRPD or NPD, and these variations can have a marked effect on the physical properties of the material.

Chapter 4. Zn_2FeBO_6 (*B* = Nb, Ta) series & $ZnSnO_3$

This section is based on the paper: Y. Han, Y. Zeng, **M. Hendrickx**, J. Hadermann, P. W. Stephens, C. Zhu, C. P. Grams, J. Hemberger, C. E. Frank, S. Li, M. Wu, M. Retuerto, M. Croft, D. Walker, D. Yao, M. Greenblatt, and M.-R. Li. *Universal A-cation splitting in $LiNbO_3$-type structure driven by intrapositional multivalent coupling*. Journal of the American Chemical Society, 2020, 142, 15 [57]

4.1. Introduction

Multiferroic materials exhibit simultaneous ferroelectric and magnetic ordering. Only in a few cases, a strong coupling between the magnetization and polarization occurs, the so-called magnetoelectric effect, which allows to electrically control the magnetism and vice versa for spin-electronic technology, such as magnetic storage and processing applications [58,59]. However, materials with both magnetic and electric properties are difficult to synthesize because of the conflicting electronic requirements of these properties [60]. So far, only a few materials are known to behave as a multiferroic material at room temperature; nevertheless, all of them have drawbacks such as a small spontaneous polarization or only weak magnetoelectric coupling [61]. Therefore, it is essential to explore new materials.

One of the strategies to produce ferroelectric polarization in perovskites is via structural distortion by locating an unusually small cation at the A-site. The small size of the A cation implies cation displacement and octahedral distortion, which induces polarization, as observed in the corundum derivative $ZnSnO_3$ [62,63]. Then, to incorporate the magnetic ordering, the presence of unpaired d^n cations is required, such as Fe. However, materials like $ZnFeO_3$ are found to be simple magnets [64,65].

First-principle theoretical calculations have shown that in double perovskites the second-order Jahn Teller (SOJT) effect of the d^0 ions at the B'-site energetically favours the formation of the polar $LiNbO_3$ (LN)-type structure (*R3c*) as demonstrated in Mn_2FeBO_6 (*B* = Nb^{5+}, Ta^{5+}) [66]. Nevertheless, to the best of our knowledge, convincing ferroelectric switching has only been observed in $ZnSnO_3$ [63] and $FeTiO_3$ [67] among the high pressure and temperature (HPT)-

prepared LN-type compounds. The Zn-compounds have the relative lowest ferroelectric reversal barrier energy ($E_{barrier}$) indicating that polar corundum with Zn at the A-site is one of the most promising ferroelectric materials [59,68–71].

These findings have extended the LN-structures to double corundum systems and lead us to investigate the isostructural $Zn_2Fe\mathit{B}O_6$ (B = Ta^{5+}, Nb^{5+}) in an attempt to create multiferroics with strong magnetoelectric coupling.

Understanding the electric dipole switching in multiferroic materials requires a deep insight in the atomic-scale local structure evolution to reveal the ferroelectric mechanism, which remains unclear and lacks a solid experimental indicator in high-pressure prepared LN-type polar magnets. Therefore, in this work, the crystal structure and the corresponding dielectric and magnetic properties of the $Zn_2Fe\mathit{B}O_6$ (B = Ta^{5+}, Nb^{5+}) LN-type phases are investigated and compared to the polar oxide $ZnSnO_3$ in order to understand the close relationship between the A and B cations on the polarization and magnetization.

My contribution to this work is the structural investigation using TEM, where I uncovered A cation splitting in these materials, which is discussed in the following section. The synthesis of the samples and the experimental details of the TEM study can be found in the appendix at the end of Part I. The experimental details of the other experiments mentioned in the next section can be found in the corresponding paper [57].

4.2. Experimental results and discussion

In a first attempt, the crystal structures of Zn_2FeTaO_6 and Zn_2FeNbO_6 were examined by synchrotron powder X-ray diffraction (SPXD) by our collaborators at Rutgers, State University of New Jersey. Zn_2FeTaO_6 could be refined using the noncentrosymmetric space group *R3c* in which the Zn and disordered Fe/Ta are displaced in opposite directions along the *c*-axis, which results in spontaneous polarization. In the case of Zn_2FeNbO_6, the SPXD data could also be indexed by the *R3c* space group, but unlike Zn_2FeTaO_6, the Rietveld refinement yielded an unacceptable fit, containing partially occupied B positions with metal-metal and metal-oxygen distances that chemically and crystallographically made no sense. These findings suggested that the crystal structure on local scale is more complicated. Therefore, I solved the structure using a combination of different electron microscopy techniques.

The SAED patterns obtained from the Zn_2FeNbO_6 sample, which are shown in **Figure 39**, confirm the hexagonal subcell with the cell parameters derived from SPXD, $a = b = 5.1739(2)$ Å, and $c = 5.1739(2)$ Å, and agree with both the *R3c* and $R\bar{3}c$ symmetry. First, it was expected that the structure demonstrates stacking-faults, as reported in other honeycomb-layered oxides (for example the Li-rich Mn-rich NMC compounds described in Part II). However, the expected streaks in the SAED patterns stemming from stacking faults are absent. Instead, the patterns show weak diffuse intensities, marked by arrows, indicating the presence of a different type of short-range order. The profile of the intensity distribution of these diffuse intensities in zone [100] is shown in **Figure 40a**. Fitting of the intensity distribution clearly shows that the diffuse scattering are concentrated around all $G = g + 2c^*$, $G = g + 4c^*$ and $G = g + 3c^*$ positions.

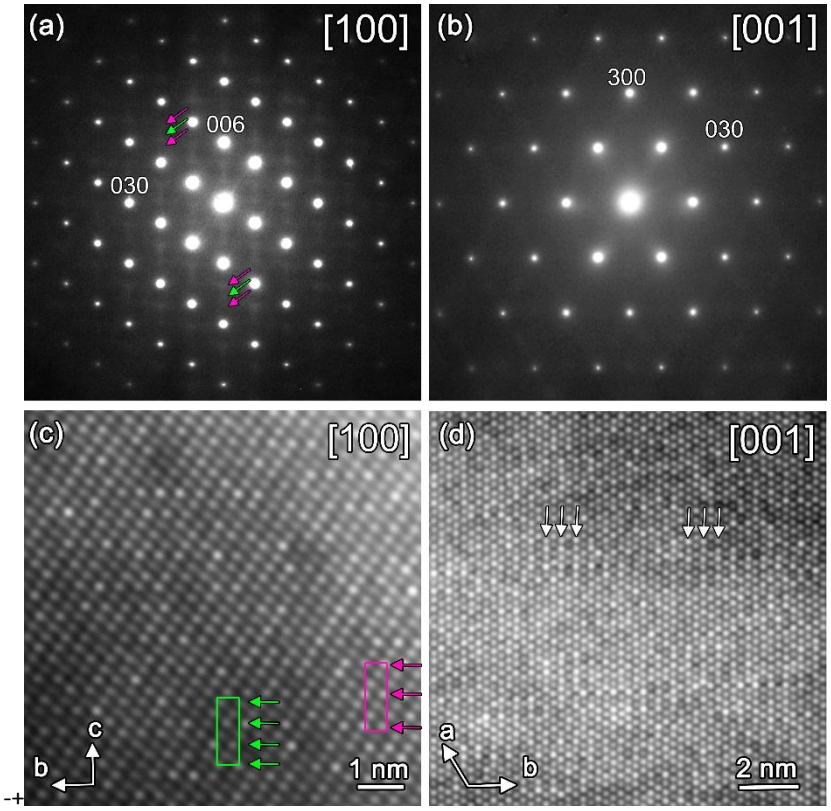

***Figure 39. Top**: Electron diffraction patterns of Zn_2FeNbO_6. SAED pattern of zone **(a)** [100] and **(b)** [001], respectively, where the weak diffuse reflections are indicated by arrows. **Bottom**: Gaussian filtered HAADF-STEM images of Zn_2FeNbO_6 along the **(c)** [100] and **(d)** [001] orientations. In the [100] HAADF-STEM only the atom columns containing the B cations are still clear due to the Gaussian filter. Note that in this zone, the projected b-axis is perpendicular to c, but in 3D it makes an angle of 30° with the plane of the image (oriented into the image). The rectangles indicate the unit cell, where the arrows mark the layers of brighter dots (more Nb), which alternate with layers of darker dots (more Fe) along the c direction. Green and pink represent two different alternations, which are related to the diffuse intensities in the SAED pattern. All the atom columns in the [001] HAADF-STEM image contain both Zn, Nb and Fe. The arrows show layers of brighter dots (more Nb) alternating with layers of darker dots (more Fe) along the b direction.*

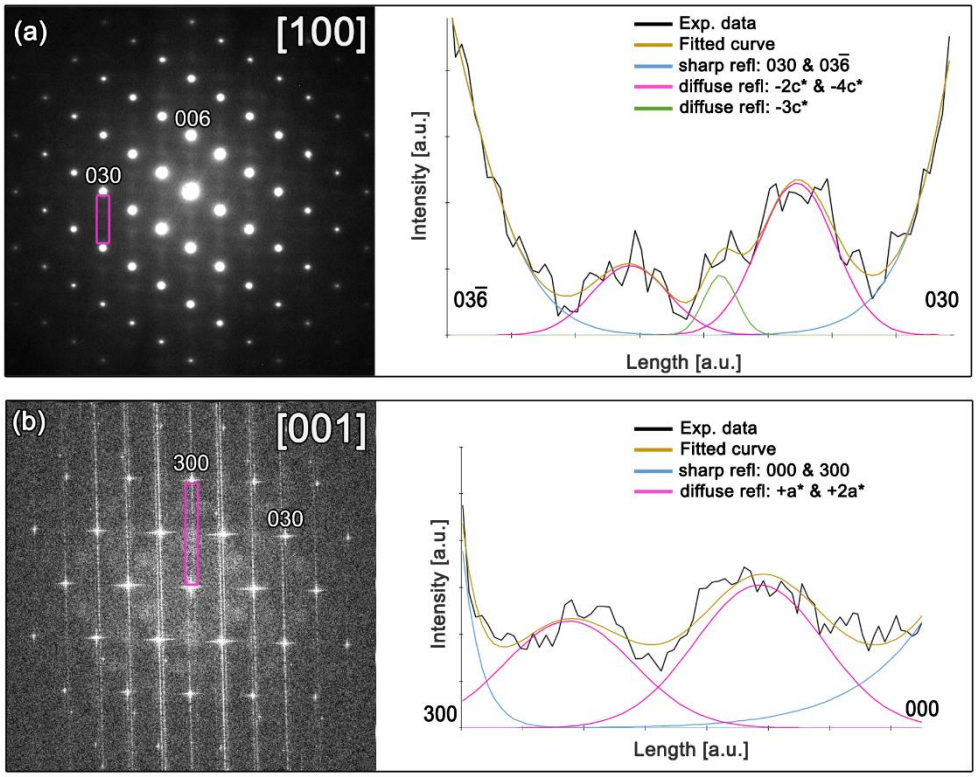

Figure 40. *Intensity distribution analysis in Zn_2FeNbO_6. (**a**) Left, the SAED pattern along the [100] orientation containing diffuse scattering where the rectangle corresponds to the area of which the profile of the intensity distribution between two sharp reflections is shown at the right. The peaks between the two Bragg peaks are fitted using Fityk, and correspond to diffuse reflections at $G = g \pm 2c^*$, $G = g \pm 3c^*$ and $G = g \pm 4c^*$. (**b**) Left, the FFT taken from the [001] HAADF-STEM image in Figure 39. The profile obtained from the area marked in the FFT shows diffuse intensities at $G = g \pm a^*$ and $G = g \pm 2a^*$.*

The HAADF-STEM image taken along [100] indeed shows visible short-range ordering, forming two dominant alternations of layers of brighter (more Nb) and darker (more Fe) dots: one brighter-one darker layer (b-d-b), and one brighter-two darker layers (b-d-d-b) as seen in **Figure 39c**. To compare the models with the two types of B cation ordering to the experimental data, we lowered the symmetry to *P1* and introduced layered ordering along the *c* direction: Nb-Fe-Fe-Nb or Nb-Fe-Nb. **Figure 41a-b** shows these two models and their calculated electron diffraction (ED) patterns for zone [100]. Note that these calculated patterns show sharp reflections as the models are long-range ordered, whereas the real structure shows short-range order. **Figure 41a** illustrates the structure including the Nb-Fe-Fe-Nb ordering, marked by the pink arrows. Without B cation ordering, the structure contains a 6_1 screw axis (rotation over 60° and shift over $1/6\vec{c}$) along the *c*-axis that corresponds to the reflection condition *00l: l = 6n*. The unit cell corresponding to the *R3c* or $R\bar{3}c$ is marked by the black rectangle. When B

cation ordering is introduced, the rows of the B cations perpendicular to the *c*-axis are not equivalent anymore and only the rows with a shift of $1/2\vec{c}$ are equivalent. Consequently, the screw axis 6_1 changes to 6_3 (i.e. rotation over 60° // *c*-axis, followed by a shift of $1/2\vec{c}$), which changes the reflection condition of *00l: l = 6n* to *l = 2n*. Similar, for the B cation ordering Nb-Fe-Nb (marked with green arrows in **Figure 41b**), only the rows with a shift of $1/3\vec{c}$ are equivalent, and thus the screw axis 6_1 reduces to 6_2, which changes the reflection condition of *00l* to *l = 3n*. The reflections that arise due to the B cation ordering are in agreement with the observed diffuse intensities in the [100] SAED pattern, corresponding to an appearance of reflections at 003 (for the b-d-b order) and at 002 and 004 (for the b-d-d-b order).

The Fe-Nb alternation can also be clearly seen in the HAADF-STEM image of zone [001] (**Figure 39d**). Each atom column consists of Zn and Nb and/or Fe atoms projected onto each other. Brighter columns contain more Nb, darker columns more Fe. The arrows on the image indicate rows of bright dots in planes perpendicular to the *b*-axis, which alternate along the *b* direction with planes of less bright dots. It is clear from the image that the order is short-range, that switches occur between bright and dark rows, that some areas show no order, *etc*. **Figure 41c-d** show the calculated ED patterns for zone [001] using the two models with different ordering patterns (simple long-range order patterns to show clear Bragg reflections at the extra positions and interpretable projected views).

In the model with layered ordering Nb-Fe-Fe-Nb (**Figure 41c**), the ordering is visible in this zone as (100) planes following a pattern of brighter-darker-darker-brighter dots, which causes extra reflections along the <a*>-direction, which agrees with the diffuse intensities observed along the <a*>-axes on the Fourier transform of the image shown in **Figure 40b**. The correspondence between the model and the experimental image (**Figure 39d**) is limited due to the long-range order in the model versus the short-range order of the real structure. The short-range order causes local overlap of domains with the two types of orders in the projected experimental image. The model for the Nb-Fe-Nb order (**Figure 41d**) shows no signs of the ordering when observing the structure along the [001] zone and also has no extra reflections in the [001] zone electron diffraction pattern. This agrees with those regions in the HAADF-STEM image of **Figure 39d** where the intensity distribution of the atom columns is homogeneous.

We have determined that the Zn_2FeNbO_6 compound shows short-range order between Fe and Nb. No superstructure peaks corresponding to the alternative *R3* structure were observed. Thus, the short-range order maintains the average LN-type structure [61,66].

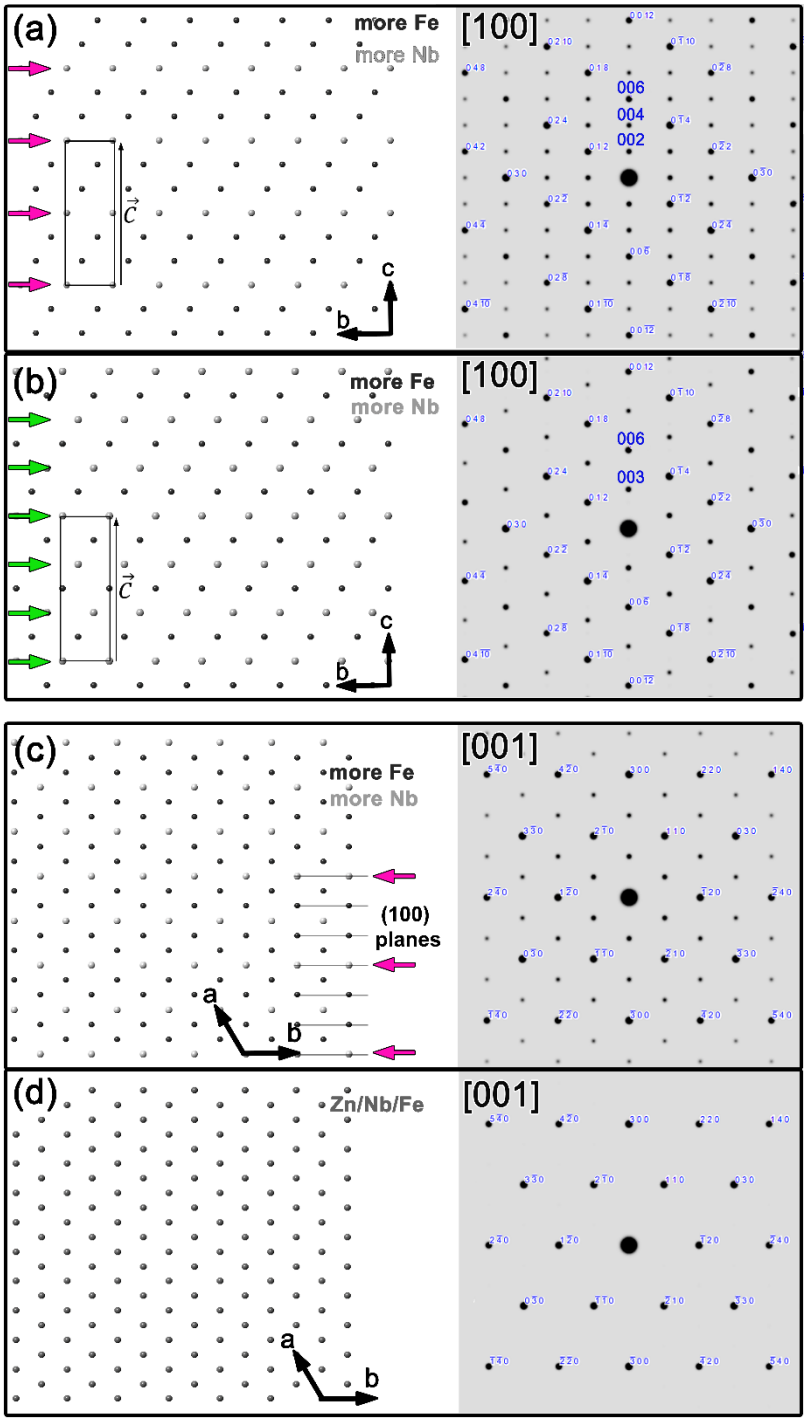

Figure 41. *The two models for Zn_2FeNbO_6 with different layered ordering (left sides) and the corresponding diffraction patterns (right sides). Only the B cation columns are shown, with more Nb in the bright atom columns and more Fe in the dark columns.* ***(a)*** *View along the [100] direction of the model with Nb-Fe-Fe-Nb layered ordering along the c direction. Extra reflections are present at G = g + 2c* and G = g + 4c*, due to the tripling of the periodicity in this projection, compared to the subcell.* ***(b)*** *View along the [100] direction of the model with b-d-b layered ordering along the c direction. Extra reflections are present at G = g + 3c*, due to the doubling of the periodicity in this projection, compared to the subcell* ***(c)*** *View along the [001] direction of the model with b-d-d-b layered ordering. Extra reflections are present at G = g + a*(b*) and G = g + 2a*(b*).* ***(d)*** *View along the [001] direction of the model with b-d-b layered ordering. All columns contain equal amounts of Fe and Nb. There are no extra reflections compared to the subcell.*

Another effect visible on the HAADF-STEM images is the Zn displacement as discerned in zone [100] and [241] in **Figure 42**, where the positions of Zn in some columns split into two sites (highlighted by rectangles) with different *z* but similar *x* and *y* coordinates. To calculate the general distance between the splitted Zn atom columns, we applied an intensity profile along the *c* direction. By fitting the intensity of the atom columns, the general distances between the split Zn atom columns are calculated to be between 1.0-1.6 ± 0.3 Å. If we go back to the initial structure refined from SPXD, the structure contained two different partially occupied B-sites close to each other with only a difference in coordinates along the *c* direction for the B cations: Fe (0, 0, 0.2929) and Nb (0, 0, 0.2209) which corresponds to a difference of ~ 1 Å. However, from TEM we have proven that there is a split of the Zn position. The Zn displacements and the Fe/Nb displacements should be correlated.

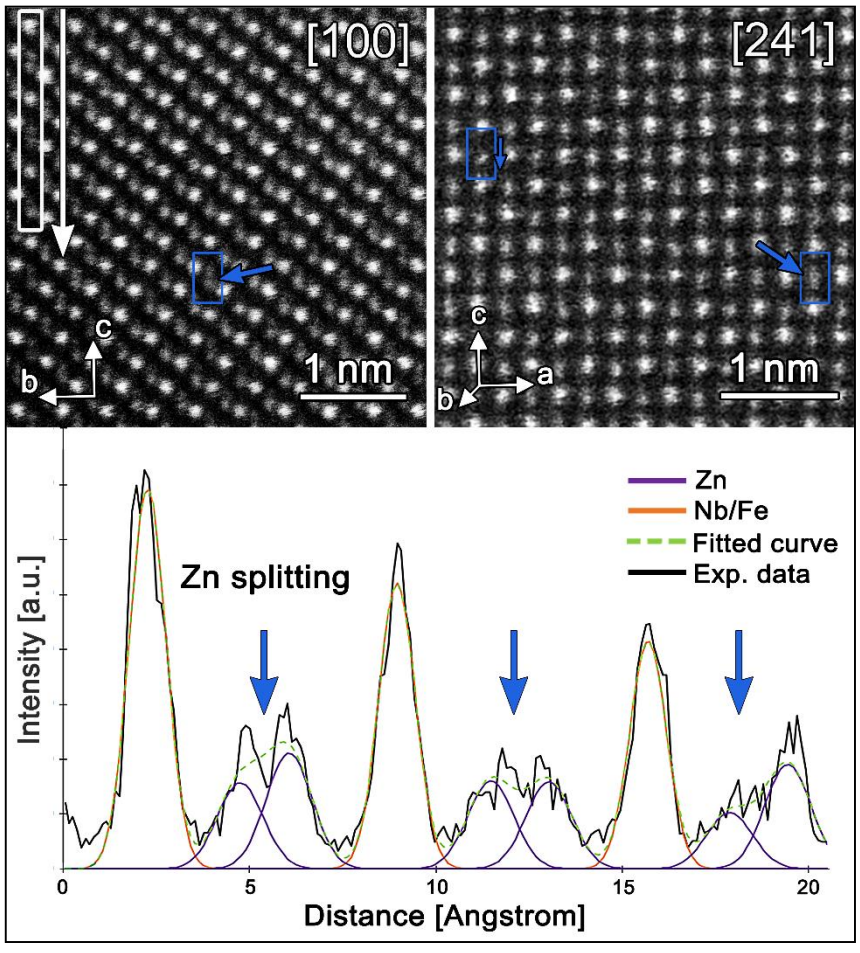

Figure 42. ***Top***: *HAADF-STEM image of Zn_2FeNbO_6 along the [100] and [241] orientation. The bright dots represent the atom columns containing Fe and Nb, whereas the dark dots are Zn atom columns. The blue rectangles mark the splitting or shift of the Zn atoms along the c-direction.* ***Bottom***: *The profile of the intensity distribution taken from the area marked by the white rectangle. The peaks are fitted using Fityk, showing clear Zn splitting.*

According to the SAED and HAADF-STEM results, the SPXD data of Zn_2FeNbO_6 were thus re-refined introducing the B-site Fe/Nb short-range order and the A-site Zn splitting along the *c*-axis that were found with TEM. The Zn-splitting is expected to be accompanied by simultaneous oxygen displacements to relax the local stress, which could not be detected on the HAADF-STEM images given the small *Z* of oxygen next to the high Z of Nb. Therefore, a defect model with both split Zn and O sites is required to better simulate the crystal structure as reported in other defect oxides [72,73]. Using this model as input, our collaborators at Rutgers refined the structure using the X-ray data. The final crystallographic data can be found in the corresponding paper [57].

It was found that about 11% of the Zn-sites are split, and accordingly, the same fraction of Fe/Nb short-range ordering is correlated via face-sharing octahedral pairs along the *c*-axis (**Figure 43b-c**). The split Zn and O atoms are marked as Zn vs Zn^* and O vs O^*, with corresponding Fe* and Nb* positions. The overall crystal structure can be viewed as an interweaving of two sets of LN-type subcells: 11% Zn_2FeNbO_6 and 89% $Zn^*{}_2Fe^*Nb^*O^*{}_6$ as illustrated in **Figure 43b**. The refined average Zn-Zn^* distance (~ 1.03 Å in **Figure 43a**) agrees well with the HAADF intensity fitting result (1-1.6 Å from **Figure 42**). The defect model yields a more reasonable coordination environment in each sublattice as shown in **Figure 43b**.

To overcome the electrostatic repulsions, Zn/Zn^* and disordered Fe/Nb in the face-sharing octahedral pairs displace away from each octahedral centroid (dashed circles in **Figure 43c** to highlight the atomic displacement (d_M)) by 0.380(1) Å (d_{Zn}), 0.411(4) Å (d_{Zn^*}), 0.284(1) Å ($d_{Fe/Nb}$), and 0.217(6) Å (d_{Fe/Nb^*}), respectively, in opposite directions along the *c*-axis. The short and long (Fe/Nb)-O/O^* bond lengths derived from the SPXD data collected at room temperature, are comparable with a difference of 0.54 Å and 0.34 Å, giving octahedral distortion parameters $\Delta_{(Fe/Nb)}$ of 172.6×10^{-4} and $\Delta_{(Fe/Nb^*)}$ of 72.9×10^{-4} [73], almost doubled compared with Δ_{Zn} (87.4×10^{-4}) and Δ_{Zn^*}(33.6×10^{-4}). Accordingly, the structural distortion in Zn_2FeNbO_6 results in spontaneous electric polarization of P_S ~ 83.8 and $P_S{}^*$~71.1μC/cm^2 calculated from the point charge model, respectively. $P_{S(total)}$ was calculated based on the sum of the proportions of each part: $P_{S(total)}$(72.3 μC/cm^2) = 0.11×P_S + 0.89×$P_S{}^*$. The polarization is larger than P_S of Zn_2FeTaO_6 (~50 μC/cm^2) [60] and $ZnSnO_3$ (~58 μC/cm^2) [63], and comparable with the P_S of LiNbO3 (67 μC/cm^2) [74].

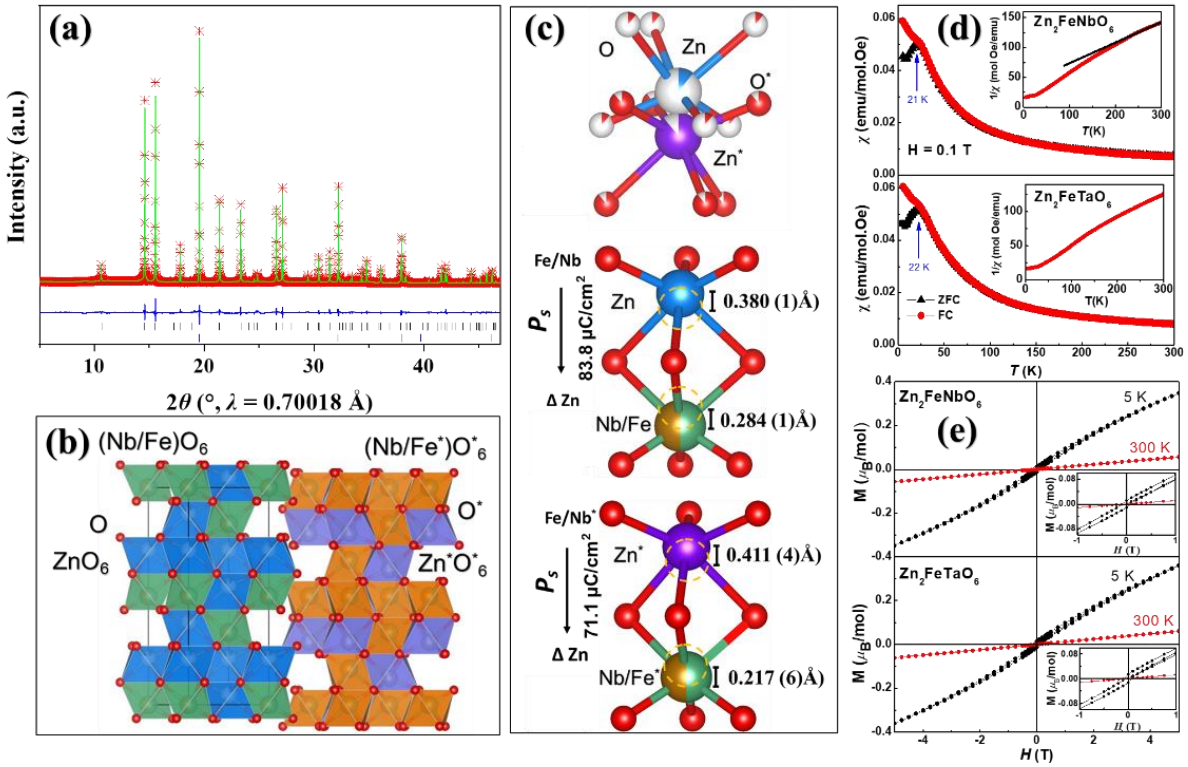

Figure 43. *(**a**) Rietveld refinement of the SPXD data for Zn_2FeNbO_6 with splitting Zn and O model. The red cross represents the calculated data, the green line the observed fit, the deep blue line the difference. The upper black and lower blue ticks mark the peak positions of Zn_2FeNbO_6 and diamond (internal standard), respectively; (**b**) The crystal structure of Zn_2FeNbO_6. The octahedral colour is set as ZnO_6 - blue, $Zn^*O^*_6$ - light violet, $(Fe/Nb)O_6$ - green, and $(Fe/Nb)^*O^*_6$ - orange, respectively; O, red spheres. (**c**) The local structure of Zn/Zn* (top), face-sharing $ZnO_6/(Fe/Nb)O_6$ (middle) and $(ZnO_6)^*/[(Fe/Nb)O_6]^*$(bottom) octahedral pairs along the c-axis in defect model viewed. The atomic displacements (d_s) away from the ZnO_6 and $(Fe/Nb)O_6$ octahedral site centroids (highlighted by dashed circles) are indicated as d_{Zn} (0.380(1) Å), $d_{Fe/Nb}$ (0.284(1) Å) and d_{Zn*} (0.411(4) Å), $d_{(\Delta Fe/Nb)}$ (0.217(6) Å), respectively; (**d**) Comparison of the temperature dependence of the ZFC and FC dc susceptibility (χ) between Zn_2FeNbO_6 and Zn_2FeTaO_6 at 0.1 T, inset shows the susceptibility inverse ($1/\chi$) vs temperature plots, the black line displays the CW fitting. (**e**) Comparison of the isothermal magnetization of Zn_2FeNbO_6 and Zn_2FeTaO_6 measured at 5 and 300 K between -5 and 5 T, respectively. Inset is the enlarged area between -1 and 1 T.*

The magnetic properties of Zn_2FeNbO_6 and Zn_2FeTaO_6 are almost identical, as shown in **Figure 43d-e**. The temperature-dependent magnetic susceptibility of Zn_2FeNbO_6 and Zn_2FeTaO_6 display a spin glass-like transition around, respectively, 21 K and 22 K (**Figure 43d**), below which the cusp-like divergence suggests the existence of magnetic frustration with competition of short-range ferromagnetic (FM) and antiferromagnetic (AFM) interactions. The isothermal magnetization curves of Zn_2FeNbO_6 at 5 K show a small hysteresis as also observed in the Ta-analogue (**Figure 43e**) and implies some weak FM interactions, but the magnetization curves do not reach saturation at the experimental conditions, which indicate the presence of competing AFM interactions that might be related to the magnetic frustration of the honeycomb layers in the *ab*-plane. In the case of Zn_2FeNbO_6, the $1/\chi$ curve deviates from strict linearity below 250 K (inset of **Figure 43d**), which suggests short-range magnetic ordering from the Fe-rich regions shown in the HAADF-STEM images (layers of dark dots in **Figure 39**d). A Curie-Weiss (CW) law fitting of the $1/\chi$ curve above 250 K yielded an effective magnetic moment of 4.99 μ_B [75], which is smaller than the calculated value of 5.92 μ_B for Fe^{3+} and is attributed to cationic disordering. The CW constant θ_{CW} = -142.5 K indicates that the AFM interactions are dominant. The same behaviour was observed for Zn_2FeTaO_6 where the $1/\chi$ curve deviates from linearity below 200 K, and the calculated CW constant is equal to -94 K [60].

The dielectric properties of Zn_2FeNbO_6 resemble what was observed in Zn_2FeTaO_6, showing a high-ε contact feature near room temperature [60], except for the absence of any small switchable component at low temperature, which was observed in Zn_2FeTaO_6. The notable similarity of physical properties of Zn_2FeNbO_6 and Zn_2FeTaO_6 suggested possible A-site Zn-splitting in Zn_2FeTaO_6 as well and motivated us to revisit the local crystal structure of Zn_2FeTaO_6.

An electron microscopy study was therefore performed on Zn_2FeTaO_6 for further confirmation of the Zn-splitting. The HAADF-STEM images along the [100] zone of the Zn_2FeTaO_6 sample (**Figure 44b** and **Figure 45**) do show similar Zn splitting (1.1-1.8 ± 0.3 Å). As discerned in zone [100] in **Figure 44c**, the same short-range ordering of the B cations as in Zn_2FeNbO_6 is also observed in Zn_2FeTaO_6 with two ordered patterns: Ta-Fe-Fe-Ta layers and Ta-Fe-Ta layers along the *c*-direction (Ta, higher Z, brighter columns; Fe, lower Z, darker columns). Weak diffuse intensities are highlighted by arrows in **Figure 44a** and **Figure 44d**. Profiles of the intensity distribution between the two sharp reflections in zone [100], namely rectangle 1 and 2, are extracted to establish the presence of diffuse intensity (**Figure 45**).

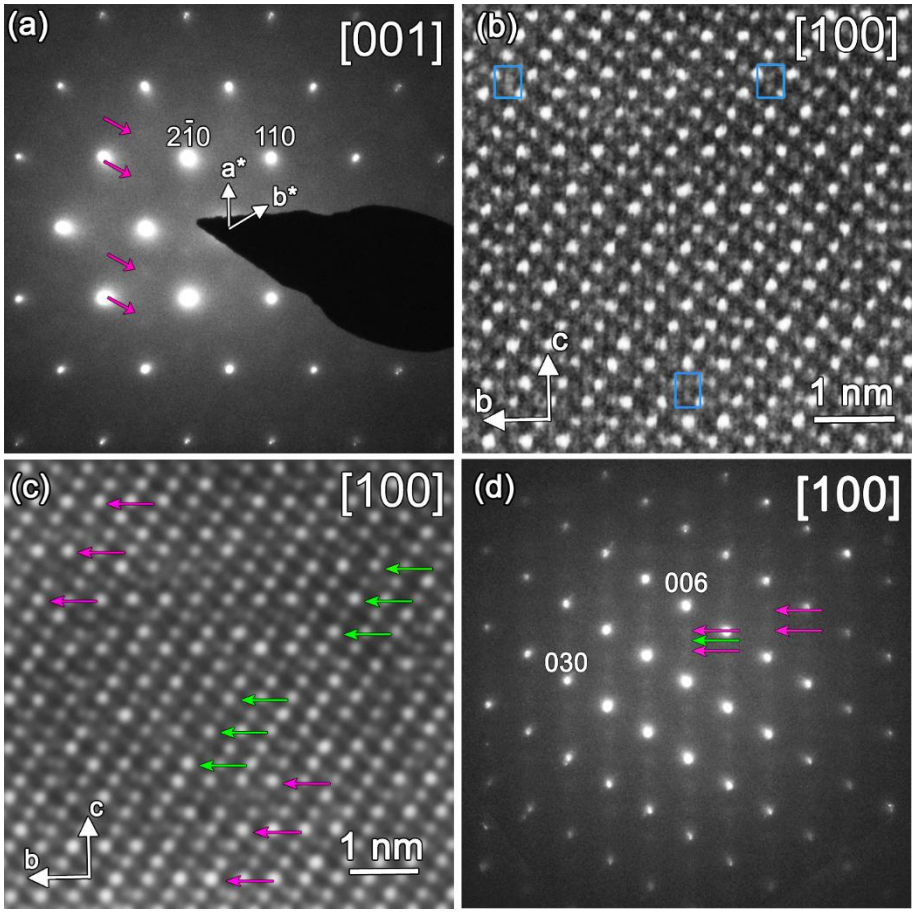

Figure 44. *SAED patterns and HAADF-STEM images of Zn_2FeTaO_6. (**a**) SAED pattern of the [001] zone, where the arrows highlight the diffuse intensities. (**b**) HAADF-STEM image of zone [100], the blue rectangles mark the splitting of the Zn atoms along the c-direction. In (**c**) a Gaussian blur filter is applied to the same HAADF-STEM image, revealing more clearly the short-range ordering of layers with darker atom columns (more Fe) and brighter atom columns (more Ta) with two variations: Ta-Fe-Fe-Ta layered ordering (pink arrows), and Ta-Fe-Ta layered ordering (green arrows). (**d**) SAED pattern along the [100] orientation, where the diffuse intensities are marked by green and pink arrows corresponding to respectively the Ta-Fe-Ta and Ta-Fe-Fe-Ta ordering.*

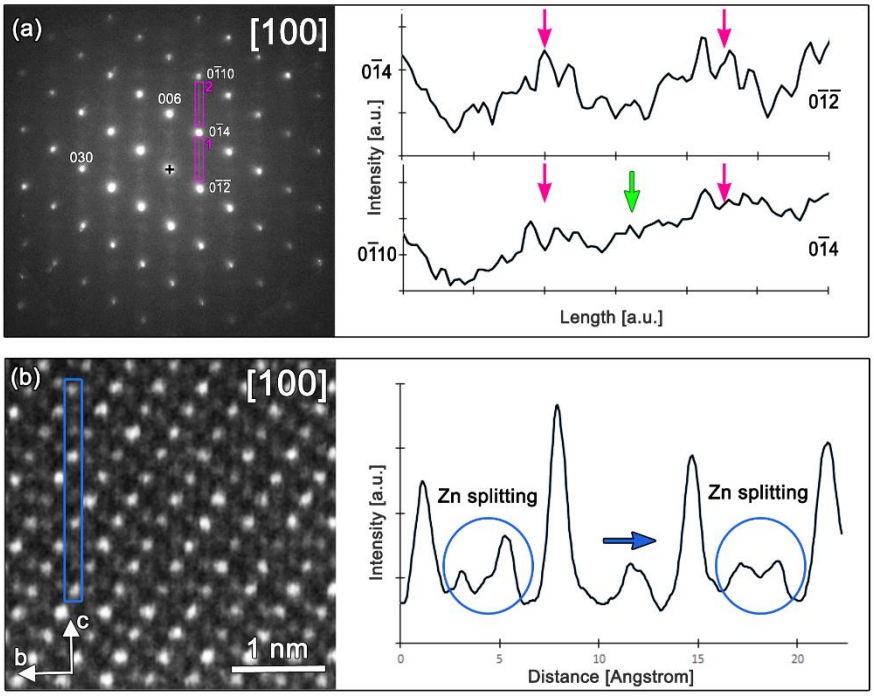

Figure 45. *SAED pattern and HAADF-STEM images of Zn_2FeTaO_6 with their line profiles. (**a**) SAED pattern along the [100] orientation with two line profiles, where we can clearly see the diffuse intensities (marked by the arrows). (**b**) HAADF-STEM image along the [100] orientation with the line profile of the intensity distribution along the blue rectangle, which clearly shows Zn splitting.*

The similar Zn-splitting experimentally discovered in Zn_2FeNbO_6 and Zn_2FeTaO_6 raises the premise of possible universal *A*-site splitting of Zn in the HPT-prepared corundum derivatives. To test this hypothesis, re-examination of other compounds like $ZnSnO_3$ was undertaken.

The SAED patterns of $ZnSnO_3$ do not show any diffuse intensities in **Figure 46**. Thus no short-range order seems to occur, which is understandable considering there is only one type of B atom and thus no B-site short-range order as in the Fe/Nb and Fe/Ta cases in $Zn_2Fe\mathit{B}O_6$ (*B* = Nb, Ta). The HAADF-STEM image along the [100] orientation (**Figure 46d**) does not show any Zn splitting along the *c*-direction in $ZnSnO_3$. However, the HAADF-STEM image along [241] (**Figure 46a**) orientation exhibits Zn displacement upwards and downwards along the *c*-direction. There was also a similar improvement in the Rietveld refinements of the LN-type $ZnSnO_3$ once the Zn-splitting was introduced, the goodness of fit (R_{wp}) was slightly reduced from 8.1% to 7.7%. The lesser prominence of Zn splitting in TEM and the lesser effect on the R_{wp} could indicate that the Zn-splitting in $ZnSnO_3$ is only present in minor amounts, or less correlated than in Zn_2FeNbO_6, and thus crystallographically acceptable refinements were still achieved when ignoring the possible Zn-splitting.

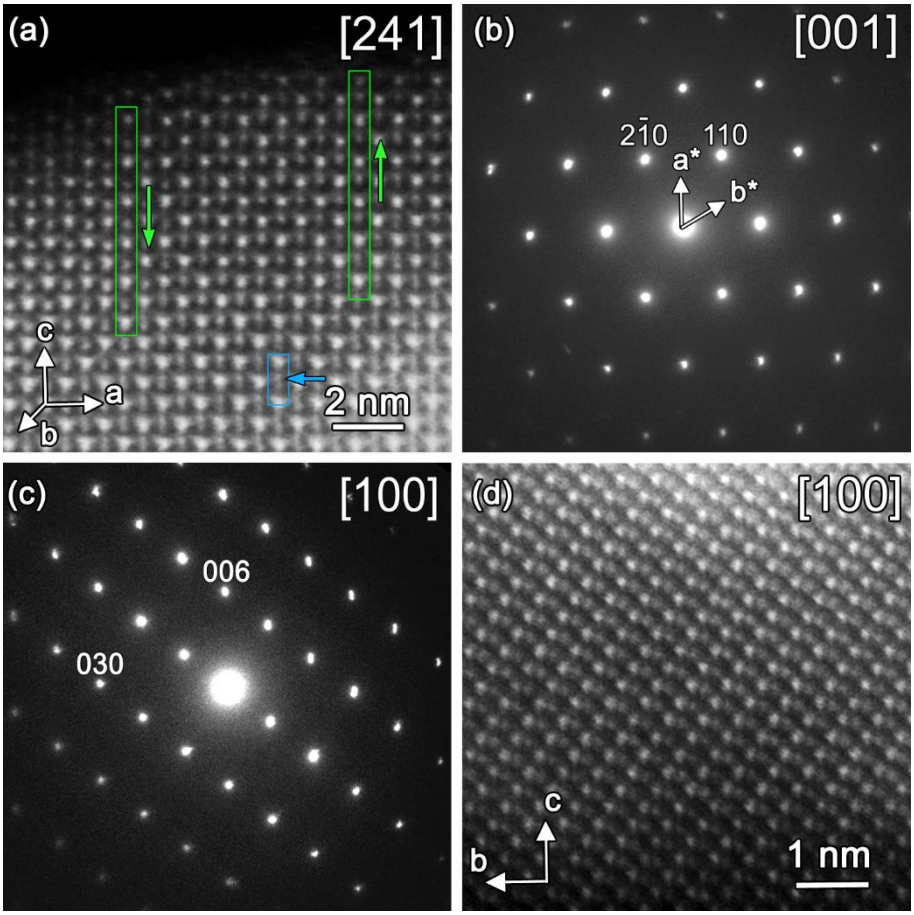

Figure 46. *SAED patterns and HAADF-STEM images of $ZnSnO_3$. (**a**) HAADF-STEM image along the [241] orientation, where the dark dots correspond to the Zn atom columns and the bright dots to the Sn atom columns. Some of the Zn atoms are shifted upwards, while some of them are shifted downwards along the c direction, which is indicated by the green rectangles with arrows showing the direction of shift. In the thicker areas, the two shifts both occur along the projected columns, appearing as splitted Zn atom columns as shown by the blue rectangle and arrow. SAED pattern of zone (**b**) [001] and (**c**) [100]. (**d**). HAADF-STEM image along the [100] orientation. No clear splitting of the Zn atom columns is observed. The bright atom columns are Sn, and the darker atom columns are Zn.*

By comparing the experimental results of the Zn-based LN-type materials, supported by first-principle density functional theory (FP-DFT) calculations on these materials, it can be concluded that the Zn-splitting in $Zn_2Fe\mathit{B}O_6$ (B = Nb, Ta) is a consequence of the charge differences between intrapositional coupled Fe and Nb, together with the short-range ordered atomic distribution. A more detailed explanation about the FP-DFT calculations can be found in the paper [57]. The FP-DFT calculations also showed that the Zn-splitting could be significantly reduced once the AFM interactions were taken into account. In the ideally disordered case, so when Fe^{3+}/B^{5+} are distributed in a fully random manner in $Zn_2Fe\mathit{B}O_6$ and equivalent to a $(Fe, \mathit{B})^{4+}$ ion, the periodic chemical potential wave (Coulomb repulsion towards

the face-shared Zn partner) renders similar displacement of Zn towards opposite direction, and thus statistically no Zn-splitting is observed as in $ZnSnO_3$. However, the short-range ordering of Fe^{3+}/B^{5+} disturbs the periodicity of the Coulomb repulsion and yields different displacement of the paired Zn atoms, which is manifested as local Zn-splitting and can be structurally taken as intergrowth of two LN-type subcells (**Figure 43b**).

The magnetic interactions can energetically suppress, but cannot completely eliminate the Zn-splitting in Zn_2FeBO_6 (*B* = Nb, Ta). Therefore, the structure is compared to the isostructural structure Mn_2FeBO_6 (*B* = Ta, Nb) where the non-magnetic Zn^{2+} is replaced by the magnetic Mn^{2+}. In this study, no *A*-site splitting has been experimentally discerned [66]. With this in mind, calculations of the density of states have revealed the impact of the magnetic nature of the A cation. In the case of Zn_2FeNbO_6, the Zn *d* orbitals lie much lower in energy than the Fe *d* orbitals, and the valence bands near the Fermi energy come mostly from Fe *d* orbitals, indicating that there is no bonding between Zn and Fe *d* electrons. However, in Mn_2FeNbO_6, the Mn *d* and Fe *d* orbitals nearly lie in the same energy range and hybridize to form the valence bands near the Fermi energy, indicating strong bonding between Mn and Fe *d* electrons. These findings show that the A-site Mn splitting can also be considered to exist, but with a Mn-Mn* distance of ~0.2 Å, which cannot be experimentally detected from either X-ray refinements or electron microscopy. Therefore, it might be safe to conclude that the degree of *A* site-splitting is higher, the larger the size and charge difference between *B* and *B*'; and the stronger the magnetic interactions and bonding (hybridization of valence bands between *d* electrons) between A and B cations, the smaller is the degree of *A*-site splitting predicted. This universal *A*-site splitting and defect structure is related to the high-temperature paraelectric state of LN, and is theoretically not beneficial to the ferroelectric state other than solely estimated by the $E_{barrier}$ values. This could be partially responsible for the absence of robust polarization switching in Zn_2FeBO_6 (*B* = Nb, Ta) [60]. Refinements on the *in-situ* variable temperature SPXD data for Zn_2FeNbO_6 reveal that the proportion of split Zn-sites increases from 11% (room temperature) to 18% and 21% at 523 and 573 K, respectively, suggesting that the LN phase can gradually transform into the paraelectric HT-LN structure, and there should be no clear ferroelectric to paraelectric transition expected upon heating

4.3. Conclusion

In this study, we have experimentally observed *A*-site atomic splitting in $Zn_2Fe\mathit{B}O_6$ (*B* = Nb, Ta), which is related to the observed short-range order of the B cations. The splitting of the A cation could be partially responsible for the absence of robust polarization switching. Comparing these results to the Mn-series $Mn_2Fe\mathit{B}O_6$ has shown that for a magnetic A cation the enhanced magnetic interactions, together with the hybridization of the valence band of *d* electrons between A- and B-site, strongly suppress the splitting displacement of A cation. However, this bonding between A and B is usually accompanied by magnetostriction and energetically disfavors ion-switching for ferroelectricity. Therefore, the incorporation of transition metals into both at the A- and B-sites in a $LiNbO_3$ structure can render strong magnetic interactions but is not favourable for ferroelectricity. A plausible approach is to place strong magnetic cations at the disordered *B*/*B*' sites for magnetic motif to suppress the *A*-site splitting, and nonmagnetic cations at the A-site to prevent bonding between *A* and *B*/*B*', as in $\mathit{A}_2Fe^{3+}\mathit{B}^{5+}O_6$ (*A* = Mg, Zn; *B* = Mo, Re) if stable compounds can be formed.

$LiNbO_3$-type ABX_3 materials without mixed-B-cationic or anionic sites are more promising to avoid the high-temperature paraelectric $LiNbO_3$-related *A*-site splitting, and achieve multiferroic magnetoelectricity as observed in the high-pressure and temperature prepared $FeTiO_3$ [67]. Accordingly, the future design of $LiNbO_3$-type multiferroic polar magnets should avoid B-cationic and/or anionic site-mixing unless magnetic interactions can significantly suppress the universal *A*-site splitting.

Conclusion Part I

In the study of these three series $A La_2 Fe B SbO_9$ (A = Ca, Sr, Ba; B = Ni, Co), $A_2 LaFe_2 SbO_9$ (A = Ca, Sr, Ba) and $Zn_2 Fe B O_6$ (B = Nb, Ta) we have shown that both A and B cation substitution has a significant effect on the physical properties. In these mixed B cation perovskites, the size of the A cation affects both the crystal structure and the degree of B cation order, which in turn affects the electric properties, where polarization arises from atomic displacement and octahedral distortion, and the magnetic properties, which are defined by the B cation order. The B cations in these perovskites are *d*-block transition metals, and we have shown that the combination of filled d^0 diamagnetic cations (Sb^{5+}, Nb^{5+} and Ta^{5+}) and unpaired d^n magnetic cations (Fe^{3+}, Ni^{2+} and Co^{2+}) can generate interesting properties, according to their B cation order and possible second-order Jahn-Teller distortions.

The triple perovskites $A La_2 Fe B SbO_9$ and $A_2 LaFe_2 SbO_9$ (A = Ca, Sr, Ba; B = Ni, Co) were synthesized to create relaxor ferromagnets, such as $La_3Ni_2SbO_9$, but showed no relaxor behaviour. The triple perovskites $A La_2 Fe B SbO_9$ are all ferrimagnets, whereas the $A_2 LaFe_2 SbO_9$ perovskites vary from ferrimagnetic to antiferromagnetic depending on the A cation substitution. The absence of relaxor behaviour might be attributed to the next-nearest-neighbour (NNN) interactions that are stronger for Fe^{3+} than for Ni^{2+}. The TEM study also exposed the complexity of the local crystal structure caused by the multiple A and B cations and their inhomogeneous distribution, which also contributed to the observed magnetic properties.

The LN-type phases $Zn_2 Fe B O_6$ (B = Nb, Ta) were synthesized in an attempt to produce multiferroics with strong magnetoelectric coupling, but only Zn_2FeTaO_6 shows a very weak ferroelectric switchable component at low temperature, whereas no switchable component is observed in Zn_2NbFeO_6. Nevertheless, the TEM study uncovered unexpected splitting of the A cation in both compounds that could be partially responsible for the absence of robust polarization switching in these materials. Moreover, this study allowed us to understand better the interactions between the A and B cations, which was used to describe and compare the mechanism of $Mn_2 Fe B O_6$ (B = Nb, Ta) and the anion mixed $A TaO_2N$ (A = Zn, Mn) [57].

A key conclusion we can make from these studies is that for a structure that is not pure monophasic and shows a more complex structure, i.e. local deviations from the average structure up to multiple phases, neutron powder diffraction and X-ray powder diffraction can miss crucial information and this can easily remain unnoticed, giving acceptable, though wrong, refinements as judged by the *R*-factors and goodness-of-fit. Local structural deviations play an important role in determining the physical properties, and electron microscopy is necessary to explore the true structural mechanisms controlling the physical properties.

Appendix Part I

Experimental details of TEM study:

The structure and composition of the perovskite compounds were studied by transmission electron microscopy (TEM). The specimens for TEM were prepared by dispersing crushed powder in ethanol and depositing a few drops of this solution on a copper grid covered with a holey carbon film. Selected area electron diffraction (SAED) patterns were recorded with a Philips CM20 microscope and an FEI Tecnai G2 microscope. High-angle annular dark-field scanning transmission electron microscopy (HAADF-STEM) images, annular bright-field STEM (ABF-STEM) images and energy-dispersive X-ray (EDX) maps were acquired with an FEI Titan 80-300 "cubed" microscope equipped with a Super-X detector and operated at 300 kV. The experimental details about the other techniques used by the collaborators can be found in the corresponding papers [37,38,57].

Synthesis ALa$_2$FeBSbO$_9$ (A=Sr,Ca; B=Ni,Co) and Ba$_2$LaFeNiSbO$_9$

Polycrystalline samples of **ALa$_2$FeCoSbO$_9$ (A=Ca, Sr)** were prepared using the standard ceramic method. ACO$_3$ (A=Ca, Sr), La$_2$O$_3$, Fe$_2$O$_3$, Co$_3$O$_4$ and Sb$_2$O$_5$ (purity >99.95%) were weighed out in the appropriate stoichiometric ratio and ground together in an agate mortar for 30 minutes to give a homogeneous mixture. La$_2$O$_3$ was heated at 800 °C for 24 hours prior to use to ensure it was completely dry. The mixture was then loaded into an alumina crucible and fired at 800 °C for 24 h. It was then quenched to room temperature, reground and pressed into a pellet which was fired in air at 1300 °C for 48 hours and subsequently annealed at 1300 °C for another 48 hours after further grinding. Finally, the furnace was allowed to cool to 800 °C, and then the sample was quenched to room temperature. Polycrystalline samples of **ALa$_2$FeNiSbO$_9$ (A=Ca, Sr, Ba)** were prepared under the same conditions with starting materials of ACO$_3$ (A=Ca, Sr, Ba), La$_2$O$_3$, Fe$_2$O$_3$, NiO and Sb$_2$O$_5$ (purity >99.95%) in the appropriate stoichiometric ratio.

Synthesis $A_2LaFe_2SbO_9$ (A=Sr, Ca, Ba)

Polycrystalline samples of ***A_2LaFe$_2$SbO$_9$* (A=Ba, Sr, Ca)** were prepared using the standard ceramic method. ACO_3 (A=Ba, Sr, Ca), La_2O_3, Fe_2O_3, and Sb_2O_5 (purity >99.95%) were weighed out in the appropriate stoichiometric ratio and ground together in an agate mortar for 30 minutes to give a homogeneous mixture. La_2O_3 was heated at 800 °C for 24 hours prior to use to ensure it was completely dry. The mixture was then loaded into an alumina crucible and fired at 800 °C for 24 h. It was then quenched to room temperature, reground and pressed into a pellet which was fired in air at 1150 °C for 48 hours and subsequently annealed at 1150 °C for another 48 hours after further grinding. Finally, the furnace was allowed to cool to 800 °C, and then the sample was quenched to room temperature.

Synthesis Zn_2Fe*B*O_6 (B=Nb, Ta)

To make phase pure **Zn_2Fe*B*O_6 (B=Nb, Ta)**, high pressure synthesis was applied. For Zn_2FeTaO_6, a stoichiometric mixture of ZnO (99.9%, Alfa Aesar), Fe_2O_3 (99.999%, Sigma Aldrich), and Ta_2O_5 (99.85%, Alfa Aesar) was pressed into a pellet and annealed between 1173 and 1523 K in air. Laboratory x-ray powder diffraction (XRPD) data, collected in a Bruker D8 Advance diffractometer, indicated that it was fully reacted to form a mixture of $ZnFe_2O_4$ (PDF#: 01 082-1042),6 $ZnTa_2O_6$ (PDF#: 00-039-1484)7, and $FeTa_2O_6$ (PDF#: 01-083-0588)8 between 1473 and 1523 K (Figure S2). The pellet melted above 1523 K. The original oxide mixture was pressurized typically over 8-12 hours and reacted at 1623 K under 9 GPa for 1 h, in a $LaCrO_3$ heater lined with Pt capsule inside a MgO crucible in a multi-anvil press, and then quenched to room temperature in a few seconds by turning off the voltage supply to the resistance furnace. The pressure is maintained during the temperature quenching and then decompressed typically in 8-12 hours.

Polycrystalline Zn_2FeNbO_6 was prepared following the conditions for the parent Zn_2FeTaO_6, by reaction of a stoichiometric mixture of ZnO (99.9%, Alfa Aesar), Fe_2O_3 (99.999%, Sigma Aldrich), and Nb_2O_5 (99.85%, Alfa Aesar) at 1623 K under 9 GPa for 1 h.

Polycrystalline **$ZnSnO_3$** was synthesized by a solid-state reaction under high pressure at elevated temperature. The mixture of stoichometric amounts of ZnO and SnO_2 was allowed to react in a cubic multianvil-type high pressure apparatus at 7 GPa and 1000 °C for 30 min and then was quenched to room temperature.

Part II: Li-ion battery cathode materials

In this second part of my thesis, I study the effects of cation substitution on the crystal structure of Li-ion battery cathode materials upon charging and discharging. In collaboration with the University of Hasselt, we investigated the structural changes that occur upon cycling and whether cation substitution can prevent these structural changes in order to improve the performance of the battery.

Chapter 5 provides a brief overview on Li-ion batteries and the relation between the crystals' structure and their performance to clarify the chosen cation substitutions.

I first investigated, in **Chapter 6**, the structural and performance differences resulting from different syntheses, using the representative and well-known cathode material LMR-NMC. I also determine and discuss the differences in structure evolution upon charging and discharging. In **Chapters 7** and **Chapter 8**, I investigate two types of cation substitutions to improve the electrochemical performance.

Chapter 5. Introduction to Li-ion battery cathode materials

Over the last decades, increased environmental pollution generated a need for clean, renewable energy sources to reduce the use of fossil energy and create a sustainable society. As these renewable sources, such as sunlight and wind, are not always available, this in turn also needs next-generation energy storage devices. Lithium-ion batteries are considered to be a promising energy-storage technology and are widely employed in portable devices and green transportation systems such as electric vehicles. However, the current lithium-ion batteries still do not fulfil the needs for their wide applications in electric vehicles and grid-scale energy storage systems, because, depending on the exact type, they are either too expensive or not safe enough, or do not have sufficient energy densities or sufficiently high charging rates.

Lithium-ion batteries consist of an anode, a cathode and an electrolyte. The electrode of the battery that releases electrons during the discharge is called anode; the electrode that absorbs the electrons is the cathode. The cathode material is a lithium-containing inorganic compound, which contains channels that allow the Li-ions to go reversibly in and out of the structure. During discharge, the chemical energy stored in the cathode is released and converted to electrical energy through insertion of the Li-ions, which means that the Li-ions migrate from the anode into the lithium-conducting electrolyte back into the host structure of the cathode. The reversible process is called charge, where removal of the Li-ions occurs.

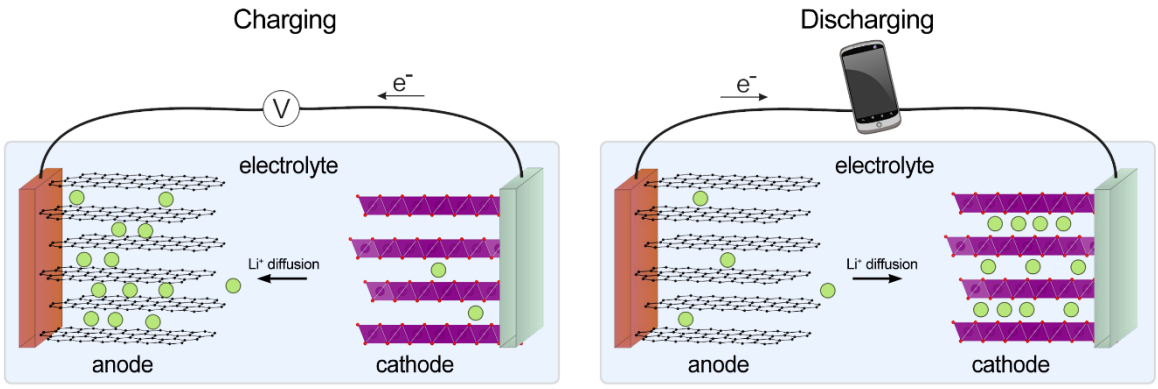

Figure 47. *Scheme of the charging and discharging processes. Left: when the battery is charged, a higher voltage is applied, which results in the removal of Li-ions from the cathode. Right: in the discharge process, the Li-ions move back to the host structure. The figure is based on* [76].

The power performance of such a lithium-ion battery strongly depends on the performance and structural stability of the cathode material. Upon charging, a higher voltage is applied, which results in electrochemical reactions (i.e. cationic and anionic redox processes), allowing the lithium to leave the structure. The amount of lithium that is extracted from the structure is translated into the capacity of the battery. In many cases, only a limited amount of Li can be extracted, because the fully charged state (no lithium left in the structure) leads to structural instability. Moreover, during the charge-discharge cycles, some irreversible electronic and structural changes can occur in the cathode material that are directly related to the failure of the battery described by capacity loss, voltage fade and oxygen loss. A better understanding of the origin of these irreversible changes is needed to improve the cathode materials and enhance the performance of the battery. Since these structural changes take place at the atomic level, this requires a combination of techniques from the micro level to the atomic scale.

5.1. Types of cathode materials

An active cathode material should allow reversible (de)insertion of lithium. Therefore, the crystal structure should contain paths for fast Li diffusion, which is realized by the formation of a two-dimensional (2D) or three-dimensional (3D) framework. In the first case, the crystal structure is layered, where the Li-ions can migrate through the interlayers. A three-dimensional framework is formed when the polyhedra are all connected, leading to a percolating network of channels through which the Li-ions diffuse during charging and discharging. The channels themselves can then also form a 3D network of diffusion paths, as seen in the spinel framework or consists of only 1D tunnels like in the olivine framework [77].

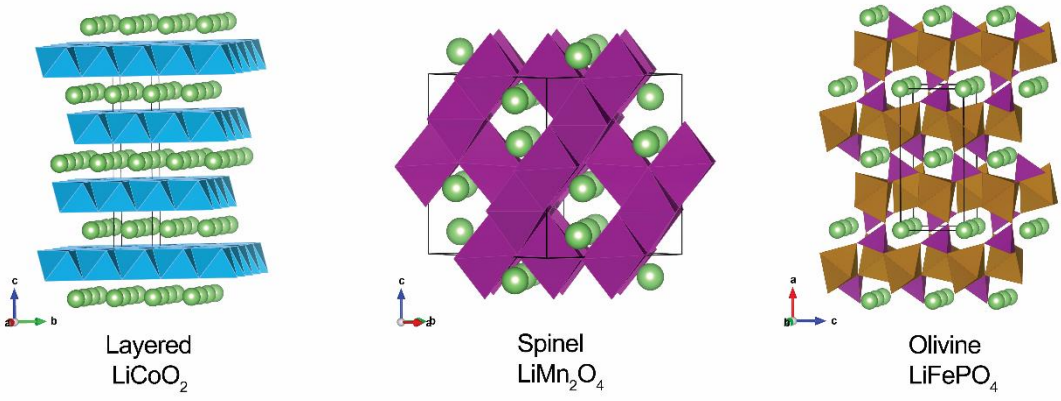

Figure 48. *The crystal structures of the different types of cathode materials. The layered structure describes a 2D Li^+ ions transport, while the spinel and olivine structures describe a 3D and 1D Li^+ ions transport, respectively.*

The cathode materials can be divided into two categories: oxide-based cathodes and poly-anionic based cathodes. In this research, the focus is on the first group, more specifically on lithium transition metal oxides.

Lithium transition metal oxides

One of the most common cathode materials for rechargeable lithium-ion batteries is $LiCoO_2$. $LiCoO_2$ has a layered rock-salt-type structure with the $R\bar{3}m$ symmetry (**Figure 49A**) and is very popular due to the structural stability, high energy density and stable quality in the production process. However, only 50% of the Li can be reversibly cycled without causing cell capacity loss, resulting in a specific capacity of only ~140 mAh/g compared to the theoretical specific capacity of 274 mAh/g. Exceeding this limit leads to changes in the $LiCoO_2$ structure, which is associated with poor stability of the electrode at low lithium contents [78,79]. In addition to the structural instability, there is limited availability of cobalt, which causes it to have a high price.

On the other hand, manganese-based oxides have long been studied as possible cathode materials because of their low cost and nontoxicity compared to cobalt-based compounds. The cathode material Li_2MnO_3 attracted much attention because it has a very high theoretical capacity of ~458 mAh/g [80]. Li_2MnO_3, also described as $Li[Li_{1/3}Mn_{2/3}]O_2$, has a layered structure and adopts the monoclinic *C2/m* symmetry, where the excess of Li occupies positions in the Mn layers, resulting in $LiMn_2$ layers, in which the Li atoms are surrounded by six Mn atoms and form a honeycomb pattern (**Figure 49B-C**). Manganese is exclusively present in a 4+ oxidation state in pristine Li_2MnO_3. The Mn^{5+}/Mn^{4+} redox couple is inaccessible as it is situated below the top of the O-2*p* band (i.e. oxygen will be oxidized first), turning Mn^{4+} to be electrochemically inactive in Li_2MnO_3 [81,82]. Nevertheless, Li_2MnO_3 demonstrates noticeable electrochemical activity, attributed to anionic redox chemistry of the oxygen sublattice. In the first charging-cycle, a characteristic voltage plateau at ca. 4.5V vs Li/Li^+ is observed, which is considered to be the activation process.

Different studies showed that this long plateau indicates that delithiation proceeds through a two-phase reaction. First, delithiation occurs without oxygen loss or phase transition and forms MnO_3:

$$Li_2MnO_3 \rightarrow 2Li^+ + MnO_3 + 2e^-. \quad \text{(Reversible anionic redox reaction)}$$

The extraction of Li is accompanied by the oxidation of O^{2-} to O^{-}, forming $(Mn^{4+})(O^{2-})(O^{-})_2$, where the O^{-} hole species are localized on the anion sites closest to the vacant Li sites [82]. In the second reaction, when the voltage plateau is reached, oxygen release is involved:

$$Li_2MnO_3 \rightarrow 2Li^{+} + MnO_2 + \tfrac{1}{2}O_2 + 2e^{-}. \quad \text{(Irreversible anionic redox reaction)}$$

During this reaction oxygen dimers are formed: $O^{-} + O^{-} \rightarrow O_2^{2-}$ (i.e. a peroxo bond), leading to oxygen release:

$$(Mn^{4+})(O^{2-})(O^{-})_2 \rightarrow (Mn^{4+})(O^{2-})_2 + \tfrac{1}{2}O_2.$$

The absence of the stabilization of the created O-O dimers due to a lack of Mn-O covalency leads to the oxygen release. The formation of strongly oxidized O-O dimers is accompanied by a significant reduction of Mn^{4+} to Mn^{3+}. In subsequent charge-discharge cycles, Mn^{3+} is able to contribute to the capacity because of the Mn^{3+}/Mn^{4+} redox couple, but the formation of the oxygen dimers will trigger the migration of Mn towards empty lithium positions with the formation of the spinel-structure and induces voltage fade [82,83].

In theory, Li_2MnO_3 has a capacity of ~458 mAh/g, but the specific discharge capacity only reaches to a maximum of ~260 mAh/g [81].

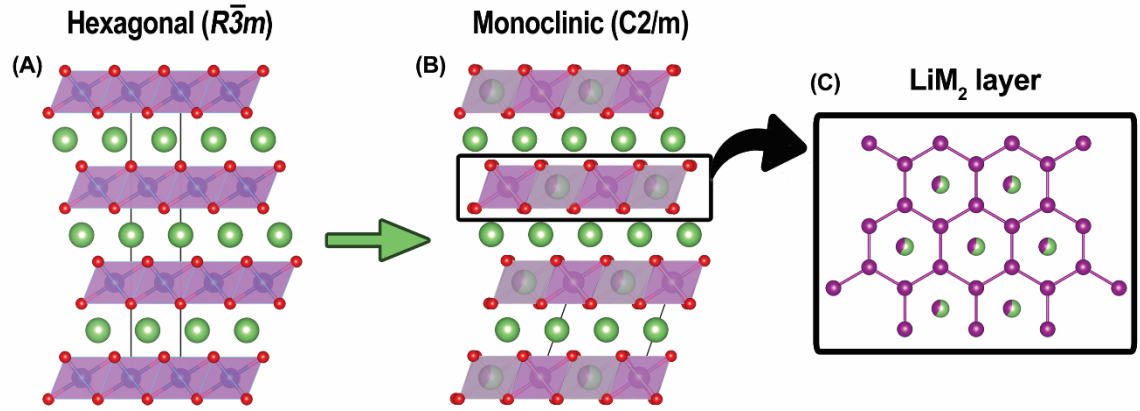

Figure 49. *The crystal structure of the layered rock-salt-type cathode materials.* ***(A)*** *represents the $R\bar{3}m$ structure of $LiCoO_2$ and NMC, while* ***(B)*** *represents the monoclinic C2/m structure of Li_2MnO_3 and LMR-NMC. For Li_2MnO_3 the lithium positions in the honeycomb layer are fully occupied by lithium, while in LMR-NMC these positions are partially occupied by lithium and transition metals (TM).* ***(C)*** *demonstrates the honeycomb order within these Li-TM layers. Figure based on [79].*

To overcome these problems, such as structural instability, oxygen release and phase transitions, and still benefit from the advantages from both structures (i.e. electrochemically active Co; anionic redox reaction in Li/Mn-rich oxides), partial cation substitution is applied. Starting from the $LiCoO_2$ structure, Co^{3+} can be partially replaced with Mn^{4+} and Ni^{2+} that leads to the $Li[Ni_xMn_yCo_z]O_2$ oxides (NMC), which have good stability and higher specific capacities of ~200 mAh/g. Further substitution of lithium in these layered oxides has led to materials termed as Li-rich NMC which combine the beneficial effects of Ni, Co and Mn with some Li in the transition metal layers, exceeding a specific capacity of 280 mAh/g [79]. Specifically, the lithium-and manganese-rich oxides (LMR-NMC) have been extensively studied as a promising alternative for the commercialised $LiCoO_2$ due to their higher initial specific capacities [84,85], higher thermal stability [85,86] and lower costs [78]. These oxides are reported as $Li[Li_xNi_yMn_{1-x-y-z}Co_z]O_2$ and follow the Li_2MnO_3 parent structure. The lithium positions in the Li-TM layers (TM = Ni, Co, Mn) are partially occupied by lithium and transition metals (TM) in contrast to Li_2MnO_3, where the lithium positions are only occupied by lithium. Despite the high capacity, the commercialisation of LMR-NMC is hampered by significant voltage decay (a gradual decrease of the discharge voltage reducing the specific energy), voltage hysteresis (voltage difference on subsequent charge and discharge, penalising energy efficiency), and sluggish (de)intercalation kinetics compromising the battery power [84,87]. Nowadays, it is understood that these drawbacks are intrinsic to the crystal and electronic structure of LMR-NMCs. In these LMR-NMCs, not only the cationic redox reactions contribute to the capacity (i.e. $Co^{3+} \rightarrow Co^{4+}$ and $Ni^{2+} \rightarrow Ni^{3+}$ and Ni^{4+}), but also the reversible oxygen redox processes [87] that were also found in the parent compound Li_2MnO_3. The irreversible oxygen redox processes are the cause of the voltage fade. As the behaviour of the first charge-discharge cycles is similar for LMR-NMC and Li_2MnO_3, it is interesting to compare the crystal structure of both materials upon cycling, in order to have a better understanding of the origin of the structural changes in LMR-NMC.

5.2. Structural changes upon cycling

When the material is charged, the lithium migrates through the structure by hopping from one octahedral site to another empty octahedral site in the lithium layer via an intermediate tetrahedral site. This is called an O-T-O diffusion path and is illustrated in **Figure 50A**. If then the material is further charged up to a potential of 4.5 – 4.6 V vs Li/Li^+ or higher, a highly delithiated (charged) state is reached, and some transition metals (TMs) migrate to occupy tetrahedral sites in the lithium layer (**Figure 50B**) and then part of them migrate further to the emptied octahedral lithium positions in the lithium layer (**Figure 50C**). The energy barrier for the migration to the tetrahedral sites is lower in the charged state compared to the discharged state because of the vacant neighbouring lithium sites. The occupation of tetrahedral sites in the TM layer is less favourable than in the lithium layer because all neighbouring octahedral sites are still occupied by transition metals in the charged state [88]. Upon discharge, the TMs are expected to return; however, this migration is not fully reversible, and some transition metal cations remain trapped at the octahedral lithium positions and/or the tetrahedral interstices. These trapped cations increase the energy barrier for Li diffusion and impede the lithium to migrate through the structure, which in turn lowers the capacity. Further, the TM migration also results in a shift of redox pairs to other potentials resulting in a shift (= fading) of the discharge voltage.

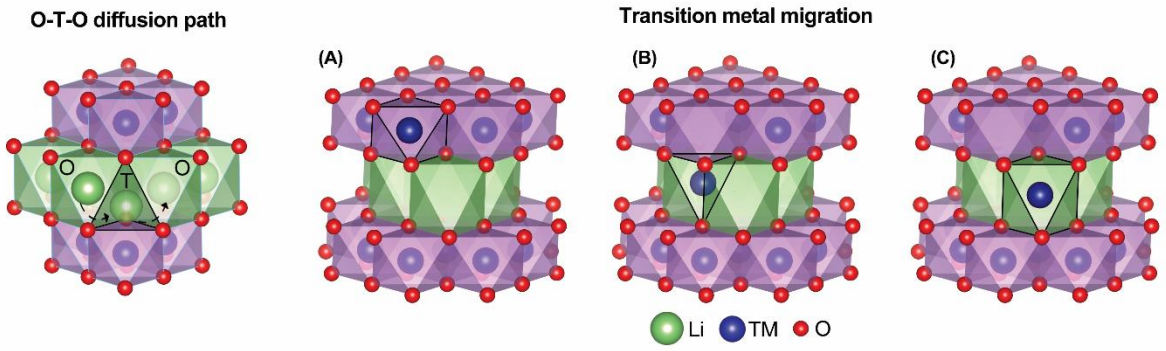

Figure 50. *Schematic illustration of lithium diffusion (left) and TM migration (right), where the TM migrates from the octahedral position in the TM layer (A) through the tetrahedral interstices in the lithium layer (B) towards the vacant octahedral position in the lithium layer (C). To simplify the illustration, we assumed a layered structure with pure TM and Li layers. Figure based on [88].*

In Li-rich NMCs and Li_2MnO_3, these defects accumulate, causing a gradual transition of the layered *C2/m* structure to a layered structure ($R\bar{3}m$), where the Li-TM layers become disordered, to then a spinel-like structure and eventually to a disordered rock-salt structure, as shown in **Figure 51** for Li_2MnO_3. After several cycles, the lithium positions within the Li-TM layers are almost not occupied anymore. The vacancies left by the Li-ions in the Li-TM layers may lower the energy barrier for transition metal migration [89], and therefore accelerate the formation of a more disordered structure [90]. These structural changes are closely related to the oxygen redox processes. The coupled oxygen redox/cation migration is believed to be the cause for the voltage hysteresis, whereas the partial irreversibility of the cation migration causes the voltage fade [91].

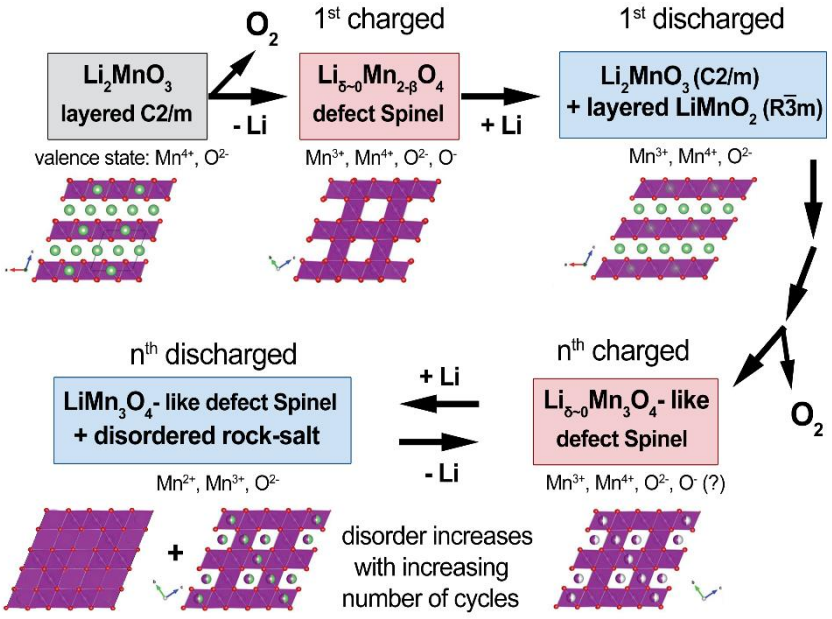

Figure 51. *The phase transition that occurs upon cycling in the case of the Li_2MnO_3 sample. After cycling, first, the degree of disorder within the honeycomb layer will increase, which is followed by the formation of a defect spinel-like structure that becomes more disordered with increasing the number of cycles. The figure is based on [83].*

5.3. Fundamental questions

As the performance of batteries mainly depends on the cathode material, the research of new Li-ion batteries with higher energy and power density, lower cost, and improved safety and long-term stability is mainly dedicated to the study of new cathode materials.

Improving the performance of the cathode material requires a fundamental understanding of how the cathode material functions and what structural and electronic properties limit the battery performance. Within this research, many fundamental questions have to be solved, such as:

- finding the optimal electronic configuration of the cations to reduce the TM migration and prevent irreversible oxygen evolution from the material;
- investigating if the formation of O_2^{n-} species would promote reversible TM migration and enhance Li diffusion;
- understanding how the surface structure changes during charge/discharge and finding the exact origin of the formation of the surface blocking layer;
- figuring out the role of the particle size and morphology in controlling the battery performance, and if an appropriate coating of the cathode particles may prevent the formation of a surface blocking layer and the associated oxygen evolution.

In this thesis, we investigated the effect of two different synthesis methods and different cation substitutions on the structure, morphology and performance of the cathode material.

We considered substitution of an element (M) that does not tend to adopt the Th coordination, in order to reduce the migration to the lithium positions, and is not redox-active within the investigated potential window, in an attempt to stabilize the structure whilst enhancing the reversible anionic redox chemistry. Furthermore, these stronger M-O bonds are also expected to stabilize the structure and prevent oxygen release. Examples of potential candidates are Sn^{4+} and Ti^{4+} [92–95].

Chapter 6. Synthesis and structure of LMR-NMC

The results of this chapter are incorporated into a paper that is in preparation:

M. Hendrickx, A. Paulus, M. Kirsanova, A.M. Abakumov, A. Hardy and J. Hadermann, *Differences in microstructure and electrochemical properties of LMR-NMC upon varying the synthesis method*

6.1. Introduction

$Li_{1.2}Ni_{0.13}Mn_{0.54}Co_{0.13}O_2$ was selected for our studies, as this composition is reported to demonstrate the best capacity within the LMR-NMC family with a high reversible capacity exceeding 250 mAh/g. However, besides the stoichiometry, the electrochemical performance also strongly depends on the used synthesis method which can control the material properties, such as the particle size and shape, phase purity, crystallinity and cation disorder [96]. Many methods have been developed to synthesize these cathode materials with the goal of controlling their material properties and enhance the performance. Initially, the LMR-NMC cathode materials were usually synthesized through a high-temperature heat treatment that leads to excessive particle growth and poor performance. Currently, among the various methods used to synthesize cathode materials, the solution-gel (SG) and co-precipitation (CP) methods are commonly applied, as they are powerful, low cost and easy preparation methods for large production. Moreover, both methods are very popular due to their ability to achieve good stoichiometry, to mix reactants homogeneously at an atomic level and to reduce the particle size; however, the particle size of the materials prepared from the SG and CP methods is different, ranging from nanoparticles to microparticles, respectively [96–98]. We compared the structures of $Li_{1.2}Ni_{0.13}Mn_{0.54}Co_{0.13}O_2$ particles prepared using the SG and CP synthesis methods and investigated the correlation of the structural differences with the electrochemical properties. The synthesis and measurements of the electrochemical properties were performed by Andreas Paulus at the University of Hasselt. The structural study is my contribution.

A brief explanation of these two synthesis methods along with the details of the SG and CP synthesis of LMR-NMC can be found in the appendix at the end of Part II. The experimental details of the used TEM techniques are listed in the same appendix.

6.2. Solution-gel vs Co-precipitation

6.2.1. Experimental results

Galvanostatic charge/discharge measurements have been performed on the $Li_{1.2}Ni_{0.13}Mn_{0.54}Co_{0.13}O_2$ sample synthesized by both the solution-gel and co-precipitation method, referred to as the solution-gel and co-precipitation samples, and are shown in **Figure 52**. The materials have been imposed to 50 charge/discharge cycles at a C-rate of C/10 preceded by an initial cycle at C/20. In both samples, the first charging step involves cation oxidation (i.e., $Ni^{2+} \rightarrow Ni^{3+} + Ni^{4+}$ and $Co_3^{+} \rightarrow Co^{4+}$) and oxygen redox processes. In **Figure 52,** the cation oxidation can be seen as the slope of the charging curve, which is followed by a voltage plateau that is partially related to oxygen release. The applied upper potential of the solution-gel sample is 0.05 V higher than for the co-precipitation sample, which might contribute to the longer voltage plateau observed in the solution-gel sample. The specific discharge capacity of the first cycle is higher for the solution-gel sample (~ 190 mAh/g) than for the co-precipitation sample (~ 148 mAh/g), but the capacity loss is significantly higher in the case of the solution-gel sample. The voltage fade is represented by the black arrow, which can be drawn by connecting the voltage values that correspond to half of the discharge capacity of each cycle. This is marked by the dashed lines in the charge-discharge plot of the solution-gel sample. The slope of the black arrow indicates the amount of voltage fade. The steeper the arrow, the higher the voltage shift (= fading) during the successive cycles. As the black arrow of the co-precipitation sample is steeper, it seems that the voltage fade is slightly higher in the case of the co-precipitation sample.

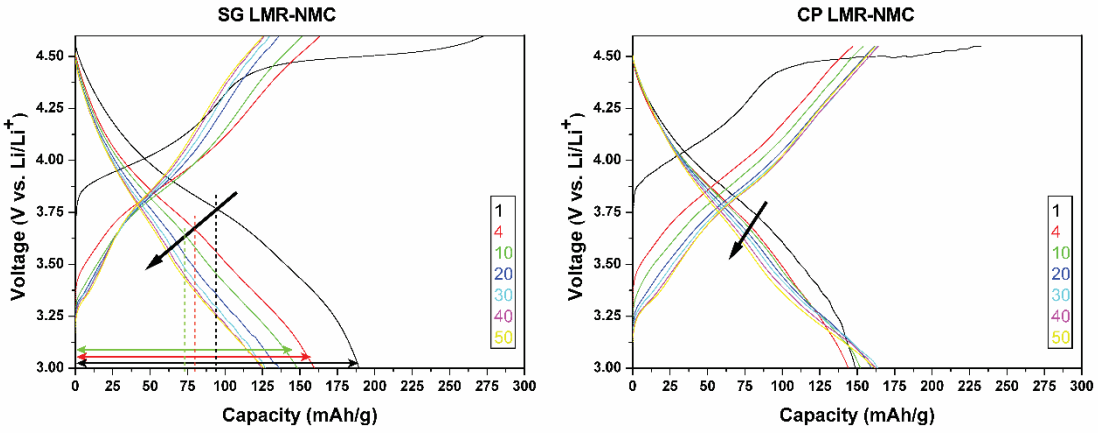

Figure 52. *The charge-discharge plot of the $Li_{1.2}Ni_{0.13}Co_{0.13}Mn_{0.54}O_2$ sample synthesized by the solution-gel (left) and the co-precipitation (right) method. Voltage fade is indicated by the arrow. The slope of the arrow corresponding to the co-precipitation sample is steeper, indicating that the voltage fade is higher for the co-precipitation sample.*

Differences in the evolution of the capacity and voltage should be related to differences in their structural properties. The HAADF-STEM images with the accompanying EDX maps (**Figure 53**) taken from both samples reveal their differences in particle size, morphology and purity of the phase. The particles from the solution-gel sample are much smaller, ranging between 100 nm to 480 nm with an elongated shape and pronounced facets, while the particles from the co-precipitation sample have a size from 250 nm up to 2 µm, and have an irregular shape and a rough surface. The average composition of both samples is in good agreement with the expected one (i.e. $Li_{1.2}Ni_{0.13}Mn_{0.54}Co_{0.13}O_2$), with ratios $Ni_{0.14(3)}Mn_{0.53(3)}Co_{0.13(2)}$ for the co-precipitation sample and $Ni_{0.13(2)}Mn_{0.52(2)}Co_{0.15(1)}$ for the solution-gel sample. Furthermore, the EDX maps show that for the main phase, the transition metals are homogeneously distributed, but also expose a Co-rich additional phase in the case of the solution-gel sample. This impurity might also contain lithium which cannot be detected by EDX as the energy of the characteristic X-rays of lithium (Z=3) are too low to detect.

In order to know whether the differences observed in the shape and size are the only cause for the differences in the electrochemical properties, a detailed structural investigation has been performed to analyse the crystal structure.

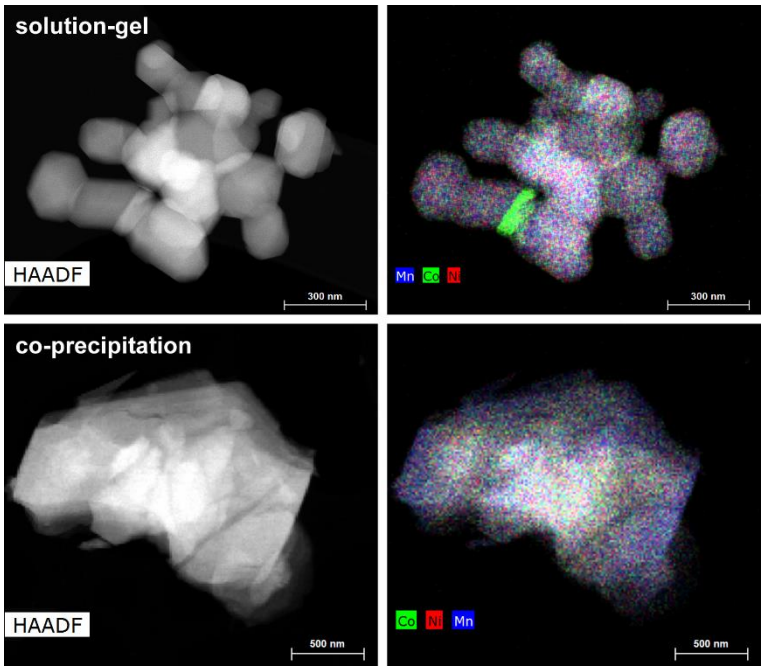

Figure 53. *The HAADF-STEM image (left) together with the mixed Mn/Co/Ni element map (right) from the $Li_{1.2}Ni_{0.13}Co_{0.13}Mn_{0.54}O_2$ sample prepared with the solution-gel (top) and co-precipitation (bottom) method. The mixed element map of the sample prepared with the solution-gel method reveals the presence of an additional Co-rich phase.*

The atomic resolution HAADF-STEM images taken from the solution-gel sample, shown in **Figure 54**, show a structural modification at specific surface planes. We define the facets using the corresponding SAED pattern (**Figure 55**). The {200} facets have a surface layer with a homogeneous thickness of ~ 1.5 nm, and the accompanied EDX maps in **Figure 54** revealed that these {200} surface planes possess Ni-segregation while other surface facets do not have a Ni-rich composition. The {002} and {202} planes exhibit Co-segregation. The Ni/Co segregation is supported by the line profiles taken perpendicular to these different facets, which are shown in **Figure 56**.

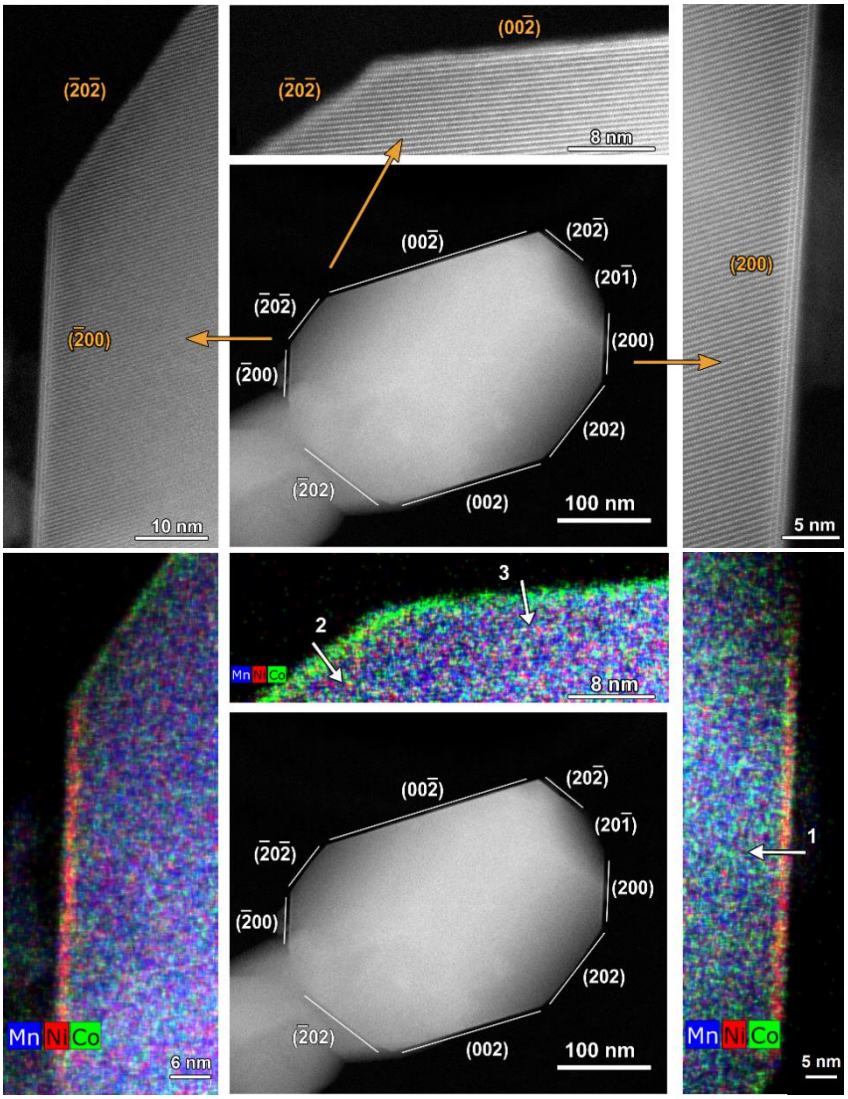

Figure 54. *The HAADF-STEM image of a $Li_{1.2}Ni_{0.13}Mn_{0.54}Co_{0.13}O_2$ particle prepared with the solution-gel method together with close-up HAADF-STEM images (top) and the corresponding element maps (bottom) of the {200}, {202} and {002} facets. The HAADF-STEM images show a spinel structure of only a few atomic layers at the {200} facets (see Figure 59 for more details). The mixed Mn/Ni/Co element maps reveal that the spinel structure at the surface is Ni-rich, while the surfaces at the {202} and {002} facets are Co-rich. The arrows marked with numbers 1, 2 and 3 correspond to the line profiles that are shown in Figure 56.*

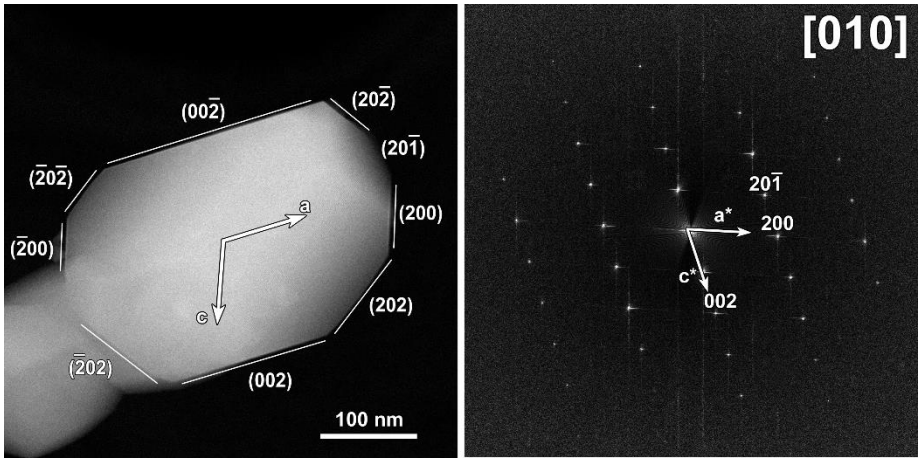

Figure 55. *HAADF-STEM image (left) of a $Li_{1.2}Ni_{0.13}Mn_{0.54}Co_{0.13}O_2$ particle prepared with the solution-gel method together with the corresponding SAED pattern (right). The axes in both the real space ($\vec{a}$ and $\vec{c}$) and reciprocal space ($\vec{a}$* and $\vec{c}$*) are shown that is used to index the facets of the particle shown in the HAADF-STEM image. Note that $\vec{a}$* (resp. $\vec{c}$*) should be perpendicular to $\vec{c}$ (resp. $\vec{a}$) and $\vec{b}$ ($\vec{b}$ is oriented perpendicular to the image).*

The line profiles (**Figure 56**) show the relative percentages of only Ni, Mn and Co, which means that the targeted ratio is Ni:Mn:Co = 16.25:67.5:16.25 (i.e. the same ratio as $Ni_{0.13}Mn_{0.54}Co_{0.13}$). Note that for the quantification of the entire line profile the observed maximum counts of the sum of Ni, Co and Mn is set to 100%, and all other values are relative to this maximum. Therefore, at regions where slightly less counts are observed the total percentage will be slightly smaller than 100%, as can be seen from the black curve representing the total amount of Ni, Co and Mn. At the surfaces, the concentration of the transition metals decreases gradually rather than abruptly, which can be attributed to beam damage during the EDX acquisition. Lu *et al.* demonstrated that lithium-containing oxides suffer from radiation damage by high-energy electron beams that involves the creation of lithium vacancies and the migration of transition metals [99]. From imaging before and after the acquisition of an EDX map (i.e. 10 min or more in order to obtain a qualitative map, while HAADF-STEM images only take a few seconds), we have observed that a cloud of contamination is formed at the surface that mainly contains carbon but also a very small amount of transition metals.

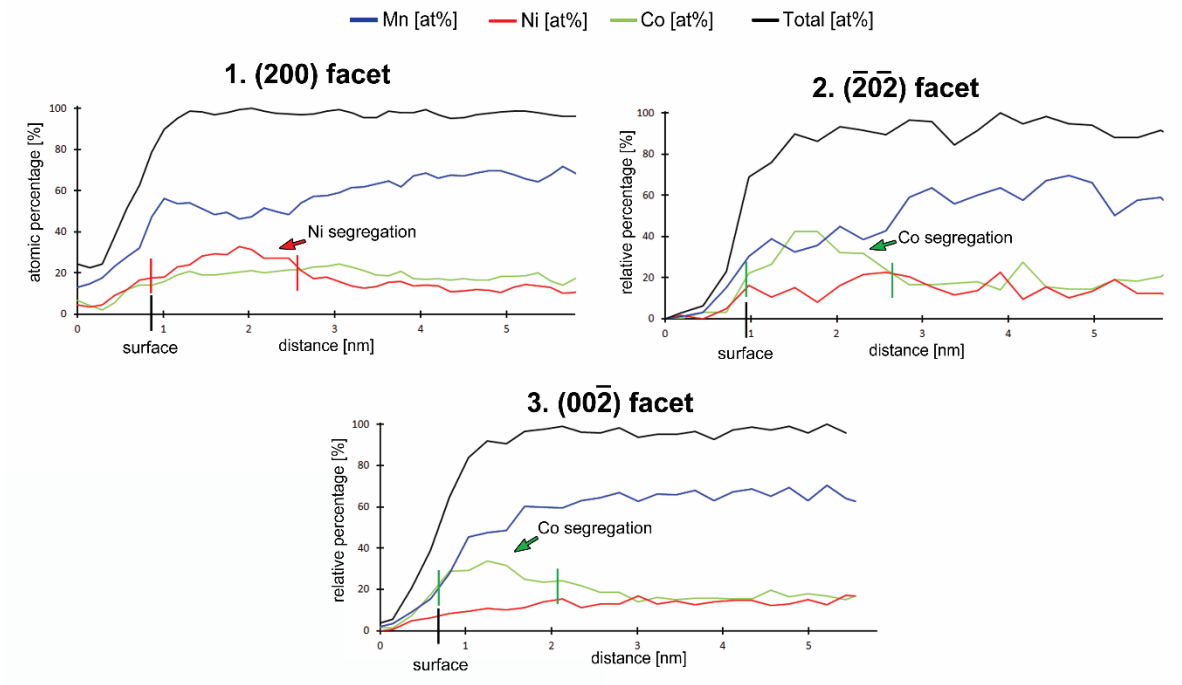

Figure 56. *Line profiles taken perpendicular to the (200) (i.e., line profile 1 shown in Figure 54), (2̄02̄) (i.e., line profile 2), and (002̄) (i.e., line profile 3) facets. The line marked by surface denotes the surface of the particle. Line profile 1 confirms the Ni segregation towards the surface at the {200} facet. Line profiles 2 and 3 confirm the Co segregation towards the surface at the {202} and {002} facets as observed in the element maps in Figure 54. The transition metal concentrations decrease gradually at the surface, which can be attributed the radiation damage at the surface.*

The same structural investigation has been performed for the co-precipitation sample, but particles with pronounced facets were rare. Eventually, a few particles were found with such facets, although not as well defined as those of the solution-gel sample. No structural modifications or segregation were observed at any of the facets as can be seen in **Figure 57**.

In general, no structural modifications or segregation were observed in any particle of the co-precipitation sample, while in the solution-gel sample every particle with pronounced {200}, {002} or {202} facets possess the described Ni/Co segregation with structural modifications.

As can be derived from the TEM results above, the solution-gel and co-precipitation samples differ in particle size and morphology, but also differ at nanoscale in element distribution and surface modifications.

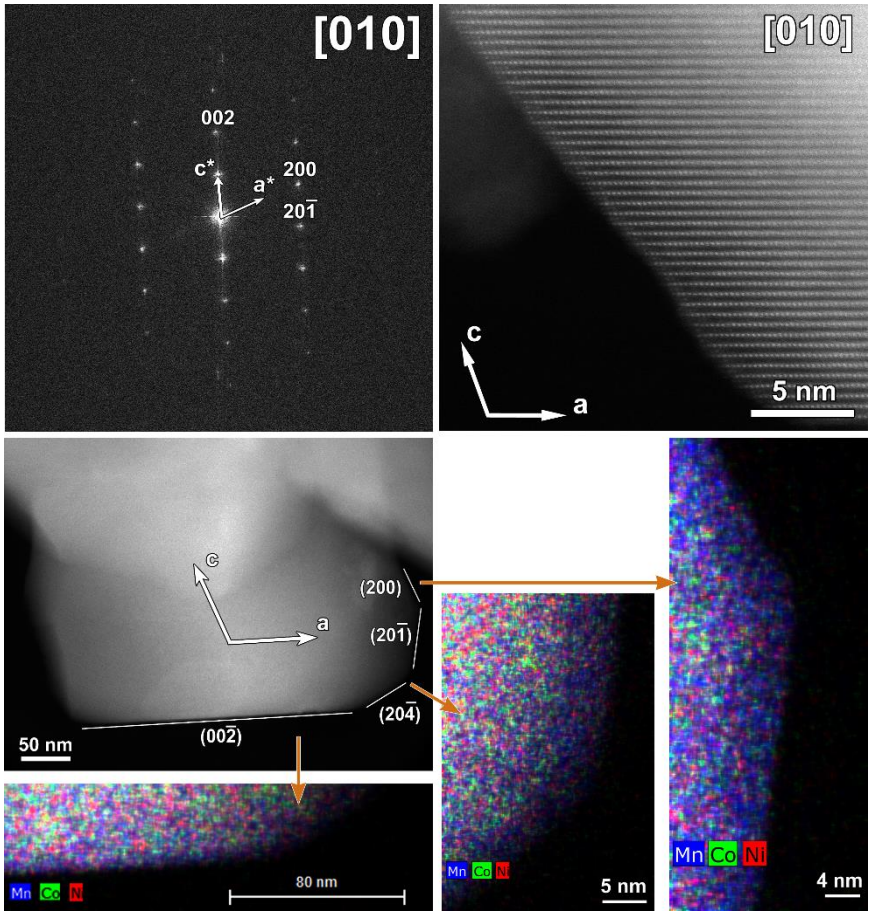

Figure 57. *At the bottom, the HAADF-STEM image of a $Li_{1.2}Ni_{0.13}Mn_{0.54}Co_{0.13}O_2$ particle prepared with the co-precipitation method is shown with the element maps of the (200), (20$\bar{4}$) and (00$\bar{2}$) facets, which do not show any segregation at any facet. At the top left the corresponding SAED pattern is shown together with a close-up HAADF-STEM image on the right of the (200) facet that clearly does not show spinel formation at the surface as was observed in the solution-gel sample.*

To investigate the evolution of the surface modification upon cycling, we investigated the surface of crystals synthesized using the SG method and 50x charged and discharged.

Figure 58 displays the atomic resolution HAADF-STEM images and SAED patterns along the [010] orientation of the $Li_{1.2}Ni_{0.13}Mn_{0.54}Co_{0.13}O_2$ sample prepared by the SG method in the pristine state and the cycled state. The intensity of the atom columns in the HAADF-STEM images is proportional to the atomic number of the elements ($I \sim Z^2$). Therefore, the bright dots in the HAADF-STEM images correspond to the transition metal atom columns, while the atom columns of lithium and oxygen are too weak to be clearly visualized.

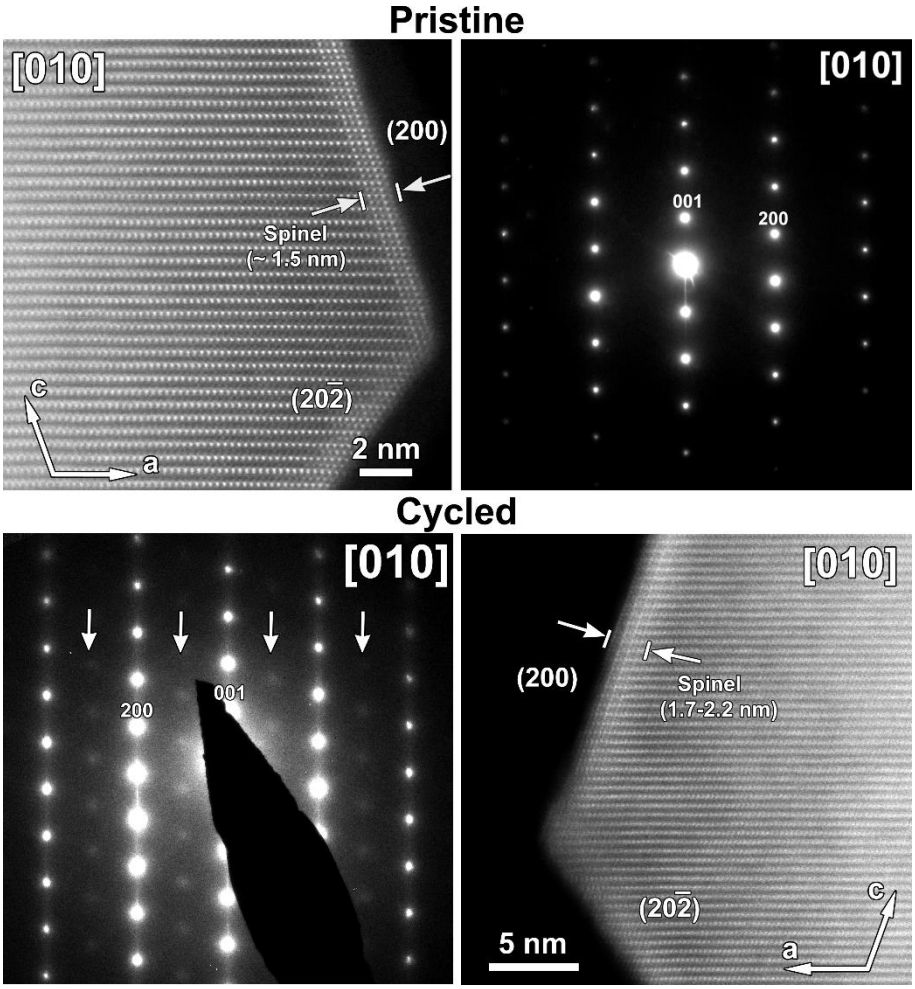

Figure 58. *HAADF-STEM images and SAED patterns taken along the [010] orientation from the pristine and cycled* $Li_{1.2}Ni_{0.13}Mn_{0.54}Co_{0.13}O_2$ *samples prepared from the solution-gel method.*

The surface of the (200) facet in the pristine sample consists of a spinel layer with on top one or two disordered atomic layers. **Figure 59** shows a close-up of the (200) facet from the pristine [010] HAADF-STEM image in **Figure 58** together with the models of the layered, spinel and disordered rock-salt structure projected along the same orientation as the [010] HAADF-STEM image. The comparison between the experimental image and the models confirms the formation of the spinel structure with on top a disordered layer. The higher intensity at the surface of the (200) facet can be associated with the higher amount of transition metals present in the spinel structure: the spinel structure $Li(TM)_2O_4$ contains a higher concentration of TM relative to oxygen and lithium than in the main structure $Li_{1.2}(TM)_{0.8}O_2$. Also the surface at the (20$\bar{2}$) facet has a much higher intensity caused by transition metals occupying the lithium positions in the lithium layer. In contrast to the ordered spinel structure at the (200) facet, the

surface layer at the $(20\bar{2})$ facet tends to form a rock-salt-like disordered structure, which is also illustrated in **Figure 59**. Such structural modifications at the surface were also reported by Shukla *et al.* in other pristine LMR-NMCs [100].

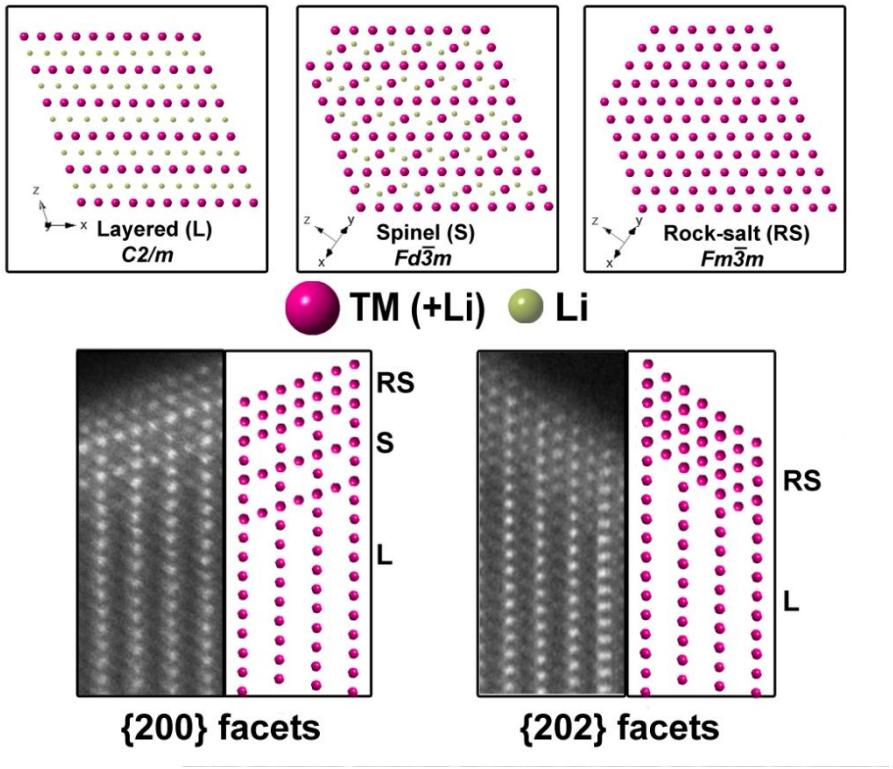

Figure 59. *Top: The models of the layered, spinel and disordered rock-salt structure projected along the [010] orientation, which is equivalent to the [-1-10] orientation in the spinel and rock-salt structures. Only TM and Li are shown in order to simplify the models. In the HAADF-STEM image, only the TM positions will be clearly visible. The models should be rotated over 90° in order to compare them to the experimental image. The surface of the (200) facet consists of a spinel layer with on top two disordered layers. The surface of the (202) facet corresponds to a disordered rock-salt-like structure.*

After 50 cycles, the [010] SAED pattern shows extra diffuse reflections, which are marked by arrows in **Figure 58**. These extra reflections can only be indexed using a spinel structure. In both the pristine and cycled sample, the SAED pattern is taken from the entire particle. In the pristine sample, the contribution of the spinel structure at the {200} facets is very small compared to the entire volume of the particle, and therefore the spinel reflections do not appear in the SAED pattern of the pristine crystals. The appearance of the spinel reflections in the cycled sample indicates that the volume-ratio of the spinel compared to the layered structure has significantly increased. The HAADF-STEM image, taken from that particle, shows that indeed the thickness of the spinel layer at the surface increased to approximately $1.7 - 2.2$ nm.

Since this is only slightly thicker than before, probably the extra reflections also originate from spinel in the bulk. To investigate the element distribution, line profiles were taken from the (200) and (20$\bar{2}$) facets (**Figure 60**) that show a reduction of the Ni- and Co-segregation, respectively. According to the line profiles, segregation is only present at the (200) facet. While in the pristine sample, only Ni-segregation was observed at the (200) facet, with an increase of more than 10 at% compared to the bulk (line profile 1 in **Figure 56**), both Ni- and Co-segregation occur in the cycled sample, but both with an increase of only approximately 5 at% compared to the bulk (line profile 1 in **Figure 60**). Most probably the transition metal migration that occurs upon cycling redistributes the elements at the surface.

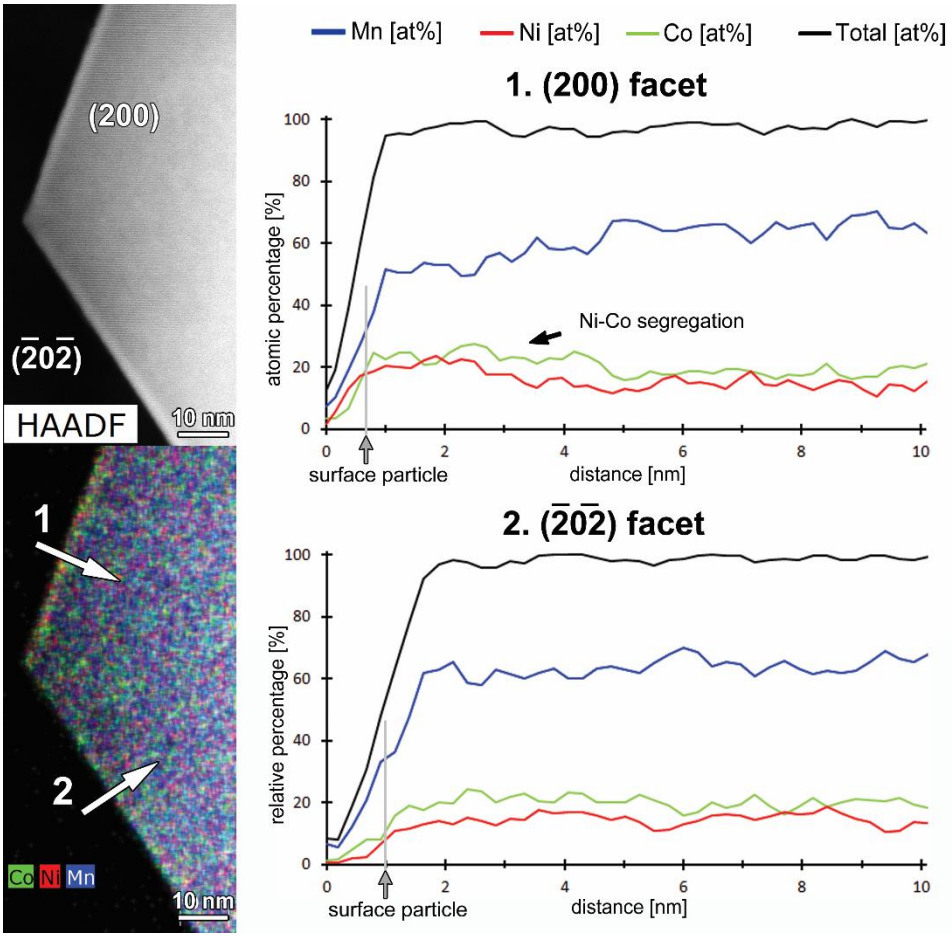

Figure 60. *Left: HAADF-STEM image and corresponding EDX map, given in counts of the cycled solution-gel sample. Right: line profiles taken perpendicular to the (200) (i.e. line profile 1) and (20$\bar{2}$) (i.e. line profile 2) facets. The EDX map show Ni and Co segregation at the (200) facet. The line profile of the (200) facet confirms the segregation. The transition metal concentrations decrease gradually at the surface, which can be attributed the radiation damage at the surface.*

6.2.2. Discussion

This study showed that the method used to synthesize the $Li_{1.2}Ni_{0.13}Mn_{0.54}Co_{0.13}O_2$ particles also affects the electrochemical performance, as the sample prepared by the solution-gel method exhibits a significant capacity decay compared to the sample prepared by the co-precipitation method. On the other hand, the initial discharge capacity of the solution-gel sample is higher and the voltage is much more stable upon cycling than for the co-precipitation sample. The observed electrochemical properties can be explained by the differences in both the morphology as well as in the atomic structure, observed by the TEM study.

The particles prepared by the solution-gel method are much smaller, ranging from 100 to 480 nm, compared to the particles obtained by the co-precipitation method, of which the size varies between 250 nm and 2 μm. Our results of the particle size and electrochemical properties are consistent with the study of Santhanam *et al.* [98] where the morphology of the $Li_{1.05}Ni_{1/3}Mn_{1/3}Co_{1/3}O_2$ sample prepared by the SG and CP methods is compared. Santhanam *et al.* suggest that for nanoparticles, the rate capability is expected to improve due to the higher surface area for charge transfer and the shorter diffusion length, but that, on the other hand, the high surface area implies a high surface reactivity, which can lead to an increase of detrimental surface side-reactions and poor inter-particle electrical contact. The solution-gel sample delivers a higher capacity in the first cycle than the co-precipitation sample, which can be ascribed to the higher kinetics due to the higher surface area; however, the capacity drastically decreases during extended cycling, which is not the case in the co-precipitation sample. The good capacity retention in the latter sample can be partially attributed to the decreased side-reactions with the electrolyte, which is related to the lower surface area.

The TEM study also revealed structural modifications at selective surface planes in case of the solution-gel method, where a Ni-rich surface layer is present at the {200} facets that adopts a spinel structure, while a Co-rich surface layer is observed at the {002} and $\{20\bar{2}\}$ facets, which tends to form a rock-salt-type structure. The formation of the spinel or the disordered rock-salt structure at the very surface of the particle essentially cuts off the lithium transport paths, making the lithium in the particle inaccessible along these particular facets, which leads to both voltage fade and capacity fade [101,102]. On the other side, as the spinel structure is highly stable, the Ni-rich spinel layer can also be considered as a protective surface layer that slows down the surface corrosion and structure degradation, which can reduce the voltage fade. This

might explain the slightly lower voltage fade observed for the solution-gel sample. However, the HAADF-STEM images of the cycled solution-gel sample clearly show the growth of the spinel structure at the surface during cycling. The thickness increased from ~1.5 nm to 1.7−2.2 nm [102–104]. During the formation of the spinel, oxygen loss will occur as the ratio between the transition metals and oxygen is 2:4 (TM:O) instead of 2:5 in $Li_{1.2}(TM)_{0.8}O_2$, which is partially responsible for the voltage plateau.

In addition to what was found by Santhanam *et al.* [98], it can be concluded that not only the particle size but also the surface modifications contribute to the electrochemical performance. The segregation of Ni and Co at selective surface facets of $Li_{1.2}Ni_{0.13}Mn_{0.54}Co_{0.13}O_2$ agrees with that reported by Yan *et al.* [104]. Similar to our results, Yan *et al.* [104] found that Ni is exclusively segregated at the {200} surfaces and adopts a spinel structure, while Co predominately enriches the $\{20\bar{2}\}$ and {002} facets with a rock-salt-like structure. However, in their case, the Co-rich surface layer demonstrated a zigzag-shaped surface, whereas in our case, no pronounced zigzag-shaped surface was observed. In literature, the appearance of Ni- and Co-segregation was also observed for samples prepared by the CP method [104,105], while our results show that it only occurs for the particles synthesized by the SG method. In our study, carbonate co-precipitation was used, while the syntheses used in the references [104] and [105] are based on hydroxide co-precipitation, which might be responsible for the differences in obtained results.

According to this study about the comparison of syntheses, we can conclude that our applied co-precipitation route is a better method, structural and electrochemical properties wise, than our applied solution-gel route to synthesize $Li_{1.2}Ni_{0.13}Mn_{0.54}Co_{0.13}O_2$. The structure is homogeneous without surface modifications, and the specific capacity is relatively stable. On top of that, the co-precipitation method ensures a pure phase, whereas the solution-gel method showed the presence of Co-rich impurities. Unfortunately, the $Li_{1.2}Ni_{0.13}Mn_{0.54}Co_{0.13}O_2$ sample prepared with the co-precipitation method suffers slightly more from voltage fade. As the voltage fade is most likely related to TM migration and phase transitions that occur upon cycling, we investigate the structure evolution of the $Li_{1.2}Ni_{0.13}Mn_{0.54}Co_{0.13}O_2$ sample synthesized by the co-precipitation method into more detail in the following section.

6.3. Co-precipitation: Crystal structure of LMR-NMC

The structure of the pristine, charged (first charge only) and cycled $Li_{1.2}Ni_{0.13}Mn_{0.54}Co_{0.13}O_2$ will be investigated. The cycled sample was charged and discharged 100 times and studied in its final discharged state.

6.3.1. Experimental results and discussion

The SAED patterns corresponding to the pristine, charged and cycled sample of $Li_{1.2}Ni_{0.13}Mn_{0.54}Co_{0.13}O_2$ are shown in **Figure 61**. The brightest reflections in all the SAED patterns could be indexed by the monoclinic layered structure with the *C2/m* symmetry, consistent with the O3-type layered structure without noticeable stacking faults in the close-packed arrangement of the oxygen layers.

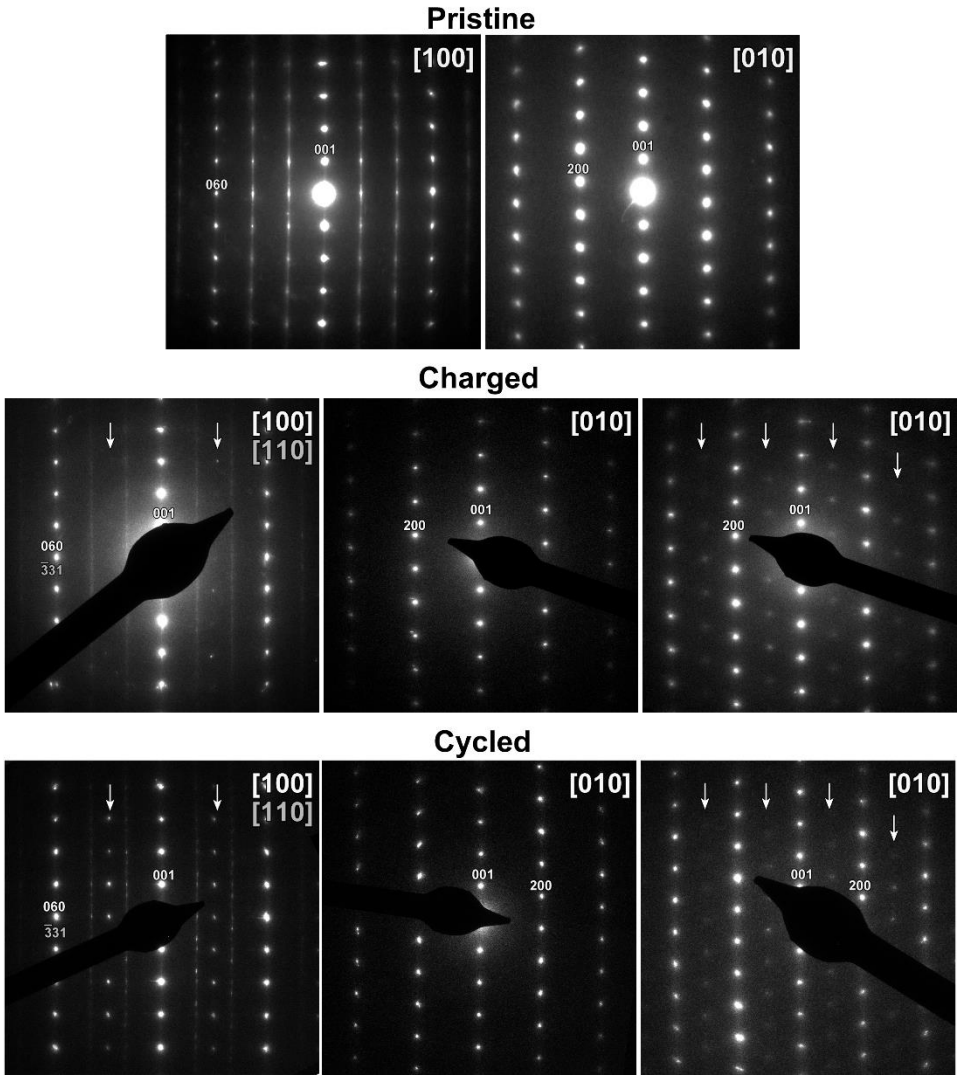

Figure 61. *SAED patterns of (top) the pristine, charged (middle) and cycled (bottom) sample along the [100] and [010] zones, where the arrows mark the extra reflections originated from the spinel structure.*

In the charged and cycled samples, reflections originating from regions with a spinel structure are also present, indicated by arrows in the [100]/[110] and [010] diffraction patterns.

For the pristine sample, the HAADF-STEM and ABF-STEM images along the [010] orientation are shown in **Figure 62**. The intensity of the atom columns in the HAADF-STEM image is proportional to the atomic number of the elements, and so the bright dots in the HAADF-STEM image correspond to the transition metal atom columns. Lithium and oxygen are too weak to clearly observe their atom columns in the HAADF-STEM images. The inset in the [010] HAADF-STEM image shows the outline of a few unit cells as corresponding to the *C2/m* space group. In order to directly visualize the O3 cubic close-packed sequence of the oxygen layers, an ABF-STEM image along the [010] orientation was acquired, where the intensity is proportional to $Z^{1/3}$ and thus more sensitive to elements with low Z compared to HAADF-STEM, and the image confirms the O3-type stacking (remember that on the ABF-STEM images the atom columns are seen as the dark dots).

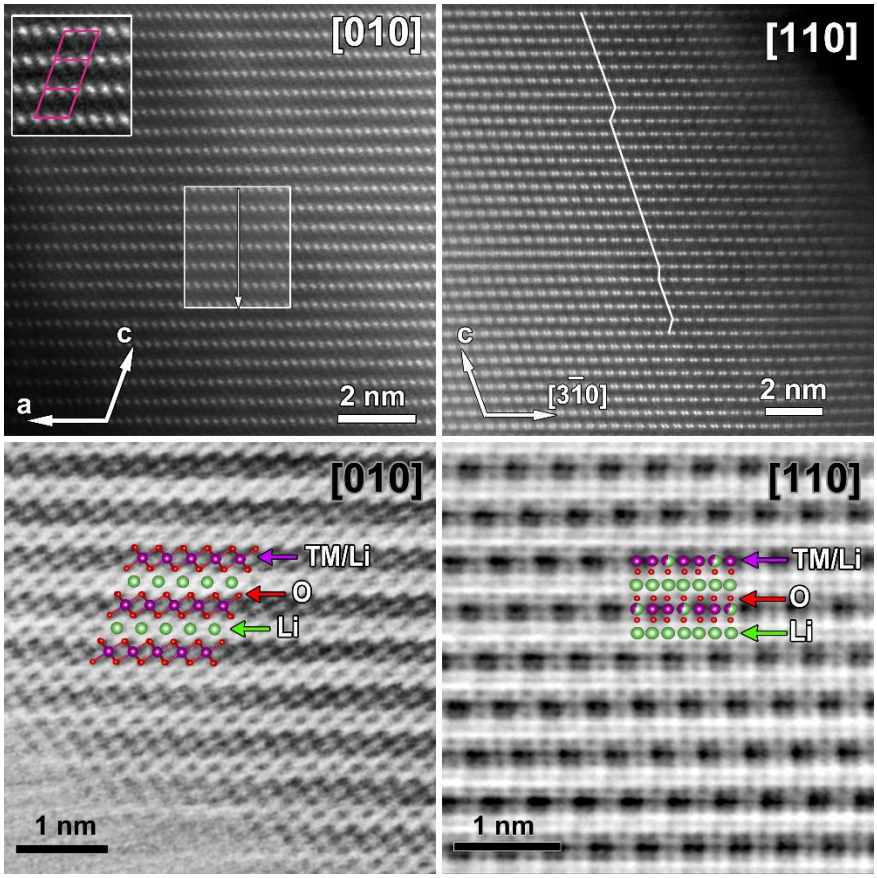

***Figure 62**. The pristine LMR-NMC sample. Top: HAADF-STEM images along the [010] and [110] orientations. The inset shows the unit cell of the structure, and the rectangle marks the area of which a line profile has been taken, which is shown in Figure 68. The white line in the [110] image shows the honeycomb stacking. Bottom: ABF-STEM images along the [010] and [110] orientations, confirming the C2/m symmetry.*

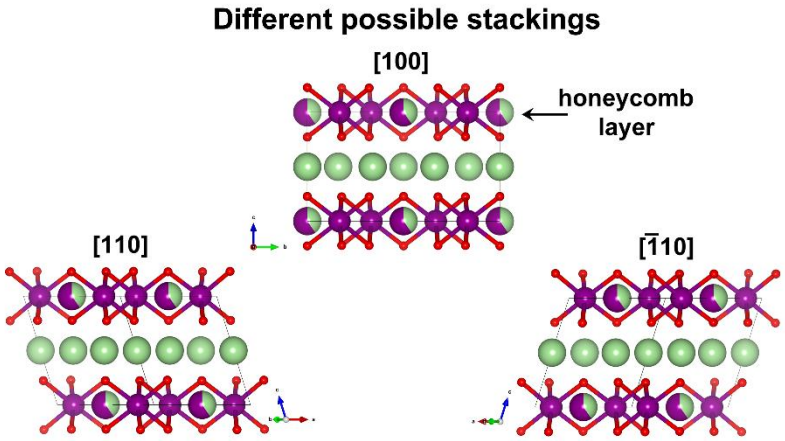

Figure 63. *A schematic model of Li-rich NMC along the [100], [110] and [-110] orientations, where the green, purple and red atoms represent Li, TM and oxygen, respectively. The three different zones show each a different projected stacking of the Li-TM layers.*

The [100]/[110] SAED patterns of the three different samples are characterized by sharp reflections (*hkl*) with $k = 3n$ and diffuse weaker spots in the $k \neq 3n$ reciprocal rows that originate from the stacking of the honeycomb layers (i.e. Li-TM layers). In **Figure 63**, the different possible stackings of the honeycomb layers are shown and their simultaneous occurrence, as stacking faults, will give rise to diffuse streaks along the $k \neq 3n$ reciprocal rows. The HAADF-STEM and ABF-STEM image along the [100]/[110] orientation of the pristine sample are shown in **Figure 62** and **Figure 64**. In the [110] HAADF-STEM images, the honeycomb ordering manifests itself by a prominent pattern of pairs of bright dots (i.e. atom columns of transition metals) and less bright dots (i.e. atom column containing both Li and transition metals) in between, which is illustrated by the blue line profile in **Figure 64**. The orange line profile is also taken from a Li-TM layer, but shows a less pronounced pattern for honeycomb ordering, indicating that this layer is partially disordered. Further, the green line profile reveals the presence of a few transition metals in the lithium layer. It shows that also the pristine material can contain initial structural defects, but these structural defects are only present in a low amount. The HAADF-STEM images and the SAED pattern along the [100]/[110] orientation of the pristine sample show that stacking faults are present in the honeycomb ordered cation pattern. The particle studied in **Figure 62** demonstrates a dominant stacking corresponding to the [110] domains in the current viewing direction, with only a few stacking faults (3 stacking faults in 32 Li-TM layers ~ 9.4%). However, the TEM study performed on different particles has shown that the amount of stacking faults can vary from particle to particle.

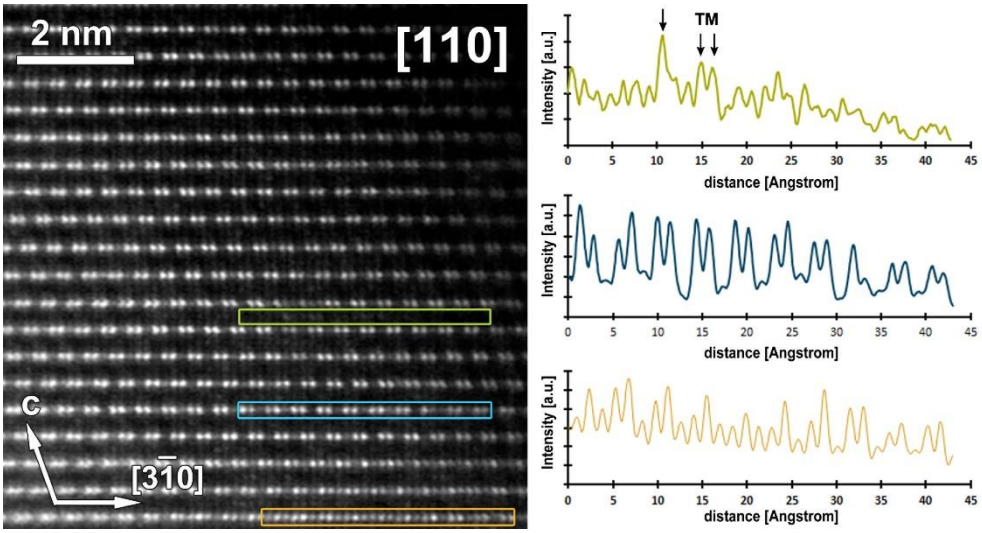

Figure 64. *The pristine LMR-NMC sample. Left: HAADF-STEM image along the [110] orientation. Right: line profiles taken from the Li layer (green line profile) or the honeycomb layer (blue and orange line profiles). The blue line profile represents the honeycomb ordering pattern. The structure does show disorder in the honeycomb layers (orange line profile) and a low amount of TM migration towards the Li layers (green line profile).*

The extra reflections in the [100]/[110] and [010] SAED patterns that originate from the formation of a spinel structure become stronger in the cycled sample which means that the TM migration that occurs during charging is partially irreversible and forms a spinel structure that grows with the number of cycles. In both the charged and cycled sample, [010] SAED patterns were found with and without the extra reflections that correspond to the formation of the spinel structure, showing that different particles do not degrade to the same amount during electrochemical cycling. To understand how these structural changes proceed, high-resolution STEM images were acquired from the charged and cycled samples, which are compared to the pristine reference sample.

The HAADF-STEM images of the charged sample in **Figure 65** prove that the TM migration occurs during charging. Transition metals were observed in the empty octahedral positions in the lithium layers (bright dots marked by yellow arrows with annotation 'TM') as well as in the tetrahedral interstices between the layers (bright dots encircled in pink with annotation 'TM'). This can be explained by the diffusion path of the transition metals. In order to migrate towards the lithium layers, the transition metals have to pass the tetrahedral holes, the so-called O-T-O diffusion path, where they can get trapped. No atoms are observed in the lithium layers in the ABF-STEM image in **Figure 65**, confirming that the lithium is extracted from the structure, which subsequently enables the TM migration. Moreover, at the surface, the TM migration leads to the formation of the spinel structure.

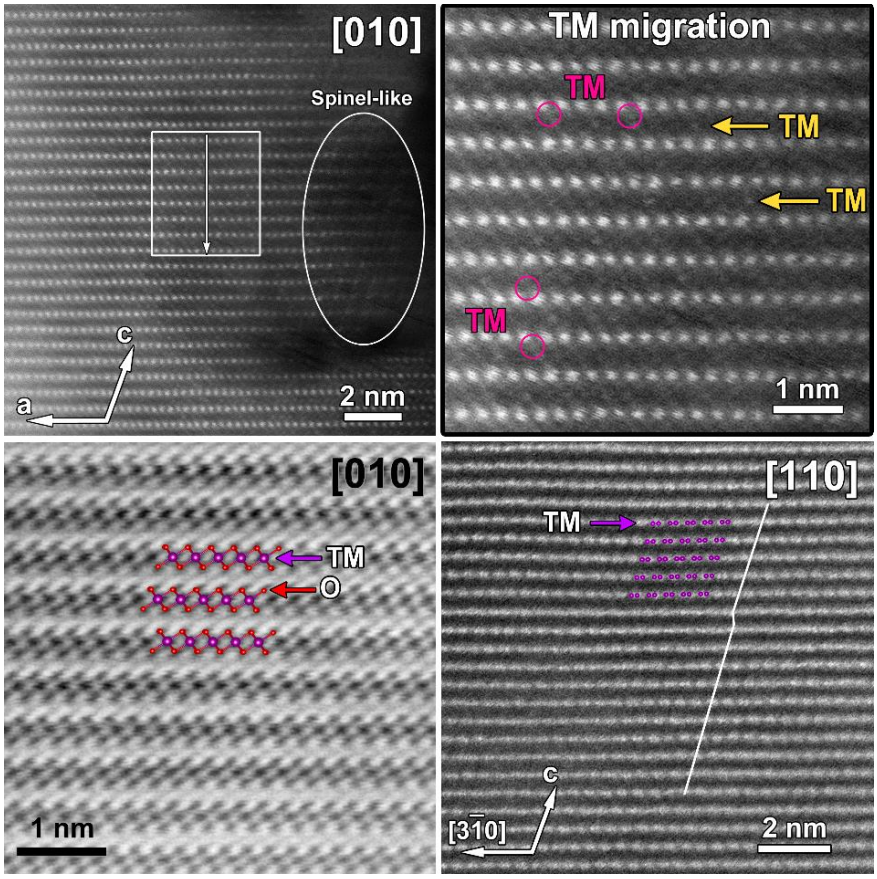

Figure 65. *The charged sample. Top: HAADF-STEM image along the [010] orientation; left: the rectangle marks the area of which a line profile has been taken that is shown in Figure 68. At the surface, the structure has changed to a spinel-like structure; right: a close-up, where TM migration is observed. The yellow arrows show TM in the empty Li positions, while the pink circles indicate TM in the tetrahedral holes between the two layers. Bottom: left: ABF-STEM image along the [010] orientation. The lithium atoms are not visible since they left the structure upon charging; right: HAADF-STEM image along the [110] orientation, in which the white line marks the stacking of the Li-TM layers.*

In several areas in the [110] HAADF-STEM image in **Figure 65**, the characteristic ordering patterns in the Li-TM layers have become unclear, meaning that the Li-TM layers in these regions are highly disordered, which is also caused by the delithiation followed by TM migration.

In addition, some particles demonstrate the presence of domains with seemingly different ordering, as shown in **Figure 66**, where a domain in [010] orientation (region 2) neighbours a domain in [101] orientation (region 3). In region 3 also a narrow stretch with different ordering pattern can be seen. This can be explained by the model shown at the bottom of **Figure 66**. When no stacking-faults are present, the structure viewed along the [101] orientation looks like a deformed honeycomb pattern, where the slightly darker columns, partially occupied by TM (only 1/3; the 2/3 Li is removed in the charged state) are surrounded by six atom columns fully

occupied by TM. When the structure contains stacking-faults, the different atom columns will overlap, and the intensity distribution of all the atom columns becomes homogeneous. In the HAADF-STEM image, the differences in the ordering pattern within region 3 can thus be explained as due to regions with and without stacking-faults. The presence of such domains with different orientations was also found in the pristine sample. (For the pristine sample, no clear HAADF-STEM images of the interface between the domains were obtained.) These domains are orientation twins that arise when the symmetry lowers from the cubic rock-salt structure ($Fm\bar{3}m$) to the layered monoclinic ($C2/m$) structure (most probably during the synthesis), as these orientations are equivalent in the cubic structure. The occurrence of orientation twins in Li-rich NMCs has already been reported by Jarvis *et al.* [106], and Shukla *et al.* [100].

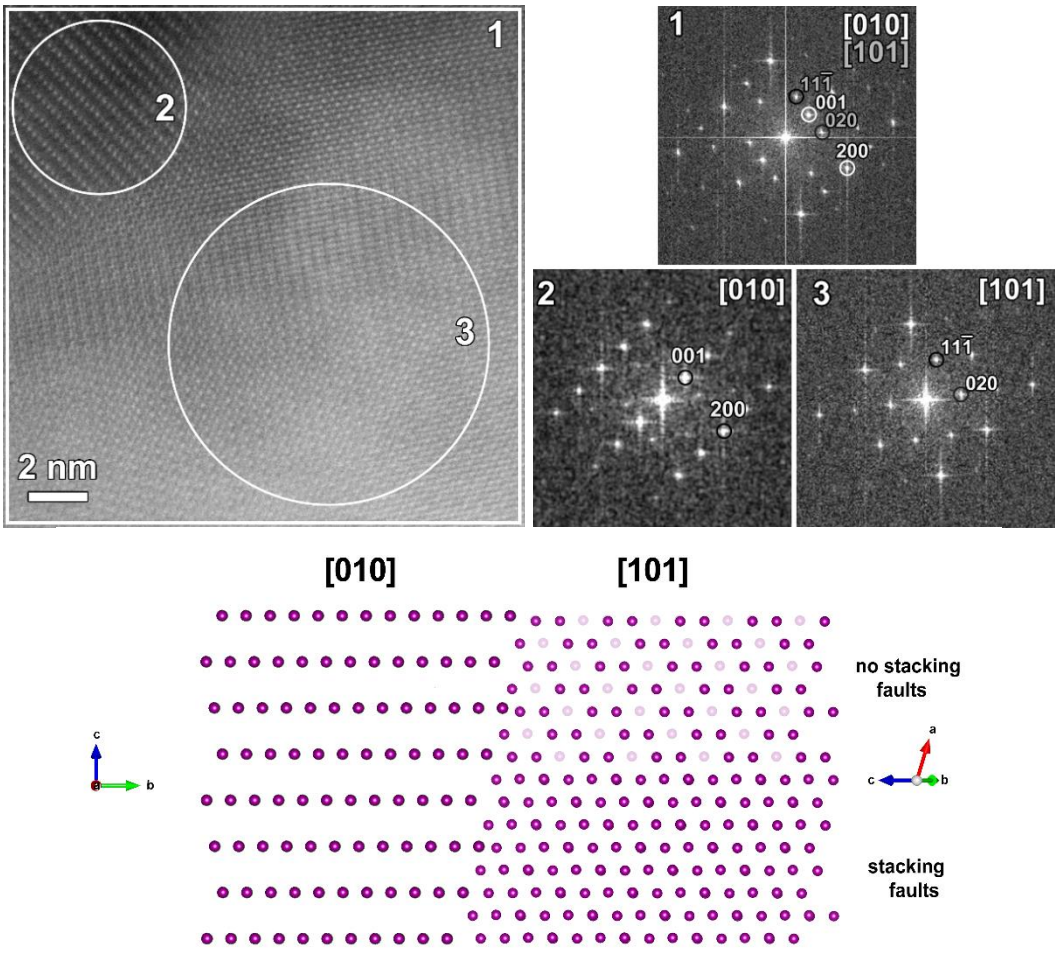

Figure 66. *Top: the charged sample. Left: HAADF-STEM image showing different domains. Right: the corresponding FFTs of the areas marked in the HAADF-STEM image. The FFTs of areas 2 and 3 correspond to the zones [010] and [101], while the FFT of area 1 is a mixture of both. Bottom: simulation of the model along the [010] and [101] orientation. In the [101] orientation, the blurred atoms correspond to the positions that are partially occupied by TM (only 1/3 TM). When stacking-faults are present, these positions will overlap with positions that are fully occupied with TM.*

The formation of these orientation twins most likely affects the diffusion paths and thus, the electrochemical properties of the LMR-NMC. Jarvis *et al.* [106] suggest that these domains result in pseudo-3D paths instead of 2D paths that would be favourable for lithium diffusion, but that the overall lithium diffusion is inhibited due to a build-up of Ni at the interface between these domains. Further, they also claim that the domain formation that arises from a disorder-to-ordered phase transition (i.e. from cubic rock-salt to layered monoclinic) is only formed in layered oxides containing nickel. On the contrary, our TEM study on Li_2MnO_3, which is discussed in **Chapter 8**, shows a SAED pattern (**Figure 85D**) that demonstrates the coexistence of the [010] and [101] domains in a single Li_2MnO_3 particle, indicating that it also occurs in layered Li-rich manganese-based oxides that do not contain nickel. In our case, we did not observe an increased Ni content at the interface between the domains for LMR-NMC. We suggest that the lithium diffusion paths of particles consisting of many domains next to each other are disturbed, which will eventually hinder the fast lithium diffusion that is required for these cathode materials. The domains with the [010] orientation have 2D planar lithium diffusion paths, while the [101] domains only have 1D lithium diffusion paths in this same plane if no stacking faults are present; stacking faults will block even these 1D paths. Consequently, these domains cannot contribute to the charging and discharging process of the material, which might explain the lower specific discharge capacity observed for the co-precipitation sample than observed for the solution-gel sample, where no such twins were observed.

When the structure is discharged, the lithium and the transition metals should move back to their initial positions; however, the HAADF-STEM images in **Figure 67** reveal that the TM migration is only partially reversible, leading after 100 cycles to a permanent spinel structure at the surface. The surface changes to a spinel structure, as shown in the [010] HAADF-STEM images. The thickness of the spinel layer increases with every cycle, while the bulk structure preserves the *C2/m* symmetry. The close-up HAADF-STEM image in **Figure 67** clearly shows the irreversible TM migration towards the Li positions at the surface (bright dots marked by yellow arrows with the annotation 'TM'). TM migration towards the tetrahedral positions is not significant (bright dots encircled in pink with the annotation 'TM'). The homogeneous intensity in the Li-TM layers in the [100] HAADF-STEM image implies disorder, which is significantly increased compared to the pristine sample.

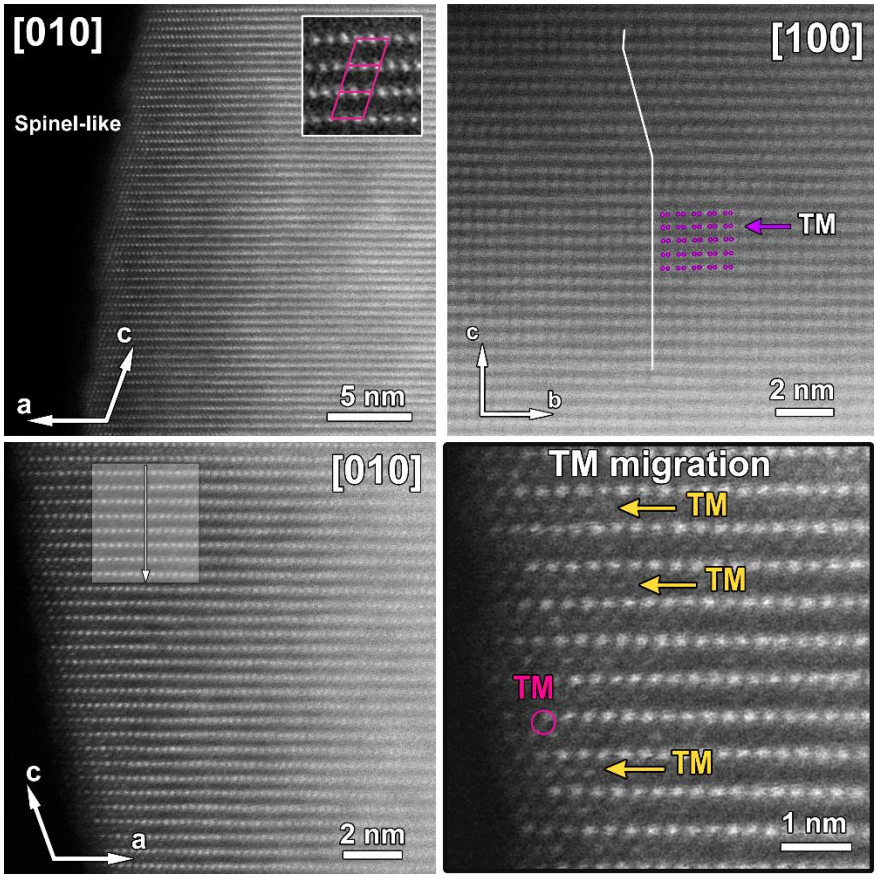

Figure 67. *HAADF-STEM images of the cycled sample. Left: HAADF-STEM images along the [010] zone where the surface has changed to a spinel-like structure. The shaded rectangle indicates the area over which a line profile is taken, which is shown in Figure 68. A close-up is shown at the bottom right, where the yellow arrows show the TM atoms in the Li layer and the pink circle shows TM in the tetrahedral hole between both layers. Top right: HAADF-STEM image along the [100] orientation. The white line marks the stacking of the honeycomb layer.*

In order to analyse the amount of TM migration at both the Li positions and the tetrahedral positions, line profiles were taken perpendicular to the layers in the HAADF-STEM images along the [010] orientation from the pristine, charged and cycled sample, marked in respectively **Figure 62**, **Figure 65** and **Figure 67**. The line profiles are shown in **Figure 68**. The peaks in the experimental data are fitted by Gaussian functions using the program Fityk [43]. All the peaks corresponding to the Li-TM layers (peaks represented by "TM layer") are refined with the same full width half maximum (FWHM). Since the lithium atoms (Z = 3) are not visible in the HAADF-STEM images, the peaks observed in the lithium layers (peaks represented by "Li layer") entirely originate from the presence of transition metals. Therefore, these peaks are refined with the same FWHM as the peaks in the TM layers. The intensity of

these peaks provides information about the amount of TM migration towards the lithium layer. The peaks corresponding to the position between these two layers correspond to either the oxygen positions or the empty tetrahedral holes, which means that these peaks can give information about the number of transition metals trapped in the tetrahedral holes. Oxygen atoms (Z = 8) are commonly expected to be too light to visualize clearly in HAADF-STEM images due to the contrast $I \sim Z^2$; however, if the other elements also have low atomic numbers, such as Mn (Z = 25), Co (Z = 27) and Ni (Z = 28), the oxygen atoms might contribute to the intensity of these peaks. This conjecture is also supported by the line profile of the pristine sample, where clear peaks were observed at these positions, while in the pristine structure no transition metals are expected at the tetrahedral positions. In order to verify the actual contribution of oxygen to these peaks, HAADF-STEM simulations have been made to compare the line profiles to the experimental data.

HAADF-STEM images along the [010] orientation were simulated with the program QSTEM [107] with three different thicknesses: 27 Å, 98.5 Å and 170 Å shown in **Figure 69**. The line profiles reveal the significant contribution of the oxygen atom columns to these peaks, where the intensity increases concomitantly with increasing thickness. On the other hand, the intensity of these peaks will also be affected by the number of transition metals trapped in the tetrahedral holes. Therefore, HAADF-STEM images were simulated with 0%, 5% and 10% Mn of the total amount of transition metals that are migrated towards the tetrahedral holes, using a constant thickness of 98.5 Å. The peak intensity significantly increases together with increasing the occupancy of the tetrahedral holes. Unfortunately, combining both the variation in thickness and the occupancy makes it impossible to derive the correct amount of TM migration towards the tetrahedral holes, and one can only suggest their presence based on variations in brightness among the peaks themselves.

In addition, HAADF-STEM images were simulated with 0%, 5% and 10% of the total amount of transition metals that are migrated towards the lithium layers, using a constant thickness of 98.5 Å (**Figure 70**). The simulations show that TM migration lower than 5% will be difficult to detect; especially when the thickness increases and the intensity of the neighbouring peaks increases due to the contribution of the oxygen atom columns

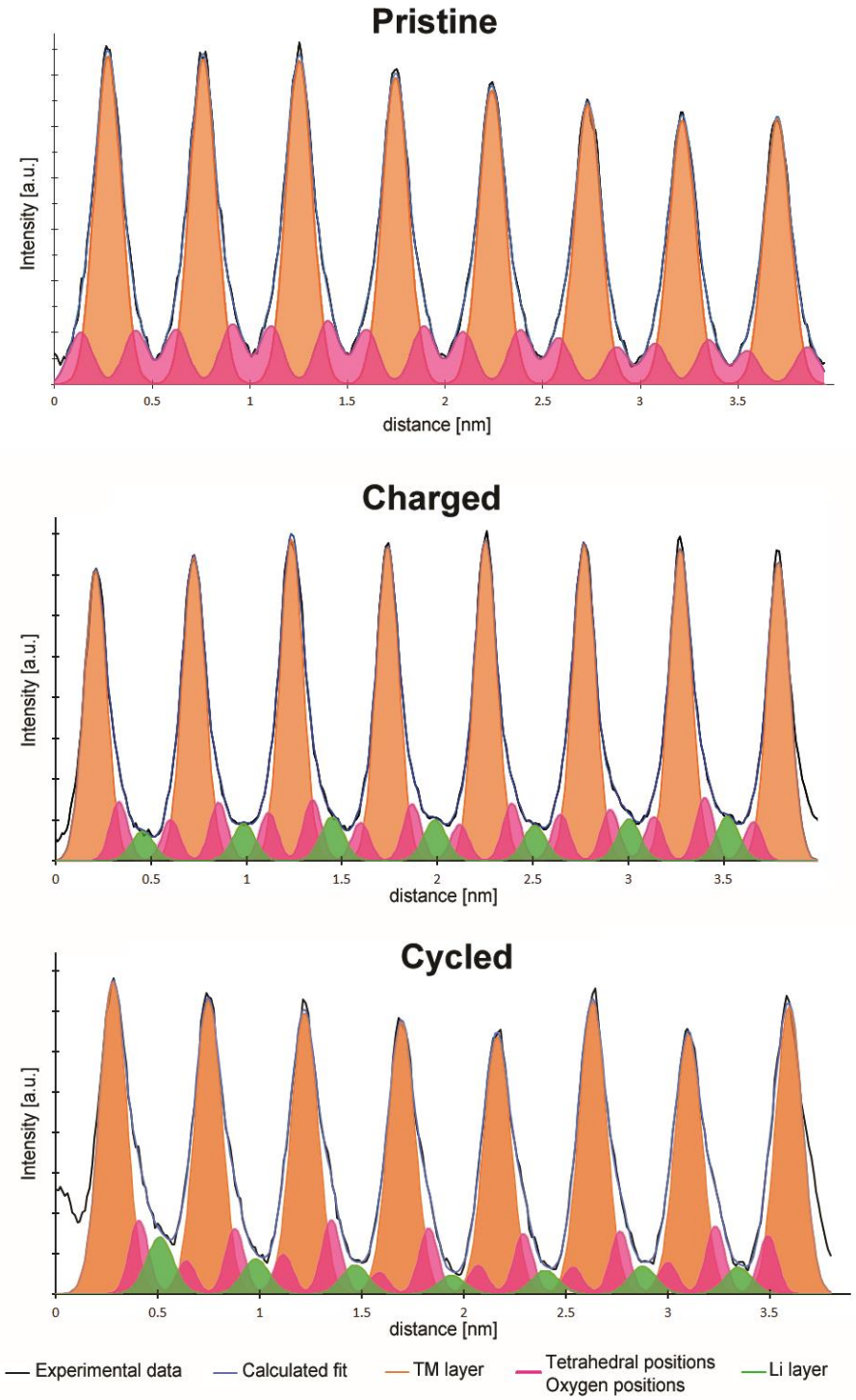

Figure 68. *Line profiles of the pristine, charged and cycled samples. The regions, of which the line profiles are taken, are marked in Figure 62, Figure 65 and Figure 67. The experimental line profile is fitted by Gaussian functions with Fityk [43].*

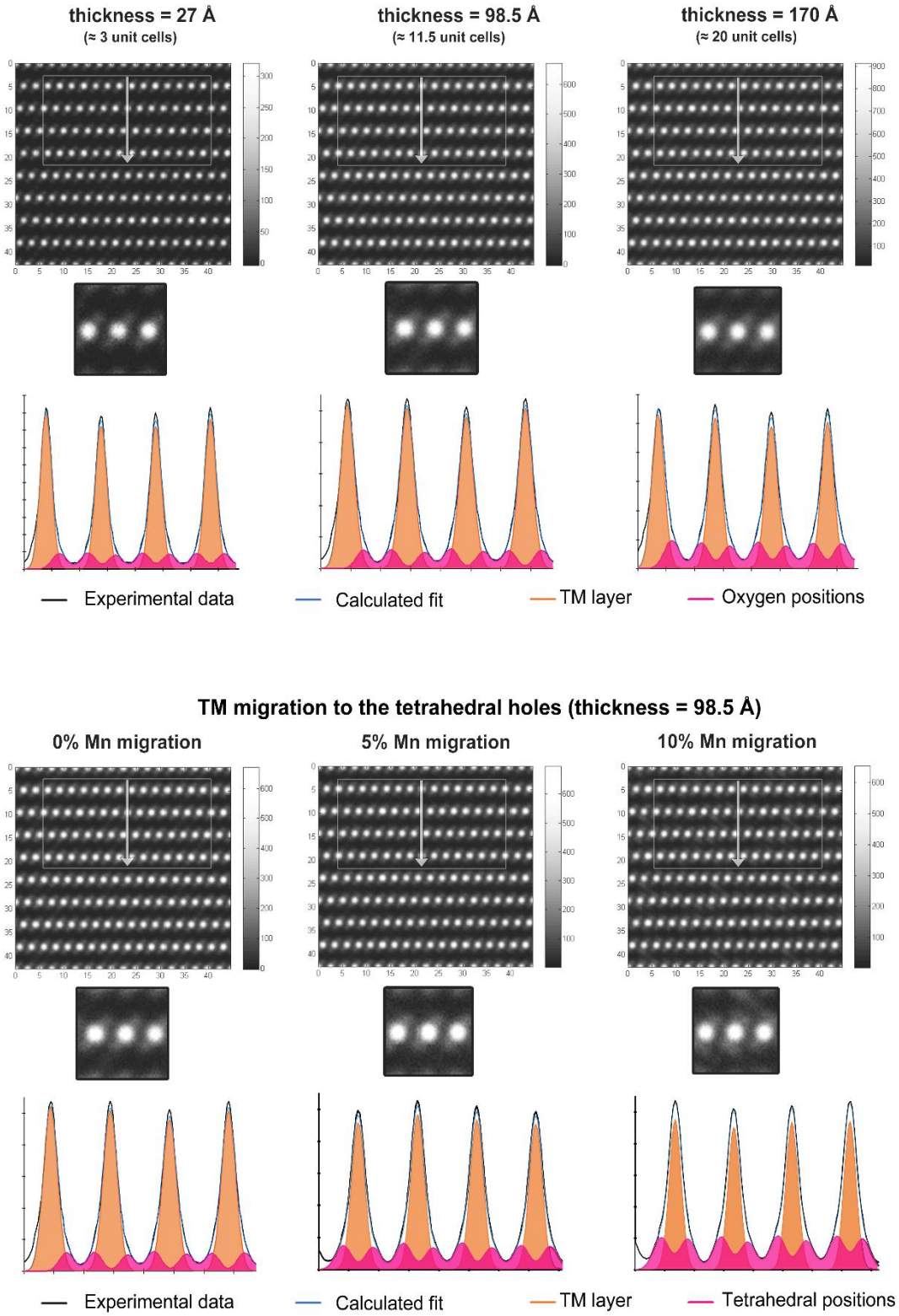

Figure 69. *Top: simulation of the HAADF-STEM image along the [010] orientation of the pristine structure for three different thicknesses. Bottom: similar simulations for one thickness, where the Mn migrations varies with 0%, 5% and 10%. In the model, Mn atoms are added in the tetrahedral positions, while the same amount of Mn is removed from the honeycomb layer. The HAADF-STEM images are simulated by using QSTEM [100].*

Taking into account the result of the simulations, we conclude that the pink peaks in the line profile of the pristine sample arise from the oxygen atoms in the structure and that there is no evidence of transition metals in the lithium layer for that sample. In the charged sample, a significant amount of transition metals are observed in the lithium layers, which is expected due to the migration of transition metals when delithiation occurs. This, in contrast to the cycled sample, where ideally no transition metals should be observed in the lithium layer. The HAADF-STEM image of the cycled sample (**Figure 67**) showed the transition to the spinel structure at the surface, but the line profile is taken at a slight distance from the surface, similar to the line profiles taken from the charged and pristine sample in order to have a better comparison. From the line profile of the cycled sample, it seems that the number of transition metals present in the lithium layer is lower compared to the charged sample, showing that part of the migration is still reversible; however, a significant part of the transition metals are still trapped in the lithium layer. Note that this is an assumption as we do not know the exact thickness of the areas from which the line profiles were taken. Furthermore, for the cycled sample, the intensity of the peaks at the oxygen positions and tetrahedral holes varies significantly. Most likely this is due to a slight misalignment of the HAADF-STEM image because the intensity varies in a periodic way that can be caused by a small misorientation of the atom columns. However, we cannot exclude structural changes such as oxygen release (lower peaks) or transition metals trapped at the tetrahedral holes (higher peaks).

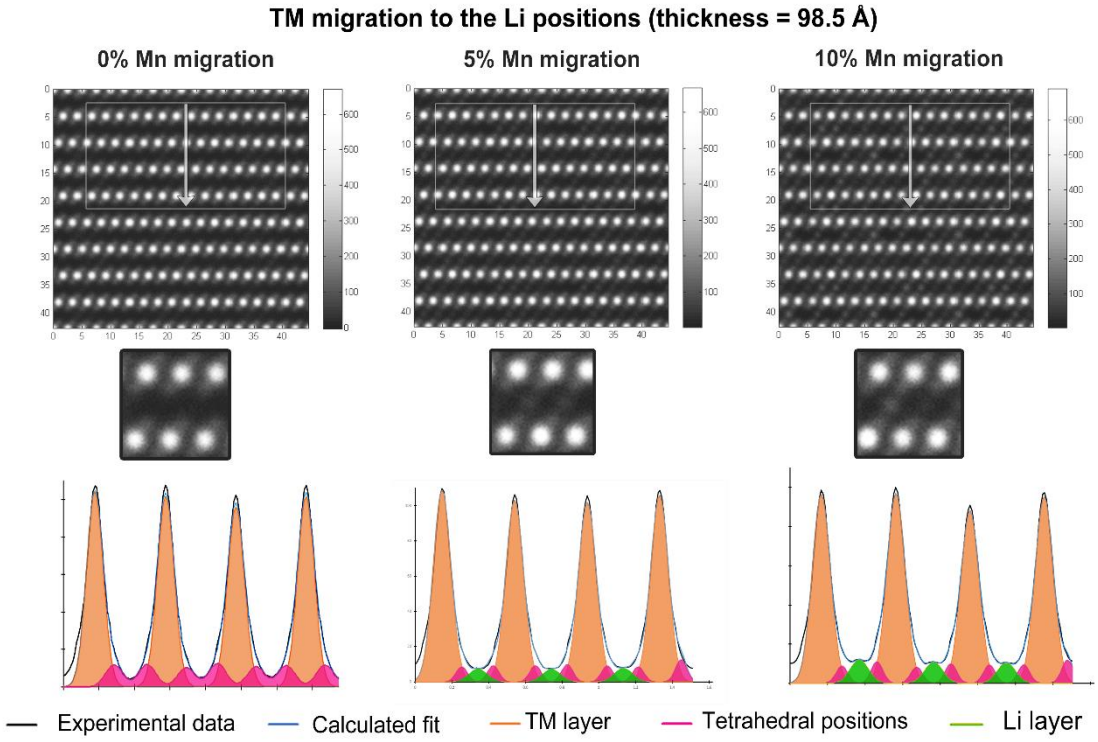

Figure 70: *similar simulations for one thickness, where the Mn migration varies with 0%, 5% and 10%. In the model, Mn atoms are added in the octahedral lithium positions, while the same amount of Mn is removed from the honeycomb layer. The HAADF-STEM images are simulated by using QSTEM [107].*

6.4. Conclusion

In the first part of this chapter, we showed that the electrochemical performance not only depends on the composition but that also the synthesis method affects the electrochemical performance. The synthesis method has an influence on the morphology, which plays an important role in the electrochemical performance. This study showed that the particles synthesized by the solution-gel method are smaller than the particles synthesized by the co-precipitation method. By comparing our observation to the electrochemical performance, we were able to conclude that the significant capacity drop observed in the solution-gel method is most likely partially related to the higher surface area which increases the surface side-reactions with the electrolyte. Moreover, our TEM study also revealed surface modifications at selective facets in the solution-gel sample that were not present in the co-precipitation sample. The surface at the {200} facets adopts a Ni-enriched spinel structure of a few atomic layers that grows with the number of cycles. The surface at the {002} and {202} facets possesses Co-segregation and has a disordered rock-salt-like structure. As the electrochemical properties of the solution-gel sample are worse than the properties observed for the co-precipitation sample, we can conclude that these structural modifications are not beneficial for the cathode material, and can only act as a barrier for Li diffusion at the surface. Consequently, we can conclude that our applied co-precipitation route is a better method, structural and electrochemical properties wise, than our applied solution-gel route to synthesize $Li_{1.2}Ni_{0.13}Mn_{0.54}Co_{0.13}O_2$. The structure is homogeneous without surface modifications, and the specific capacity is relatively stable.

The Li-rich, Mn-rich NMC synthesized by the co-precipitation method suffers from voltage fade. We suggested that the observed voltage fade is caused by transition metal migration and phase transition to the spinel structure upon cycling. Our TEM study indeed showed that part of the TM migration is irreversible, leading to the formation of a spinel structure. The HAADF-STEM images clearly show a high degree of phase transition to spinel and/or rock-salt at the surface. For the charged and cycled sample, SAED patterns existed both with and without the extra reflections corresponding to the spinel phase (the rock-salt reflections overlap with existing reflections), showing that different particles do not degrade to the same amount during electrochemical cycling. Furthermore, we also observed the formation of orientation twins in the co-precipitations sample, which was not present in the solution-gel sample. These domains

might hinder the Li diffusion paths, which might be the cause of the lower specific capacity observed in the co-precipitation sample than in the solution-gel sample.

Finally, we also want to emphasize the complexity of examining the structural changes that are directly related to the charging and discharging of the material. The TEM study showed that the amount of stacking faults can vary from particle to particle and that the pristine sample can contain initial randomly distributed structural defects. As we cannot investigate, with current existing techniques, the same particles in the pristine, charged and cycled state, no knowledge is available about the pre-existing condition of any of the structural features prior to the charging or cycling.

Chapter 7. Sn-substitution in LMR-NMC

This section is based on the paper:

A. Paulus, **M. Hendrickx**, M. Bercx, O. Karakulina, M. Kirsanova, D. Lamoen, J. Hadermann, A. Abakumov, M. K. Van Bael and A. Hardy. *An in-depth study of Sn substitution in Li-rich/Mn-rich as a cathode material for Li-ion batteries.* Dalton Trans, 2020, 49, 10486 [108]

7.1. Introduction

$Li_{1.2}Ni_{0.13}Mn_{0.54}Co_{0.13}O_2$ demonstrates a high reversible capacity exceeding 250 mAh/g, and only part of it (up to 140 mAh/g) originates from the $Ni^{2+} \rightarrow Ni^{3+,4+}$ and $Co^{3+} \rightarrow Co^{4+}$ cationic redox reactions, whereas a significant contribution comes from the reversible anionic redox processes ($2O^{2-} \rightarrow O_2^{n-}$, with $3 > n > 1$) above the potential of ~ 4.5 V vs Li/Li^+ [91,109,110]. As shown in the previous chapter, LMR-NMC suffers from oxygen release and phase degradation, caused by the irreversible anionic redox processes, which is detrimental for the voltage and capacity. Partial substitution of Mn^{4+} is suggested as a viable strategy for stabilizing the layered structure upon cycling in order to prevent TM migration.

Sn^{4+} is believed to act as a structure stabiliser, as Sn^{4+} is not easily reduced to Sn^{2+} and does not tend to adopt tetrahedral coordination [111]. Substitution of Sn^{4+} for Mn^{4+} is, therefore, a potential way to decrease the voltage fade of the LMR-NMC. The substitution of Sn^{4+} for Mn^{4+} has already been reported for Ni-rich NMC ($Li[Ni_{0.82}Co_{0.12}Mn_{0.06}]_{1-x}Sn_xO_2$) [94], LMR-LNMO (Sn-stabilized $Li[Li_{0.17}Ni_{0.25}Mn_{0.58}]O_2$) [111] and LMR-NMC ($Li_{1.2}Ni_{0.13}Mn_{0.54-x}Co_{0.13}Sn_xO_2$) [112]. All the studies showed an enhanced reversible performance, which has been ascribed to the stabilisation of the lattice upon electrochemical cycling. Further, the materials exhibit lower discharge capacities compared to the pristine materials, as expected due to the presence of Sn that preserves its 4+ oxidation state. The significantly larger ionic radius of octahedrally coordinated Sn^{4+} (0.69 Å) than of Mn^{4+} (0.53 Å) [47] will introduce strain, and only a limited percentage of Mn^{4+} is expected to be replaced by Sn^{4+} in order to still retain the structure of the pristine LMR-NMC. On the other hand, its larger size could enhance lithium diffusion as it broadens intercalation pathways [111].

Despite that Sn substitution in LMR-NMC, $Li_{1.2}Ni_{0.13}Mn_{0.54-x}Co_{0.13}Sn_xO_2$ with $x \leq 0.2$ [112], has already been reported in literature, neither a structural investigation probing the Sn substitution limit nor the influence of Sn^{4+} on voltage fade in partially charged LMR-NMC were reported yet.

In this study, we have investigated the Sn concentration in $Li_{1.2}Ni_{0.13}Mn_{0.54-x}Co_{0.13}Sn_xO_2$, where 5% (x = 0.027), 10% (x = 0.054), 20% (x = 0.108) and 100% (x = 0.54) of Mn is replaced by Sn. The samples are studied by using a combination of X-ray powder diffraction (XRPD), transmission electron microscopy (TEM) and calculations within the Density Function Theory (DFT) formalism. The effect of Sn substitution on the voltage fade was determined using galvanostatic cycling. The samples are synthesized by co-precipitation, as discussed in the previous chapter, including an extra begin product $SnSO_4$. The reference sample is the LMR-NMC discussed in the previous chapter. The DFT calculations were performed by Marnik Bercx, the synthesis, XRD analysis and electrochemical measurements by Andreas Paulus. The structural study is my contribution. The experimental details of the TEM study can be found in the appendix at the end of Part II, the experimental details of the other experiments can be found in the corresponding paper [108].

7.2. Experimental results and discussion

7.2.1. Morphology, microstructure and electrochemical properties of Sn-doped LMR-NMC

The powder XRD patterns of the $Li_{1.2}Ni_{0.13}Mn_{0.54-x}Co_{0.13}Sn_xO_2$ samples LNMC (x=0), LNMCS5 (x=0.027), LNMCS10 (x=0.054), LNMCS20 (x=0.108) and LNCS (x=0.54) synthesized via the co-precipitation route are displayed in **Figure 71**. The sharp peaks show that the samples are well crystallised. Within the x range of 0 to 0.108, the strongest peaks can be ascribed to the monoclinic *C2/m* structure typical for LMR-NMCs. The unit cell parameters refined with the Le Bail method are listed in **Table 8**.

The samples demonstrate an increase in the unit cell parameters and volume with increasing nominal Sn content, in agreement with the larger ionic radius of Sn^{4+} (0.69 Å) as compared to Mn^{4+} (0.53 Å). However, the unit cell parameters and volume of the LNMCS20 sample are close to those derived from the LNMCS10 sample, while between these two samples the difference is expected to be more significant due to the much higher Sn concentration in the LNMCS20. Moreover, in the XRD patterns of LNMCS10 and LNMCS20, extra peaks appear (marked by asterisks) which reveal the presence of an additional phase. These peaks grow in intensity with increasing x content and become dominant in the LNCS sample. From the XRD pattern of LNCS, the phase could be identified as Li_2SnO_3 [113]. This means that the real substitution degree is smaller than the nominal Sn content. Assuming the main phase is similar to that of LNMCS10, the XRD patterns show that the contribution of the additional phase increases for the LNMCS20 compared to LNMCS10, explaining why the differences observed in the unit cell parameters and volume are smaller than would be expected if all Sn were incorporated in the main phase.

***Table 8**. Cell parameters of LNMC (x=0), LNMCS5 (x=0.027), LNMCS10 (x=0.054) and LNMCS20 (x=0.108) derived from the XRPD data.*

	LNMC	LNMCS5	LNMCS10	LNMCS20
a (Å)	4.9360(2)	4.9507(2)	4.9560(2)	4.9668(4)
b (Å)	8.5479(3)	8.5699(3)	8.5780(4)	8.5806(5)
c (Å)	5.0172(2)	5.0265(2)	5.0417(4)	5.0345(4)
β (°)	109.017(3)	108.969(4)	109.302(4)	109.305(6)
V ($Å^3$)	200.133(9)	201.6781(9)	202.2875(9)	202.4966(1)

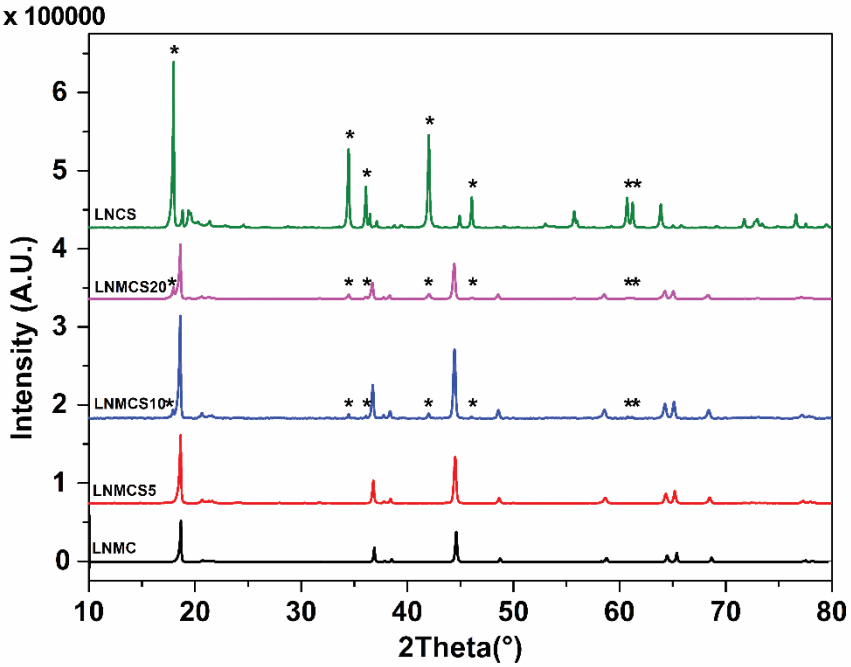

***Figure 71**. XRPD patterns of LNMC (x=0), LNMCS5 (x=0.027), LNMCS10 (x=0.054), LNMCS20 (x=0.108) and LNCS (x=0.54). The peaks marked by an asterisk (*) do not correspond to the C2/m monoclinic structure, but can be ascribed to the Li_2SnO_3 structure, which is mainly present in the LNCS sample.*

The real substitution degree has been assessed by EDX analysis. Mixed (Ni, Mn, Co, (Sn)) elemental maps of the LNMC, LNMCS5, LNMCS10 and LNMCS20 samples are presented in **Figure 72**. The unsubstituted LNMC material consists of a single phase showing a homogeneous transition metal distribution. Its derived transition metal ratio, $Ni_{0.14(2)}Mn_{0.53(3)}Co_{0.13(2)}$, is in agreement with the expected stoichiometry. The Ni, Mn, Co and Sn distribution in the LNMCS5 sample appear to be very homogeneous with a transition metal ratio of $Ni_{0.13(1)}Mn_{0.51(2)}Co_{0.13(1)}Sn_{0.033(5)}$ confirming that Sn preferentially substitutes Mn in the LMR-NMC structure. No additional phase has been detected. The majority of the crystallites in the LNMCS10 sample are also very homogeneous, providing the cation composition of $Ni_{0.13(1)}Mn_{0.50(2)}Co_{0.13(1)}Sn_{0.044(6)}$. However, small Sn-rich crystals are already present indicating exsolution of the Li_2SnO_3 phase. The LNMCS20 sample consists of two phases: one is LMR-NMC with the homogeneous $Ni_{0.14(1)}Mn_{0.48(2)}Co_{0.14(1)}Sn_{0.04(1)}$ cation composition, identical to the LMR-NMC phase in the LNMCS10 sample taking into account the standard deviation; the other one is Li_2SnO_3 slightly doped with Ni and Mn ($Ni_{0.06(1)}Mn_{0.07(4)}Co_{0.01(2)}Sn_{0.85(6)}$). Thus, the Sn for Mn replacement does not exceed $x \approx 0.045$, which is a substitution limit of *ca.* 8.3% of the Mn content.

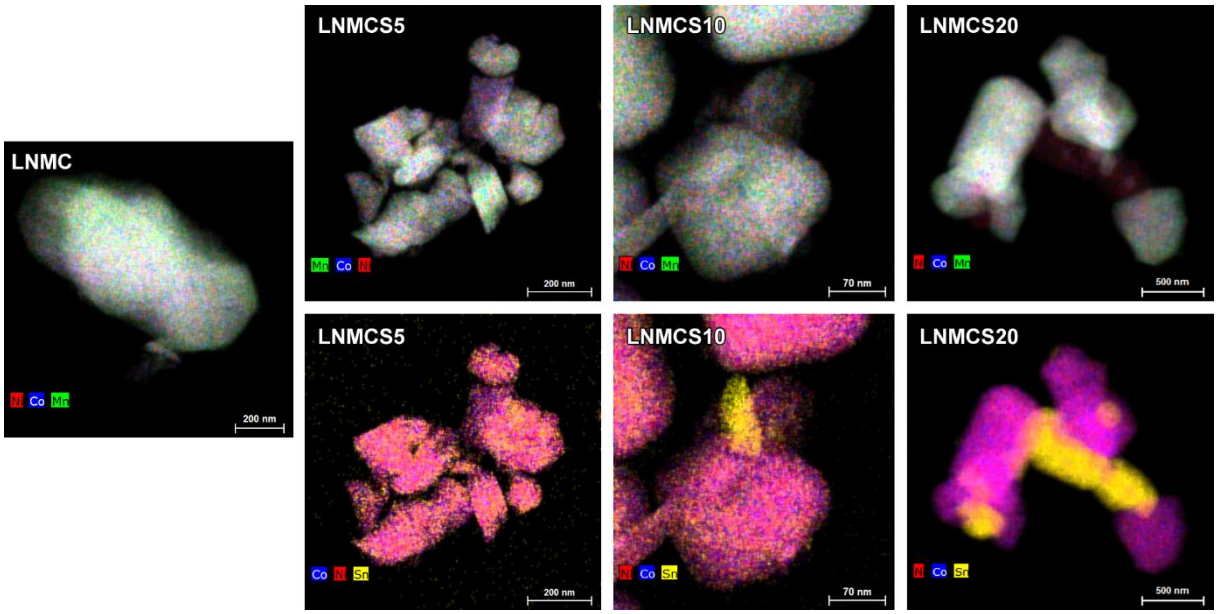

Figure 72. *From left to right: The mixed (Ni, Mn, Co) elemental maps of a representative LNMC (x=0) particle and the mixed (Ni, Mn, Co) and (Ni, Co, Sn) elemental maps of respective particles of LNMCS5 (x=0.027), LNMCS10 (x=0.054) and LNMCS20 (x=0.108). The elemental maps are given in counts.*

Besides the unit cell parameters, also minor differences have been observed between the particle sizes of the different samples. HAADF-STEM images of $Li_{1.2}Ni_{0.13}Mn_{0.54-x}Co_{0.13}Sn_xO_2$ (x=0-0.108) are shown in **Figure 73**, and the particle size is presented in **Table 9**. In contrast to the unit cell dimensions, the average particle size becomes slightly smaller upon increasing the Sn content to x = 0.054 (LNMCS10). The average particle size of LNMCS20 is comparable to LNMCS10, which is expected regarding the Sn substitution limit. The non-doped LNMC consists of large agglomerates of randomly shaped particles, whereas the Sn-doped samples consist of more elongated particles.

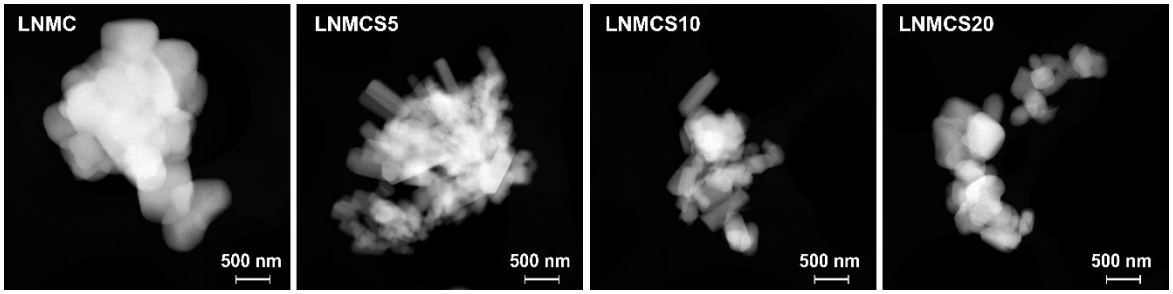

Figure 73. *HAADF-STEM images of $Li_{1.2}Ni_{0.13}Mn_{0.54-x}Co_{0.13}Sn_xO_2$: LNMC (x=0), LNMCS5 (x=0.027), LNMCS10 (x=0.054) and LNMCS20 (x=0.108).*

Table 9. *Particle size distribution of LNMC, LNMCS5, LNMCS10 and LNMCS20.*

Particle size [nm]	LNMC	LNMCS5	LNMCS10	LNMCS20
Mean	682	411	380	373
Standard deviation	363	216	171	149
Minimum	256	70	100	145
Maximum	1960	1141	902	951

In order to further investigate the Sn solubility in $Li_{1.2}Ni_{0.13}Mn_{0.54-x}Co_{0.13}Sn_xO_2$, the formation energies of Sn-substituted structures for a range of x-values have been calculated within the DFT framework. In an effort to reduce the computational complexity, the calculations were limited to $Li_{1.2}Mn_{0.80-x}Sn_xO_2$, which can be considered a reasonable strategy due to the similar ionic radii of Mn, Co and Ni, as well as the low concentration of Ni and Co. The solubility of Sn in this compound can be studied by considering the following decomposition reaction (Li_2SnO_3 corresponds to the admixture phase as detected by XRPD):

$$Li_{1.2}Mn_{0.8-x}Sn_xO_2 \rightarrow \left(1-\frac{x}{0.8}\right)\cdot Li_{1.2}Mn_{0.8}O_2 + \frac{x}{0.8}\left(0.6\cdot Li_2SnO_3 + 0.2\cdot SnO\right),$$

with formation energy:

$$E_f(x) = E(Li_{1.2}Mn_{0.8-x}Sn_xO_2) - \left(1-\frac{x}{0.8}\right)E(Li_{1.2}Mn_{0.8}O_2) - \frac{x}{0.8}\left[0.6\,E(Li_2SnO_3) + 0.2\,E(SnO)\right].$$

Figure 74 shows the calculated formation energies for the Sn substituted structures compared to their decomposition in $Li_{1.2}Mn_{0.8}O_2$, Li_2SnO_3 and SnO. The limited solubility of Sn is confirmed by the DFT calculations. For the lowest Sn concentration, x = 0.042, the formation energy of the lowest energy configuration is only 6.5 meV/atom above the convex hull. This structure can reasonably be considered as metastable [114], and as such, the formation of a single phase is feasible at low Sn concentrations. However, as the Sn-concentration x is increased, the $Li_{1.2}Mn_{0.8-x}Sn_xO_2$ configurations become more unstable, increasing the likelihood of a decomposition in $Li_{1.2}Mn_{0.8}O_2$, Li_2SnO_3 and SnO phases, as observed in the XRPD results for the high Sn concentration samples. Note that if the Sn substituted orderings

are generated randomly, i.e. without respecting the honeycomb pattern, the energies are significantly higher compared to the honeycomb structures at each Sn concentration. This matches the preservation of the honeycomb ordering for the Sn substituted structure found for the HAADF-STEM results.

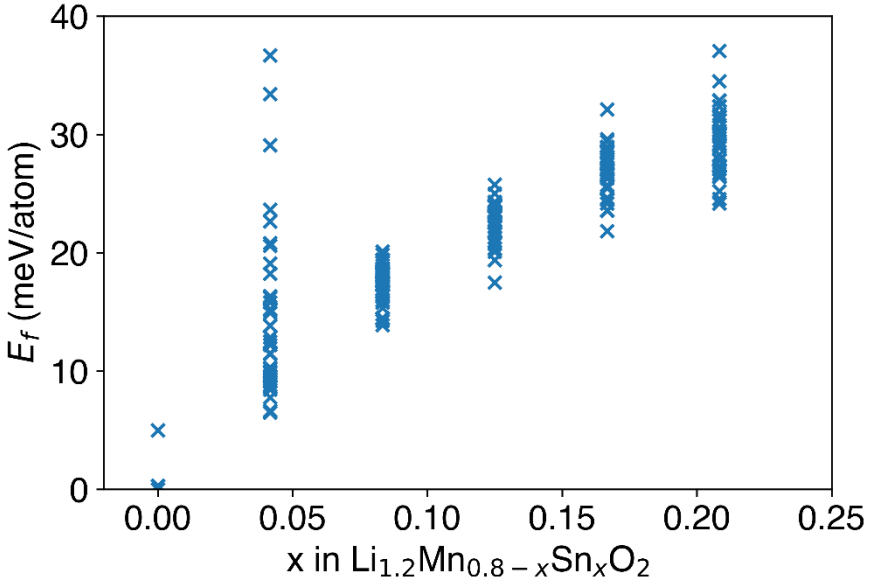

Figure 74. *Calculated formation energies of the Sn substituted structures for a range of Sn concentrations x. Within the 2x2x2 supercell, this corresponds to a set of 5 different values for x: {i/24 | i = 1, 2, 3, 4, 5}. Every mark corresponds to a symmetrically non-equivalent Li-Mn-Sn ordering at a specific Sn concentration.*

As the main phases of LNMCS5, LNMCS10 and LNMCS20 are comparable based on the STEM-EDX and XRPD investigation and as LNMCS10 and LNMCS20 are not a single phase, the further electrochemical characterization and structural study (discussed in the next section) is exclusively presented for LNMCS5, and will be compared to the unsubstituted LNMC reference material, of which the structural study was discussed in the previous chapter. Moreover, the additional Sn-rich phase of LNMCS10 and LNMCS20 immediately turns amorphous under the electron beam, preventing its structural analysis via HAADF-STEM. As this additional phase is believed to have no significant electrochemical activity within the probed potential window, mainly due to the very low content of nickel and cobalt and the redox inactivity of Sn^{4+}, no further characterization has been performed.

In order to comparatively assess voltage fade for LNMC and LNMCS5 samples, galvanostatic cycling has been performed within the 3.00 V - 4.55 V vs Li/Li^+ potential window. The lower potential limit has been set at 3.00 V, as voltage fade dominates in the ~3.1 - 3.3 V voltage

interval for LMR-NMC [115]. Selected charge/discharge curves are shown in **Figure 75B** and **Figure 75C**. The slope region observed for both samples up to ~4.4 V is related to the oxidation of Ni^{2+} to Ni^{3+} and Ni^{4+} and Co^{3+} to Co^{4+} [86]. Evidence for anionic redox chemistry of the oxygen sublattice can be found for both samples in the voltage plateau, observed at around 4.5 V vs Li/Li^+ during the first charging step, which is shown in **Figure 75A** [116–118]. Currently, it is still under debate in literature whether the released oxygen during the first charging step originates from the bulk lattice or from the near-surface region of the LMR-NMC particles [116–118]. Among the transition metal cations, localised hole formation on oxygen is most facilitated by Mn^{4+} as the Mn^{4+}-O bond is less covalent than Ni^{4+}-O or Co^{4+}-O. The Li^+-O bond is characterized by an even lower covalency than Mn^{4+}-O and by consequence contributes more to the localised hole formation on oxygen [109]. On the other hand, Sn^{4+} has completely filled *d* orbitals, resulting in less directional bonds with oxygen, which enables the rotation of the neighbouring oxygen bonds needed to form stable peroxo-like species (i.e. species with $O^- - O^-$ bonds), which is expected to reduce the irreversible oxygen redox processes [119]. The voltage plateau depicted in **Figure 75A** at around ~4.5 V is comparable for both unsubstituted LNMC and Sn substituted LNMCS5, both reaching capacities of ~250 mAh/g. Plausible explanations can be found in the low Sn^{4+} dopant concentration. For the subsequent 99 charge/discharge cycles, comparable voltage fade for both samples is observed, as presented in **Figure 75B** and **Figure 75C.** It is unlikely that the replacement of just a few molar percent of Mn^{4+} by Sn^{4+} will have a significant impact on the occurrence of transitions from layered to spinel-type structure, despite the lower tendency of Sn^{4+} to undergo O-T-O migration during galvanostatic cycling. In contrast to our study, Zhou *et al.* [112] observed enhanced electrochemical properties upon Sn doping (0 - 3.7%) for fully charged LNMC up to ~4.8 V vs Li/Li+. The study showed that the optimal electrochemical performance is obtained at $Li_{1.2}Ni_{0.13}Mn_{0.53}Co_{0.13}Sn_{0.01}O_2$ (~ 1.85% Mn^{4+} replaced by Sn^{4+}) with a higher specific discharge capacity and slightly reduced voltage fade. In our study, a minimum of 5% Sn is substituted, and the specific discharge capacity measured after 100 cycles is slightly lower for the Sn substituted LNMCS5 (~140 mAh/g) than for the unsubstituted LNMC (~150 mAh/g); no reduced voltage fade was observed. Moreover, we would not expect a significantly improvement of the electrochemical performance with only a few percentage of Sn in LMR-NMC.

To fully understand the electrochemical properties, a structural TEM investigation was performed on LNMCS5, which is discussed in the following section. The crystal structure of LNMCS5 was studied in the pristine state (i.e. pristine sample), the first charged state (i.e. charged sample), and the discharged state after 100 cycles (i.e. cycled sample). The galvanostatic cycling was performed between 3.0 V and 4.55 V at a rate of 0.1C.

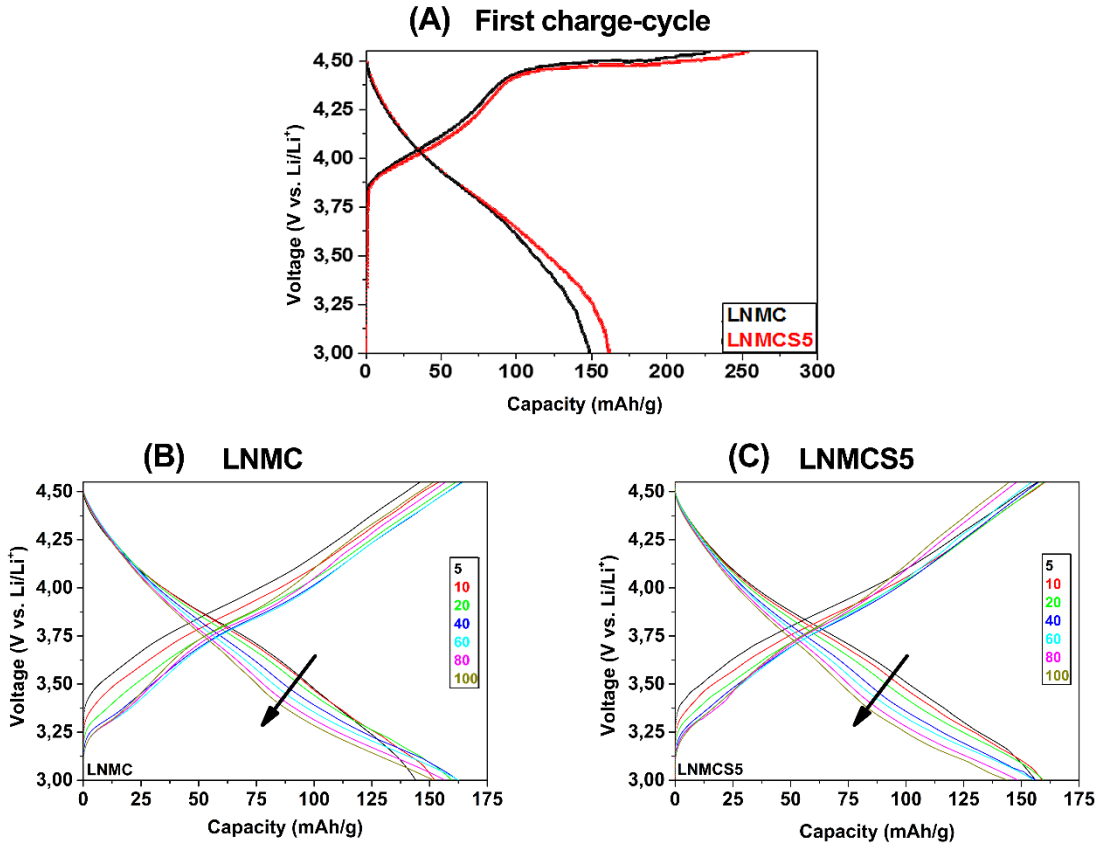

Figure 75. (A) *Initial charge/discharge cycle at C/20 for LNMC and LNMCS5.* ***(B)/(C)*** *Selected charge/discharge curves (cycle number is given in the legend) in the 3.00V-4.55V vs. Li/Li+ voltage window at a rate of C/10 for respectively LNMC and LNMCS5. Voltage fade is indicated by the arrow. The slope of the arrow is the same for both, showing that the voltage fade is similar for both.*

7.2.2. Crystal structure of Sn-doped LMR-NMC

The SAED patterns corresponding to the pristine, charged and cycled samples of $Li_{1.2}Ni_{0.13}Mn_{0.513}Co_{0.13}Sn_{0.027}O_2$ are shown in **Figure 76.** The SAED patterns of the pristine sample do not show an obvious difference with the SAED of the unsubstituted pristine sample (**Chapter 6**, **Figure 61**), and thus the structure can be described by the monoclinic *C2/m* layered structure with the O3 cubic close-packed sequence of the oxygen layers.

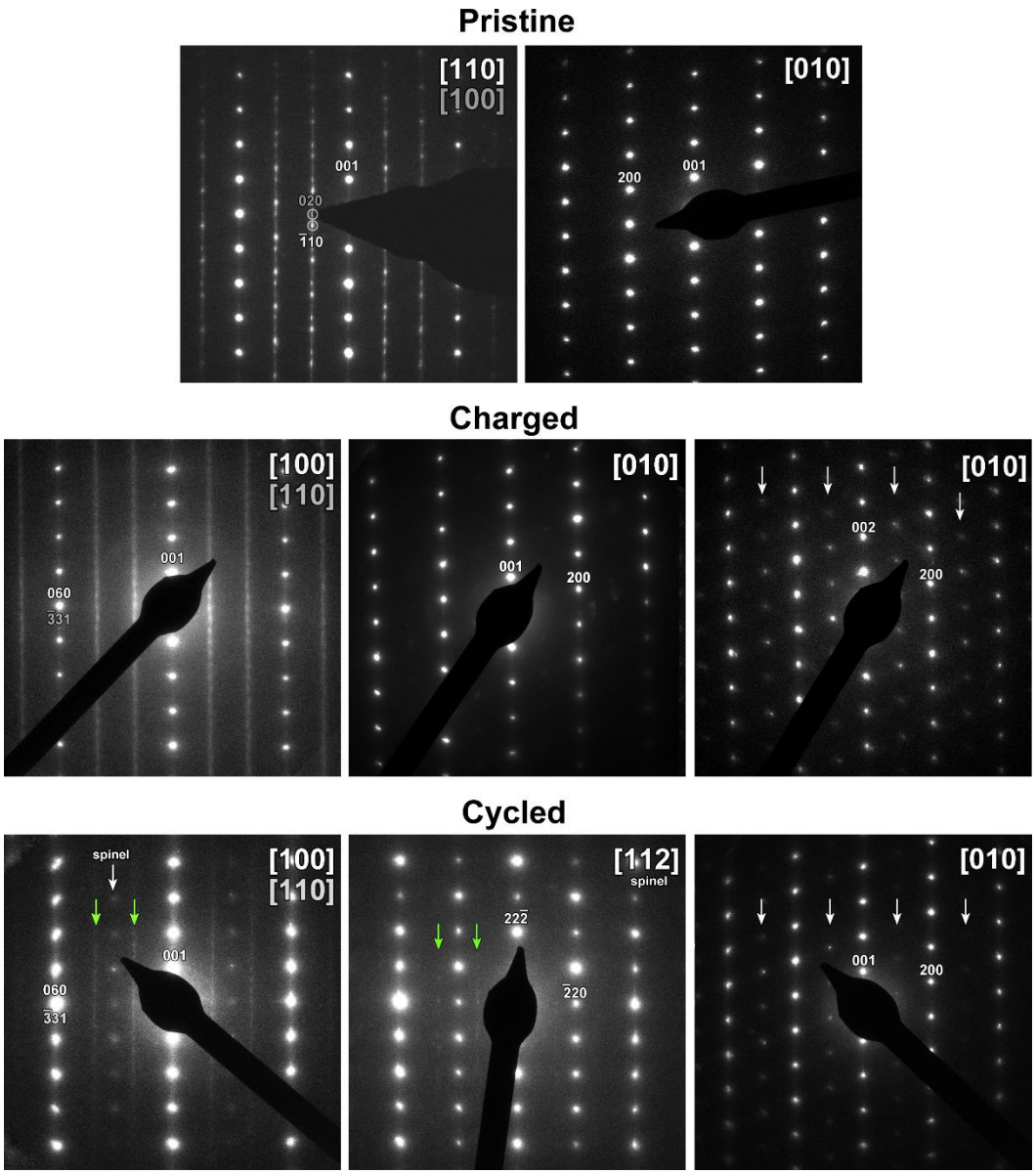

Figure 76. *SAED patterns of (top) the pristine and (middle) charged sample along the [100]/[110] and [010] zones; (bottom) the cycled sample after 100 cycles along the [100]/[110] and [010] orientation indexed in the layered C2/m structure, and along the [112] orientation indexed in the spinel structure. The white arrows mark the extra reflections, originated from the formation of the spinel structure, while the green arrows indicate the streaks associated with the honeycomb stacking in the layered C2/m structure.*

The HAADF-STEM and ABF-STEM images shown in **Figure 77** confirm the layered structure. A line profile was taken perpendicular to the layers in the [010] HAADF-STEM image, which is shown in **Figure 80**. In order to obtain a good fit, we had to include peaks at the lithium layers, where we would not expect to have any transition metals. However, the atom columns indicated by arrows in the inset in the [010] HAADF-STEM image in **Figure 77** affirm the presence of transition metals in the lithium layer. Since no extra reflections were observed in the SAED patterns of the pristine sample, we can assume that these transition metals are in low amount and/or randomly distributed. Further, the Sn atoms are homogeneously distributed in the structure because, if nano-scale Sn-rich domains were present, a clear intensity difference would be observed in the atom columns since Sn has a much higher atomic number (Z = 50) than Mn (Z = 25), Co (Z = 27) and Ni (Z = 28), resulting in much brighter projected columns. Similar to the non-substituted $Li_{1.2}Ni_{0.13}Mn_{0.54}Co_{0.13}O_2$, particles are found consisting of domains in [010] orientation neighbouring domains in [101] orientation (Figure not shown; *similar to* **Figure 66**).

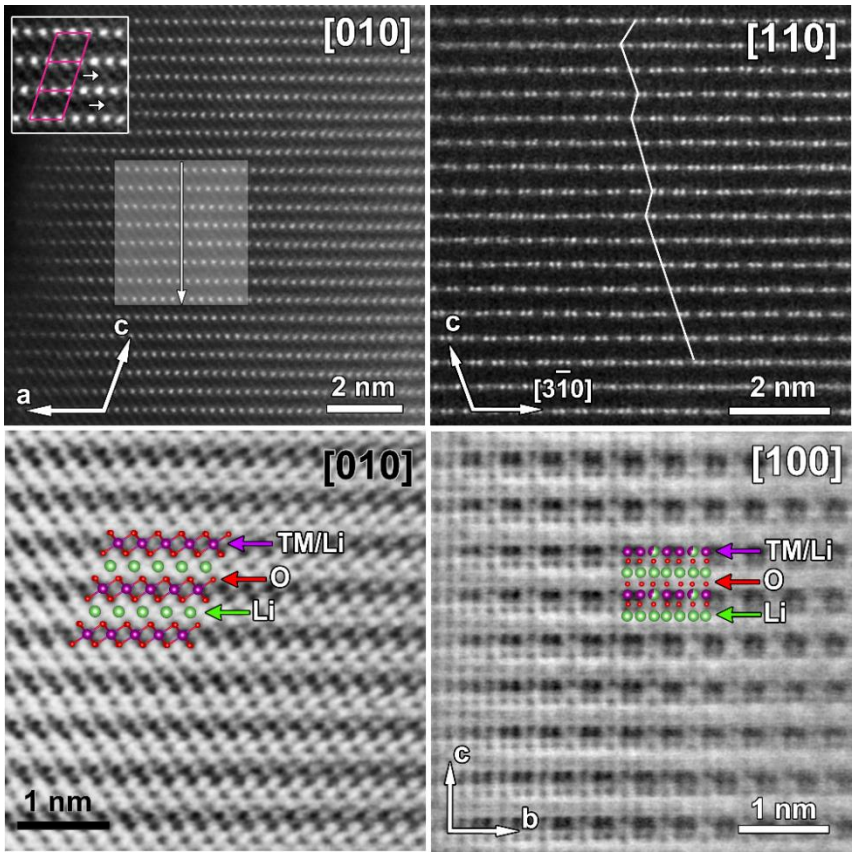

Figure 77. *The pristine sample. Top: HAADF-STEM images along the [010] and [110] orientations. The inset shows the unit cell of the layered structure, where the arrows indicate transition metals at the lithium positions, and the rectangle marks the area of which a line profile has taken, which is shown in Figure 80. The white line in the [1110] image shows the honeycomb stacking. Bottom: ABF-STEM images along the [010] and [110] orientations, confirming the C2/m symmetry.*

The SAED patterns of the charged and cycled samples show extra reflections that originate from the formation of the spinel structure. The middle [010] SAED pattern of the charged sample shows no extra reflections and thus no phase transition to the spinel structure, whereas the extra reflections are clearly present in the right side [010] SAED pattern, which demonstrates that different particles do not degrade to the same amount during electrochemical cycling. The middle SAED pattern of the cycled sample is mainly spinel, because the joint spinel-honeycomb reflections are very clear, while the reflections only due to honeycomb are only barely visible, marked by the green arrows. For this particle, the structure has almost entirely changed to the spinel structure. The presence of spinel reflections in the cycled sample, as well as particles that are mainly spinel, indicate that the TM migration is partially irreversible and forms a permanent spinel structure. Comparing the SAED patterns of the charged and cycled sample with those obtained from the unsubstituted sample discussed in the previous chapter, the reflections associated to the formation of the spinel structure are much brighter in the Sn substituted sample. It seems that the structure degradation in the Sn substituted sample is higher than in the unsubstituted sample and that the Sn substitution did not help to mitigate the structural degradation.

HAADF-STEM and, in the case of the charged sample, ABF-STEM images were also obtained. Due to the structure degradation in the cycled sample, the sample became too sensitive to acquire clear ABF-STEM images. For ABF-STEM imaging, a higher electron dose is needed than for HAADF-STEM imaging in order to visualize the oxygen atoms. The high-resolution STEM images of the charged sample, shown in **Figure 78,** prove that the *C2/m* structure is preserved, where the close-up HAADF-STEM image along the [010] marks the TM migration towards the lithium positions (bright dots marked by yellow arrows) and the tetrahedral holes (bright dots encircled in pink). This is also confirmed by the line profile (**Figure 80**), which clearly shows some high peaks at the tetrahedral positions and peaks at the lithium layers. Some of the peaks corresponding to either the oxygen or tetrahedral positions in the line profile of the charged sample are significantly decreased, which might be associated to oxygen release occurring after the oxidation of the transition metals.

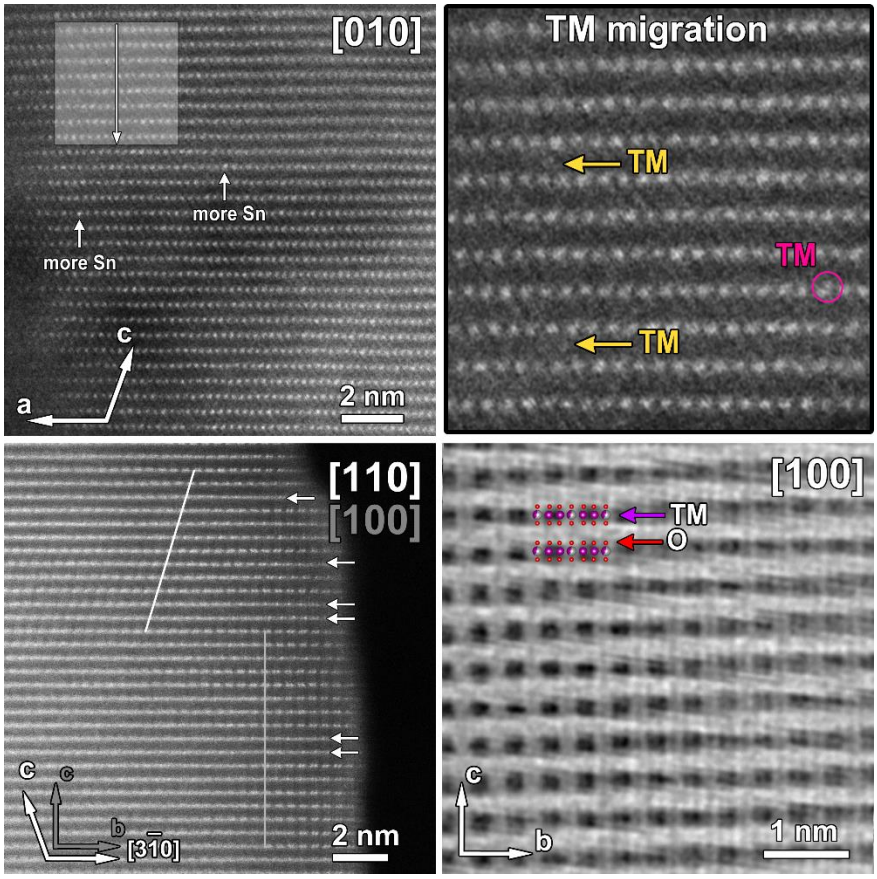

Figure 78. *The charged sample. Top: HAADF-STEM images along the [010] orientation; left: the rectangle marks the area of which a line profile has been taken that is shown in Figure 80, and the arrows indicate atom columns that are brighter meaning that these atom columns contain more Sn; right: a close-up, where TM migration is observed. The yellow arrows show TM in the empty Li positions, while the pink circle indicates TM in the tetrahedral hole between the two layers. Bottom: left: HAADF-STEM image along the [100]/[110] orientation, where the arrows show disorder within the honeycomb layers, and the white lines mark the stacking of the honeycomb layers; right: ABF-STEM image along the [100] orientation. The lithium atoms are not visible since they are extracted from the structure during charging.*

The HAADF-STEM images of the cycled sample along the [010] and [100] orientation in **Figure 79** clearly support the formation of the spinel structure at the surface. The [110] and [100] HAADF-STEM images also reveal high disorder within the honeycomb layer (homogeneous intensity in the Li-TM layers instead of the honeycomb pattern).

The line profile of the cycled sample also displays the migration of transition metals towards the lithium, which supports our assumption of the formation of the spinel structure. Besides that the line profile proves the TM migration to the lithium layer, the line profile also reveals transition metals trapped at the tetrahedral positions. Some peaks at the tetrahedral positions are much higher than only the contribution of the oxygen atom columns. This TM migration

observed in the line profiles demonstrates that substitution of only 5% is not enough to inhibit transition metal migration and the structural degradation during electrochemical cycling.

Both the HAADF-STEM images and SAED patterns reveal a higher structural degradation for the Sn substituted LNMCS5 than for the unsubstituted sample. However, if the structural degradation upon cycling would be significantly higher for LNMCS5 than for LNMC, we would expect to also observe a higher voltage fade for the LNMCS5 sample, while that is not the case.

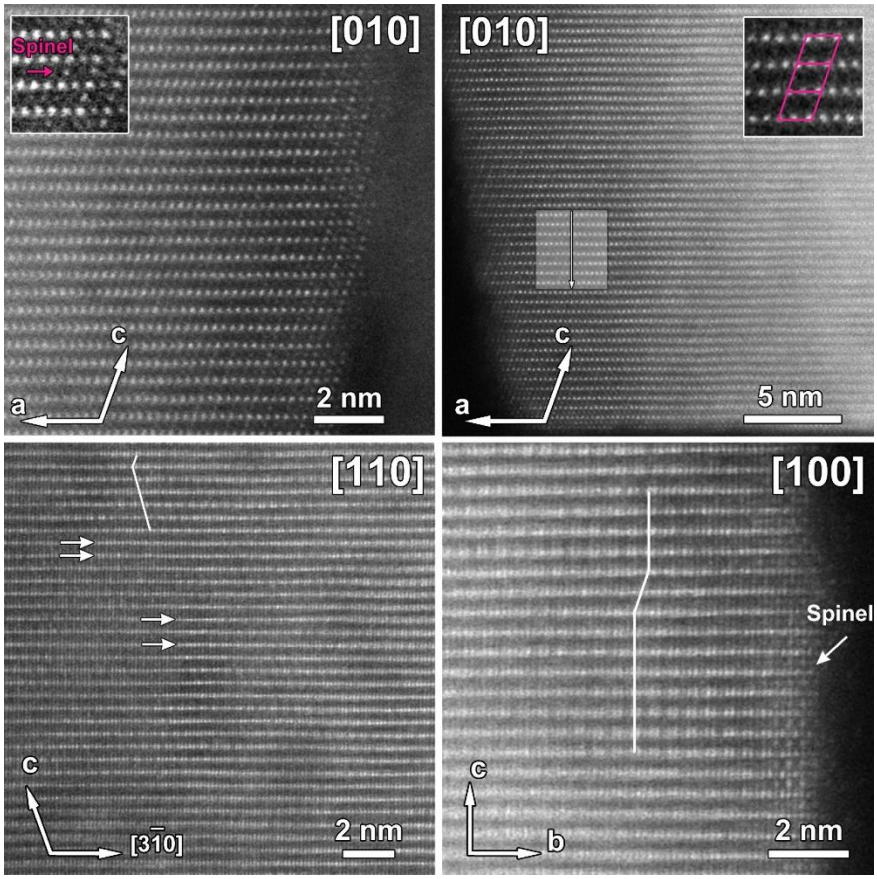

Figure 79. *HAADF-STEM images of the cycled sample along the [110] and [010] orientations. Top: the left HAADF-STEM image and the inset show the spinel structure that is present at the surface, while the right one shows that the layered structure is still preserved more towards the bulk. The rectangle marks the area of which a line profile is taken, which is shown in Figure 80. Bottom: The arrows in the [110] HAADF-STEM image indicate the disorder within the honeycomb layers, while the white lines show the stacking of these layers; At the right, the structure clearly shows the formation of a spinel structure at the surface.*

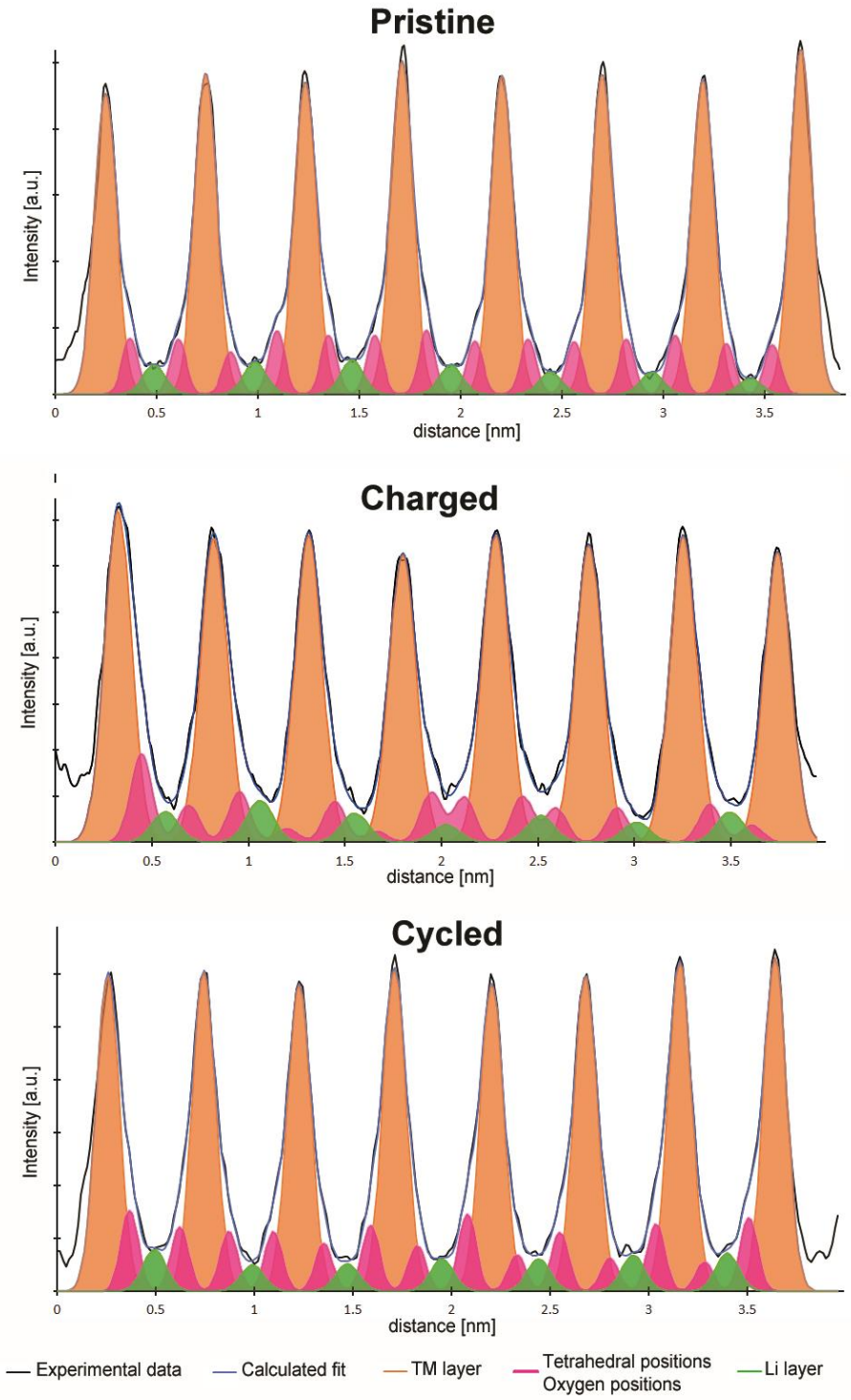

Figure 80. *Line profiles of the pristine, charged and cycled samples. The regions of which the line profiles are taken are marked in Figure 77, Figure 78 and Figure 79. The experimental line profile is fitted by Gaussian functions with Fityk [43].*

7.3. Conclusion

The XRPD and STEM-EDX analysis showed that the limited Sn^{4+} substitution degree does not exceed x = 0.045 in $Li_{1.2}Ni_{0.13}Mn_{0.54-x}Co_{0.13}Sn_xO_2$. For x = 0.054 and x = 0.108 an additional Sn-rich phase is formed next to a Sn-doped Li-rich/Mn-rich main phase, which is assumed to be electrochemically inactive. The composition of the Sn-doped main phase is comparable for all the Sn substituted samples, where the transition metals and Sn are homogeneously distributed in the Li-rich/Mn-rich phase. Up to x = 0.108, a highly crystalline, layered structure is formed, as confirmed by XRPD. A slight increase of the lattice parameters and volume is observed when increasing the substitution of Mn^{4+} by Sn^{4+} up to the sample x = 0.54 and stabilises around x = 0.108. This is in agreement with the larger ionic radius of Sn^{4+} as compared to Mn^{4+} and the limited solubility of Sn. Honeycomb ordering is maintained upon replacing 5% of Mn^{4+} by Sn^{4+}.

Galvanostatic cycling has been performed on the x=0 and x=0.027 compositions. LNMC and LNMCS5 are characterized by discharge capacities around respectively ~150 mAh/g and ~140 mAh/g at C/10 for 100 cycles. The comparable electrochemical properties are in agreement with the similar structural properties of the x = 0 and x = 0.027 compositions based on our TEM and qualitative XRPD study. The substituted (x = 0.027) sample adopts a layered structure with a honeycomb ordering in the TM layer similar to the unsubstituted LMNC sample.

For the substituted sample, the TEM study showed that TM migration occurs during charging and that it is only partly reversible, leading to trapped transition metals in the lithium positions and the tetrahedral positions in the lithium layers. After 100 cycles, the TEM study showed that a permanent spinel structure is formed at the surface that grows concomitantly with the number of cycles. The TM migration and the phase transition at the surface hinder the lithium diffusion paths and eventually lead to voltage fade and capacity loss. Based on the TEM study, the structural degradation of the Sn substituted LNMCS5 seems to be significantly higher than observed for the unsubstituted sample after 100 cycles.

To conclude, we observed that, under our synthesis conditions, replacing a few molar percent of Mn^{4+} by Sn^{4+} in LMR-NMC is not considered a valuable strategy to significantly inhibit voltage fade upon extended galvanostatic cycling below the fully charged state. This is most probably related to the inability of Sn^{4+} to inhibit the structural transition from a layered structure to a spinel-type structure upon extended galvanostatic cycling.

Chapter 8. Ti-substitution in Li_2MnO_3

This section is based on the paper (in preparation):

A. Paulus, **M. Hendrickx**, M. Batuk, G. Reekmans, A. M. Abakumov, P. Adriaensens, J. Hadermann, M. K. Van Bael and A. Hardy. *Understanding the role of local coordination environment on the coupling between cationic and anionic redox chemistry in Ti^{4+} substituted Li_2MnO_3 as a cathode material for Li-ion batteries*

8.1. Introduction

Both Li_2MnO_3 and LMR-NMC suffer from irreversible anionic redox reactions, which results in voltage fade due to oxygen release and phase transition. In contrast to LMR-NMC, where mainly cationic redox reactions contribute to the capacity, the redox chemistry in Li_2MnO_3 is dominated by the anionic redox reactions. Therefore, Li_2MnO_3 is an interesting material to study the influence of cation substitution on the structural degradation and oxygen release upon cycling, which can be used as a building block for other Li-rich, Mn-rich cathode materials.

In the continuation of the previous study, we will investigate the partial substitution of Mn^{4+} by an element (M) which is able to form a solid solution in $Li_2Mn_{1-x}M_xO_3$, which does not tend to adopt T_h coordination (to impede migration to other octahedral sites via these tetrahedral sites) and is not redox-active within the investigated potential window. Titanium substitution is proposed as a potential stabiliser for Li_2MnO_3 [120,121]. I studied the structure, and its evolution upon cycling of the Li_2MnO_3 and $Li_2Mn_{0.8}Ti_{0.2}O_3$ samples using transmission electron microscopy, expect for the compositional analysis, which is performed by Maria Batuk. The effect of Ti substitution on the electrochemical properties is determined using galvanostatic cycling by Andreas Paulus. Li_2MnO_3 and $Li_2Mn_{0.8}Ti_{0.2}O_3$ have been prepared via an aqueous solution-gel method by Andreas Paulus, and the details of the synthesis can be found in the appendix at the end of Part II. The appendix also contains the experimental details of the TEM study.

8.2. Experimental results and discussion

8.2.1. Morphology, microstructure and electrochemical properties of Li_2MnO_3 and $Li_2Mn_{0.8}Ti_{0.2}O_3$

A preliminary TEM study showed that substitution of 30% titanium ($Li_2Mn_{0.7}Ti_{0.3}O_3$) demonstrated significant Ti segregation at the surface of the particles. When the titanium concentration was lowered to 20% ($Li_2Mn_{0.8}Ti_{0.2}O_3$), the titanium distribution is rather uniform. Therefore the study was continued using this sample $Li_2Mn_{0.8}Ti_{0.2}O_3$. A few TiO_2 crystals were found, and a very small amount of titanium segregation at the surface of some particles was observed, as can be seen in **Figure 81**. Since the TiO_2 particles do not contain lithium, this additional phase does not contribute to the electrochemical reactions upon cycling and can be ignored. The average Mn:Ti atomic ratio measured with EDX from the main phase of $Li_2Mn_{0.8}Ti_{0.2}O_3$ is close to 82(1):18(1), which is close to the expected composition. The crystal structure and electrochemical properties of the $Li_2Mn_{0.8}Ti_{0.2}O_3$ (LMTO) sample will be compared to the reference sample Li_2MnO_3 (LMO), prepared using the same synthesis method except for the Ti doping.

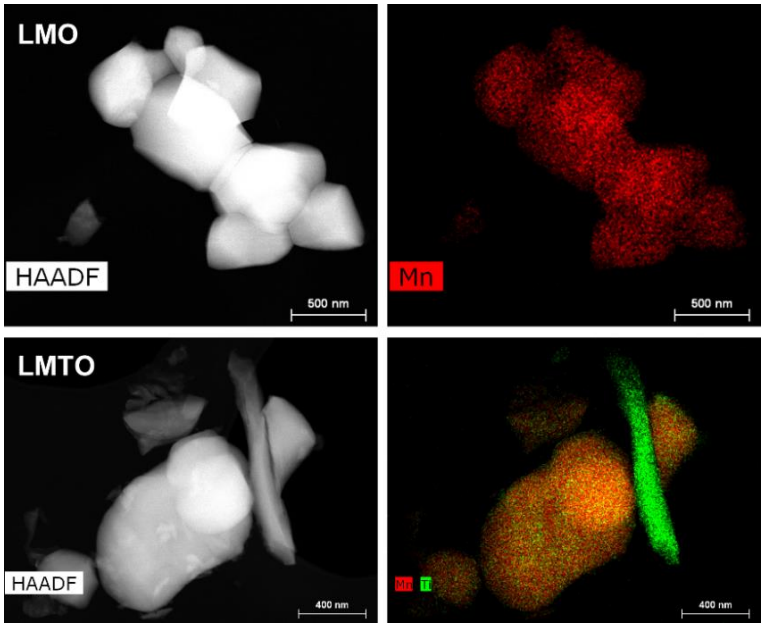

Figure 81. *The HAADF-STEM image (left) together with the individual Mn or mixed Mn/Ti element map (right) from the Li_2MnO_3 sample, referred as LMO, and the Ti-substituted $Li_2Mn_{0.8}Ti_{0.2}O_3$ sample, referred as LMTO (Images courtesy of Maria Batuk).*

The particles of the Li_2MnO_3 reference sample and the Ti substituted $Li_2Mn_{0.8}Ti_{0.2}O_3$ sample have similar morphologies. Some particles have smooth edges with sizes between 300 nm - 600 nm (LMO) and 100 nm - 700 nm (LMTO), present as both individual particles and agglomerates. In the case of LMTO, these particles have a shape close to spherical. In both samples, there is also another type of particles with an irregular shape and a rough surface, with a size from a few tens of nanometre to 1 μm (LMO) or to 700 nm (LMTO).

Table 10 shows the unit cell parameters and volume derived from the XRPD analysis done by Andreas Paulus. The unit cell increases with the substitution of titanium, which can be explained by the larger Ti^{4+}(0.605 Å) than Mn^{4+} (0.53 Å) [73].

Table 10. *Refined cell parameters and volume of $Li_2Mn_{1-x}Ti_xO_3$, LMO (x=0) and LMTO (x=0.2)*

	LMO	LMTO
a (Å)	4.9342(6)	4.9554(8)
b (Å)	8.5335(3)	8.5784(5)
c (Å)	5.0226(0)	5.0556(0)
β (°)	108.879(9)	109.331(4)
V ($Å^3$)	200.100(0)	202.794(3)

The LMO and LMTO samples were galvanostatically cycled for 50 cycles at C/10 after two initial cycles at C/20 in the voltage interval 2.0 V – 4.8 V vs Li/Li^+. The corresponding charge/discharge plots are depicted in **Figure 82**.

The shape of the initial charging step is similar for both samples. The voltage plateau at around 4.5 V vs Li/Li^+ dominates the first charge capacity that is related to irreversible oxygen redox processes. The slope region for the charging steps of subsequent charge/discharge cycles can be ascribed to the Mn^{3+}/Mn^{4+} redox couple.

The obtained first charge capacity of Li_2MnO_3 only reaches ~ 60 mAh/g at 4.8 V, which is considerably lower than the theoretical capacity of Li_2MnO_3 (460 mAh/g). The discharge capacity only reaches ~50 mAh/g and subsequently drops to ~35 mAh/g. In literature, the described discharge capacity varies from publication to publication, with values ranging from a few to ~ 200 mAh/g. The electrochemical performance of the material is found to depend strongly on synthesis conditions and test conditions [81,83,122–124].

The voltage plateau of LMTO is only half of the voltage plateau of LMO, with a first charge capacity of ~30 mAh/g. The smaller voltage plateau could indicate that Ti^{4+} is able to effectively hamper the oxygen release from the lattice and the corresponding migration of manganese. The significantly smaller voltage plateau also means that less lithium has been extracted from the active material, and thus, less Mn^{4+} is expected to be reduced to Mn^{3+}. As a consequence, the discharge capacity of LMTO (~ 25 mAh/g) is significantly lower than for the LMO sample. In contrast to LMO, during the first 30 cycles, the discharge capacity of the LMTO increases up to ~70 mAh/g but eventually drops to a discharge capacity similar to LMO (~35 mAh/g) in the subsequent 70 cycles. The substitution of Ti^{4+} for Mn^{4+} enlarges the Li^+ diffusion channels due to its larger ionic radius compared to Mn^{4+}, which might contribute to the higher discharge capacity before the capacity drop.

The voltage fade is represented by the arrows in **Figure 82**, where the steeper the slope of the arrow means the higher the voltage fade. Since the capacity of LMTO first increases and then decreases, the arrow corresponding to LMTO only takes into account the cycles 20 to 50, where the capacity decreases. Therefore, we can only compare the voltage fade from the last 30 cycles, where voltage fade is higher for LMO than for the LMTO sample.

In the following section, the crystal structure of LMO and LMTO is investigated before cycling and after 50 cycles.

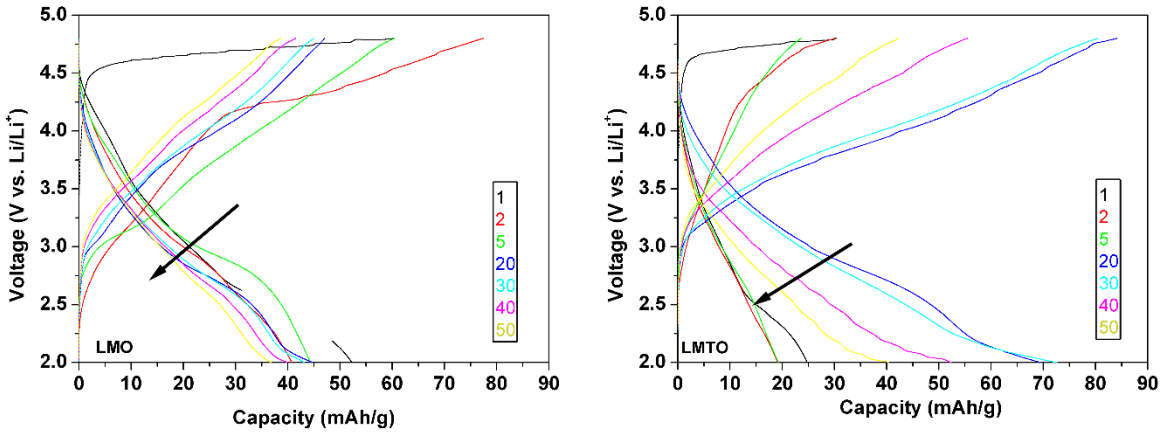

Figure 82. *The charge and discharge plot of the LMO (left) and LMTO (right) sample. The LMO and LMTO samples are galvanostatically cycled for 50 cycles at C/10 after two initial cycles at C/20 in the voltage interval 2.0 V to 4.8 V vs Li/Li$^+$. The arrows represent the voltage fade. The slope of the arrow corresponding to LMO is steeper than the arrow corresponding to LMTO, indicating that the voltage fade is higher for LMO.*

8.2.2. Crystal structures of Li_2MnO_3 and $Li_2Mn_{0.8}Ti_{0.2}O_3$

The SAED patterns and HAADF-STEM images for both samples, which are shown in respectively **Figure 83** and **Figure 84**, confirm the monoclinic *C2/m* symmetry with the O3-stacking. In the pristine state, the structure is similar for both samples. The amount of stacking faults strongly varies from crystal to crystal, for example, the [100]/[110] SAED patterns of LMTO suggest that LMTO has a higher amount of stacking faults than LMO (LMTO shows diffuse streaks; LMO shows discrete reflections with weak streaks), while the [100]/[110] HAADF-STEM images in **Figure 84** show no significant difference in the amount. These samples are made by the solution-gel method, similar to the LMR-NMC particles we discussed in Chapter 6, where we found that particles synthesized by the solution-gel method showed segregation and structural modifications at the surface. The structural modifications were related to Ni- and Co-segregation (Ni-rich spinel structure at the {200} facets; Co-rich rock-salt-type structure at the {002} and {202} facets). As mentioned above, a very small amount of Ti segregation was observed in the current samples, but no structural modifications were observed at the surface. As no Ni or Co is present in these samples and such structural modifications are absent, it further supports our observation that the structural modifications are specifically related to the Ni and Co-presence in LMR-NMC.

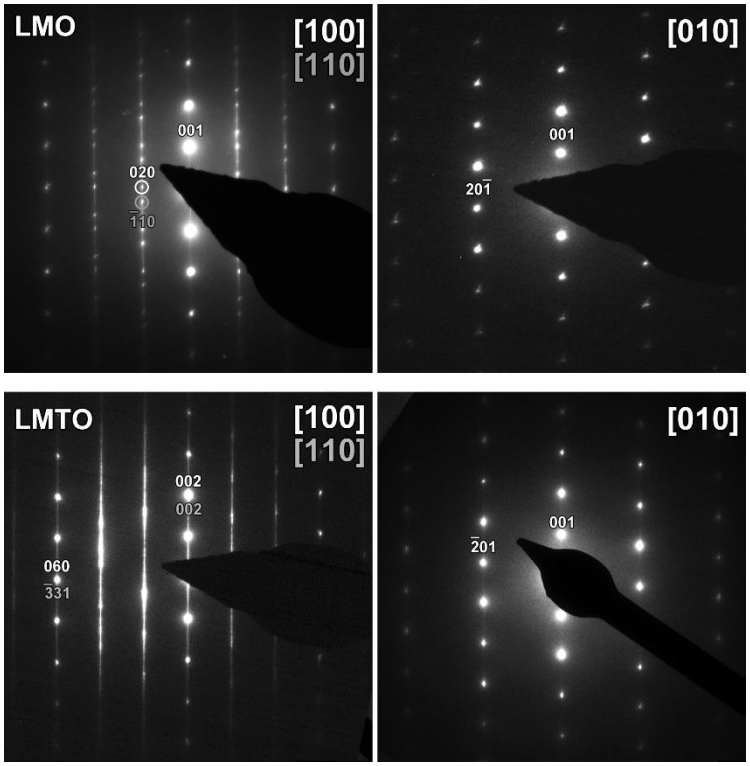

Figure 83. *SAED patterns along the [100]/[110] and [010] zones obtained from the LMO and LMTO samples.*

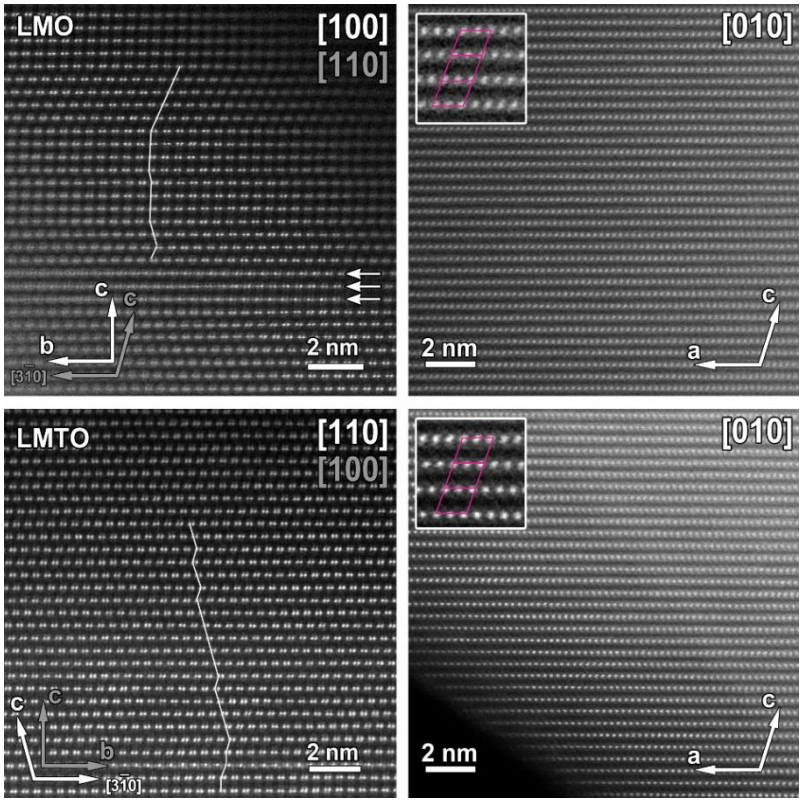

Figure 84. *HAADF-STEM images along the [100]/[110] and [010] orientation of the LMO and LMTO samples. The white lines indicate the stacking, while, in the case of the LMO samples, the white arrows show disorder within the honeycomb layer. The [010] HAADF-STEM images confirm for both samples the O3-type stacking, where the inset shows the monoclinic unit cell.*

Next, the crystal structure was investigated to explain the capacity drop. The structures from LMO and LMTO samples after 50 charge/discharge cycles have been comparatively assessed by HAADF-STEM and SAED. For both samples, the SAED patterns show particles that preserve the layered *C2/m* symmetry and particles that are partially degraded towards a spinel-type structure with symmetry $Fd\bar{3}m$ and a rock-salt-type structure with $Fm\bar{3}m$ symmetry.

For the cycled LMO sample, the SAED patterns **A** and **C** depicted in **Figure 85** are taken from the same particle, along the same orientation, showing that the structural degradation does not evolve homogeneously within a single particle. Many reflections in the SAED patterns are broad and slightly diffuse, which points towards a reduced crystallinity. The SAED pattern in **Figure 85D** represents a particle that is partially degraded. The bright reflections could be indexed by the rock-salt structure, while the weak broad reflections marked in blue correspond to the spinel structure. This means that the structure has partially degraded to the spinel and further to the rock-salt structure. The sharp reflections, encircled in orange**,** could only be indexed by the [101] orientation of the *C2/m* layered structure, indicating that this domain is not affected by the degradation during cycling. Since this domain is oriented differently, it is

possible that the Li was not able to leave the structure upon charging (as explained in Chapter 6), making the domain inactive, and consequently, not subjected to TM migration and structural degradation. It shows that the domain formation prevents some domains of contributing to the performance of the active cathode material. **Figure 86** shows the calculated ED patterns of the different domains that are observed in **Figure 85D**. It shows that domains with two different orientations ([010] and [101]) of the layered *C2/m* structure (i.e. orientation twins) are present in the investigated particle of which the [010] domains are degraded to the spinel structure (the equivalent zone is [110]) and the rock-salt structure (the equivalent zone is [110]).

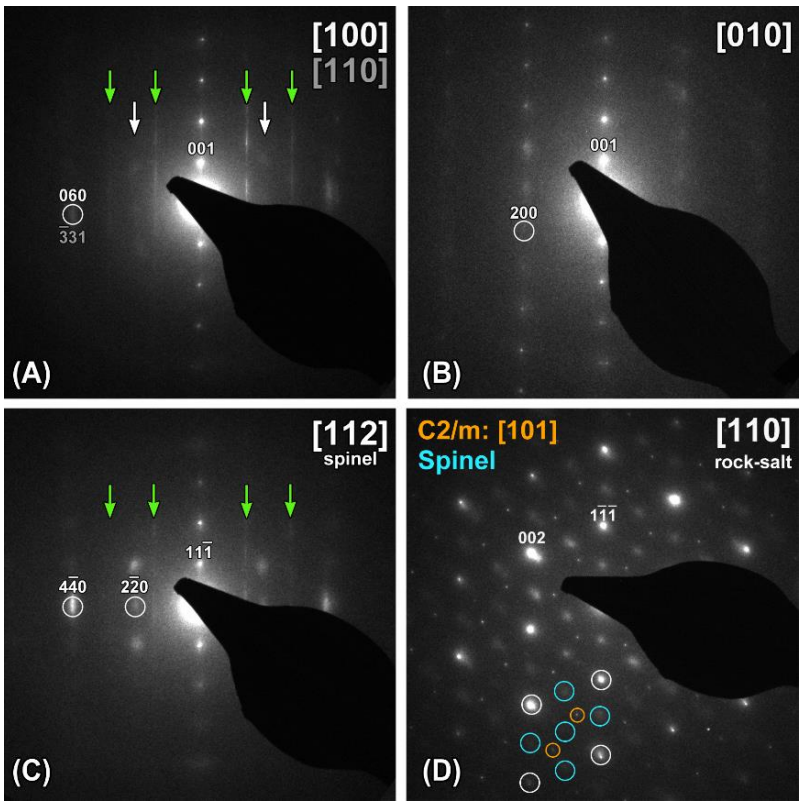

Figure 85. *SAED patterns of the cycled LMO sample, taken along the [*100*]/[110] and [010] orientation in the C2/m symmetry, where the two top patterns (A-B) show that the C2/m symmetry is mainly preserved, in which the white arrows indicate the diffuse reflections that arise from the formation of the spinel structure, while the two bottom patterns (C-D) show the same [100]/[110] and [010] orientations but already degraded to the spinel and rock-salt structure, respectively. The SAED patterns (A) and (C) are obtained from the same particle, showing that the structure does not degrade homogeneously within a single particle during electrochemical cycling. The SAED pattern (D) indexed in the [110] orientation of the rock-salt structure shows some diffuse reflections corresponding to the spinel structure (blue circles), and the sharp reflection marked by orange circles show the presence of a separate domain that still preserves the C2/m symmetry. For the latter SAED pattern, calculated ED patterns corresponding to the different domains and symmetries are shown in Figure 86.*

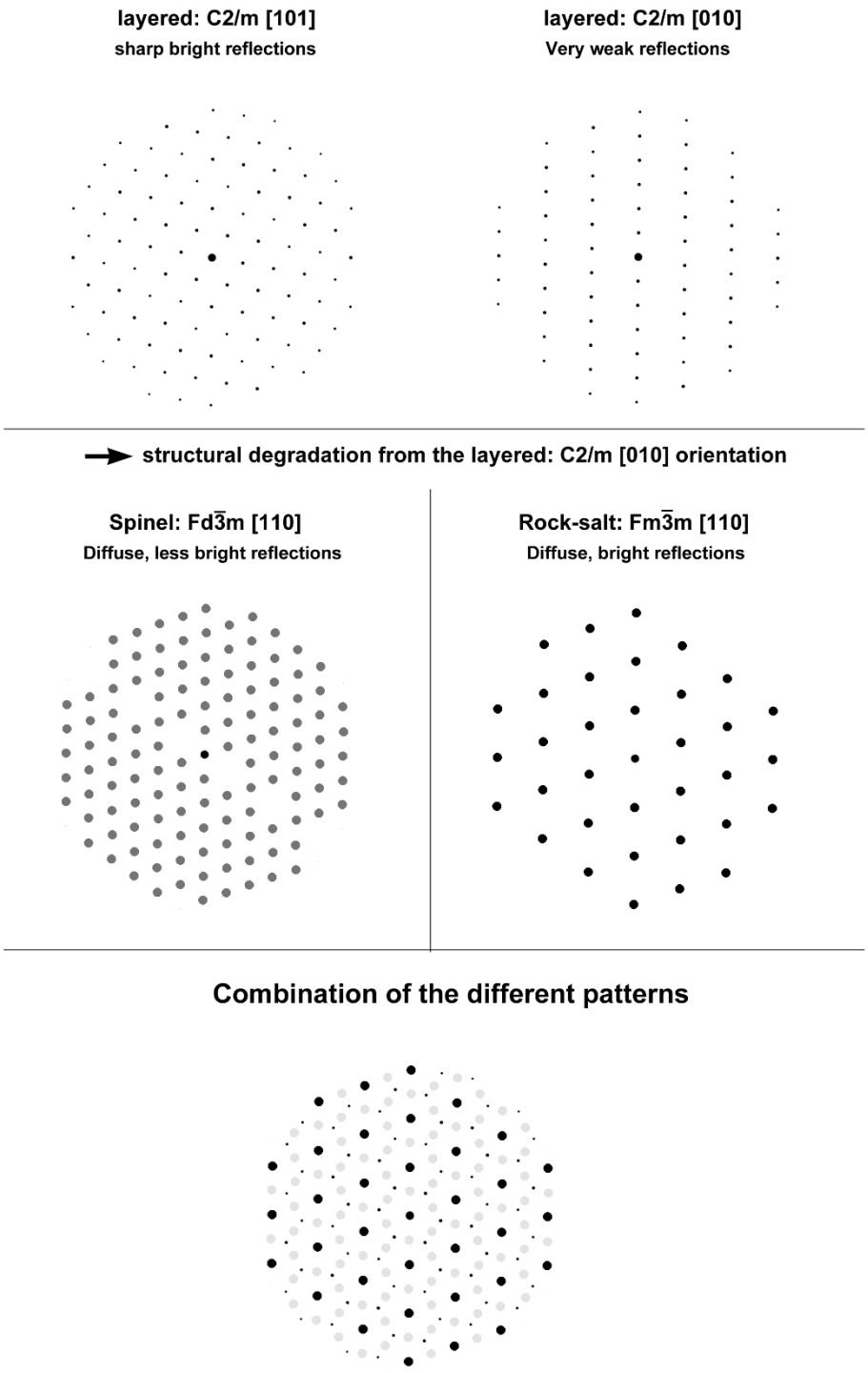

Figure 86. *The different calculated ED patterns that are present in the experimental SAED patterns at the bottom right in Figure 85 are shown separately and combined as in the experimental SAED pattern. Top: the SAED patterns along the two orientations [101] and [010] in the C2/m structure. Middle: SAED patterns along the [110] orientation in the spinel structure Fd-3m and the rock-salt structure Fm-3m (equivalent to [010] in C2/m). The domains corresponding to [010] in the C2/m structure are degraded to these SAED patterns in the spinel and rock-salt structure. Bottom: The combined SAED patterns comparable to the experimental pattern in Figure 85.*

As for the cycled LMO sample, an inhomogeneous structural degradation is observed for the LMTO sample. The SAED patterns of LMTO depicted in **Figure 87C-D** show the presence of spinel $Fd\bar{3}m$ and rock-salt $Fm\bar{3}m$ type structures within a single particle. The indexed reflections are present in the three different structures: layered, spinel and rock-salt, but for both the layered and spinel structure, additional reflections should be present. The weak streaks and reflections that correspond to the *C2/m* symmetry are marked by green arrows and circles respectively, while the blue circles show the weak reflections that could only be indexed by the spinel structure. The indexed reflections are much brighter than those marked by arrows or circles, which indicates that the particle has partially changed to a rock-salt structure where the structure has mixed Li and TM positions. Nevertheless, the weak reflections marked by the arrows (resp. circles), reveal that a small part of the particle still has a layered (resp. spinel) structure. A reduced crystallinity is also observed for the LMTO, as indicated by the broad slightly diffuse reflections in the SAED patterns.

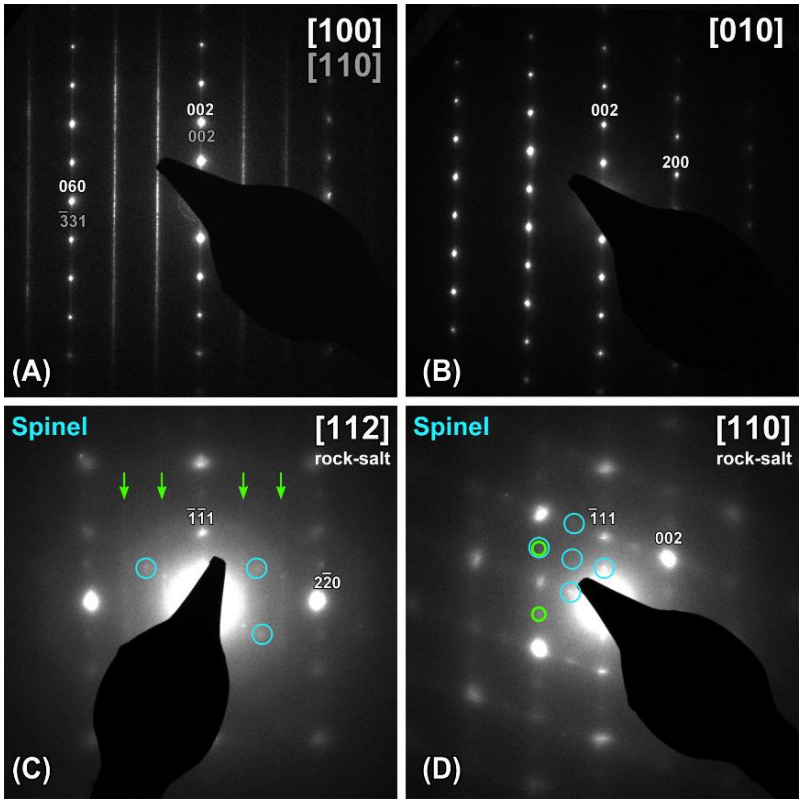

Figure 87. *SAED patterns of the cycled LMTO sample, taken from two different particles divided in top and bottom. The top SAED patterns (A-B) taken along the [010] and [100]/[110] orientations could be indexed in the monoclinic C2/m symmetry, indicating the layered structure is preserved for this particular particle. The bottom two SAED patterns (C-D) could be indexed in the rock-salt structure. The weak streaks and reflections, marked by green arrows and circles respectively, correspond to the C2/m symmetry, while the blue circles show the weak reflections that could only be indexed by the spinel structure.*

Although the SAED patterns show similar structure degradation, the HAADF-STEM images of the cycled LMO and LMTO, shown in respectively **Figure 88** and **Figure 89**, reveal the structural difference that arises after 50 cycles. The majority of the particles of the cycled LMO sample are still crystalline with exclusively an amorphous surface layer, of which the thickness varies between 0 – 10 nm, while in the case of the cycled LMTO, the amorphous surface layer varies from a few nanometres to entire amorphous particles. The average amount of amorphous phase present in the structure is significantly higher for the cycled LMTO sample than for the cycled LMO sample. This difference can be missed by a SAED investigation since particles that are completely amorphous do not show any reflections, thus while mapping the sample in reciprocal space, these particles will go unnoticed.

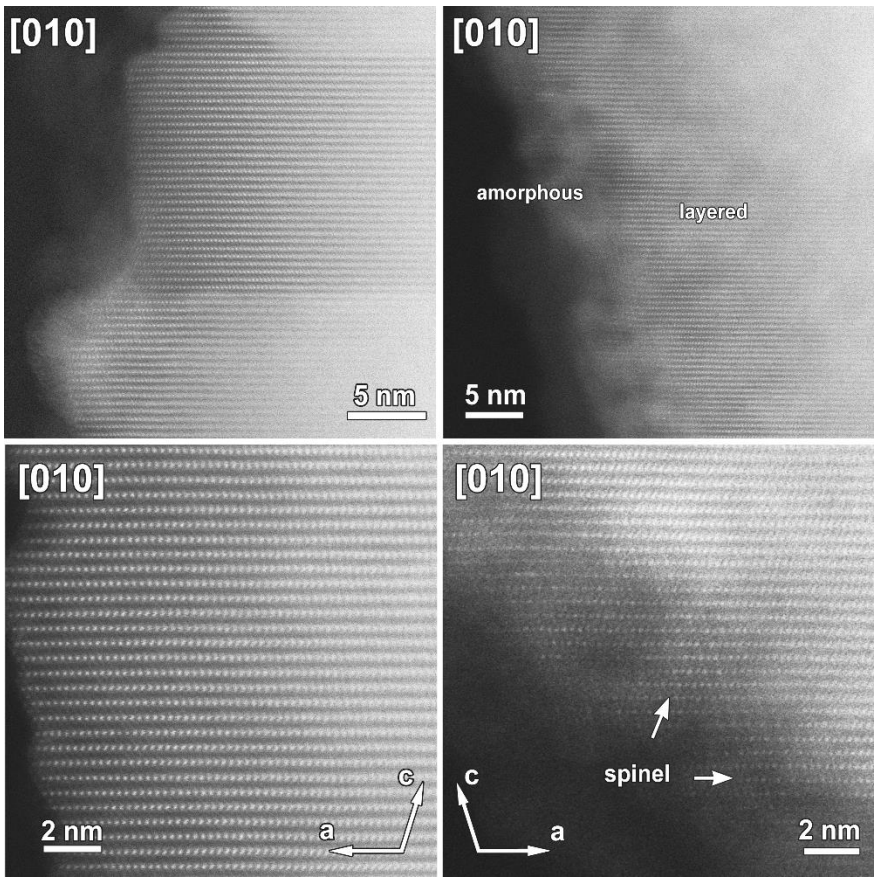

Figure 88. *Representative HAADF-STEM images taken from the cycled LMO sample. Left: particles that remained mainly layered, right: particles with considerable structural degradation at the surface, either amorphous or spinel.*

Based on the TEM study, the structural degradation of the LMTO sample after 50 cycles is significantly higher than for the LMO sample, while the voltage fade is slightly smaller for LMTO. However, the voltage fade of LMTO can only be determined for the last 30 cycles, as the capacity of LMTO first increases in the former 20 cycles. We suggest that the Ti^{4+} stabilises the structure in the first cycles and that the ~20^{th} cycle can be seen as a turning point where the structure becomes subjected to structural degradation. In order to understand how the crystal structure changes during the different cycles, the crystal structure should also be investigated after 20 cycles (i.e. when the capacity is the highest), but to investigate the sample, the electrochemical cell should be opened, which prevents further cycling.

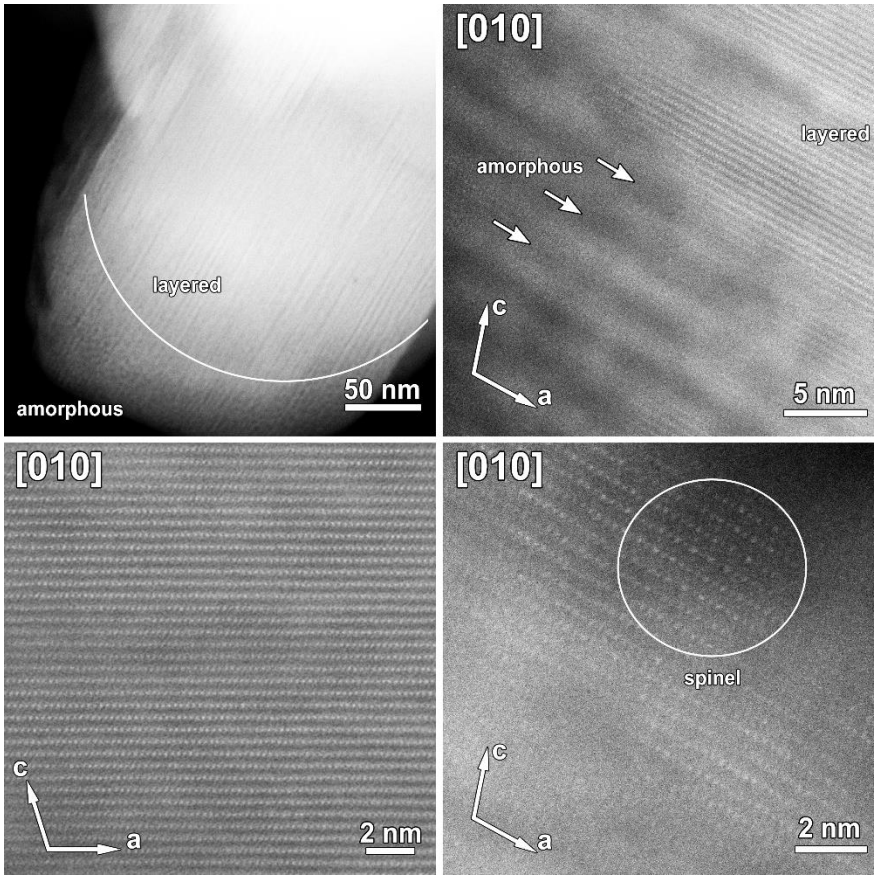

Figure 89. *Representative HAADF-STEM images taken from the cycled LMTO sample. The bulk of the particles is mainly layered (left side images), while the surface is a combination of amorphous and spinel (right-side images). The darker regions are amorphous.*

8.3. Conclusion

The XRPD and STEM-EDX analysis showed that Ti^{4+} could be substituted in Li_2MnO_3. Additional TiO_2 particles were found in the $Li_2Mn_{0.8}Ti_{0.2}O_3$ sample, which is expected to be electrochemical inactive as it does not contain lithium. The TEM study showed that the Ti substituted Li_2MnO_3 preserves the monoclinic *C2/m* symmetry with honeycomb ordering.

Galvanostatic cycling was performed on Li_2MnO_3 (LMO) and $Li_2Mn_{0.8}Ti_{0.2}O_3$ (LMTO) in the voltage interval 2.0 V to 4.8 V vs Li/Li^+. The obtained first charge capacity for LMO only reaches ~60 mAh/g at 4.80 V, which is considerably lower than the theoretical capacity of Li_2MnO_3 of 460 mAh/g, which indicates that the synthesis conditions are most probably not optimal. The synthesis (i.e. solution-gel method) is the same as discussed in Chapter 6 that showed structural modifications at the surface. However, in this case, no structural modifications were observed, which is most probably due to the absence of nickel and cobalt. The observed voltage plateau of both LMO and LMTO is related to irreversible oxygen redox processes, and as the observed voltage plateau of LMTO is significantly smaller than the one observed from LMO, this could indicate that, in the first cycles, Ti^{4+} is able to effectively hamper oxygen release from the sublattice and the corresponding migration of manganese. The discharge capacity during the first cycle of the LMTO sample is about half of the one of LMO, but in the subsequent 20 cycles, the discharge capacity increases up to ~70 mAh/g and eventually drops to a discharge capacity similar to the LMO sample (~35 mAh/g).

Based on the TEM study, we can conclude that after 50 cycles the structural degradation is significantly higher for the LMTO sample than for the LMO sample. Both samples are partially degraded to the spinel and the disordered rock-salt structure, but the HAADF-STEM images reveal that the average amount of amorphous phase present in the structure is significantly higher for the cycled LMTO sample than for the cycled LMO sample.

The comparison between the TEM results and the measured electrochemical properties shows that Ti^{4+} might help to reduce the TM migration in the first cycles, but that after extended cycling the structure is subjected to structural degradation, and Ti^{4+} substitution is not sufficient to mitigate TM migration and voltage fade.

Conclusion Part II

First, the crystal structure and properties resulting from different syntheses were studied. Two different syntheses were performed to produce $Li_{1.2}Ni_{0.13}Mn_{0.54}Co_{0.13}O_2$ (LMR-NMC): solution-gel and co-precipitation. We found that the LMR-NMC particles synthesized by our solution-gel route possess Ni and Co segregation at selective facets, related to a phase transition at these surfaces: Ni-rich spinel structure at the {200} facets; Co-rich rock-salt structure at the {002} and {202} facets. These structural modifications were not observed in the particles synthesized by our co-precipitation route. In literature, we found that for other studies these structural modifications also appear for particles synthesized by the co-precipitation method, indicating that even with the same type of synthesis, small differences in the synthesis method can lead to structural changes which subsequently will result in differences in the electrochemical properties.

The other two studies were performed in an attempt to mitigate the voltage fade present in lithium-rich manganese-based layered oxides: $Li_{1.2}Ni_{0.13}Mn_{0.54}Co_{0.13}O_2$ (LMR-NMC) and Li_2MnO_3. The voltage fade is related to oxygen release and phase transition to the spinel structure, and therefore, we tried to substitute cations (M = Ti^{4+}, Sn^{4+}) with stronger M-O bonds and larger ionic radius, in order to reduce the TM migration and oxygen release.
The Sn substitution in LMR-NMC revealed a limit of Sn solubility of about 8-9%. The TEM study also showed that the substituted $Li_{1.2}Ni_{0.13}Mn_{0.54-x}Co_{0.13}Sn_xO_2$ (x = 0.027) sample preserves the monoclinic *C2/m* symmetry with honeycomb ordering within the Li-TM layers. Similarly, in the study where Ti was substituted in Li_2MnO_3, the substituted $Li_2Mn_{0.8}Ti_{0.2}O_3$ sample preserves the monoclinic *C2/m* symmetry. Unfortunately, for both studies, the cation substitution did not stabilise the structure upon charging, and so, did not succeed in mitigating the voltage fade.

In all these studies, we have investigated these samples *ex-situ.* This means that the sample is cycled outside the TEM, and thus different particles are investigated. Therefore, the crystals investigated of the pristine, charged and cycled state are inevitably always different particles. Consequently, the possible prior existence of structural defects in a specific studied charged/cycled crystal before it was charged or cycled is unknown. For example, we showed in our studies that the amount of stacking faults varies from particle to particle. As a result, using *ex-situ* investigations, it is impossible to track the evolution of defects during cycling. This information is needed to understand better the cause of the TM migration and structural degradation, which are needed to figure out which cation substitutions will succeed in the stabilization of the structure. This can be realized by investigating the particles *in-situ*, which is discussed in the following Part III.

Appendix Part II

Experimental details of TEM study:

The structure and composition of the Li-ion battery cathode materials were studied by transmission electron microscopy (TEM). The samples for SAED, STEM and STEM-EDX were made by crushing the powder in ethanol and subsequently dispersing it in this solution using an ultrasonic bath. The powder used for the particle size investigation was not crushed. A few droplets of the obtained suspension were deposited on a Cu grid covered with a holey carbon layer. The SAED patterns were recorded with a Philips CM 20 and an FEI Tecnai G2 microscope, the HAADF-STEM and ABF-STEM images were acquired with an FEI Titan 80-300 "cubed" microscope operated at 300 kV, and the STEM-EDX mapping was acquired at an FEI Osiris microscope equipped with a Super-X detector and operated at 200 kV.

The charged and cycled samples were transferred to the TEM via a vacuum transfer holder to exclude contact with ambient atmosphere. The charged and cycled samples were prepared in the glove box, where the powder is scratched from the cathode punch and crushed. Then a copper grid with holey carbon layer is dipped into the dry powder.

The experimental details about the other techniques used by the collaborators can be found in the corresponding paper [108].

Synthesis LMR-NMC: sol-gel vs co-precipitation

Aqueous solution-gel method

The first step of the solution-gel synthesis typically involves mixing of dissolved metal salts (e.g. nitrates) with a chelating agent. Citric acid is often used as a chelating agent because due to its three carboxylic groups per molecule, it can form bridges between different metal ions upon deprotonation by increasing the pH. The following step is the solvent evaporation that results in the formation of a viscous gel by crosslinking of the different metal ion ligands. Finally, the thermal decomposition of the multimetal ligand gel during the calcination at elevated temperature leads to highly crystalline particles [96,125].

$Li_{1.2}Ni_{0.13}Mn_{0.54}Co_{0.13}O_2$ was prepared via an aqueous solution-gel method by using aqueous $LiNO_3$, $Ni(NO_3)_2$, $Co(NO_3)_2$ and $Mn(NO_3)_2$ monometal precursors. Consecutively, citric acid ($C_6H_8O_7$, Sigma Aldrich, 99%) was added to an aqueous mixture containing stoichiometric amounts of before mentioned metals in a 1.5:1 ratio of citric acid:TM (TM = transition metal ion). A lithium excess of 5 molar % has been used to compensate for the loss of volatile Li-

containing products at elevated calcination temperatures. After stirring for about 15 min at room temperature to dissolve the citric acid, the pH was increased till ~7 by dropwise addition of NH_3 (Merck, extra pure, 32%). The resulting mixture was refluxed at 80 °C for 1 hour. Afterwards, the mixture was placed in an air flow oven for gelation under atmospheric conditions at 60 °C overnight. The obtained viscous gel was pre-calcined under atmospheric conditions at 200 °C in an air flow oven. The grinded pre-calcined brown-colored powder was decomposed and calcined in a tube furnace at a heating rate of 10 °C/min up to 900 °C with an isothermal period for 12 hours. The heating step up to 900 °C was performed under a dynamic dry air atmosphere (AirLiquide, α1, 99.999%). The isothermal period at 900 °C was performed under static ambient air. After naturally cooling down to room temperature the end product has been grinded and stored in closed glass vials in an Argon glovebox for further use.

Co-precipitation method

The co-precipitation synthesis involves two main steps: in the first step, particles are formed and precipitated during the co-precipitation reaction initiated by the simultaneous addition of dissolved metal salt starting products and co-precipitating agent at controlled pH. The precipitate is typically washed and centrifuged for multiple times to remove the precipitating agent's metal cation, the metal salt's counterion and non-reacted starting products. Inevitably, a fraction of the precipitate is also washed away. The materials after washing are dried to remove the remaining solvent. In the second step, the precursors are mixed with a lithium source and calcined at elevated temperatures to produce the final active cathode material [97]. $Li_{1.2}Ni_{0.13}Mn_{0.54}Co_{0.13}O_2$ was prepared by a carbonate co-precipitation method, where the precursor is a mixed Ni, Mn, Co carbonate phase. The co-precipitation reaction was performed in a stirred Globe batch reactor (Syrris Ltd., UK) under N_2 atmosphere at 60 °C. Stoichiometric amounts of $NiSO_4.7H_2O$, $CoSO_4.7H_2O$, $MnSO_4.H_2O$ (all – Ruskhim, ≥ 99 %.) are dissolved in distilled water. On forehand, the water content has been determined via TGA measurements (Netzsch STA 449 F3 Jupiter). The mixture with a total metal ion concentration of 2 mol/L was added dropwise at room temperature simultaneously with a 2 mol/L Na_2CO_3 (Ruskhim, 99.5 %) solution at a fixed rate of 1 mL/min into the reactor (preheated at 60 °C) under continuous stirring whilst adjusting the pH to stay constant at 7.5 by addition of dilute NH_3 (Khimmed, puriss. p.a. ≥ 25% NH_3 in H_2O) or H_2SO_4 (Khimmed, 98 w. % H_2SO_4 in H_2O). After six hours the stirrer and temperature controller were automatically switched off. The resulting precipitate was washed by distilled water and centrifuged for three minutes at 5700

rpm for three times. After drying at 75 °C overnight in a vacuum furnace, the intermediate precipitate NMC was obtained, which was dry mixed with Li_2CO_3 (Sigma Aldrich, anhydrous ≥99%). An excess of 10 mol % Li_2CO_3 was added over the stoichiometric amount to compensate for lithium loss during calcination. After grinding, the samples were consecutively calcined at a heating rate of 5 °C/min up to 500 °C with an isothermal period for 5 hours. Then they were naturally cooled down, grinded again for 15 min by mortar and pestle, and calcined at a heating rate of 5 °C/min up to 900 °C with an isothermal period for 12 hours in a tube furnace. The heating step up to 500 °C was performed under a dynamic dry air (AirLiquide, α1, 99.999%) atmosphere. The isothermal period at 500 °C and the full calcination at 900 °C were performed under static ambient air. The resulting product LMR-NMC was grinded after naturally cooling down to room temperature and stored in closed glass vials sealed with parafilm under ambient air for further use.

Synthesis unsubstituted and Ti-substituted Li_2MnO_3:

$Li_2Mn_{1-x}Ti_xO_3$ has been prepared via an aqueous solution-gel method. Aqueous Li citrate and $Mn(NO_3)_2$ precursors are obtained by dissolving respectively Li(I) citrate hydrate ($Li_3C_6H_5O_7.xH_2O$, Sigma Aldrich, 97%) and Mn(II) nitrate hydrate ($Mn(NO_3)_2.xH_2O$, Sigma Aldrich, 98%) in Milli-Q water. An aqueous Ti^{4+} solution precursor is prepared by adjusting the protocol described by Hardy *et al.* [126] An amount of 6 mL of Ti(IV) isopropoxide ($Ti[OCH(CH_3)_2]_4$, Acros Organics 98+%) has been added to 60 mL of Milli-Q H_2O. The obtained titanium oxyhydroxide precipitate has been washed with water by means of vacuum filtration. In the meantime, 3.84 g of citric acid ($C_6H_8O_7$, Sigma Aldrich, 99%) has been dissolved in 10 mL of Milli-Q H_2O and subsequently mixed with 2 mL hydrogen peroxide (H_2O_2, Merck, 35%). This mixture has been added to the washed precipitate and stirred at 60 °C to dissolve the precipitate. Hereafter the pH is increased till 6.5 by dropwise addition of ammonia (NH_3, Merck, extra pure, 32%). Nextly, the precursor is heated at 108 °C for about 10 min. After cooling down to room temperature the pH has been increased by the dropwise addition of NH_3 till 7. After vacuum filtration and adjusting the total volume to 100 mL, the final 0.2 M Ti^{4+} solution precursor has been obtained. The concentrations of the monometal precursors have been determined by inductively coupled plasma coupled with atomic emission spectroscopy (ICP-AES, Optima 3300 DV, PerkinElmer). Citric acid (CA, Sigma Aldrich, 99%) has been added to an aqueous mixture containing stoichiometric amounts of Li citrate, $Mn(NO_3)_2$ and Ti^{4+} solution precursors in a 2:1 CA:$Mn(NO_3)_2$ molar ratio. A lithium excess of

10 molar % has been used to compensate for the loss of volatile Li-containing products at elevated anneal temperatures. After stirring for about 15 min at room temperature (RT) to dissolve the citric acid, the pH is increased till ~7 by dropwise addition of NH_3 (NH_3, Merck, extra pure, 32%). The resulting mixture is refluxed at 80 °C for 1 hour. Afterwards, the mixture is placed in an oven for gelation under atmospheric conditions at 60 °C overnight. The obtained viscous gel is pre calcined under atmospheric conditions at 200 °C. The grinded pre calcined brown-colored powder is consecutively annealed at 500 °C for 5 hours under dynamic O_2 (Air Liquide, industrial) atmosphere, cooled down and grinded for 15 min by mortar and pestle and annealed at 900 °C for 12 hours under dynamic dry air atmosphere (DA, Air Liquide, α1) during the heating step (DA gas bottle is closed after reaching a furnace temperature of 900 °C). Both anneals were performed in a tube furnace. A heating rate of 5°C/min has been applied for heating up to respectively 500 °C and 900 °C. Li_2MnO_3 has been prepared via the same procedure as described above while excluding the addition of Ti^{4+} solution precursor. The obtained end products have been grinded and stored sealed in glass vials in an Argon-filled glovebox for further use.

Part III: *In-situ* TEM

In the last part of my thesis, I will dedicate a short Chapter to my first attempts at working with an *in-situ* electrochemical liquid cell inside the TEM. In **Chapter 9**, I will first explain the importance of these *in-situ* experiments. Then I will point out the challenges and problems I have encountered during the experiments along with the possible solutions to tackle these problems. Finally, in the conclusion, I will summarize the following steps needed to progress with these *in-situ* experiments.

Chapter 9. *In-situ* electron diffraction using an electrochemical liquid holder

9.1. Introduction

As discussed in Part II, *ex-situ* experiments are not sufficient to solve all the questions related to the structural changes induced during charging and discharging of the Li-ion battery cathode materials and leaves room for misinterpretation of artefacts due to air exposure, vacuum exposure and relaxation as being real cycling-related changes. Furthermore, we have shown that the pristine layered cathode materials can contain initial structural defects, such as disordered honeycomb layers and transition metals in the tetrahedral positions or in the lithium layers. When the charged material is investigated *ex-situ*, there is no knowledge of the initial structural defects that might be present, which complicates the investigation of the structural changes directly caused by the charging and discharging. In addition to that, stacking faults are known to exist in pristine as well as in charged layered battery cathode materials, but their evolution upon cycling has not yet been studied, due to a lack of appropriate techniques. As the stacking faults change the available diffusion paths, they might very well also be correlated with battery degradation. Therefore, it would be of great interest to investigate the crystal- and microstructure evolution upon cycling.

In order to solve these questions and follow the structure evolution upon cycling, the same particle should be studied in the different stages, i.e. pristine, charged, discharged, which can be achieved by *in-situ* TEM. This means that the particle is studied in the same environment in which it underwent changing conditions, in this case charging and discharging. Therefore, in the last part of my PhD, I started to work *in-situ* using an environmental liquid holder in order to create an electrochemical cell inside the transmission electron microscope to study the structural changes directly upon charging (**Figure 90A**). Although the cell itself is commercially available, it has not yet been used in literature to study changes in the crystal structure, only for low magnification imaging.

In order to investigate the crystal structure of these particles in liquid, the final goal is to be able to use electron diffraction tomography (EDT). EDT is based on the acquisition of a series of electron diffraction patterns by tilting a crystal around a random single axis, from which the complete structure can be refined (**Figure 90B-D**) [127,128]. In this chapter, we will only focus on the acquisition of a single electron diffraction pattern in the filled liquid cell, as even this has not yet been reported in literature.

The acquisition of an electron diffraction pattern in liquid is challenging due to the strong scattering of the electrons by the thick liquid layer, which significantly decreases the signal-to-noise ratio [129,130]. The liquid also drastically reduces the resolution, which makes it impossible to acquire high-resolution images to solve the crystal structure. Up to date, the only successful *in situ* EDT experiment in an electrochemical cell was only possible after partially evaporating this thick layer of liquid using an intense electron beam [131]. This evaporating of the liquid left contamination behind on the investigated crystal, both a carbon layer and in the form of nanoparticles, blocking further electrochemical reactions. Thus, such procedure would not allow following the structure evolution among different cycles. It can only observe one step per crystal and per experiment. Therefore, we want to explore the possibilities for eliminating the need for partially evaporating the liquid by using a thinner cell.

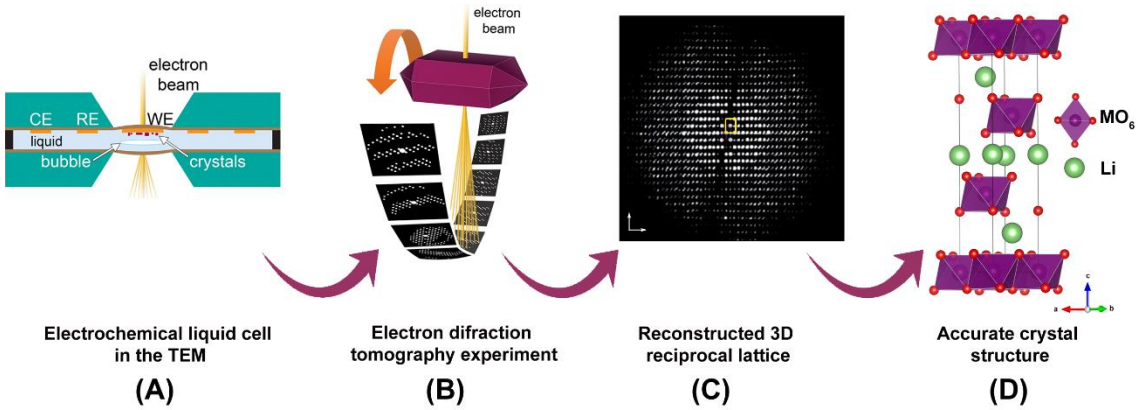

Figure 90. *The in-situ EDT procedure to determine the crystal structure, based on [131].* ***(A)*** *illustrates the electrochemical liquid cell inside the TEM, whereas* ***(B)*** *demonstrates the EDT experiment that will be performed on a particle in the liquid cell.* ***(C)*** *shows the reconstructed reciprocal space acquired from the EDT series, that will be used to refine the structure* ***(D)****.*

We carry out our *in-situ* experiments using the Liquid Stream holder that has considerably less space between the windows, and thus a thinner liquid layer, than previously available TEM electrochemistry cells. The nano-cell chip is composed of a bottom and top chip with a spacing between both chips of 200 nm that create the electrochemical nano-cell. The windows of both chips are 50 nm thick SiN membranes that are transparent for the electrons. The bottom chip is shown in **Figure 91** and contains a counter (C), a reference (R) and a working (W) electrode, which are all non-transparent Pt electrodes. The end of the working electrode is decomposed in branches that partially lie in the SiN window. Particles should be deposited on the working electrode where the electrochemical reaction takes place (i.e. charging and discharging).

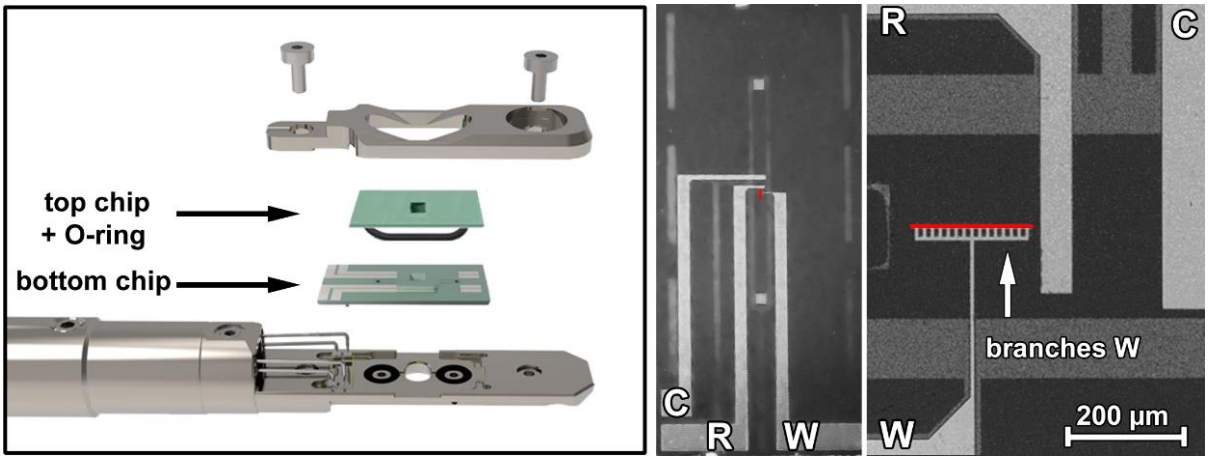

Figure 91. *Left: Design of the liquid Stream holder that consists of a bottom and top chip with an O-ring in between to seal the nano-cell. Right: images of the bottom chip, where W, C and R represent the Pt working, counter and the reference electrode, respectively. The end of the working electrode is composed of branches that partially lie in the SiN window, which is coloured in red.*

In the environmental liquid holder, the liquid flows through the electrochemical cell by internal tubing that is connected to a flow system based on the differential pressure, where the flow is controlled by the pressure in the inlet and outlet tube. This flow system should allow reducing the thickness of the liquid that can make the signal from the crystal itself stand out better from the signal from the liquid. The flow system also allows refreshing the liquid in between data sets if necessary, removing contamination.

An electrochemical cell is composed of an anode, cathode and an electrolyte. In the nano-cell in the environmental liquid holder, the working electrode, together with the investigated Li-ion battery cathode material that is attached to the working electrode, operates as the cathode, whereas the counter electrode will function as the anode. The electrolyte is a lithium conducting liquid, and in our experiments, we will use $LiPF_6$ in a solution of (1:1) EC/DMC.

One of the main challenges is the fact that the electron beam reacts with the liquid and causes a high amount of inelastic scattering, which will drastically reduce the signal-to-noise ratio, and thus the quality of the electron diffract pattern. Therefore, it is very important to control the thickness of the liquid inside the electrochemical cell and optimize the sample preparation and the set-up of the experiment. These challenges will be discussed in the next section.

9.2. Experimental results

9.2.1. Sample preparation and deposition

The spacing between the bottom and top chip is 200 nm without liquid. When liquid goes through the nano-cell, the SiN windows will bulge, and the spacing between the bottom and top window will increase to approximately 500 nm. As the layer of liquid will disperse the electron beam, the thinner the liquid layer, the better the signal-to-noise ratio. Therefore, the particles of interest should be big enough, because when the particles are too small (**Figure 92A**), the contribution of the inelastic scattering of the liquid is much higher than the elastic scattering of the particle, resulting in a bad signal-to-noise ratio. On the other hand, when the particles are too big (**Figure 92B**), the SiN windows can break when the top and bottom chips are sealed, or can bulge which significantly increases the liquid thickness, which in turn leads to a bad signal-to-noise ratio. Therefore, we want to achieve a particle size ranging between 100 - 200 nm.

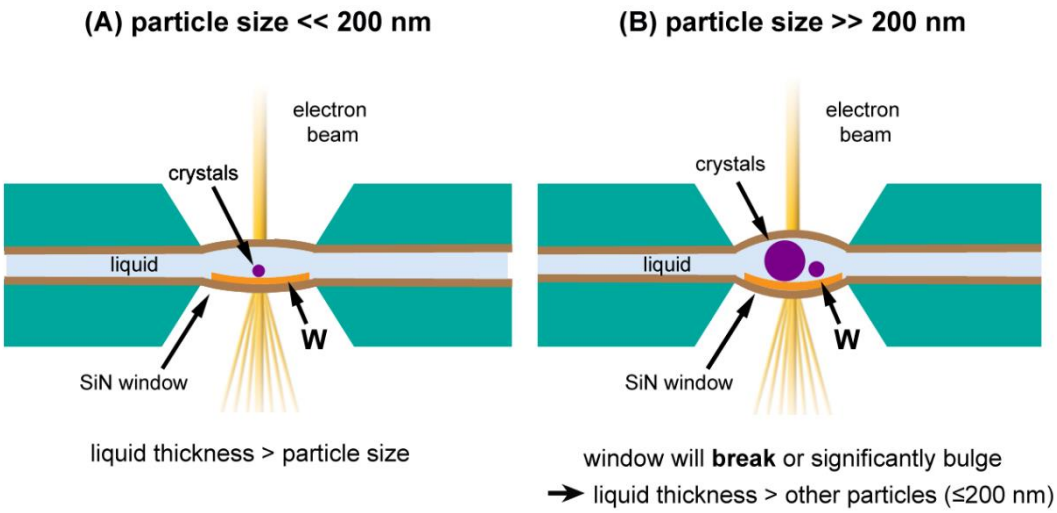

Figure 92. *Illustration of the influence of the particle size on the signal-to-noise ratio.* ***(A)*** *When the particles are too small, the contribution of the liquid will be much higher than the contribution of the particle, resulting in a bad signal-to-noise ratio.* ***(B)*** *When the particles are too big, either the windows can break or bulge. In the case the windows bulge, the thickness of the liquid will significantly increase, and will also result in bad signal-to-noise ratio. Ideally, the particles should range between 100-200nm.*

To obtain a particle size between 100-200 nm, the sample is crushed in a mortar with ethanol, followed by sonication of about 60 min to prevent clustering. Then by sedimentation between 24-48 hours, depending on the sample, the top layer is separated and used as a new solution. Depending on the size distribution, this procedure can be repeated. The solution is always stored in a glass vial to avoid contamination. We have also tried to make use of a sterile cellulose filter with a pore size of 200 nm, but it absorbs almost all particles larger than approximately 100 nm.

The next step is to drop cast the particles onto the bottom chip. In order to investigate the deposited sample on top of the chip, scanning electron microscopy (SEM) is used. This technique is based on the detection of the secondary electrons, which originate from the surface and the near-surface regions of the sample and provides information about the surface of the sample [132]. As shown in **Figure 93**, the window on which the sample will be deposited has a width of only 7-8 µm. The bottom chip is first plasma cleaned with Ar 100% for 60 seconds to make the SiN window hydrophilic in order to attract the particles in the solution. Once the droplet of solution has dried, we examine the bottom chip in the TEM or SEM to check for the presence of particles on the SiN membrane. When no particles are attached to the SiN membrane, this procedure can be repeated until we find a few particles on the SiN membrane, after which we can seal the top and bottom chip in the liquid holder.

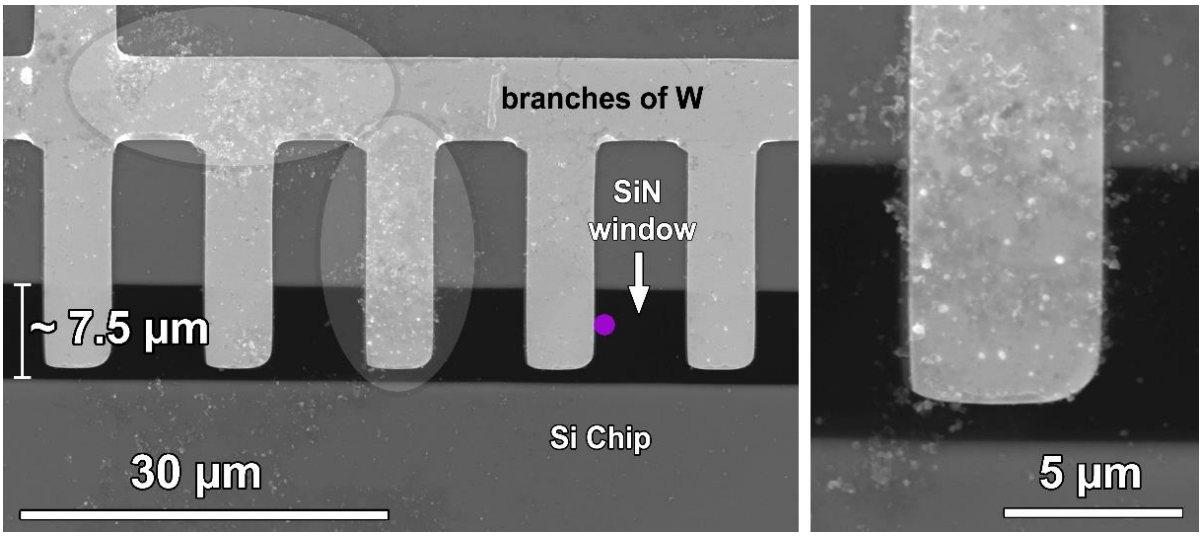

Figure 93. *SEM images of the deposition of the powder onto the bottom chip. The particles are first attracted to the Pt electrodes, which are approximately 70 nm thick and lie on top of the SiN window. The purple dot shows the ideal position for a particle to investigate.*

As can be seen in **Figure 93**, the particles are attracted to the Pt electrode and the surrounding Si chip rather than to the SiN windows. As the Pt electrodes are not transparent for electrons, the investigated particle should lie at the side of the electrode (position is marked as a purple dot in **Figure 93**). In this way, the particle is connected to the electrode and can be cycled, while the particle lies in the transparent region (i.e. the SiN window) that allow us to investigate the particle. The Pt electrode lies on top of the SiN window and has a thickness of ~70 nm. This means that the droplet of solution will first touch the electrode. In order to get particles on the window, many drops are needed resulting in a large cluster on the Si chip and electrode. This will eventually lead to an increase of the spacing between the top and bottom chip which is detrimental for the liquid thickness and thus the signal-to-noise ratio for the diffraction patterns.

We have also tried to reduce the accumulation of particles at the electrodes and Si chip by using double-sided tape to protect the chip, as shown in **Figure 94**. Most of the chip is covered with the tape to keep it clean, but still, the area that is exposed to the solution is too big compared to the size of the window. This means that the particles will still cluster on top of the electrodes. We have also observed that the glue of the tape dissolves due to the ethanol present in the solution. The contamination originating from the glue and the clusters of particles will also lead to an increased distance between the top and bottom chip.

Figure 94. *Illustration of the double-sided tape method we have tried. The left image is a photo of the tape used to cover the chip. The right image is an SEM image of how the chip looks after the deposition with the double-sided tape method.*

To overcome this problem, a high-resolution deposition technique should be used to control the deposition on micro-scale. One of the strategies in literature is a silicon mask with an opening of the same size as the SiN window to allow the whole SiN window to be covered with particles after drop-casting, as shown by Ortiz Peña [133]. Another strategy was proposed very recently by Tarnev *et al.* [134], where they deposit particles on micro-scale by scanning electrochemical cell microscopy (SECCM) derived approach using a pulled glass capillary filled with the solution of interest. The capillary approaches the chip surface in air until a fast feedback loop stops the approach when the droplet at the end of the capillary comes in contact with the chip surface. Subsequently, the particles from the solution are deposited at the droplet landing site of only a few micrometres.

9.2.2. Flushing the liquid through the nano-cell

During the experiment, the liquid (i.e. the electrolyte DMC/EC (1:1) with 1M $LiPF_6$) flushes through the nano-cell by changing the pressure difference from the inlet and outlet. During the TEM study, the liquid flow is stopped by setting the pressure difference to zero. However, during the acquisition, we have observed that the thickness of the liquid fluctuates, as shown in **Figure 95**. Besides the particles, also the electrodes are not visible through the bubble of liquid, indicating that the liquid is at least a micrometre thick or even thicker. These variations will vary the contribution of inelastic scattering, which, in turn, will affect the intensity of the reflections and introducing errors in the structure refinement.

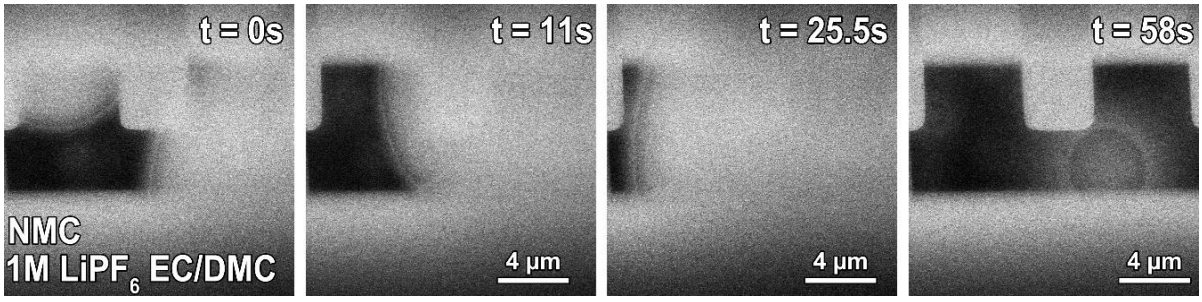

Figure 95. *STEM images of the SiN window with the branches of the working electrode. As the electrode is Pt, these electrodes are not transparent and are shown as bright branches on the transparent dark window. When no pressure difference is applied, the liquid moves inhomogeneously through the nano-cell.*

The variation of the thickness of the liquid is a result of the drop-casting of the particles. As mentioned in the previous section, the particles cluster on top of the electrode, which increases the space between the bottom and top chip, giving the liquid more freedom to flush through the chip. When the cluster of particles on top of the electrodes exceeds the thickness of 200 nm, the spacing between the top and bottom chip also become more than 200 nm. In **Figure 96**, the blue lines represent the spacers that control the spacing between both chips. Inside these spacers, the flow of the liquid is controlled, where the liquid enters the nano-cell at the inlet and leaves the nano-cell at the outlet. When the spacing between the chips is larger than 200 nm, the liquid is able to pass the spacers and will cover the whole chip. When such a big area is covered with liquid, the liquid is not controllable anymore and will create liquid bubbles even without a differential pressure.

In order to control the liquid flow better and to achieve a homogeneous flow, we first have to tackle the problem of the deposition of the particles. When the particles (size ≤ 200 nm) are deposited on the window, the spacing between the top and bottom chip will only be defined by the spacers, which are 200 nm thick. Consequently, the liquid should only flow within the blue area (**Figure 96**) and should be much better controlled.

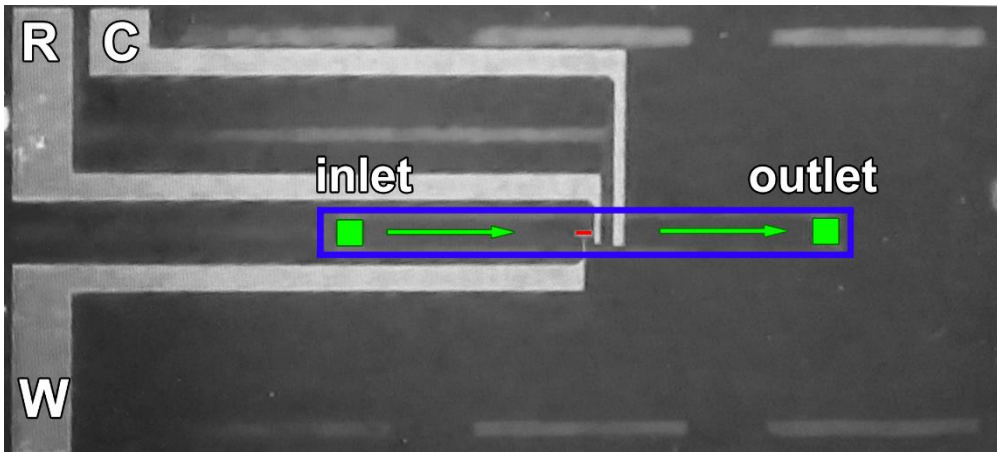

Figure 96. *Image of the bottom chip. The blue line marks the spacers that have a thickness of 200 nm to create the spacing of 200nm between the top and bottom chip. The green arrows show the flow direction from the inlet to the outlet, which are both marked by green squares. The SiN window is marked in red.*

9.2.3. Acquisition of diffraction patterns

Despite the problems with the liquid flow and the deposition of the particles, we have tried to acquire electron diffraction patterns. The problems above will increase the liquid thickness, and therefore, we have chosen to first work with gold nanoparticles in water to investigate and optimize the TEM conditions in order to acquire an electron diffraction pattern. Gold (Au, Z = 79) has a much larger scattering factor than the layered battery cathode materials, which consist of relatively light elements (Z < 30), resulting in a better signal-to-noise ratio for the diffraction pattern.

Gold nanoparticles were deposited onto the window of the bottom chip. **Figure 97A** shows a clear electron diffraction (ED) ring pattern (i.e. a combination of ED patterns of multiple particles randomly oriented) taken from the gold nanoparticles without liquid. The electron diffraction patterns shown in **Figure 97A-C** are obtained with conventional SAED in TEM mode. **Figure 97B** shows a diffraction pattern when the nanoparticles are embedded in water. Due to the inelastic scattering of the water, no clear reflections originating from the nanoparticles are observed. Then the liquid was partially removed, and only very weak reflections could be observed (**Figure 97C**). However, for our experiments, the acquisition has to be done when the cell is completely filled with liquid to ensure the particles are completely embedded in liquid.

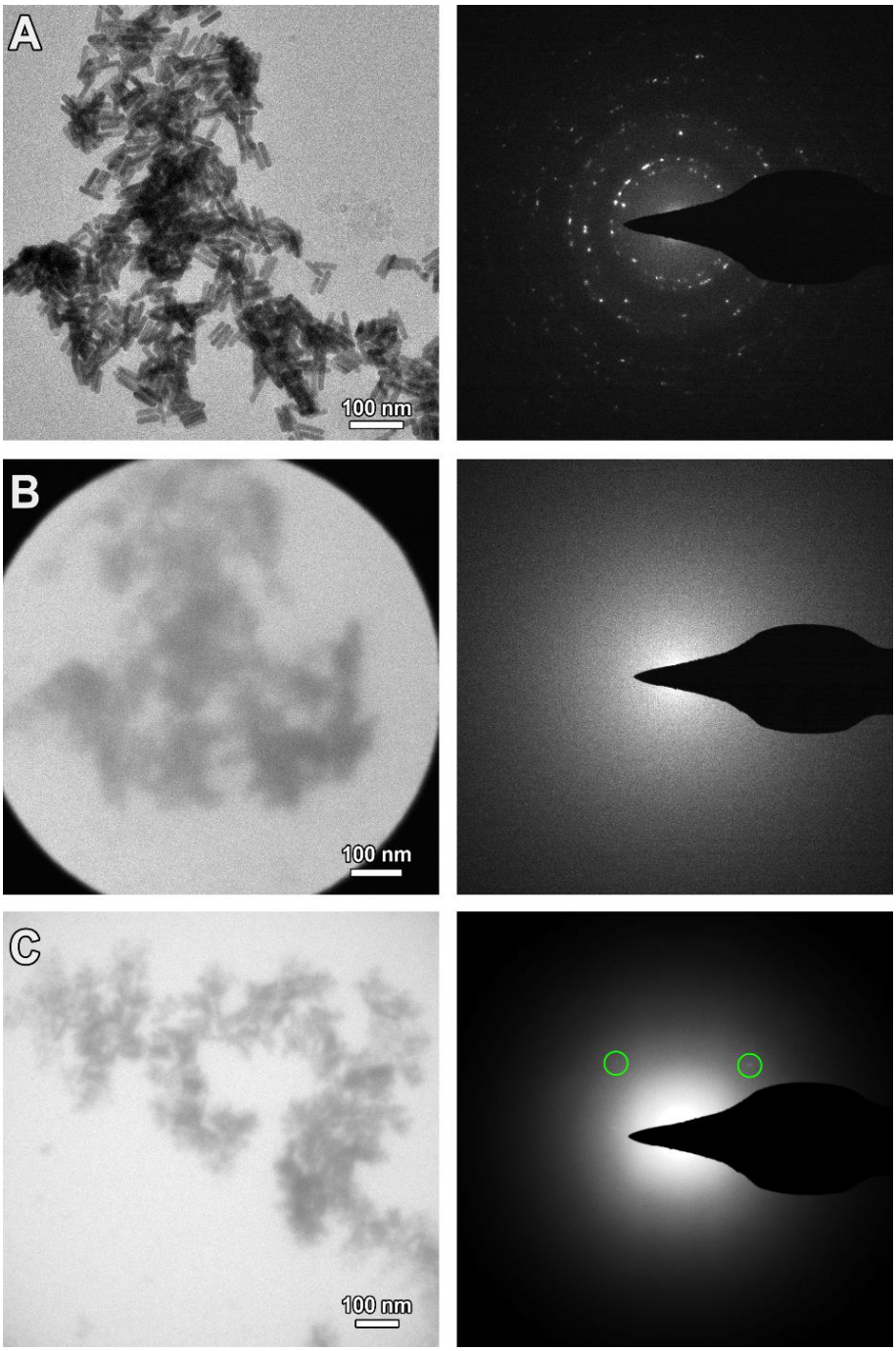

Figure 97. *Selected area electron diffraction patterns taken from gold nanoparticles* ***(A)*** *without liquid,* ***(B)*** *with liquid and* ***(C)*** *when the liquid is partially removed.*

In order to improve the signal-to-noise ratio, we started to work in STEM microprobe, which provided a better signal for diffraction. In liquid, it is important to minimize the area exposed by the beam during the TEM acquisition in order to reduce contamination, but more importantly, to reduce the contribution of the inelastic scattering from the liquid. Therefore, I tried to use scanning-TEM (STEM) diffraction with a quasi-parallel microprobe [135–137]. Conventional TEM diffraction works with a widespread parallel beam, where a selected area (SA) aperture selects the region of interest to create the corresponding diffraction pattern, whereas, in STEM microprobe only the area needed for the diffraction pattern is illuminated. The size of the microprobe can be adjusted to the size of the particle of interest, which improves the signal-to-noise ratio by reducing the contribution of background scattering. In our experiments, the size of the microprobe was approximate ~ 200 ± 50 nm.

Figure 98 shows diffraction patterns from gold nanoparticles in liquid obtained in the STEM microprobe mode. The diffraction patterns taken from the gold nanoparticles in **Figure 98A-B** shows reflections, indicating that this method provides a better signal for diffraction patterns than conventional SAED in TEM mode. However, the intensity and sharpness of the reflections in both patterns are significantly different, which arises from the thickness of the liquid. The ED pattern shown in **Figure 98A** is taken from nanoparticles that are flushed through the nano-cell with the water (i.e. without drop-casting). In contrast, the nanoparticles in **Figure 98B** are drop-casted, which proves the detrimental influence of the deposition of the particles on the thickness of the liquid and thus, the quality of the diffraction patterns. Finally, we also used this technique for a lithium-ion battery cathode material (LMR-NMC) in the lithium conducting electrolyte. The quality of the pattern is worse compared to the gold nanoparticles. However, this ED pattern confirms that with this technique, we are able to observe reflections without the need to evaporate the liquid. Note that the reflections in the last image are more disc-shaped than in the other two ED patterns because in this case, a bigger C2 aperture was used that causes a higher convergence angle (i.e. incident beam is not quasi-parallel anymore). Bragg reflections are sharp reflections when the incident beam is parallel, but when the beam is converged, the reflections become disk-shaped reflections.

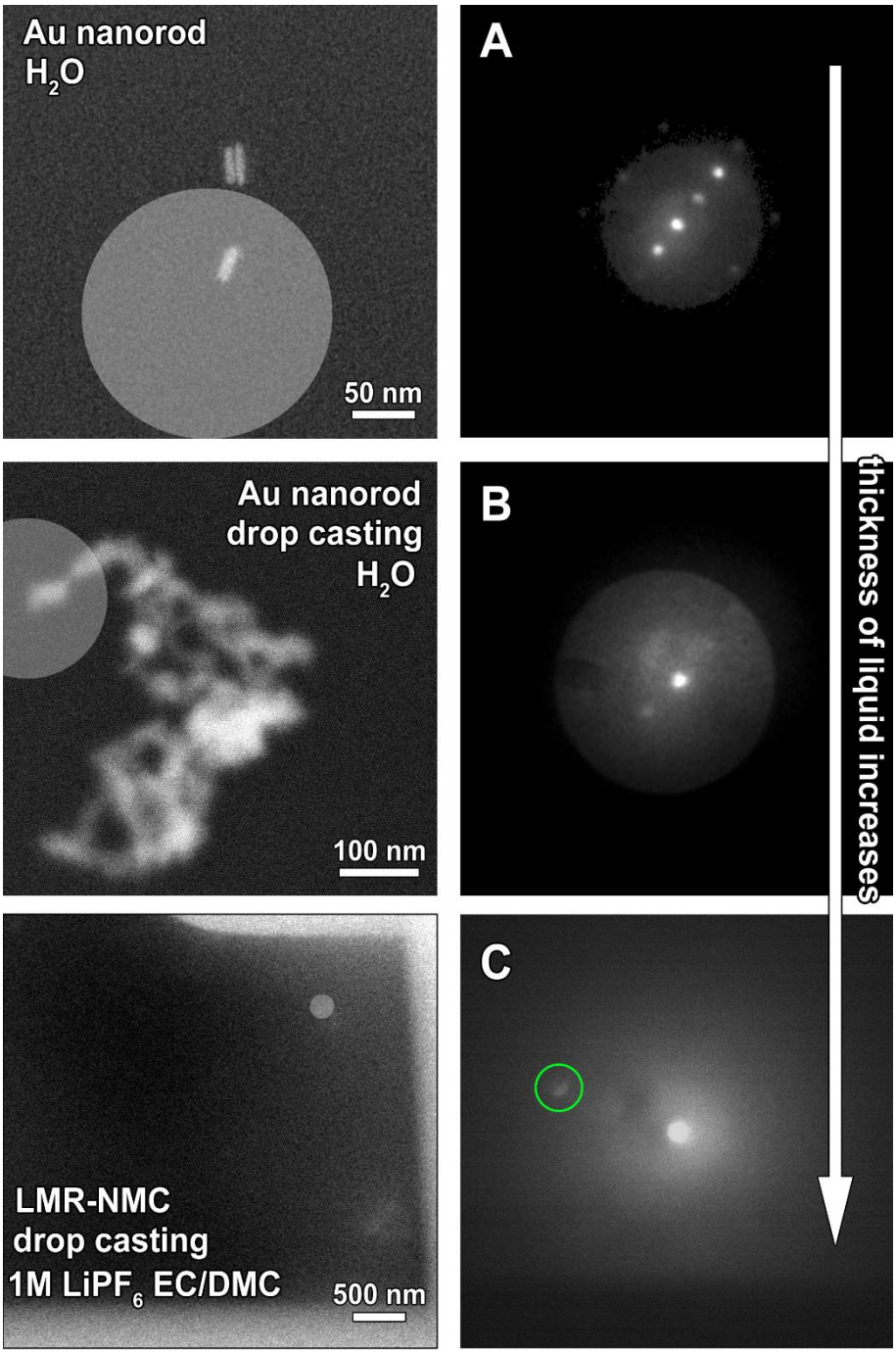

Figure 98. *Electron diffraction patterns taken with a STEM microprobe of* ***(A)*** *gold nanoparticles in water that were flushed,* ***(B)*** *gold nanoparticles in water that were deposited onto the window, and* ***(C)*** *Li-ion cathode material in the electrolyte, which was also deposited onto the window. The grey circles mark the electron beam position.*

We also investigated the stability of the nanoparticles under the electron beam to investigate whether we have to consider to flush our particles rather than depositing them. **Figure 99** shows that the orientation of the flushed gold nanoparticles is unstable under the electron beam, as the diffraction pattern slightly changes. The nanoparticles are not well attached to the SiN window, and thus, will rotate under the electron beam. The rotation of the particle due to the electron beam will affect both the position and intensity of the reflections of the diffraction pattern. Stability of the particles is very important during the acquisition of the EDT series; otherwise, it can introduce artefacts in the reconstructed 3D reciprocal lattice used for the characterization of the crystal structure.

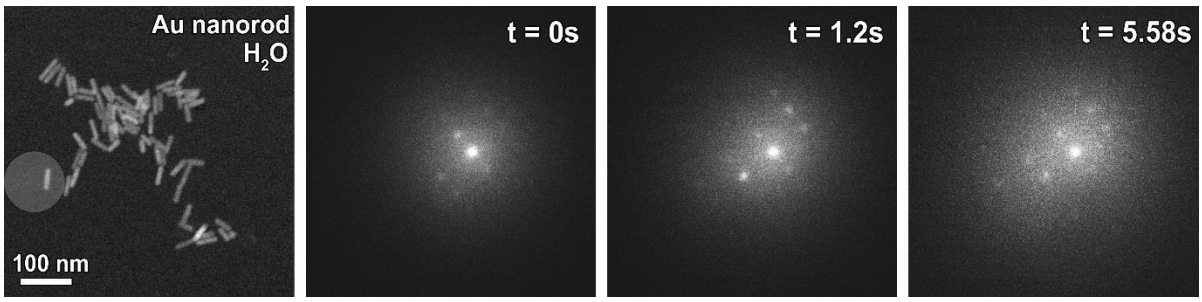

Figure 99. *Left: HAADF-STEM image of the gold nanoparticles. Right: The electron diffraction patterns obtained in STEM microprobe mode of the region marked in the HAADF-STEM image. The electron diffraction pattern changes due to a change in orientation of the particle caused by the electron beam.*

From the different studies done with the environmental liquid holder, we suggest that with the microprobe STEM mode it is possible to obtain a useable signal-to-noise ratio for the electron diffraction patterns, at least in the case of heavy atom compounds already, which scatter strongly.

The next step is the optimization of the deposition of the particles on the SiN window but in contact with the working electrode. A very promising method proposed in literature is based on using a drop dangling from a nanocapillary, which closes an electric circuit when touching the electrode, leading to an automatic stop of all movement [112]. For this, a scanning electrochemical microscope is necessary, which currently is not available in our group. Therefore, the deposition method has to be left for future research outside of the scope of this thesis.

9.3. Conclusion

In this study, we have investigated the optimal method to acquire electron diffraction patterns in the filled liquid cell, by comparing two techniques: conventional SAED in TEM mode and STEM microprobe ED. From the experiment, we can conclude that the signal-to-noise ratio of the electron diffraction patterns obtained with the microprobe STEM method is better than for the patterns obtained with conventional SAED in TEM.

The studies have also shown that the deposition of the particles onto the SiN window is the main problem. The particles are more likely to cluster on top of the non-transparent Pt electrodes and Si chip than on the transparent SiN window, which results in an increase of the liquid thickness and reduces the controllability of the liquid flow. This, in turn, drastically decreases the signal-to-noise ratio of the electron diffraction patterns.

We have tried different strategies to overcome this problem. We have investigated the possibility of flushing the sample with the liquid through the nano-cell instead of drop-casting. This study was done with gold nanoparticles, and flushing the particles after sealing the nano-cell prevented the particles to cluster, which resulted in a better signal-to-noise ratio of the diffraction pattern. However, the orientation of the flushed particles slightly changed under the electron beam as they were not well attached to the SiN window or electrode. Therefore, to ensure the immobilization of the particles, we conclude that flushing the particles is not a valuable strategy to avoid clustering. Another strategy we have tried was creating a mask of double-sided tape to cover the chip except for the window, but the exposed area was still too large, and the tape left contamination behind on the chip. Because of the micrometre dimensions of the window, a high-resolution deposition technique is needed to deposit the particle at the area of interest. A possible solution was published recently, using the nano-capillary based method [134]. Unfortunately, the necessary instrumentation for this technique is currently not available in our group. Therefore, further research into the deposition method is left for future research outside of the scope of this thesis.

The next step is to optimize the deposition of the sample on the SiN window at the side of the electrode by trying the nano-capillary based method [134]. Next, the TEM conditions should be optimized for the acquisition of microprobe STEM electron diffraction specifically for Li-ion battery cathode materials instead of nanoparticles. In this case, a balance has to be found between a high enough electron dose to achieve a good signal-to-noise ratio of the electron diffraction pattern and a low enough electron dose to prevent decomposition of the electrolyte or radiation damage of the Li-ion battery cathode material itself during cycling.

General conclusion

The main focus of my thesis is the investigation of the crystal structure of new materials and the correlation with their physical properties. I focussed on two groups of materials: perovskites and layered lithium-ion battery cathode materials, where, in collaboration with other groups, we tried to adjust the physical properties by cation substitution.

In **Part I** and **Part II** of my thesis, I investigated the crystal structure of these two groups of materials by using advanced transmission electron microscopy (TEM) in both reciprocal space (i.e. electron diffraction) and real space (i.e. imaging techniques) combined with energy-dispersive X-ray spectroscopy (EDX). In the last part of my thesis, **Part III**, I extend my work to initiate the implementation of *in-situ* electron diffraction tomography using an electrochemical liquid cell in order to follow the structural changes in Li-ion cathode materials induced by electrochemical cycling.

In Part I, I studied the effect of cation substitution on the crystal structure of triple and double perovskites and the correlation to their physical properties.

I investigated the crystal structure of the series $A La_2 Fe B SbO_9$ and $A_2 LaFe_2 SbO_9$ (*A* = Ca, Sr, Ba; *B* = Ni, Co) in **Chapter 3.** In collaboration with the group of Prof. Dr. Peter Battle at Oxford University, triple perovskites containing Fe^{3+} were synthesized in an attempt to create perovskites that exhibit relaxor ferromagnetism, as was observed in $La_3Ni_2SbO_9$ [22]. Both series, unfortunately, did not show relaxor behaviour. The absence of the relaxor behaviour might be attributed to the next-nearest-neighbour (NNN) interactions that are stronger for Fe^{3+} than for Ni^{2+}. The TEM study also revealed an inhomogeneous distribution of the A and B cations, missed by XRPD and NPD, where the A and B contents vary while preserving their total net charge. We also determined that increasing the size of the substituting *A* cation (Ca < Sr < Ba) will reduce the distortions in the structure, and thus increase the symmetry.

For the ALa$_2$FeBSbO$_9$ (A = Ca, Sr; B = Ni, Co) and BaLa$_2$FeNiSbO$_9$ series, the compounds with calcium and strontium adopt the same monoclinic $P2_1/n$ symmetry, while for BaLa$_2$FeNiSbO$_9$, the A and B cation inhomogeneity results in two phases: monoclinic $P2_1/n$ and $I2/m$. The latter arises from a higher Ba content that reduces the structural distortions. All triple ALa$_2$FeBSbO$_9$ perovskites show B cation ordering between Ni/Co and Sb. As the magnetic moment between both B-sites differs, these perovskites behave as ferrimagnets at relative high Curie temperatures.

The second series A_2LaFe$_2$SbO$_9$ (A = Ca, Sr, Ba) uncovered that the degree of ordering decreases with increasing the size of the substituting A cation. Ca$_2$LaFe$_2$SbO$_9$ adopts a monoclinic $P2_1/n$ symmetry with B cation ordering between Fe and Sb. The substitution by Ba, which is much larger, results in the disordered cubic $Pm\bar{3}m$ symmetry with the formation of a few ordered nanodomains within the disordered matrix. In the case of Sr$_2$LaFe$_2$SbO$_9$, the inhomogeneity causes a significant degree of phase separation within the sample, consisting of an ordered ($I2/m$ or $I4/m$) and a disordered ($Pbnm$) phase. The variation in the degree of cation ordering leads to a change from ferrimagnetism in Ca$_2$LaFe$_2$SbO$_9$ to antiferromagnetism in Ba$_2$LaFe$_2$SbO$_9$. In both cases, the inhomogeneity results also in the presence of a spin glass phase.

I also investigated partial B cation substitution in the LN-type Zn$_2$FeBO$_6$ (B = Nb, Ta), synthesized by our collaborators at Rutgers, State University of New Jersey, in an attempt to produce multiferroics with strong magnetoelectric coupling, which is discussed in **Chapter 4**. In the case of Zn$_2$FeTaO$_6$, a weak polarization switchable component is present, which is absent in the Zn$_2$FeNbO$_6$ sample. In the TEM study, I uncovered unexpected splitting of the A cation that is related to the observed short-range order of the B cations. The splitting of the A cation could be partially responsible for the absence of robust polarization switching in these materials. These observations also allowed us to understand the interactions between the A and B cations. Comparing these results to the Mn-series Mn$_2$FeBO$_6$ (B = Nb, Ta) has shown that for a magnetic A cation the enhanced magnetic interactions, together with the hybridization of the valence band of d electrons between A- and B-site, strongly suppress the splitting displacement of A cation. However, this bonding between A and B is usually accompanied by magnetostriction and energetically disfavours ion-switching for ferroelectricity. Therefore, the incorporation of transition metals into both the A- and B-sites in LiNbO$_3$ structure can render strong magnetic interactions but is not favourable for ferroelectricity.

Finally, from the studies in **Part I**, I can also conclude that for a structure that has local deviations from the average structure, up to multiple phases being present within the crystals not only among the crystals, neutron powder diffraction and X-ray powder diffraction analyses fail in the characterization although it is not always apparent that they fail. I have shown that the local structural deviations play an important role in the physical properties, and electron microscopy is therefore necessary to explore the true structural mechanisms controlling the physical properties.

In Part II, I investigated the structure evolution of Li-ion battery cathode materials upon electrochemical cycling and the effect of synthesis and cation substitution on the crystal structure and the performance.

In the first study, discussed in **Chapter 6**, I studied the crystal structure and the structure evolution of the promising layered cathode material $Li_{1.2}Ni_{0.13}Mn_{0.54}Co_{0.13}O_2$ (LMR-NMC) upon electrochemical cycling. Our collaborators at the University of Hasselt synthesized LMR-NMC using both the solution-gel and the co-precipitation method. I first compared these two different syntheses, where I have shown that not only the composition but also the synthesis strongly affects the electrochemical properties. I found that the LMR-NMC particles synthesized by our solution-gel route possess segregation accompanied by a phase transition at selective facets: Ni-rich spinel structure at the {200} facets and Co-rich rock-salt structure at the {002} and {202} facets, which was not observed in the particles synthesized by our co-precipitation route.

In literature, these structural modifications were also reported for particles synthesized by the co-precipitation method, indicating that differences in the synthesis conditions can also lead to differences in the structure, which will affect the electrochemical properties.

In **Chapter 7** and **Chapter 8**, I studied the crystal structure of two series of cation substitution in an attempt to mitigate the voltage fade observed in these lithium-rich manganese-based layered oxides: $Li_{1.2}Ni_{0.13}Mn_{0.54}Co_{0.13}O_2$ (LMR-NMC) and Li_2MnO_3 by substituting Sn^{4+} and Ti^{4+}, respectively. The larger ionic radius of Sn and Ti and their stronger bond with oxygen are expected to reduce the transition metal (TM) migration and the oxygen release that is related to the voltage fade.

The Sn substitution in LMR-NMC (**Chapter 7**) showed that the Sn solubility is limited to 8-9% and that the substituted $Li_{1.2}Ni_{0.13}Mn_{0.54-x}Co_{0.13}Sn_xO_2$ (x = 0.027) sample preserves the monoclinic *C2/m* symmetry with honeycomb ordering within the mixed Li-TM layers. Similarly, in the study where Ti was substituted in Li_2MnO_3 (**Chapter 8**), the substituted $Li_2Mn_{0.8}Ti_{0.2}O_3$ sample preserves the monoclinic *C2/m* symmetry. Unfortunately, for both studies, the cation substitution did not stabilize the structure upon charging, and so, did not succeed in mitigating the voltage fade.

In all these studies of **Part II**, we have investigated the pristine, charged and cycled state of a specific sample *ex-situ,* which means that the sample is cycled outside the TEM and the different states had to be studied from different particles. Consequently, the initial structural defects that might be present in the investigated particle are unknown when investigating the charged or cycled state. As a result, we were unable to investigate, for example, the evolution of the stacking faults, as we showed in our studies that the amount of stacking faults varies from particle to particle which prevented us from comparing the stacking faults in the pristine, charged and cycled state. In general, investigating these samples *ex-situ* complicates the investigation of any structural changes that are directly related to charging and discharging. This investigation is needed to understand better the cause of the TM migration and structural degradation, which will help us to find better cation substitutions to stabilize the structure. This can be realized by investigating the particles *in-situ,* which is discussed in the following part: **Part III**.

Finally in Part III, I investigated the ability to acquire electron diffraction patterns from Li-ion battery cathode materials in an electrochemical liquid cell without evaporating the liquid in an attempt to follow the structural changes caused by charging and discharging.

In **Chapter 9**, I explained the steps I have undertaken in order to enable the future acquisition of electron diffraction patterns in filled electrochemical cells.

I have shown that the deposition of the particles on the SiN window is the main problem. The particles prefer to cluster on top of the non-transparent electrode and on the Si chip, which increases the liquid thickness and decreases the signal-to-noise ratio of the electron diffraction pattern. We investigated the possibility to flush the particles instead of drop-casting, but the particles are then not well attached to the SiN window and will rotate under the beam, which for our goal of electron diffraction tomography series is unacceptable. I have tried different strategies to drop-cast the particles on the window, but because of the micrometre dimension of the window and the electrode, a high-resolution deposition technique is needed to deposit the particle at the area of interest [134], which could not be performed in the current thesis due to the unavailability of the necessary equipment.

I have also compared two methods to acquire electron diffraction patterns and found that the signal-to-noise ratio for the electron diffraction patterns obtained with the microprobe scanning-TEM (STEM) method is better than for the patterns obtained with conventional selected area electron diffraction (SAED) in TEM. The microprobe STEM mode will be used as a starting point to improve the setup of these *in-situ* experiments.

Algemene conclusie

De focus van mijn thesis is het onderzoeken van de kristalstructuur van nieuwe materialen en de relatie met de overeenkomstige fysische eigenschappen. De bestudeerde materialen kunnen worden opgedeeld in twee groepen: perovskieten en gelaagde lithium-ion batterij kathode materialen. In samenwerking met andere groepen hebben we geprobeerd de fysische eigenschappen van deze materialen te verbeteren of aan te passen door kation substitutie toe te passen.

In **deel I** en **deel II** van mijn thesis heb ik de kristalstructuur van deze twee materialengroepen onderzocht met behulp van geavanceerde transmissie elektronenmicroscopie (TEM) in zowel de reciproke ruimte (elektronendiffractie) als in de reële ruimte (beeldvormingstechnieken) gecombineerd met energie dispersie X-stralen spectroscopie (EDX). In het laatste deel van mijn thesis, **deel III**, onderzoek ik de mogelijkheden om de lithium materialen te bestuderen aan de hand van *in-situ* elektronendiffractietomografie in een elektrochemische cel gevuld met vloeistof. Op deze manier kan men tijdens het laden van het lithium-ion batterij kathode materiaal, de structurele veranderingen volgen die veroorzaakt worden door het opladen en ontladen van de batterij.

In Deel I heb ik het effect van kation substitutie bestudeerd op de kristalstructuur van drievoudige en dubbele perovskieten en de relatie met de overeenkomstige fysische eigenschappen.

Ik heb de kristalstructuur van de series $A La_2 Fe B SbO_9$ en $A_2 LaFe_2 SbO_9$ (A = Ca, Sr, Ba; B = Ni, Co) onderzocht en uitgelegd in **Hoofdstuk 3**. De perovskieten met Fe^{3+} zijn gesynthetiseerd in een poging om relaxor ferromagneten te creëren, zoals $La_3Ni_2SbO_9$ [22]. Beide series vertoonden echter geen relaxor-gedrag. Dit kan gedeeltelijk worden toegeschreven aan de tweede-naaste-buur (NNN) interacties die sterker zijn voor Fe^{3+} dan voor Ni^{2+}. Daarnaast onthulde de TEM studie een inhomogene verdeling voor de A en B kationen, waarbij de A en B concentraties variëren met behoud van de totale netto lading, die de magnetische eigenschappen ook zal beïnvloeden. We hebben ook een verandering in symmetrie waargenomen als gevolg van de vervanging van het *A* kation met verschillende grootte: hoe groter het gesubstitueerde *A* kation (Ca < Sr < Ba) hoe minder vervormingen er aanwezig zijn in de structuur, en dus hoe hoger de symmetrie.

Voor de *A*La_2Fe*B*SbO_9 (*A* = Ca, Sr; *B* = Ni, Co) en $BaLa_2FeNiSbO_9$ perovskieten, kan de structuur van de calcium en strontium materialen worden beschreven door de monokliene $P2_1/n$ symmetrie, terwijl in het geval van $BaLa_2FeNiSbO_9$, de inhomogeniteit van de A en B kationen resulteert in twee fasen: monoklien $P2_1/n$ en *I2/m*, waarbij de tweede fase (*I2/m*) het gevolg is van een hogere concentratie aan Ba die de structurele vervormingen verlaagt. Alle onderzochte *A*La_2Fe*B*SbO_9 perovskieten bevatten kation ordening tussen Ni/Co en Sb. Aangezien het magnetische moment tussen beide bezette posities verschilt, zijn deze perovskieten ferrimagneten bij relatief hoge Curie temperaturen.
De TEM studie van de tweede serie $A_2LaFe_2SbO_9$ (*A* = Ca, Sr, Ba) heeft aangetoond dat naast symmetrie ook de mate van ordening verandert met de *A* kation substitutie: de mate van B kation ordening neemt af naarmate de grootte van het gesubstitueerde *A* kation toeneemt. De structuur van $Ca_2LaFe_2SbO_9$ kan worden beschreven door een monokliene $P2_1/n$ symmetrie met B kation ordening tussen Fe en Sb. De substitutie van Ba, die groter is dan La, Ca en Sr, resulteert in een ongeordende kubische $Pm\bar{3}m$ structuur met de vorming van enkele geordende nano-domeinen binnen de ongeordende matrix. In het geval van $Sr_2LaFe_2SbO_9$, veroorzaakt de inhomogeniteit de vorming van twee fasen, namelijk een geordende (*I2/m* of *I4/m*) en een ongeordende fase (*Pbnm*). De variatie in de mate van kation ordening leidt tot een verandering van ferrimagnetisme in $Ca_2LaFe_2SbO_9$ naar antiferromagnetisme in $Ba_2LaFe_2SbO_9$. In beide gevallen zorgt de inhomogeniteit van de A en B kationen ervoor dat er bij lage temperatuur een spin glass fase aanwezig is.

Vervolgens, heb ik ook gedeeltelijke B kation substitutie in de van perovskiet afgeleide LN-type fasen Zn_2Fe*B*O_6 (*B* = Nb, Ta) onderzocht in een poging om multiferroic materialen te produceren met een sterke magneto-elektrische koppeling. Dit onderzoek wordt besproken in **Hoofdstuk 4**. In het geval van Zn_2FeTaO_6 is er een zwakke schakelbare polarisatie aanwezig bij lage temperatuur, die afwezig is in Zn_2FeNbO_6. In de TEM studie heb ik een onverwachte splitsing van de A kation positie ontdekt dat verband houdt met de waargenomen korte-afstands-ordening van de B kationen. De splitsing van het A kation kan de oorzaak zijn voor de afwezigheid van robuuste schakelbare polarisatie in deze materialen. Deze waarnemingen lieten ons toe de interacties tussen de A en B kationen beter te begrijpen. De vergelijking van deze resultaten met de Mn-serie Mn_2Fe*B*O_6 (*B* = Nb, Ta) heeft aangetoond dat bij een magnetisch A kation de verhoogde magnetische interacties, samen met de hybridisatie van *d*-elektronen van de valentie band, de splitsing van de A kation positie sterk kan onderdrukken. Echter, dit gaat meestal gepaard met magnetostrictie en is nadelig voor de ionenwisseling voor

ferro-elektriciteit. De substitutie van overgangsmetalen in zowel de A als B positie in de $LiNbO_3$-structuur kan dus sterke magnetische interacties veroorzaken, maar kan ook nefast zijn voor ferro-elektriciteit.

Tot slot, kan er uit de studies in **Deel I** worden geconcludeerd dat voor een structuur die niet puur monofasisch is en een complexere structuur vertoont, de structuuranalyse gebaseerd op neutronenpoederdiffractie en X-stralen poederdiffractie kan falen, hoewel het niet altijd duidelijk is dat ze falen. Ik heb aangetoond dat lokale structurele afwijkingen een belangrijke rol spelen bij het bepalen van de fysische eigenschappen, en daarom is elektronenmicroscopie nodig om de structurele mechanismen te onderzoeken die de fysische eigenschappen bepalen.

In Deel II heb ik de structuurevolutie van Li-ion batterij kathode materialen voor en na opladen/ontladen onderzocht. Ook het effect van de synthese en kationen substitutie op de kristalstructuur en de elektrochemische eigenschappen is bestudeerd.

In de eerste studie, besproken in **Hoofdstuk 6**, heb ik de kristalstructuur en de structuurevolutie voor en na opladen en ontladen van het veelbelovende gelaagde kathode materiaal $Li_{1.2}Ni_{0.13}Mn_{0.54}Co_{0.13}O_2$ (LMR-NMC) bestudeerd. Ik heb eerst twee verschillende syntheses vergeleken: oplossing-gel en co-precipitatie, waarbij ik heb aangetoond dat niet alleen de samenstelling, maar ook de synthese de elektrochemische eigenschappen sterk beïnvloedt. In de LMR-NMC-deeltjes gesynthetiseerd door de oplossing-gel methode, is Ni en Co-segregatie aanwezig op bepaalde facetten. De segregatie is gerelateerd aan een verandering van de structuur: Ni-rijke spinelstructuur aan de {200} facetten en Co-rijke zeezout structuur aan de {002} en {202} facetten. Deze structurele veranderingen aan het oppervlak werden niet waargenomen in de deeltjes die werden gesynthetiseerd door de co-precipitatie methode. In de literatuur zijn er echter studies waarin deze structurele veranderingen wel zijn waargenomen voor deeltjes die zijn gesynthetiseerd met de co-precipitatie methode, wat aangeeft dat zelfs met dezelfde type synthese kleine verschillen in de synthesemethode kunnen leiden tot structurele veranderingen die vervolgens zullen resulteren in verschillen in de elektrochemische eigenschappen.

In **Hoofdstuk 7** en **Hoofdstuk 8** heb ik de kristalstructuur van twee reeksen met kation substitutie bestudeerd in een poging het spanningsverlies in lithiumrijke mangaan gebaseerde gelaagde oxiden te verminderen: $Li_{1.2}Ni_{0.13}Mn_{0.54}Co_{0.13}O_2$ (LMR-NMC) en Li_2MnO_3. Het spanningsverlies is gerelateerd aan zuurstofverlies en een fasetransformatie naar de spinelstructuur. Daarom hebben we geprobeerd Mn te vervangen door kationen (M = Ti^{4+}, Sn^{4+}) die sterkere M-O-bindingen vormen en een grotere ionenstraal hebben, om op deze manier de transitiemetaal (TM)-migratie en het zuurstofverlies te verminderen.
De studie van de Sn-substitutie in LMR-NMC (**Hoofdstuk 7**) heeft aangetoond dat de oplosbaarheid van Sn gelimiteerd is tot ongeveer 8-9%, en dat het gesubstitueerde $Li_{1.2}Ni_{0.13}Mn_{0.54-x}Co_{0.13}Sn_xO_2$ (x = 0.027) sample een monokliene *C2/m* symmetrie heeft met een honingraatordening binnen de gemengde Li-TM lagen. Gelijkaardig, toont de studie waarin Ti werd gesubstitueerd in Li_2MnO_3 (**Hoofdstuk 8**) aan dat ook hier de structuur van het gesubstitueerde $Li_2Mn_{0.8}Ti_{0.2}O_3$ materiaal de monokliene *C2/m* symmetrie behoudt. Helaas, voor beide studies zorgt de kation substitutie niet voor een stabilisatie van de structuur tijdens het opladen en ontladen en slagen we er bijgevolg niet in om met deze strategie het spanningsverlies te verminderen.

Voor alle studies van **Deel II** geldt dat het niet mogelijk is om eenzelfde deeltje van een bepaald materiaal te bekijken in de pristine, opgeladen en ontladen toestand, doordat de deeltjes *ex-situ* worden bestudeerd, wat betekent dat het materiaal buiten de microscoop wordt opgeladen en ontladen, en dus verschillende deeltjes worden onderzocht. Bijgevolg is de voorkennis van de initiële lokale structurele defecten die aanwezig kunnen zijn onbekend bij het onderzoeken van een deeltje in de geladen toestand. Als gevolg hiervan is het niet mogelijk om bijvoorbeeld de evolutie van de stapelfouten te onderzoeken. Onze studies tonen aan dat de hoeveelheid stapelfouten varieert van deeltje tot deeltje, waardoor de hoeveelheid stapelfouten in de verschillende toestanden niet kan worden vergeleken. In het algemeen, wordt het onderzoek naar de structurele veranderingen die veroorzaakt zijn door opladen en ontladen bemoeilijkt doordat de deeltjes *ex-situ* bestudeerd worden. Het onderzoeken van eenzelfde deeltje is nodig om de oorzaak van de TM migratie en structurele afbraak beter te begrijpen dat op zijn beurt nodig is om erachter te komen welke kation substitutie leidt tot stabilisatie van de structuur. Dit kan worden gerealiseerd door de deeltjes *in-situ* te onderzoeken, wat in het volgende deel wordt besproken: **Deel III**.

Ten slotte heb ik in Deel III de mogelijkheden onderzocht om elektrondiffractiepatronen op te nemen van Li-ion batterij kathode materialen in een elektrochemische cel gevuld met vloeistof. Op deze manier kunnen de structurele veranderingen die veroorzaakt worden door laden en ontladen direct worden onderzocht.

In **Hoofdstuk 9** heb ik stapsgewijs uitgelegd wat ik heb onderzocht om de toekomstige opname van elektronendiffractiepatronen in gevulde elektrochemische cellen mogelijk te maken. Uit ons onderzoek is gebleken dat het deponeren van de deeltjes op het SiN membraan van de chip het grootste probleem is dat moet worden opgelost. Het is waarschijnlijker dat de deeltjes bovenop de niet transparante elektroden clusteren in plaats van op het transparante membraan, wat resulteert in een toename van de vloeistofdikte en vervolgens een drastisch verlaagde signaal-ruisverhouding van het elektronendiffractiepatroon oplevert.
We hebben de mogelijkheid onderzocht om de deeltjes door de nano-cel te spoelen in plaats van te deponeren, maar de deeltjes bevestigen dan niet goed aan het SiN membraan. Vervolgens zullen de deeltjes roteren onder de elektronenbundel, wat voor ons doel, namelijk elektronendiffractietomografie, niet werkbaar is. Ik heb verschillende strategieën toegepast om de deeltjes op het membraan te deponeren, maar vanwege de micrometer-afmeting van het membraan en de elektrode is een depositietechniek met hoge resolutie nodig [128]. Dit is de volgende stap om dit *in-situ* onderzoek mogelijk te maken, waarvoor nieuwe apparatuur nodig is.
Ik heb ook twee methoden vergeleken om elektronendiffractiepatronen op te nemen. In deze studie heb ik ontdekt dat de signaal-ruisverhouding voor de elektronendiffractiepatronen verkregen met de microprobe scanning-TEM (STEM)-methode beter is dan voor de patronen verkregen met conventionele SAED in TEM. De microprobe STEM-methode zal als beginpunt worden gebruikt om deze *in-situ* experimenten te verbeteren.

Outlook

The research about the cation substitution in perovskites presented in this thesis has opened a number of research lines that can be further investigated. The complexity of the crystal structure of cation substituted perovskites due to short-range order or the coexistence of multiple phases hinders the XRPD and NPD refinement. Therefore, another strategy to refine the crystal structure is to use electron diffraction tomography (EDT). EDT is based on the acquisition of a series of electron diffraction patterns by tilting a crystal around a random single axis, of which the complete structure can be refined. EDT has already been successfully used for quantitative structural characterization of numerous materials [138–140]. By extending the refinement to multiple phases, it might be possible to refine both phases present in the structure. In electron diffraction, we showed that we could distinguish both phases, and thus, it should be possible to also distinguish both phases in the 3D reconstructed reciprocal lattice.

In the continuation of my research on Li-ion battery cathode materials, I aim to enable the *in-situ* experiments in liquid. The ability to investigate the crystal structure of the same particle of a Li-ion battery cathode material in different stages (i.e. pristine, charged and discharged), will enable us to follow the evolution of the crystal structure upon cycling and correlate it to the electrochemical performance. These *in-situ* experiments would help understanding better which electrochemical processes are related with which structural changes in order to choose better the possible cation substitutions.

In order to succeed in these *in-situ* experiments, I will first focus on optimizing the deposition of the particles at the side of the electrode without forming clusters. Besides the particle preparation, I will also focus on the optimization of the TEM conditions to improve the signal-to-noise ratio of the electron diffraction patterns without damaging the electrolyte and the investigated material. When I succeed in acquiring qualitative electron diffraction patterns, I will extend the experiment to the acquisition of an EDT series, and characterize the crystal structure in different stages and for different cycles. For example for the Ti-doped Li_2MnO_3 sample, I only investigated the crystal structure before and after 50 cycles, while the capacity fluctuates (first increases from 20 mAh/g to 70 mAh/g and then drops to 40 mAh/g) within these 50 cycles. In *ex-situ* experiments, the cathode materials can only be investigated when the electrochemical cell is opened, which prevents the researcher from investigating the

material every 10 cycles to follow the structural changes. With *in-situ* TEM, I will be able to investigate the crystal structure of the Ti-doped Li_2MnO_3 at, for example, every 5 cycles to study whether these fluctuations are caused by changes in the structure, while at this point one can only suggest the reason for the observed fluctuations.

Scientific contribution

Publications related to this PhD work

Ferrimagnetism as a consequence of unusual cation ordering in the perovskite $SrLa_2FeCoSbO_9$

Y. Tang, E. C. Hunter, M. Hendrickx, J. M. Cadogan, J. Hadermann and P. D. Battle. *Inorganic chemistry*, 57, 12, 7438-7445, **2018**

$CaLa_2FeCoSbO_9$ and $ALa_2FeNiSbO_9$ (A = Ca, Sr, Ba): cation-ordered, inhomogeneous, ferrimagnetic perovskites

M. Hendrickx, Y. Tang, E. C. Hunter, P. D. Battle, J.M. Cadogan and J. Hadermann.
Journal of Solid State Chemistry, 285, 121226, **2020**

Universal A-cation splitting in LiNbO3-type structure driven by intrapositional multivalent coupling

Y. H., Y. Zeng, M. Hendrickx, J. Hadermann, P. W. Stephens, C. Zhu, C. P. Grams, J. Hemberger, C. E. Frank, S. Li, M. Wu, M. Retuerto, M. Croft, D. Walker, D. Yao, M. Greenblatt, and M. Li
Journal of the American Chemical Society, 142, 15, **2020**

An in-depth study of Sn substitution in Li-rich/Mn-rich NMC as a cathode material for Li-ion batteries

A. Paulus, M. Hendrickx, M. Bercx, O. M. Karakulina, M. A. Kirsanova, D. Lamoen, J. Hadermann, A. M. Abakumov, M. K. Van Bael and A. Hardy.
Dalton Transactions, Advance Article, **2020**

Publications not discussed in this PhD work

Crystal structure study of manganese and titanium substituted $BaLaFe_2O_6$
A. B. Hafsia, M. Hendrickx**,** M. Batuk, M. Khitouni, J. Hadermann, J.-M. Greneche and N. Rammeh
Journal of Solid State Chemistry, 251, 186-193, **2017**

Comparative study of the magnetic properties of $La_3Ni_2B'O_9$ for B' = Nb, Ta or Sb
C.-M. Chin, P.D. Battle, S. J. Blundell, E. Hunter, F. M. Lang, M. Hendrickx, R. P. Sena and J. Hadermann
Journal of Solid State Chemistry, 258, 825-834, **2018**

Tetragonal $Cs_{1.17}In_{0.81}Cl_3$: A charge-ordered Indium Halide Perovskite Derivative
X. Tan, P. W. Stephens, M. Hendrickx, J. Hadermann, C. U. Segre, M. Croft, C.-J. Kang, Z. Deng, S. H. Lapidus, S. W. Kim, C. Jin, G. Kotliar and M. Greenblatt.
Chemistry of Materials, 31, 6, 1981-1989, **2019**

M**agnetic properties of $La_3Ni_2Sb_xTa_yNb_{1-x-y}O_9$: from relaxor to spin glass**
C.-M. Chin, P. D. Battle, E. C. Hunter, M. Avdeev, M. Hendrickx and J. Hadermann.
Journal of Solid Chemistry, 273, 175-185, **2019**

Stabilization of magnetic ordering in $La_3Ni_{2-x}Cu_xBO_9$ (*B*=Sb, Ta, Nb) by the introduction of Cu^{2+}
C.-M. Chin, P. D. Battle, E. C. Hunter, M. Avdeev, M. Hendrickx and J. Hadermann.
Journal of Solid State Chemistry, 276, 164-172, **2019**

Nanoscale photovoltage mapping in CZTSe/Cu_xSe heterostructure by using kelvin probe force microscopy
M. Vishwakarma, D. Varandani, M. Hendrickx, J. Hadermann and B.R. Mehta.
Materials Research Express, 7, 016418, **2020**

Publications in preparation:

Understanding the role of local coordination environment on the coupling between cationic and anionic redox chemistry in Ti^{4+} substituted Li_2MnO_3 as a cathode material for Li-ion batteries

A. Paulus, M. Hendrickx, M. Batuk, G. Reekmans, A. M. Abakumov, P. Adriaensens, J. Hadermann, M. K. Van Bael and A. Hardy

Structural and Magnetic Properties of the Perovskites: $A_2LaFe_2SbO_9$ (A = Ba, Sr, Ca)

M. Hendrickx, Y. Tang, E. C Hunter, P. D. Battle and J. Hadermann

Differences in microstructure and electrochemical properties of LMR-NMC upon varying the synthesis method

M. Hendrickx, A. Paulus, M. Kirsanova, A.M. Abakumov, A. Hardy, J. Hadermann

Universal occurrence of twinning in honeycomb structured lithium battery cathode materials

M. Hendrickx, A. Paulus, A. Hardy, J. Hadermann

Research Stay

University of Limerick, Ireland. 28/10/2019 – 23/11/2019

"**STEM based electron diffraction and exchange experience on the practical use of in situ electrochemistry TEM holders**"

Poster Presentations

Poster: "**Structural determination of the perovskite (La,Ba)(Mn,Fe)O_3 based on electron diffraction and XRD**"

(Presented at the Belgian Crystallography Symposium BCS-9, 26 October 2016)

Poster: "**Structural behaviour of *A*La_2Fe*B*SbO_9 (*A* = Sr, Ba; *B* = Ni, Co) perovskites at local scale**"

(Presented at the International school of Electron Crystallography, 1-10 June 2018)

Poster: "**In situ electron diffraction tomography using an electrochemical liquid cell for crystal structure determination of Li-ion battery cathode materials**"

(Presented at the Liquid Phase Electron Microscopy conference, 26-31 January 2020)

References

[1] A. J. Smith and A. J. E. Welch, *Some Mixed Metal Oxides of Perovskite Structure*, Acta Cryst **13**, 653 (1960).

[2] I. R. Shein, V. L. Kozhevnikov, and A. L. Ivanovskii, *Energy-Band Structure of the $A(Sn_{1-x}M_x)O_3$ (A = Ca, Sr, Ba; M = Mn, Fe, Co) Perovskite-Type Phases: A Search for New Magnetic Semimetals*, Semiconductors **40**, 1261 (2006).

[3] D. B. Williams and C. B. Carter, *Transmission Electron Microscopy: A Textbook for Materials Science*, 2nd ed (Springer, New York, 2008).

[4] V. K. Pecharsky and P. Y. Zavalij, editors , *Fundamentals of Crystalline State and Crystal Lattice*, in *Fundamentals of Powder Diffraction and Structural Characterization of Materials* (Springer US, Boston, MA, 2009), pp. 1–15.

[5] V. K. Pecharsky and P. Y. Zavalij, editors , *Fundamentals of Diffraction*, in *Fundamentals of Powder Diffraction and Structural Characterization of Materials* (Springer US, Boston, MA, 2009), pp. 133–149.

[6] M. D. Graef and M. E. McHenry, *Structure of Materials: An Introduction to Crystallography, Diffraction and Symmetry* (Cambridge University Press, 2007).

[7] M. Johnsson and P. Lemmens, *Crystallography and Chemistry of Perovskites*, ArXiv:Cond-Mat/0506606 (2005).

[8] V. M. Goldschmidt, *Die Gesetze der Krystallochemie*, Naturwissenschaften **14**, 477 (1926).

[9] C. J. Howard and H. T. Stokes, *Group-Theoretical Analysis of Octahedral Tilting in Perovskites*, Acta Crystallogr B Struct Sci **54**, 782 (1998).

[10] D. I. Woodward and I. M. Reaney, *Electron Diffraction of Tilted Perovskites*, Acta Crystallogr B Struct Sci **61**, 387 (2005).

[11] I. M. Reaney, E. L. Colla, and N. Setter, *Dielectric and Structural Characteristics of Ba- and Sr-Based Complex Perovskites as a Function of Tolerance Factor*, Jpn. J. Appl. Phys. **33**, 3984 (1994).

[12] A. A. Demkov and A. B. Posadas, *Introduction*, in *Integration of Functional Oxides with Semiconductors*, edited by A. A. Demkov and A. B. Posadas (Springer, New York, NY, 2014), pp. 1–24.

[13] M. W. Lufaso and P. M. Woodward, *Jahn–Teller Distortions, Cation Ordering and Octahedral Tilting in Perovskites*, Acta Crystallogr B Struct Sci **60**, 10 (2004).

[14] I. B. Bersuker, *Pseudo-Jahn–Teller Effect—A Two-State Paradigm in Formation, Deformation, and Transformation of Molecular Systems and Solids*, Chem. Rev. **113**, 1351 (2013).

[15] R. G. Pearson, *Concerning Jahn-Teller Effects*, Proc Natl Acad Sci U S A **72**, 2104 (1975).

[16] M. C. Knapp and P. M. Woodward, *A-Site Cation Ordering in $AA'BB'O_6$ Perovskites*, Journal of Solid State Chemistry **179**, 1076 (2006).

[17] G. King and P. M. Woodward, *Cation Ordering in Perovskites*, J. Mater. Chem. **20**, 5785 (2010).

[18] G. F. Newell and E. W. Montroll, *On the Theory of the Ising Model of Ferromagnetism*, Rev. Mod. Phys. **25**, 353 (1953).

[19] S. Pal Singh, *The Ising Model: Brief Introduction and Its Application*, in *Solid State Physics* (IntechOpen, 2020).

[20] S. F. Edwards and P. W. Anderson, *Theory of Spin Glasses*, J. Phys. F: Met. Phys. **5**, 965 (1975).

[21] G. Parisi, *The Order Parameter for Spin Glasses: A Function on the Interval 0-1*, J. Phys. A: Math. Gen. **13**, 1101 (1980).

[22] P. A. Joy, P. S. A. Kumar, and S. K. Date, *The Relationship between Field-Cooled and Zero-Field-Cooled Susceptibilities of Some Ordered Magnetic Systems*, J. Phys.: Condens. Matter **10**, 11049 (1998).

[23] A. A. Bokov and Z.-G. Ye, *Recent Progress in Relaxor Ferroelectrics with Perovskite Structure*, J Mater Sci **41**, 31 (2006).

[24] T. Kimura, Y. Tomioka, R. Kumai, Y. Okimoto, and Y. Tokura, *Diffuse Phase Transition and Phase Separation in Cr-Doped $Nd_{1/2}Ca_{1/2}MnO_3$: A Relaxor Ferromagnet*, Phys. Rev. Lett. **83**, 3940 (1999).

[25] P. D. Battle, S. I. Evers, E. C. Hunter, and M. Westwood, *$La_3Ni_2SbO_9$: A Relaxor Ferromagnet*, Inorg. Chem. **52**, 6648 (2013).

[26] P. D. Battle, M. Avdeev, and J. Hadermann, *The Interplay of Microstructure and Magnetism in $La_3Ni_2SbO_9$*, Journal of Solid State Chemistry **220**, 163 (2014).

[27] Y. Tokura, S. Seki, and N. Nagaosa, *Multiferroics of Spin Origin*, Rep. Prog. Phys. **77**, 076501 (2014).

[28] M. Fiebig, T. Lottermoser, D. Meier, and M. Trassin, *The Evolution of Multiferroics*, Nat Rev Mater **1**, 16046 (2016).

[29] I. Sosnowska, T. P. Neumaier, and E. Steichele, *Spiral Magnetic Ordering in Bismuth Ferrite*, J. Phys. C: Solid State Phys. **15**, 4835 (1982).

[30] T. Kimura, T. Goto, H. Shintani, K. Ishizaka, T. Arima, and Y. Tokura, *Magnetic Control of Ferroelectric Polarization*, Nature **426**, 6962 (2003).

[31] W. Eerenstein, N. D. Mathur, and J. F. Scott, *Multiferroic and Magnetoelectric Materials*, Nature **442**, 759 (2006).

[32] A. K. Kundu, *Magnetic Perovskites* (Springer India, New Delhi, 2016).

[33] C. Kursun, M. Gogebakan, E. Uludag, M. S. Bozgeyik, and F. S. Uludag, *Structural, Electrical and Magnetic Properties of Nd – A – CoO_3 (A = Sr, Ca) Perovskite Powders by Mechanical Alloying*, Scientific Reports **8**, 1 (2018).

[34] E. A. R. Assirey, *Perovskite Synthesis, Properties and Their Related Biochemical and Industrial Application*, Saudi Pharmaceutical Journal **27**, 817 (2019).

[35] M. Shang, C. Zhang, T. Zhang, L. Yuan, L. Ge, H. Yuan, and S. Feng, *The Multiferroic Perovskite $YFeO_3$*, Appl. Phys. Lett. **102**, 062903 (2013).

[36] F. Shao, Z. Y. Ren, C. J. Lu, Y. D. Yang, Q. Zhan, Z. P. Li, J. K. Chen, Y. Wu, K. K. Meng, X. G. Xu, J. Miao, and Y. Jiang, *Self-Assembled Hexagonal $Lu_{1-x}In_xFeO_3$ Nanopillars Embedded in Orthorhombic $Lu_{1-x}In_xFeO_3$ Nanoparticle Matrixes as Room-Temperature Multiferroic Thin Films for Memory Devices and Spintronic Applications*, ACS Appl. Nano Mater. **3**, 7516 (2020).

[37] M. Hendrickx, Y. Tang, E. C. Hunter, P. D. Battle, J. M. Cadogan, and J. Hadermann, *$CaLa_2FeCoSbO_9$ and $ALa_2FeNiSbO_9$ (A = Ca, Sr, Ba): Cation-Ordered, Inhomogeneous, Ferrimagnetic Perovskites*, Journal of Solid State Chemistry **285**, 121226 (2020).

[38] Y. Tang, E. C. Hunter, P. D. Battle, M. Hendrickx, J. Hadermann, and J. M. Cadogan, *Ferrimagnetism as a Consequence of Unusual Cation Ordering in the Perovskite $SrLa_2FeCoSbO_9$*, Inorg. Chem. **57**, 7438 (2018).

[39] M. T. Anderson, K. B. Greenwood, G. A. Taylor, and K. R. Poeppelmeier, *B-Cation Arrangements in Double Perovskites*, Progr in Solid State Chem **22**, 197 (1993).

[40] S. Vasala and M. Karppinen, *$A_2B'B''O_6$ Perovskites: A Review*, Progress in Solid State Chemistry **43**, 1 (2015).

[41] D. G. Franco, V. C. Fuertes, M. C. Blanco, M. T. Fernández-Díaz, R. D. Sánchez, and R. E. Carbonio, *Synthesis, Structure and Magnetic Properties of $La_3Co_2SbO_9$: A Double Perovskite with Competing Antiferromagnetic and Ferromagnetic Interactions*, Journal of Solid State Chemistry France **194**, 385 (2012).

[42] Y. Tang, E. C. Hunter, P. D. Battle, R. P. Sena, J. Hadermann, M. Avdeev, and J. M. Cadogan, *Structural Chemistry and Magnetic Properties of the Perovskite $Sr_3Fe_2TeO_9$*, Journal of Solid State Chemistry **242**, 86 (2016).

[43] *Fityk --- Curve Fitting and Peak Fitting Software — Fityk 1.3.1 Manual*, https://fityk.nieto.pl/.

[44] P. Lu, E. Romero, S. Lee, J. L. MacManus-Driscoll, and Q. Jia, *Chemical Quantification of Atomic-Scale EDS Maps under Thin Specimen Conditions*, Microscopy and Microanalysis **20**, 1782 (2014).

[45] P. Lu, J. Xiong, M. Van Benthem, and Q. Jia, *Atomic-Scale Chemical Quantification of Oxide Interfaces Using Energy-Dispersive X-Ray Spectroscopy*, Appl. Phys. Lett. **102**, 173111 (2013).

[46] C. J. Howard, B. J. Kennedy, and P. M. Woodward, *Ordered Double Perovskites – a Group-Theoretical Analysis*, Acta Cryst B **59**, 4 (2003).

[47] *Shannon Radii*, http://abulafia.mt.ic.ac.uk/shannon/ptable.php.

[48] Q. Zhou, T.-Y. Tan, B. J. Kennedy, and J. R. Hester, *Crystal Structures and Phase Transitions in Sr Doped Ba_2InTaO_6 Perovskites*, Journal of Solid State Chemistry **206**, 122 (2013).

[49] E. J. Cussen and P. D. Battle, *The Influence of Structural Disorder on the Magnetic Properties of $Sr_2Fe_{1-x}Ga_xTaO_6$ ($0 \leq x \leq 1$)*, J. Mater. Chem. **13**, 1210 (2003).

[50] S. Chanda, S. Saha, A. Dutta, B. Irfan, R. Chatterjee, and T. P. Sinha, *Magnetic and Dielectric Properties of Orthoferrites $La_{1-x}Pr_xFeO_3$ (x = 0, 0.1, 0.2, 0.3, 0.4 and 0.5)*, Journal of Alloys and Compounds **649**, 1260 (2015).

[51] A. K. Azad, A. Mellergård, S.-G. Eriksson, S. A. Ivanov, S. M. Yunus, F. Lindberg, G. Svensson, and R. Mathieu, *Structural and Magnetic Properties of $LaFe_{0.5}Cr_{0.5}O_3$ Studied by Neutron Diffraction, Electron Diffraction and Magnetometry*, Materials Research Bulletin **40**, 1633 (2005).

[52] A. K. Azad, S.-G. Eriksson, and J. T. S. Irvine, *Structural, Magnetic and Electrochemical Characterization of $La_{0.83}A_{0.17}Fe_{0.5}Cr_{0.5}O_{3-\delta}$ (A=Ba, Ca) Perovskites*, Materials Research Bulletin **44**, 1451 (2009).

[53] A. Faik, J. M. Igartua, E. Iturbe-Zabalo, and G. J. Cuello, *A Study of the Crystal Structures and the Phase Transitions of Sr_2FeSbO_6, $SrCaFeSbO_6$ and Ca_2FeSbO_6 Double Perovskite Oxides*, Journal of Molecular Structure **963**, 145 (2010).

[54] E. C. Hunter, P. D. Battle, S. J. Blundell, C. V. Topping, F. K. K. Kirschner, and F. Lang, *Muon-Spin Relaxation and AC Magnetometry Study of the Ferrimagnet $LaSr_2Cr_2SbO_9$*, Journal of Solid State Chemistry **279**, 120935 (2019).

[55] E. J. Cussen, J. F. Vente, P. D. Battle, and T. C. Gibb, *Neutron Diffraction Study of the Influence of Structural Disorderon the Magnetic Properties of Sr_2FeMO_6 (M=Ta,Sb)*, J. Mater. Chem. **7**, 459 (1997).

[56] P. Woodward, R.-D. Hoffmann, and A. W. Sleight, *Order-Disorder in $A_2M^{3+}M^{5+}O_6$ Perovskites*, J. Mater. Res. **9**, 2118 (1994).

[57] Y. Han, Y. Zeng, M. Hendrickx, J. Hadermann, P. W. Stephens, C. Zhu, C. P. Grams, J. Hemberger, C. Frank, S. Li, M. Wu, M. Retuerto, M. Croft, D. Walker, D.-X. Yao, M. Greenblatt, and M.-R. Li, *Universal A-Cation Splitting in $LiNbO_3$-Type Structure Driven by Intrapositional Multivalent Coupling*, J. Am. Chem. Soc. **142**, 7168 (2020).

[58] X. Z. Lu and H. J. Xiang, *Designing Asymmetric Multiferroics with Strong Magnetoelectric Coupling*, Phys. Rev. B **90**, 104409 (2014).

[59] P. S. Wang, W. Ren, L. Bellaiche, and H. J. Xiang, *Predicting a Ferrimagnetic Phase of Zn_2FeOsO_6 with Strong Magnetoelectric Coupling*, Phys. Rev. Lett. **114**, 147204 (2015).

[60] M.-R. Li, P. W. Stephens, M. Retuerto, T. Sarkar, C. P. Grams, J. Hemberger, M. C. Croft, D. Walker, and M. Greenblatt, *Designing Polar and Magnetic Oxides: Zn_2FeTaO_6 - in Search of Multiferroics*, J. Am. Chem. Soc. **136**, 8508 (2014).

[61] G.-H. Cai, M. Greenblatt, and M.-R. Li, *Polar Magnets in Double Corundum Oxides*, Chem. Mater. **29**, 5447 (2017).

[62] Y. Inaguma, M. Yoshida, and T. Katsumata, *A Polar Oxide $ZnSnO_3$ with a $LiNbO_3$-Type Structure*, J. Am. Chem. Soc. **130**, 6704 (2008).

[63] J. Y. Son, G. Lee, M.-H. Jo, H. Kim, H. M. Jang, and Y.-H. Shin, *Heteroepitaxial Ferroelectric $ZnSnO_3$ Thin Film*, J. Am. Chem. Soc. **131**, 8386 (2009).

[64] A. Jain, S. P. Ong, G. Hautier, W. Chen, W. D. Richards, S. Dacek, S. Cholia, D. Gunter, D. Skinner, G. Ceder, and K. A. Persson, *Commentary: The Materials Project: A Materials Genome Approach to Accelerating Materials Innovation*, APL Materials **1**, 011002 (2013).

[65] Y. Zhu, Q. Zhan, J.-C. Yang, Y. Bitla, P. Liu, C.-I. Li, H.-J. Liu, V. S. Kumar, E. Arenholz, Q. He, and Y.-H. Chu, *Enhanced Structural and Magnetic Coupling in a Mesocrystal-Assisted Nanocomposite*, ACS Appl. Mater. Interfaces **8**, 1104 (2016).

[66] M.-R. Li, D. Walker, M. Retuerto, T. Sarkar, J. Hadermann, P. W. Stephens, M. Croft, A. Ignatov, C. P. Grams, J. Hemberger, I. Nowik, P. S. Halasyamani, T. T. Tran, S. Mukherjee, T. S. Dasgupta, and M. Greenblatt, *Polar and Magnetic Mn_2FeMO_6 (M=Nb, Ta) with $LiNbO_3$ -Type Structure: High-Pressure Synthesis*, Angew. Chem. Int. Ed. **52**, 8406 (2013).

[67] T. Varga, A. Kumar, E. Vlahos, S. Denev, M. Park, S. Hong, T. Sanehira, Y. Wang, C. J. Fennie, S. K. Streiffer, X. Ke, P. Schiffer, V. Gopalan, and J. F. Mitchell, *Coexistence of Weak Ferromagnetism and Ferroelectricity in the High Pressure $LiNbO_3$-Type Phase of $FeTiO_3$*, Phys. Rev. Lett. **103**, 047601 (2009).

[68] M. Ye and D. Vanderbilt, *Domain Walls and Ferroelectric Reversal in Corundum Derivatives*, Phys. Rev. B **95**, 014105 (2017).

[69] M. Ye and D. Vanderbilt, *Ferroelectricity in Corundum Derivatives*, Phys. Rev. B **93**, 134303 (2016).

[70] M.-R. Li, E. E. McCabe, P. W. Stephens, M. Croft, L. Collins, S. V. Kalinin, Z. Deng, M. Retuerto, A. Sen Gupta, H. Padmanabhan, V. Gopalan, C. P. Grams, J. Hemberger, F. Orlandi, P. Manuel, W.-M. Li, C.-Q. Jin, D. Walker, and M. Greenblatt, *Magnetostriction-Polarization Coupling in Multiferroic Mn2MnWO6*, Nat Commun **8**, 2037 (2017).

[71] M.-R. Li, M. Croft, P. W. Stephens, M. Ye, D. Vanderbilt, M. Retuerto, Z. Deng, C. P. Grams, J. Hemberger, J. Hadermann, W.-M. Li, C.-Q. Jin, F. O. Saouma, J. I. Jang, H. Akamatsu, V. Gopalan, D. Walker, and M. Greenblatt, *Mn_2FeWO_6: A New Ni_3TeO_6 - Type Polar and Magnetic Oxide*, Adv. Mater. Weinheim **28**, 2098 (2016).

[72] M.-R. Li, X. Kuang, S. Y. Chong, Z. Xu, C. I. Thomas, H. Niu, J. B. Claridge, and M. J. Rosseinsky, *Interstitial Oxide Ion Order and Conductivity in $La_{1.64}Ca_{0.36}Ga_3O_{7.32}$ Melilite*, Angewandte Chemie International Edition **49**, 2362 (2010).

[73] I. D. Brown and R. D. Shannon, *Empirical Bond-Strength–Bond-Length Curves for Oxides*, Acta Crystallographica Section A **29**, 266 (1973).

[74] R. Hsu, E. N. Maslen, D. du Boulay, and N. Ishizawa, *Synchrotron X-Ray Studies of $LiNbO_3$ and $LiTaO_3$*, Acta Cryst B **53**, 3 (1997).

[75] C. P. Poole, H. A. Farach, R. J. Creswick, and R. Prozorov, *5 - Magnetic Properties*, in *Superconductivity (Second Edition)*, edited by C. P. Poole, H. A. Farach, R. J. Creswick, and R. Prozorov (Academic Press, Amsterdam, 2007), pp. 113–142.

[76] O. Karakulina, S. Fedotov, V. Sumanov, O. Drozhzhin, N. Khasanova, E. Antipov, A. Abakumov, and J. Hadermann, *Quantitative Electron Diffraction Tomography for the Structure Solution of Cathode Materials for Li-Ion Batteries*, in *European Microscopy Congress 2016: Proceedings*, edited by European Microscopy Society (Wiley-VCH Verlag GmbH & Co. KGaA, Weinheim, Germany, 2016), pp. 790–791.

[77] C. Julien, A. Mauger, K. Zaghib, and H. Groult, *Comparative Issues of Cathode Materials for Li-Ion Batteries*, Inorganics **2**, 132 (2014).

[78] M. S. Whittingham, *Lithium Batteries and Cathode Materials*, Chem. Rev. **104**, 4271 (2004).

[79] P. Rozier and J. M. Tarascon, *Review—Li-Rich Layered Oxide Cathodes for Next-Generation Li-Ion Batteries: Chances and Challenges*, J. Electrochem. Soc. **162**, A2490 (2015).

[80] D. Ye, G. Zeng, K. Nogita, K. Ozawa, M. Hankel, D. J. Searles, and L. Wang, *Understanding the Origin of Li_2MnO_3 Activation in Li-Rich Cathode Materials for Lithium-Ion Batteries*, Adv. Funct. Mater. **25**, 7488 (2015).

[81] D. Y. W. Yu, K. Yanagida, Y. Kato, and H. Nakamura, *Electrochemical Activities in Li_2MnO_3*, Journal of The Electrochemical Society 9 (n.d.).

[82] H. Chen and M. S. Islam, *Lithium Extraction Mechanism in Li-Rich Li_2MnO_3 Involving Oxygen Hole Formation and Dimerization*, Chem. Mater. **28**, 6656 (2016).

[83] K. Shimoda, M. Oishi, T. Matsunaga, M. Murakami, K. Yamanaka, H. Arai, Y. Ukyo, Y. Uchimoto, T. Ohta, E. Matsubara, and Z. Ogumi, *Direct Observation of Layered-to-Spinel Phase Transformation in Li_2MnO_3 and the Spinel Structure Stabilised after the Activation Process*, J. Mater. Chem. A **5**, 6695 (2017).

[84] W. Yin, A. Grimaud, G. Rousse, A. M. Abakumov, A. Senyshyn, L. Zhang, S. Trabesinger, A. Iadecola, D. Foix, D. Giaume, and J.-M. Tarascon, *Structural Evolution at the Oxidative and Reductive Limits in the First Electrochemical Cycle of $Li_{1.2}Ni_{0.13}Mn_{0.54}Co_{0.13}O_2$*, Nat Commun **11**, 1252 (2020).

[85] G. Wang, L. Yi, R. Yu, X. Wang, Y. Wang, Z. Liu, B. Wu, M. Liu, X. Zhang, X. Yang, X. Xiong, and M. Liu, *$Li_{1.2}Ni_{0.13}Co_{0.13}Mn_{0.54}O_2$ with Controllable Morphology and Size for High Performance Lithium-Ion Batteries*, ACS Appl. Mater. Interfaces **9**, 25358 (2017).

[86] H. Koga, L. Croguennec, P. Mannessiez, M. Ménétrier, F. Weill, L. Bourgeois, M. Duttine, E. Suard, and C. Delmas, *$Li_{1.20}Mn_{0.54}Co_{0.13}Ni_{0.13}O_2$ with Different Particle Sizes as Attractive Positive Electrode Materials for Lithium-Ion Batteries: Insights into Their Structure*, J. Phys. Chem. C **116**, 13497 (2012).

[87] G. Assat and J.-M. Tarascon, *Fundamental Understanding and Practical Challenges of Anionic Redox Activity in Li-Ion Batteries*, Nat Energy **3**, 373 (2018).

[88] K. Kleiner, B. Strehle, A. R. Baker, S. J. Day, C. C. Tang, I. Buchberger, F.-F. Chesneau, H. A. Gasteiger, and M. Piana, *Origin of High Capacity and Poor Cycling Stability of Li-Rich Layered Oxides: A Long-Duration in Situ Synchrotron Powder Diffraction Study*, Chem. Mater. **30**, 3656 (2018).

[89] A. Van der Ven and G. Ceder, *Ordering in $Lix(Ni_{0.5}Mn_{0.5})O_2$ and Its Relation to Charge Capacity and Electrochemical Behavior in Rechargeable Lithium Batteries*, Electrochemistry Communications **6**, 1045 (2004).

[90] J. Bréger, M. Jiang, N. Dupré, Y. S. Meng, Y. Shao-Horn, G. Ceder, and C. P. Grey, *High-Resolution X-Ray Diffraction, DIFFaX, NMR and First Principles Study of Disorder in the Li_2MnO_3–$Li[Ni_{1/2}Mn_{1/2}]O_2$ Solid Solution*, Journal of Solid State Chemistry **178**, 2575 (2005).

[91] G. Assat, D. Foix, C. Delacourt, A. Iadecola, R. Dedryvère, and J.-M. Tarascon, *Fundamental Interplay between Anionic/Cationic Redox Governing the Kinetics and Thermodynamics of Lithium-Rich Cathodes*, Nat Commun **8**, 2219 (2017).

[92] Z. Q. Deng and A. Manthiram, *Influence of Cationic Substitutions on the Oxygen Loss and Reversible Capacity of Lithium-Rich Layered Oxide Cathodes*, J. Phys. Chem. C **115**, 7097 (2011).

[93] Z. He, Z. Wang, H. Chen, Z. Huang, X. Li, H. Guo, and R. Wang, *Electrochemical Performance of Zirconium Doped Lithium Rich Layered $Li_{1.2}Mn_{0.54}Ni_{0.13}Co_{0.13}O_2$ Oxide with Porous Hollow Structure*, Journal of Power Sources **299**, 334 (2015).

[94] G. Kang, K. Lee, K. Kwon, and J. Song, *The Effects of Incorporated Sn in Resynthesized Ni-Rich Cathode Materials on Their Lithium-Ion Battery Performance*, Metals **7**, 395 (2017).

[95] M. Sathiya, G. Rousse, K. Ramesha, C. P. Laisa, H. Vezin, M. T. Sougrati, M.-L. Doublet, D. Foix, D. Gonbeau, W. Walker, A. S. Prakash, M. Ben Hassine, L. Dupont, and J.-M. Tarascon, *Reversible Anionic Redox Chemistry in High-Capacity Layered-Oxide Electrodes*, Nature Mater **12**, 827 (2013).

[96] V. Etacheri, *Sol-Gel Processed Cathode Materials for Lithium-Ion Batteries*, in *Sol-Gel Materials for Energy, Environment and Electronic Applications*, edited by S. C. Pillai and S. Hehir (Springer International Publishing, Cham, 2017), pp. 155–195.

[97] H. Dong and G. M. Koenig, *A Review on Synthesis and Engineering of Crystal Precursors Produced* via *Coprecipitation for Multicomponent Lithium-Ion Battery Cathode Materials*, CrystEngComm **22**, 1514 (2020).

[98] R. Santhanam and B. Rambabu, *High Rate Cycling Performance of $Li_{1.05}Ni_{1/3}Co_{1/3}Mn_{1/3}O_2$ Materials Prepared by Sol–Gel and Co-Precipitation Methods for Lithium-Ion Batteries*, Journal of Power Sources **195**, 4313 (2010).

[99] P. Lu, P. Yan, E. Romero, E. D. Spoerke, J.-G. Zhang, and C.-M. Wang, *Observation of Electron-Beam-Induced Phase Evolution Mimicking the Effect of the Charge–Discharge Cycle in Li-Rich Layered Cathode Materials Used for Li Ion Batteries*, Chem. Mater. **27**, 1375 (2015).

[100] A. K. Shukla, Q. M. Ramasse, C. Ophus, H. Duncan, F. Hage, and G. Chen, *Unravelling Structural Ambiguities in Lithium- and Manganese-Rich Transition Metal Oxides*, Nat Commun **6**, 8711 (2015).

[101] M. T. Tung and V. D. Luong, *Electrochemical Properties of $LiNi_{0.8}Co_{0.1}Mn_{0.1}O_2$ Synthesized by Sol-Gel and Co-Precipitation Methods*, Vietnam Journal of Chemistry **54**, 6 (2016).

[102] P. Yan, J. Zheng, J. Xiao, C.-M. Wang, and J.-G. Zhang, *Recent Advances on the Understanding of Structural and Composition Evolution of LMR Cathodes for Li-Ion Batteries*, Front. Energy Res. **3**, (2015).

[103] B. Hai, A. K. Shukla, H. Duncan, and G. Chen, *The Effect of Particle Surface Facets on the Kinetic Properties of $LiMn_{1.5}Ni_{0.5}O_4$ Cathode Materials*, J. Mater. Chem. A **1**, 759 (2013).

[104] P. Yan, J. Zheng, J. Zheng, Z. Wang, G. Teng, S. Kuppan, J. Xiao, G. Chen, F. Pan, J.-G. Zhang, and C.-M. Wang, *Ni and Co Segregations on Selective Surface Facets and Rational Design of Layered Lithium Transition-Metal Oxide Cathodes*, Adv. Energy Mater. **6**, 1502455 (2016).

[105] J. Zheng, M. Gu, A. Genc, J. Xiao, P. Xu, X. Chen, Z. Zhu, W. Zhao, L. Pullan, C. Wang, and J.-G. Zhang, *Mitigating Voltage Fade in Cathode Materials by Improving the Atomic Level Uniformity of Elemental Distribution*, Nano Lett. **14**, 2628 (2014).

[106] K. A. Jarvis, C.-C. Wang, J. C. Knight, L. Rabenberg, A. Manthiram, and P. J. Ferreira, *Formation and Effect of Orientation Domains in Layered Oxide Cathodes of Lithium-Ion Batteries*, Acta Materialia **108**, 264 (2016).

[107] fengwang, *QSTEM: Quantitative TEM/STEM Simulations — Strukturforschung / Elektronenmikroskopie*,https://www.physik.huberlin.de/en/sem/software/software_qstem.

[108] A. Paulus, M. Hendrickx, M. Bercx, O. M. Karakulina, M. A. Kirsanova, D. Lamoen, J. Hadermann, A. M. Abakumov, M. K. V. Bael, and A. Hardy, *An In-Depth Study of Sn Substitution in Li-Rich/Mn-Rich NMC as a Cathode Material for Li-Ion Batteries*, Dalton Trans. **49**, 10486 (2020).

[109] K. Luo, M. R. Roberts, R. Hao, N. Guerrini, D. M. Pickup, Y.-S. Liu, K. Edström, J. Guo, A. V. Chadwick, L. C. Duda, and P. G. Bruce, *Charge-Compensation in 3d-Transition-Metal-Oxide Intercalation Cathodes through the Generation of Localized Electron Holes on Oxygen*, Nature Chem **8**, 684 (2016).

[110] K. Shimoda, T. Minato, K. Nakanishi, H. Komatsu, T. Matsunaga, H. Tanida, H. Arai, Y. Ukyo, Y. Uchimoto, and Z. Ogumi, *Oxidation Behaviour of Lattice Oxygen in Li-Rich Manganese-Based Layered Oxide Studied by Hard X-Ray Photoelectron Spectroscopy*, J. Mater. Chem. A **4**, 5909 (2016).

[111] Q.-Q. Qiao, L. Qin, G.-R. Li, Y.-L. Wang, and X.-P. Gao, *Sn-Stabilized Li-Rich Layered $Li(Li_{0.17}Ni_{0.25}Mn_{0.58})O_2$ Oxide as a Cathode for Advanced Lithium-Ion Batteries*, J. Mater. Chem. A **3**, 17627 (2015).

[112] L. Zhou, J. Liu, L. Huang, N. Jiang, Q. Zheng, and D. Lin, *Sn-Doped $Li_{1.2}Mn_{0.54}Ni_{0.13}Co_{0.13}O_2$ Cathode Materials for Lithium-Ion Batteries with Enhanced Electrochemical Performance*, J Solid State Electrochem **21**, 3467 (2017).

[113] J. Mou, Y. Deng, Z. Song, Q. Zheng, K. H. Lam, and D. Lin, *Excellent Rate Capability and Cycling Stability in Li^+-Conductive Li_2SnO_3-Coated $LiNi_{0.5}Mn_{1.5}O_4$ Cathode Materials for Lithium-Ion Batteries*, Dalton Trans. **47**, 7020 (2018).

[114] W. Sun, S. T. Dacek, S. P. Ong, G. Hautier, A. Jain, W. D. Richards, A. C. Gamst, K. A. Persson, and G. Ceder, *The Thermodynamic Scale of Inorganic Crystalline Metastability*, Science Advances **2**, e1600225 (2016).

[115] K. G. Gallagher, J. R. Croy, M. Balasubramanian, M. Bettge, D. P. Abraham, A. K. Burrell, and M. M. Thackeray, *Correlating Hysteresis and Voltage Fade in Lithium- and Manganese-Rich Layered Transition-Metal Oxide Electrodes*, Electrochemistry Communications **33**, 96 (2013).

[116] N. Yabuuchi, K. Yoshii, S.-T. Myung, I. Nakai, and S. Komaba, *Detailed Studies of a High-Capacity Electrode Material for Rechargeable Batteries, Li_2MnO_3−$LiCo_{1/3}Ni_{1/3}Mn_{1/3}O_2$*, J. Am. Chem. Soc. **133**, 4404 (2011).

[117] P. Lanz, H. Sommer, M. Schulz-Dobrick, and P. Novák, *Oxygen Release from High-Energy $xLi_2MnO_3{\cdot}(1-x)LiMO_2$ (M=Mn, Ni, Co): Electrochemical, Differential Electrochemical Mass Spectrometric, in Situ Pressure, and in Situ Temperature Characterization*, Electrochimica Acta **93**, 114 (2013).

[118] Z. Lu, L. Y. Beaulieu, R. A. Donaberger, C. L. Thomas, and J. R. Dahn, *Synthesis, Structure, and Electrochemical Behavior of $Li[Ni_xLi_{1/3-2x/3}Mn_{2/3-x/3}]O_2$*, J. Electrochem. Soc. **149**, A778 (2002).

[119] D.-H. Seo, J. Lee, A. Urban, R. Malik, S. Kang, and G. Ceder, *The Structural and Chemical Origin of the Oxygen Redox Activity in Layered and Cation-Disordered Li-Excess Cathode Materials*, Nature Chem **8**, 7 (2016).

[120] W. Zhao, M. Oyama, H. Yamada, and H. Noguchi, *Influence of Ti Substitution on the Structure and Electrochemical Properties of Lithium-Excess Layered Manganese Based Oxide for Lithium Ion Batteries*, Electrochimica Acta **168**, 157 (2015).

[121] S. Yamamoto, H. Noguchi, and W. Zhao, *Improvement of Cycling Performance in Ti Substituted $0.5Li_2MnO_3$–$0.5LiNi_{0.5}Mn_{0.5}O_2$ through Suppressing Metal Dissolution*, Journal of Power Sources **278**, 76 (2015).

[122] S.-H. Park, Y. Sato, J.-K. Kim, and Y.-S. Lee, *Powder Property and Electrochemical Characterization of Li_2MnO_3 Material*, Materials Chemistry and Physics **102**, 225 (2007).

[123] A. D. Robertson and P. G. Bruce, *Mechanism of Electrochemical Activity in Li_2MnO_3*, Chem. Mater. **15**, 1984 (2003).

[124] S. H. Park, H. S. Ahn, G. J. Park, J. Kim, and Y. S. Lee, *Cycle Mechanism and Electrochemical Properties of Lithium Manganese Oxide Prepared Using Different Mn Sources*, Materials Chemistry and Physics **112**, 696 (2008).

[125] F. Zheng, X. Ou, Q. Pan, X. Xiong, C. Yang, and M. Liu, *The Effect of Composite Organic Acid (Citric Acid & Tartaric Acid) on Microstructure and Electrochemical Properties of $Li_{1.2}Mn_{0.54}Ni_{0.13}Co_{0.13}O_2$ Li-Rich Layered Oxides*, Journal of Power Sources **346**, 31 (2017).

[126] A. Hardy, J. D'Haen, M. K. Van Bael, and J. Mullens, *An Aqueous Solution–Gel Citratoperoxo–Ti(IV) Precursor: Synthesis, Gelation, Thermo-Oxidative Decomposition and Oxide Crystallization*, J Sol-Gel Sci Technol **44**, 65 (2007).

[127] U. Kolb, T. Gorelik, and M. T. Otten, *Towards Automated Diffraction Tomography. Part II—Cell Parameter Determination*, Ultramicroscopy **108**, 763 (2008).

[128] U. Kolb, T. Gorelik, C. Kübel, M. T. Otten, and D. Hubert, *Towards Automated Diffraction Tomography: Part I—Data Acquisition*, Ultramicroscopy **107**, 507 (2007).

[129] N. de Jonge and F. M. Ross, *Electron Microscopy of Specimens in Liquid*, Nature Nanotech **6**, 695 (2011).

[130] M. Tanase, J. Winterstein, R. Sharma, V. Aksyuk, G. Holland, and J. A. Liddle, *High-Resolution Imaging and Spectroscopy at High Pressure: A Novel Liquid Cell for the Transmission Electron Microscope*, Microsc Microanal **21**, 1629 (2015).

[131] O. M. Karakulina, A. Demortière, W. Dachraoui, A. M. Abakumov, and J. Hadermann, *In Situ Electron Diffraction Tomography Using a Liquid-Electrochemical Transmission Electron Microscopy Cell for Crystal Structure Determination of Cathode Materials for Li-Ion Batteries*, Nano Lett. **18**, 6286 (2018).

[132] *SEM: Types of Electrons and the Information They Provide*, https://www.thermofisher.com/blog/microscopy/sem-types-electrons-and-the-information-they-provide/.

[133] N. Ortiz Peña, D. Ihiawakrim, M. Han, B. Lassalle-Kaiser, S. Carenco, C. Sanchez, C. Laberty-Robert, D. Portehault, and O. Ersen, *Morphological and Structural Evolution of Co_3O_4 Nanoparticles Revealed by* in Situ *Electrochemical Transmission Electron Microscopy during Electrocatalytic Water Oxidation*, ACS Nano **13**, 11372 (2019).

[134] T. Tarnev, S. Cychy, C. Andronescu, M. Muhler, W. Schuhmann, and Y. Chen, *A Universal Nano-capillary Based Method of Catalyst Immobilization for Liquid-Cell Transmission Electron Microscopy*, Angew. Chem. Int. Ed. **59**, 5586 (2020).

[135] K. J. Ganesh, M. Kawasaki, J. P. Zhou, and P. J. Ferreira, *D-STEM: A Parallel Electron Diffraction Technique Applied to Nanomaterials*, Microsc Microanal **16**, 614 (2010).

[136] D. Alloyeau, C. Ricolleau, T. Oikawa, C. Langlois, Y. Le Bouar, and A. Loiseau, *STEM Nanodiffraction Technique for Structural Analysis of CoPt Nanoparticles*, Ultramicroscopy **108**, 656 (2008).

[137] A. Khelfa, C. Byun, J. Nelayah, G. Wang, C. Ricolleau, and D. Alloyeau, *Structural Analysis of Single Nanoparticles in Liquid by Low-Dose STEM Nanodiffraction*, Micron **116**, 30 (2019).

[138] L. Palatinus, M. Klementová, V. Dřínek, M. Jarošová, and V. Petříček, *An Incommensurately Modulated Structure of H'-Phase of $Cu_{3+x}Si$ Determined by Quantitative Electron Diffraction Tomography*, Inorg. Chem. **50**, 3743 (2011).

[139] Y.-B. Zhang, J. Su, H. Furukawa, Y. Yun, F. Gándara, A. Duong, X. Zou, and O. M. Yaghi, *Single-Crystal Structure of a Covalent Organic Framework*, J. Am. Chem. Soc. **135**, 16336 (2013).

[140] Q. Sun, Y. Ma, N. Wang, X. Li, D. Xi, J. Xu, F. Deng, K. B. Yoon, P. Oleynikov, O. Terasaki, and J. Yu, *High Performance Nanosheet-like Silicoaluminophosphate Molecular Sieves: Synthesis, 3D EDT Structural Analysis and MTO Catalytic Studies*, J. Mater. Chem. A **2**, 17828 (2014).

Acknowledgement

First of all, I want to express my gratitude to my supervisor Prof. Dr. Joke Hadermann for her guidance over the years and giving me the opportunity to start a PhD. I decided to do my bachelor's thesis with Joke, after she introduced me to Crystallography during the class *Structuur van de Vaste Stof,* where my interest in materials science and electron microscopy started. Now, seven years later, after a bachelor's thesis, a master's thesis and a doctoral thesis, I want to thank Joke for allowing me to develop as a scientist. She helped me push my boundaries and encouraged me to pursue goals that I would not have achieved without her support.

I want to thank the members of my doctoral committee: Prof. Dr. Jan Sijbers, Prof. Dr. Sofie Cambré, Prof. Dr. Dirk Lamoen, Prof. Dr. An Hardy and Prof. Dr. Peter Battle for taking the time to carefully read my thesis, provide valuable comments and participate in discussion.

I want to acknowledge all collaborators of the group of Prof. Dr. Peter Battle of the University of Oxford, the group of Prof. Dr. Martha Greenblatt of the University of Rutgers and the group of Prof. Dr. An Hardy of the University of Hasselt for providing me with very interesting and beautiful samples. In addition, I would like to thank all EMAT members for their contributions and support during my PhD, the scientific discussions and the pleasant moments during our working days.

I want to specially express my gratitude to my (past) colleagues of the research group of Joke: Dmitry, Maria, Robert, Olesia, Carolien, Stefano and Romy, who supported me at any time and shared knowledge and experience.

Also special thanks to Daniel, Adrian and Liesbet for the relaxing coffee moments during the day which were accompanied by both scientific as well as amusing non-scientific conversations. A very special thanks to two colleagues that became very good friends over the years. First of all, thank you Eva for the support during all the years. In both professional and private life, you were always there to advise and encourage me when I doubted myself. I hope we will spend many more years as good friends and colleagues! Secondly, I would like to thank Hans, with whom I started my bachelor 9 years ago. We have been through every step from

student to doctor together. From the first moment we met each other, I could say literally *anything* to you that came to my mind. Thank you for all the conversations, walks, advice and drinks during all these years!

Finally, I want to thank my family and friends for always believing in me and listening to me when I was talking about work even if it was not always clear what I was actually doing during these four years. A special thank you to my parents and my sister for supporting me, not only during the past four years but my whole life. I want to thank my friends for always being there when I needed a moment to clear my mind, to relax and to have fun.
Most of all I want to thank my boyfriend, Tobias, who was always there, every up and down during this journey we experienced together. You always make me realize that I stress about the smallest things and that I have to let go from time to time. I could not have done this without you. Thank you for being there for me, Tobias.